OAK RIDGE NATIONAL LABORATORY LIBRARY

3 4456 0043900 5

ORNL/SUB/76-01617/18

DEVELOPMENT PROGRAM FOR A 200 KW, CW, 28 GHz GYROKLYSTRON

J. Shively, C. Conner, S. Evans, F. Friedlander, E. Galli, S. Hegji, H. Jory, F. Kinney, A. LaRue, K. Miller, J. Moran, W. Sayer, D. Stone, R. Symons, N. Taylor and G. Thomas

FINAL REPORT

FUSION ENERGY DIVISION LIBRARY

APRIL 1976 THROUGH SEPTEMBER 1980

FED LIBRARY JUN 22 1995

Prepared for
Oak Ridge National Laboratory
Oak Ridge, Tennessee 37830

Operated by
Union Carbide Corporation

For the
U.S. Department of Energy

Contract No. W-7405-eng-26

Varian Associates, Inc.
Microwave Tube Division
611 Hansen Way
Palo Alto, California 94303

Printed in the United States of America. Available from:
National Technical Information Service
U.S. Department of Commerce
5255 Port Royal Road, Springfield, Virginia 22161
NTIS price codes — Printed Copy: A-12 Microfiche A01

This report was prepared as an account of work sponsored by an agency of the United States Government. Neither the United States Government nor any agency thereof, nor any of their employees, makes any warranty, express or implied, or assumes any legal liability or responsibility for the accuracy, completeness, or usefulness of any information, apparatus, product, or process disclosed, or represents that its use would not infringe privately owned rights. Reference herein to any specific commercial product, process, or service by trade name, trademark, manufacturer, or otherwise, does not necessarily constitute or imply its endorsement, recommendation, or favoring by the United States Government or any agency thereof. The views and opinions of authors expressed herein do not necessarily state or reflect those of the United States Government or any agency thereof.

DEVELOPMENT PROGRAM FOR A 200 kW, CW, 28 GHz GYROKLYSTRON

J. Shively, C. Conner, S. Evans, F. Friedlander,
E. Galli, S. Hegji, H. Jory, F. Kinney, A. LaRue,
K. Miller, J. Moran, W. Sayer, D. Stone, R. Symons,
N. Taylor and G. Thomas

Final Report
April 1976 through September 1980

Prepared for:
Oak Ridge National Laboratory
Oak Ridge, Tennessee 37830

Operated by:
Union Carbide Corporation

For the
U.S. Department of Energy

Contract No. W-7405-eng-26

Varian Associates, Inc.
Palo Alto Microwave Tube Division
611 Hansen Way
Palo Alto, California 94303

OAK RIDGE NATIONAL LABORATORY LIBRARY
3 4456 0043900 5

ABSTRACT

The objective of this program was to develop a microwave amplifier or oscillator capable of producing 200 kW, CW power output at 28 GHz. The use of the gyrotron or cyclotron resonance interaction was pursued.

A room temperature hollow core solenoid magnet with an iron case was designed to produce the magnetic field required for electron cyclotron resonance.

Three pulsed gyroklystron amplifiers were built providing increasing stable output powers of 6, 65 and 76 kw. A back-up pulsed gyrotron oscillator produced 248 kw.

A ceramic cone broadband water load was developed.

The first CW oscillator design was pulsed tested up to 167 kw peak and 20 kW average output. CW testing of the tube was satisfactory provided parameters were set for zero microwave output, but operation with CW output was plagued with gassing and arcing internal to the tube.

A second tube was constructed with minor design changes to eliminate the gassing problems. Testing of this tube indicated improvement.

The second CW oscillator design was pulse tested up to 132 kw peak and 20 kW average output. In subsequent CW testing, the tube was operated with full 640 kW beam power and with CW output of 105 kW. At that power output, a thermal break occurred in the output window. The tube was rebuilt with no design changes, shipped to Oak Ridge, and considerable operation was realized at power levels up to 50 kW CW. This included operation heating a plasma load in EBT-S.

Modification of the second CW oscillator with the new double-disc output window design is described, and test results for the modified tube are presented. Full CW testing was not completed, however, because of a problem in the window cooling system. This required an additional rebuild

of the tube. It was rebuilt with a number of minor design changes, and produced 92.1 kW CW at Varian for a short time before failure as a result of a vacuum leak at the output window.

With minor modifications since previous testing, it was operated to 100 kw pulsed. It failed at 63 kW CW after several hours of operation, due to a cracked collector ceramic. The succeeding miter bend tube, S/N 7, incorporated several changes intended to reduce the heating of that ceramic.

Construction of a third CW oscillator incorporated a number of design changes. One change, a reduced beam tunnel diameter, was verified in pulsed oscillator tests. Other changes pertained to damping of undesired resonances and the use of a dielectric-cooled double disc output window.

Test results are described. The design changes did not result in significantly improved performance.

Tube No. 4 was made, as much as possible, identical to tube No. 2. Both tubes were intended for 100 kW operation at Oak Ridge.

Tube No. 4, which used a miter bend output system, was tested to 97.2 kW CW output at Varian. It was shipped to Oak Ridge and failed from rf heating damage to the collector ceramic insulator.

Alternative output coupling schemes were studied with emphasis on axisymmetric coupling straight through 5" or 2.5" beam collectors. Computer simulation was used to analyze beam power distribution in the collector regions.

The design of CW oscillator No. 5 is described. This tube used an axisymmetric output coupling system with a 5-inch-diameter collector region tapering down to a 2.5-inch diameter output guide.

Construction and cold testing of tube No. 5 are described. It was tested in pulsed operation but a large reflection from the output window assembly restricted the power output to 120 kw. Tests were made using a

short pulse oscillator with external structures to simulate the collector waveguide tapers, and window of this tube. The results supported the conclusion that an anomaly in the window was the cause of the low output. Tube No. 5 was also operated in equilibrium at full dc beam power under non-oscillatory conditions to check the collector dissipation capability.

Tube 5R1 was rebuilt to incorporate a new water-cooled collector seal and was successfully operated at a measured power output of 212 kW establishing a new world record for CW power generation at 28 GHz. Further tests with various output guide components simulating the EBT-S load were made. This tube was shipped to ORNL and successfully installed and operated.

S/N 6, the second axisymmetric tube, was tested to 200 kW, CW at 50.3% efficiency and 52% efficiency at 170 kW. The tube was delivered to Oak Ridge.

Miter bend output tube, S/N 7M was designed to reduce collector resonances by reducing the coupling to, and the loading, of the collector.

Testing of miter bend tube S/N 7M was completed and the tube shipped to Oak Ridge. Unfortunately, it suffered a vacuum leak and was returned to Palo Alto where it was repaired, tested and returned to ORNL. It was then operated at 50 to 60 kW CW into the EBT-S plasma.

S/N 7 RM was returned to Palo Alto after operation ceased due to an open heater. It was replaced by S/N 12M which was tested to 113 kW CW and shipped to ORNL.

Two additional axisymmetric tubes, S/Ns 8 and 11 were built, and testing will be completed on a follow-on program.

Construction of miter bend tubes S/Ns 9 and 10 was terminated. The last miter bend tube, S/N 12, was delivered to Oak Rdige after producing 113 kW CW at Varian.

A high power mode filter was designed and tested.

TABLE OF CONTENTS

Section		Page
I.	INTRODUCTION	1
II.	REPORTS	3
III.	GYROKLYSTRON AMPLIFIERS	5
	A. Electron Gun	5
	B. Input Cavity	5
	C. Input Window	12
	D. Output Cavity	12
	E. Output Coupling	16
	F. Output Window	19
	G. Drift Tube Coupling and Loss	19
	H. Collector	28
	I. Magnetics	33
	J. Tube Layout	41
	K. Output Water Load	45
	L. Pulsed Gyroklystron Amplifiers	48
IV.	GYROTRON OSCILLATORS	83
	A. Oscillator Cavity Design	83
	B. First Experimental Pulsed Oscillator	86
	C. Second Experimental Pulsed Oscillator	103
	D. CW Oscillator Design	110
	E. CW Oscillator Design Changes Considered	111
	F. Output Window	114
	G. Output Coupling Systems	121
	H. VFA-8000A3 Mode Filter	150
	I. Triple Miter Bend Models	150
	J. Axisymmetric Models	195
V.	SUMMARY	219
VI.	REFERENCES	221
	Appendix A - Theory of Gyroklystrons	

LIST OF ILLUSTRATIONS

Figure		Page
1.	Gyrotron Electron Gun Simulation	6
2.	Input Cavity Layout	7
3.	Input Cavity Q_L for Round Coupling Holes at 28 GHz	9
4.	Effect of Diameter of Coupling Holes on Input Cavity Frequency	10
5.	Input Cavity with Lossy Ring Loading	11
6.	Input Window Assembly	13
7.	Output Cavity Loading	14
8.	Output Cavity Dimensions	15
9.	Mode Chart for Cylindrical TE_{om} Modes	17
10.	Miter Elbow	18
11.	Output Window Assembly	20
12.	Coupling Between Cavities with Variable Air Gap in Drift Tube	22
13.	Relative Dielectric Constant of Water at 28 GHz	24
14.	Loss Tangent for Water at 28 GHz	25
15.	Lossy Cylinder	26
16.	Lossy Plates	26
17.	Lossy Wedges	27
18.	Silicon Carbide Loaded Beryllia Loading	27
19.	Model for Calculating Collector Dissipation Assuming a Point Source of Electrons	31
20.	Maximum Collector Power Density with no Collector Coils	34
21.	Field on Axis in Center of Solenoid, from TRIM	36
22.	LAPLACE Solution for 5-inch Diameter Gun Coil	37
23.	Computed Field on Axis from LAPLACE for Thin 5-inch Diameter Gun Coil	38

LIST OF ILLUSTRATIONS (Cont'd)

Figure		Page
24.	LAPLACE Run for Flux Tubes in Collector with 121 A.T. and 3737 A.T. Coils Simulated with Ideal Return Paths	39
25.	Magnetic Field Contributions of Individual Coil Sets	42
26.	Cathode Magnetic Field	43
27.	Layout Drawing, Second Revision	44
28.	Required Thickness of a 2.5-inch Diameter BeO Disc Water Load Window	46
29.	Ceramic Cone	47
30.	Water Load Assembly	49
31.	Layout Drawing of Pulsed Tube No. 1	51
32.	Pulsed Gyroklystron Before Bakeout	53
33.	Oscillation Frequencies	56
34.	Bore Details of Second Pulsed Amplifier	59
35.	Input Cavity Voltage Reflection Coefficient	60
36.	Uncertainty of Saturation for Feedback Loop Driven Amplifier	62
37.	Beam Current as a Function of Heater Power	64
38.	Beam Current as a Function of Gun Voltage	65
39.	Bore Details of Third Pulsed Amplifier	68
40.	Third Pulsed Amplifier Peak Output Power vs Frequency with Operating Parameters Optimized at Each Point	70
41.	Third Pulsed Amplifier Gain at Saturation vs Frequency with Operating Parameters Optimized	71
42.	Third Pulsed Gyroklystron Amplifier Input Cavity VSWR	72
43.	Third Pulsed Gyroklystron Relative Peak Output Power for Constant Small-Signal Drive for Different Test Conditions	73

LIST OF ILLUSTRATIONS (Cont'd)

Figure		Page
44.	Third Pulsed Gyroklystron Saturated Power and Gain Sensitivity to Gun Anode Voltage	75
45.	Third Pulsed Gyroklystron Power Current Characteristics	76
46.	Third Pulsed Gyroklystron Power Current Characteristics with Increased Anode Voltage	77
47.	Third Pulsed Gyroklystron Amplifier Input-Output Characteristics	79
48.	Oscillator Power and Cavity Q vs Normalized Cavity Field for L = 5λ, TE_{021} Mode, Beam = 80 kV, 8A	85
49.	Oscillator Cavity	87
50.	Cavity Frequency of TE_{021} Mode vs Axial Position of Dielectric Perturbation.....	88
51.	Pulsed Oscillator Efficiency Sensitivity to Gun Anode Voltage, Magnetic Fields Optimized	90
52.	Pulsed Oscillator Efficiency Sensitivity to Gun Anode Voltage, Magnetic Fields Constant	91
53.	Pulsed Oscillator Peak Output Power Sensitivity to Cathode Current	93
54.	Pulsed Oscillator Peak Output Power Sensitivity to Gun No. 1 Coil Current	94
55.	Pulsed Gyrotron Frequency and Calculated Cavity Temperature as a Function of Average Power	96
56.	Pulsed Gyrotron Oscillator Magnetic Field Extremes	98
57.	Pulsed Gyrotron Oscillator Efficiency as a Function of Gun No. 1 Coil Current with 0.030-inch Thick Teflon Disc in Output Guide	100
58.	Pulsed Gyrotron Oscillator Efficiency as a Function of Gun No. 1 Coil Current with 0.030-inch Teflon Disc	101
59.	Pulsed Gyrotron Oscillator Efficiency as a Function of Gun No. 1 Coil Current with 0.062-inch Thick Teflon Disc	102

LIST OF ILLUSTRATIONS (Cont'd)

Figure		Page
60.	Peak RF Output vs Focusing Solenoid Current No. 1 .	105
61.	Peak RF Output vs Solenoid Current No. 2.....	106
62.	Peak RF Output vs Focusing Solenoid Current No. 3 .	107
63.	Peak RF Output vs Solenoid Current No. 4	108
64.	Layout Drawing of CW Gyrotron Oscillator	112
65.	Tube No. 8 Beryllia Window	116
66.	Tube No. 6 Beryllia Window	117
67.	Tube No. 5 Alumina Window	118
68.	Output Power vs FC-75 Dissipation	119
69.	FC-75 Dissipation S/N 5R2	120
70.	Mode Probing Arrangement	123
71.	Modal Output Along Diameter of 1.125-inch Diameter Guide	124
72.	Modal Output After Triple Miter Scan Parallel to Axis of Gyrotron	126
73.	Modal Output After Triple Miter Scan Perpendicular to Gyrotron Axis	127
74.	Schematic of Mirror Output	128
75.	Radiation Pattern from 2.5-Inch-Diameter Aperture, TE_{01} Mode	131
76.	E_θ^2 Perpendicular to and Across the Axis of the Aperture as a Function of Distance from the Aperture	132
77.	Cavity Resonance Curve as a Function of Mirror Separation, TE_{01} Mode	133
78.	Q as a Function of Mirror Separation	134
79.	Output from 2.5-Inch-Diameter Guide After Reflection Through Mirrors	135

LIST OF ILLUSTRATIONS (Cont'd)

Figure		Page
80.	Effect on Output of a Single Miter Bend Following a Mirror System	137
81.	5-inch-Diameter Collector, Window and Output Guide	139
82.	Distribution at 2.5-Inch-Diameter Collector Wall of Electrons from Front of Cathode	142
83.	DC Beam Power Density as Function of Distance Along Collector	143
84.	Magnetic Field for Trajectories of Figure 83	144
85.	2.5-Inch-Diameter Collector, Window and Output Guide	145
86.	Collector/Output Circuit	147
87.	VFA-8000A3 Mode Filter	151
88.	VGA-8000 S/N 1 Arc Damage After Pulse Operation	153
89.	CW Oscillator Peak Output Power as a Function of Frequency VGA-8000 S/N 1	155
90.	CW Oscillator Peak Output Power as a Function of Frequency VGA-8000 S/N 1R	158
91.	Pulsed CW Oscillator Peak Output Power and Efficiency as Functions of Peak Cathode Current VGA-8000 S/N 1R	159
92.	Collector Flow Characteristics VGA-8000 S/N 1R	160
93.	Body Flow Characteristics VGA-8000 S/N 1R	161
94.	VGA-8000 S/N 1R2 - Peak Output Power vs Frequency	164
95.	VGA-8000 S/N 1R2 - Power (Peak) and Efficiency vs Cathode Current	165
96.	Peak Output Power and Efficiency vs Peak Cathode Current for Pulsed Gyrotron Oscillator VGA-8000 S/N X-1R3	166
97.	Peak Output Power as a Function of Frequency for S/N 2R	169

LIST OF ILLUSTRATIONS (Cont'd)

Figure		Page
98.	Peak Output Power and Efficiency as a Function of Peak Cathode Current for S/N 2R	170
99.	Frequency vs Main Magnet Coil No. 2 Current	171
100.	CW Power Output Sensitivity to Gun Coil No. 1 Current	175
101.	CW Power Output Sensitivity to Gun Anode Voltage ..	176
102.	VGA-8000 S/N 2R9 Collector Ceramic (inner and end surfaces)	181
103.	VGA-8000 S/N 2R9 Collector Ceramic (outer surfaces)	182
104.	Collector Assembly and Ceramic Assembly from S/N 4R After Failure	187
105.	Collector Ceramic Assembly from S/N 4R after Failure, View 1	188
106.	Collector Ceramic Assembly from S/N 4R After Failure, View 2	189
107.	VGA-8000 Gyrotron, S/N 12M Efficiency vs Beam Current in Pulse Mode; 8% Duty	194
108.	Layout Drawing of an Axisymmetric CW Gyrotron with Tapered Output Waveguide	197
109.	Frequency and Power Characteristics for CW Tube Number 5R in Pulsed Testing	198
110.	Frequency and Power vs Main Magnet No. 2 Current for VGA-8000 S/N 5R2 (I_{Beam} = 3.6 A)	200
111.	Frequency and Power vs Main Magnet No. 2 Current for VGA-8000 S/N 5R2 (I_{Beam} = 4.9 A)	201
112.	Frequency and Power vs Main Magnet No. 2 Current for VGA-8000 S/N 5R2 (I_{Beam} = 6.0 A)	202
113.	Efficiency vs Beam Current for VGA-8000 S/N 5R2 with Gun Anode Voltage Values Optimized for Peak Efficiency	203
114.	Efficiency vs Gun Anode Voltage (I_{Beam} = 3.5 A) ...	204
115.	Frequency and Power vs Gun Anode Voltage (I_{Beam} = 5A)	205

LIST OF ILLUSTRATIONS (Cont'd)

Figure		Page
116.	Waveguide Configuration No. 1	208
117.	Waveguide Configuration No. 2	209
118.	Waveguide Configuration No. 3 (Tube, Mode Filter and Miter Bend Configuration at ORNL)	210
119.	VGA-8000 S/N 5R2 and S/N 6 CW Power Output and Efficiency vs Beam Current	212
120.	Mode Filter, Miter Bends and Tube Configuration for Testing High Power Mode Filter VFA-8000A3	214
121.	Comparison of VFA-8000A2 and VFA-8000A3 Mode Filters	215

LIST OF TABLES

Table		Page
1.	Frequency Sensitivity of Input Cavity	8
2.	Radiating Drift Tube Loss	21
3.	Collector Wall Temperatures	30
4.	Approximate Maximum Power Densities for Different Collector Geometries	32
5.	Output Cavity Parameters	50
6.	Input Cavity Parameters	52
7.	Input Window Matches	52
8.	Amplification Results	54
9.	Kanthal Composition	57
10.	Best Test Results for the Second Pulsed Amplifier	61
11.	Undesired Oscillations	61
12.	Attenuation in Lossy Rectangular Guide at 28 GHz .	66
13.	Attenuation in Lossy Circular Guide	67
14.	Best Performance of First Three Gyroklystrons	74
15.	Effect of Load on Amplifier Operation	80
16.	Cutoff Diameters at 28 GHz	84
17.	Oscillator Cavity Dimensions, Frequency, and Q ...	86
18.	Best Test Results for the First Pulsed Oscillator	89
19.	Best Average Power Test Results for the First Pulsed Oscillator	95
20.	Output Power Sensitivity to Variation of Parameters	97
21.	Effect of Load on Oscillator Operation with Magnetic Perturber	103
22.	Baseline Experimental Operating Parameters	104

LIST OF TABLES (Cont'd)

Table		Page
23.	Best Test Results for the Second Pulsed Oscillator	110
24.	Straight Through Collectors	138
25.	Characteristics of VFA-8000A3 Mode Filter	150
26.	Comparison of the First Pulsed CW Oscillator and the First Experimental Pulsed Oscillator Performance	156
27.	Best Peak and Average Power Performance of the Rebuilt CW Oscillator	162
28.	Best Power Performance of Serial Number 1R2	167
29.	Best Power Performance of Serial Number 2R	172
30.	Best Power Performance of Serial Number 2R2	173
31.	Mode Filter and Window Losses for VGA-8000 S/N 2R3	174
32.	Operating Parameters at Varian for the Fifth Rebuild of the Second CW Oscillator	178
33.	Pulsed Operating Parameters for the Third CW Oscillator	183
34.	Pulsed Operating Parameters for the Rebuild of the Third CW Oscillator	184
35.	Operating Points for Maximum Peak and Average Power in Pulsed Operation for the Fourth CW Oscillator	185
36.	Pulsed Operating Point for the Rebuilt Fourth CW Oscillator	186
37.	VGA-8000 S/N 4R CW Test Data	190
38.	VGA-8000 Serial Number 7RM Operating Parameters	192
39.	VGA-8000 S/N 12M Test Performance	195
40.	VGA-8000 S/N 5R2 Test Performance	206

I. INTRODUCTION

The objective of this program is to develop a microwave amplifier capable of producing 200 kW of CW power at a frequency of 28 GHz. In addition, the program is intended to serve as the first step toward development of an amplifier to produce a similar power level at a frequency of 120 GHz. Feasibility for the 120 GHz device will be demonstrated whenever practical in the design of the 28 GHz amplifier. Tunability or bandwidth is not considered an important parameter in the design but efficiency is. Mode purity in the output waveguide is not a requirement for the device, but the circular E mode is considered desirable because of its low loss properties.

With these objectives in mind, the decision was made to pursue an approach based on a cyclotron resonance interaction between an electron beam and microwave fields. The detailed arguments leading to this choice are contained in the final report of the preceding study program.[1] The device configuration of particular interest, called a gyrotron, has been discussed in recent literature.[2] It employs a hollow electron beam interacting with cylindrical resonators of the TE_{0m1} class. The experimental gyrotrons described in the literature have all been of the form of single-cavity oscillators. However, a similar device[3] has demonstrated moderate (16 dB) gain as an amplifier.

A goal of this development program is to achieve an amplifier having significantly higher gain (30 dB). Stability of the device becomes a very important technical consideration at this level of gain. To fully capitalize on the advantages of the cyclotron resonance interaction, large beam diameters are used. This exposes the device to the effect of microwave coupling between amplifier stages through the beam tunnel. Prevention of this coupling is an important consideration in the design.

The optimum beam for the cyclotron resonance interaction is one in which the electrons have most of their energy in velocities perpendicular to the axial magnetic field. Another requirement is that the small component of axial velocity be essentially the same for all electrons. An electron

which has a different axial velocity will not interact efficiently. Generation of a beam with high transverse velocity and small axial velocity spread is another important design problem.

The approach chosen to generate the beam is a magnetron type of gun as was used in the devices described in the Russian literature. With this type of gun, the shaping of the magnetic field in the gun region becomes quite important.

As the program proceeded, experiments with pulsed gyrotron oscillators gave power outputs well in excess of 200 kW, whereas experimental pulsed gyroklystrons were severely limited in performance by various technical difficulties. The main thrust of the program, therefore, shifted to gyrotron oscillators, and the goal of the program became the development and construction of these tubes for use in the EBT-S system.

II. REPORTS

The Development Program for a 200 kW, CW, 28 GHz Gyroklystron extended from the second quarter, April 20, 1976 through the third quarter of 1980. Seventeen quarterly reports were issued during this period. The eighteenth quarterly report is included as part of this final report. The quarterly reports give details of the experimental work in chronological order. This final report summarizes the important features of the work according to subject. The two principal technical portions of the final report discuss gyroklystron amplifiers in Section III and gyrotron oscillators in Section IV.

III. GYROKLYSTRON AMPLIFIERS

This section covers work on gyroklystron amplifiers through construction of gyroklystron pulsed amplifier No. 4. Subsections A through K describe design details of tube components and peripheral equipment, such as the electromagnet and water load. Section L lists special design details pertaining to individual models and discusses cold and hot test data obtained with the tubes. At the time of construction of No. 4, very significant results had been obtained in parallel efforts with gyrotron oscillators, and the main thrust of the program was redirected toward work with those tubes.

A. ELECTRON GUN

An electron gun of the magnetron injection type was chosen as the preferred approach. The goals of the gun design were an 80 kV, 8 A beam with a transverse to axial velocity ratio of two-to-one. To minimize velocity spread, the gun electrode shapes were adjusted and the results evaluated using computer simulation. A simulation of the electron trajectories is shown in Figure 1. The simulation predicted a spread in transverse velocity of 3% and a corresponding axial velocity spread of 11%.

The cathode emitter is a conventional impregnated type. The surface is polished to minimize roughness.

The gun anode is of copper with internal passages for oil cooling. Similar passages are included in the focus electrode, in close proximity to the cathode. Cooling of this electrode served to minimize or eliminate unwanted primary emission.

B. INPUT CAVITY

The geometry of the first input cavity, determined from cold test measurements, is shown in Figure 2. The 0.280" x 0.140" rectangle represents the inside dimensions of the input waveguide. Three coupling holes were used instead of one in order to minimize excitation of the TE_{11}

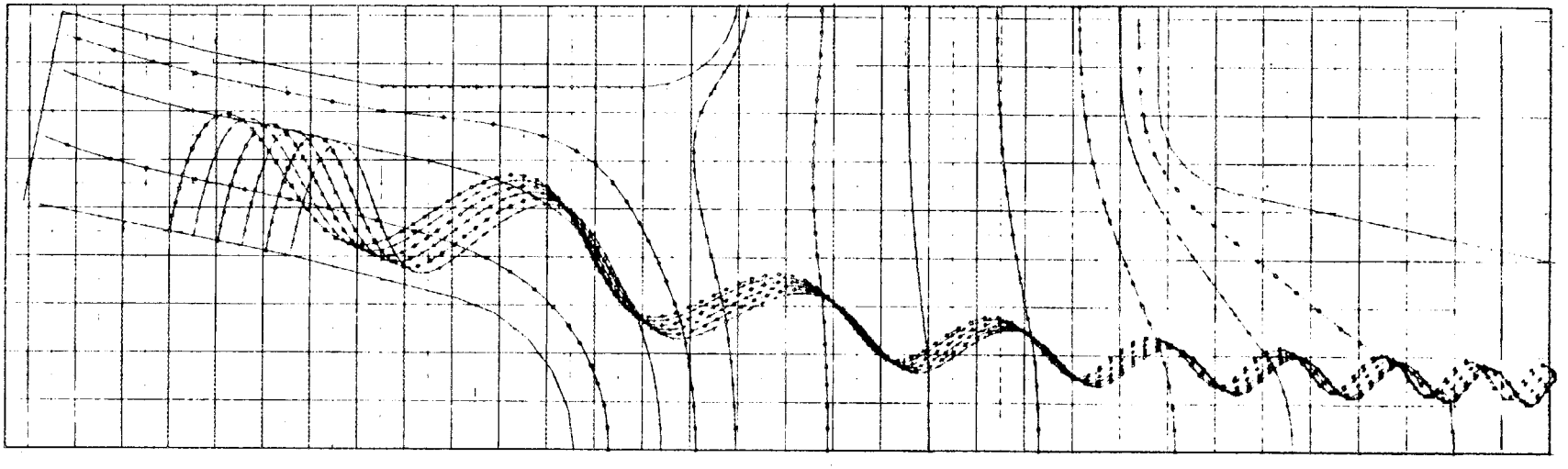

Figure 1. 28 GHz Gyrotron Gun Simulation

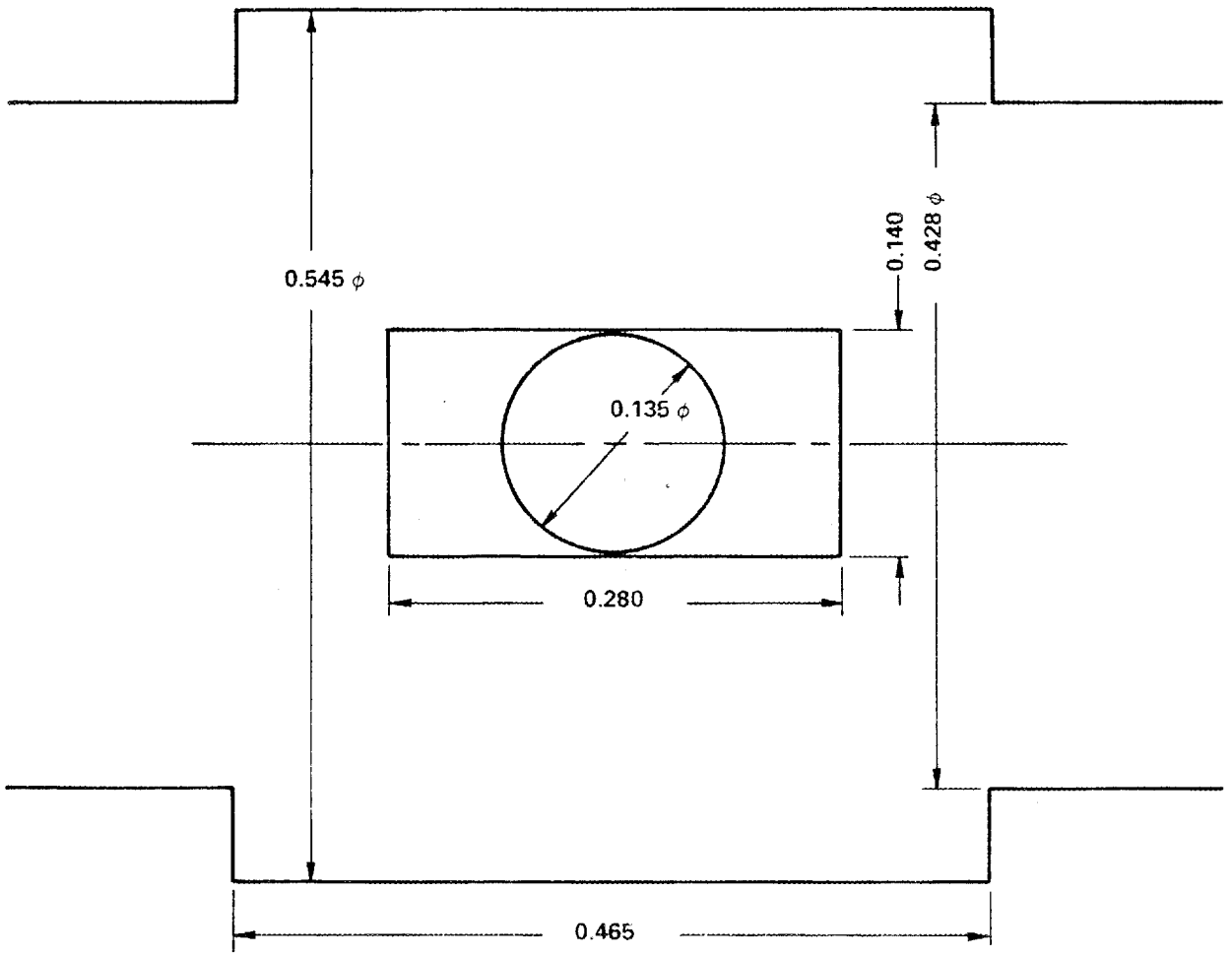

Figure 2. Input Cavity Layout

and TE_{21} modes. These modes can propagate in the drift tubes. Round coupling holes were employed to enhance dimensional control.

The sensitivity of Q_L to coupling hole diameter was measured in cold test. A graph of the test data is shown in Figure 3. Dimensional sensitivity of cavity resonant frequency is indicated in Table 1.

TABLE 1

Frequency Sensitivity of Input Cavity

Parameter	Sensitivity (MHz/mil)
Cavity Length	-12
Cavity Diameter	-46
Coupling Hole Diameter	-10

The effect of the diameter of the coupling holes on frequency is shown in Figure 4. It was anticipated that cavity dimensions would require trimming adjustments to ensure the correct resonant frequency in actual tube models.

A lossy, silicon carbide loaded beryllia ring was introduced in the input cavity used in the second pulsed amplifier to load all modes with axial cavity wall currents. One such mode, the TE_{212}, was suspected of causing oscillation at 27 GHz. Details of that input cavity geometry are shown in Figure 5.

The third pulsed amplifier did not make use of the lossy ring, relying instead on increased drift tunnel loss. The fourth pulse amplifier, however, returned to employment of the lossy ring. In addition, the three coupling ports were increased in area to lower the loaded Q from 333 to 110. It was anticipated that the change would make the driver match less sensitive to beam loading. Further, a matching element was used in the input drive line to improve the match at input cavity resonance.

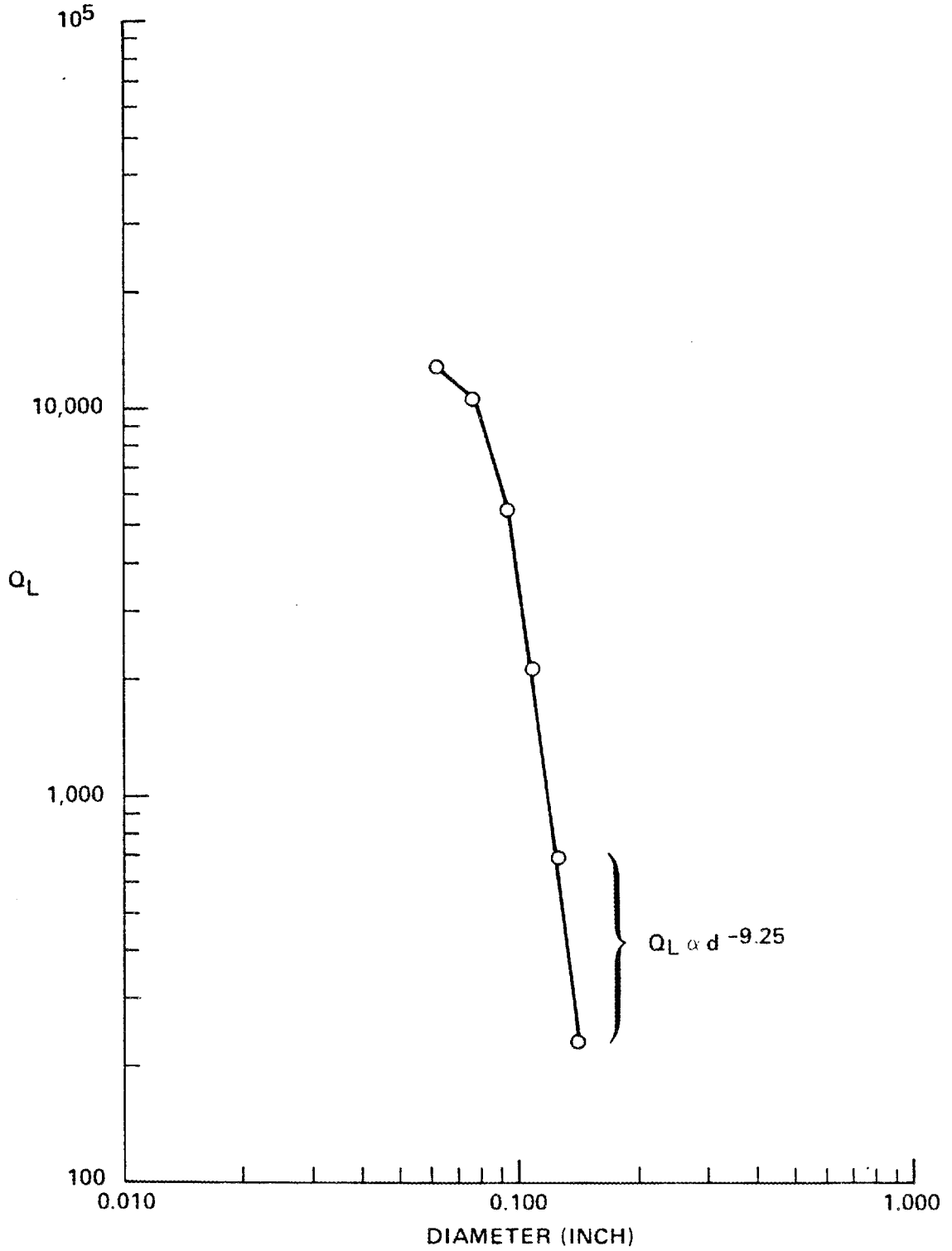

Figure 3. Input Cavity Q_L for Round Coupling Holes at 28 GHz

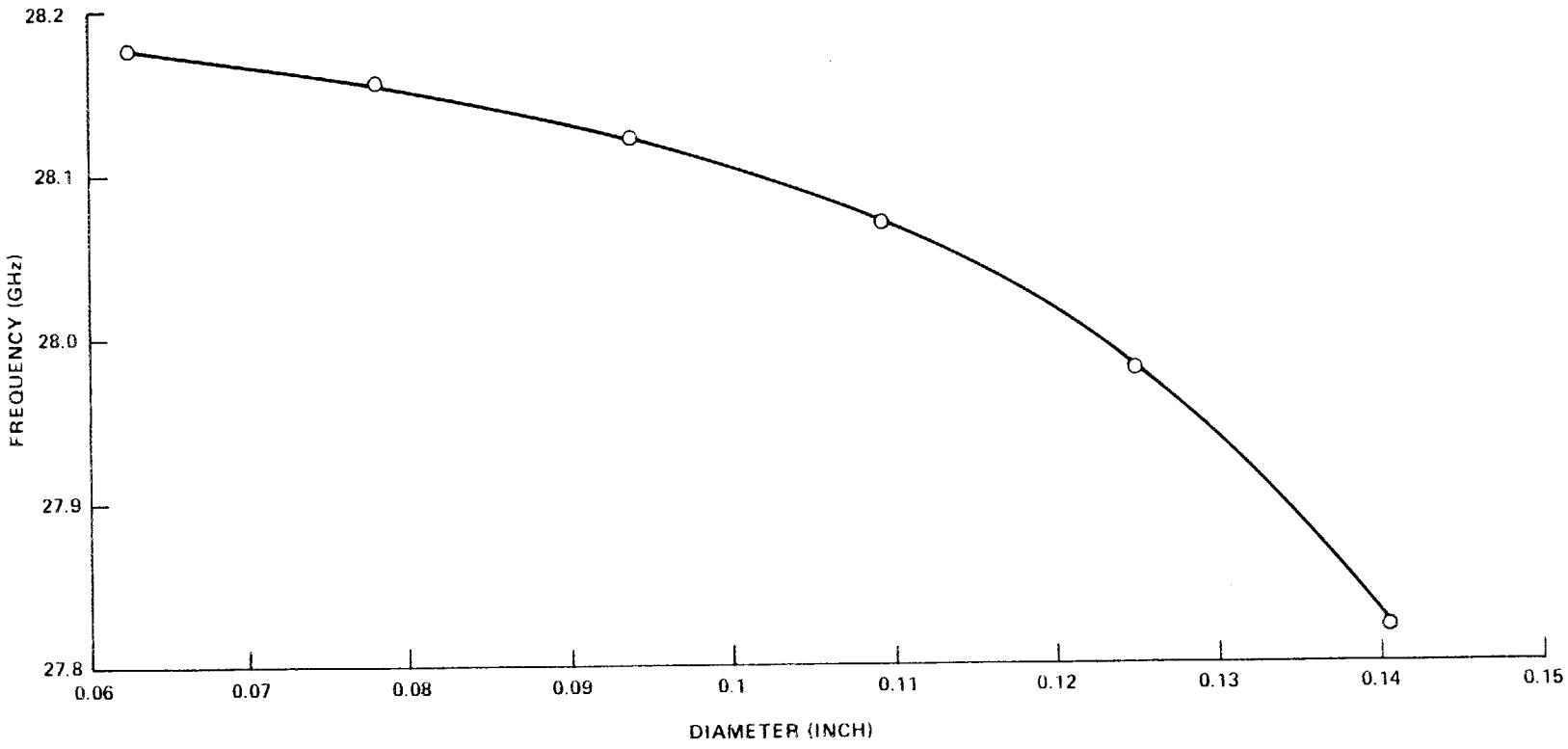

Figure 4. Effect of Diameter of Coupling Holes on Input Cavity Frequency

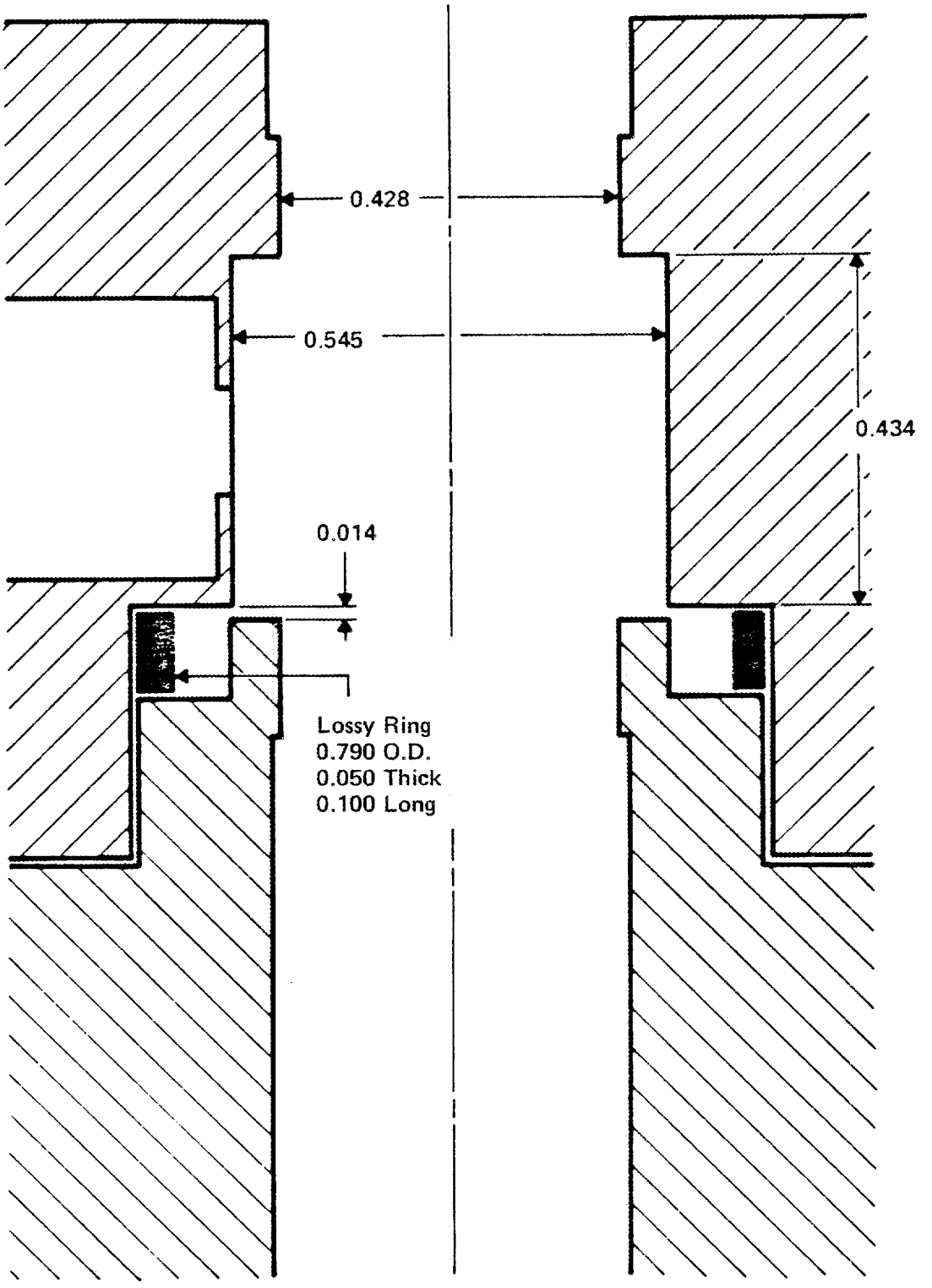

Figure 5. Input Cavity with Lossy Ring Loading

C. INPUT WINDOW

Three identical windows were employed with the input cavity, one for each of the coupling holes (irises). The design made use of a half-wavelength thick alumina disc centered between two TE_{10} - TE^{0}_{11} transitions spaced for reflection cancellation. Figure 6 shows the input window assembly. A cold test model of the window showed 1.08 VSWR at 28 GHz and under 1.3 VSWR between 27.453 and 29.459 GHz.

D. OUTPUT CAVITY

In experimenting with an X-band scaled cavity, it soon became apparent that output cavity loading through the cylindrical cavity wall would be both extremely difficult and time consuming. Efforts then centered on coupling through the end of the cavity. TE^{0}_{01} mode coupling resulted in a minimum Q_L of about 430, considerably in excess of the desired value of the 195. TE^{0}_{02} mode coupling obtained with a substantially larger iris diameter, however, yielded an acceptable value of Q_L. The X-band scaled cavity data are shown in Figure 7. The cold test data led to the 28 GHz output cavity geometry of Figure 8. It was anticipated that some of the dimensions would require trimming to obtain the required resonant frequency in actual tubes.

The X-band cold test output cavity used initially had microwave coupling slots in the cylinder wall, not a desirable feature in actual 28 GHz output cavities. Cold test techniques were, therefore, investigated to avoid this form of test signal coupling. A TE_{10} to TE^{0}_{01} transition, a mode filter made up of alternate conducting and nonconducting rings, and a dielectric-loaded drift tube at the electron gun end of the output cavity were used for signal injection. A dummy drift tube with a diagnostic coupling slot was positioned just outside the output cavity iris for test signal detection. Penetration of the dielectric plug into the drift tube and adjustment of the size of the detection coupling port permitted a compromise between sensitivity and detuning. The arrangement proved marginally satisfactory for testing actual tube output cavities.

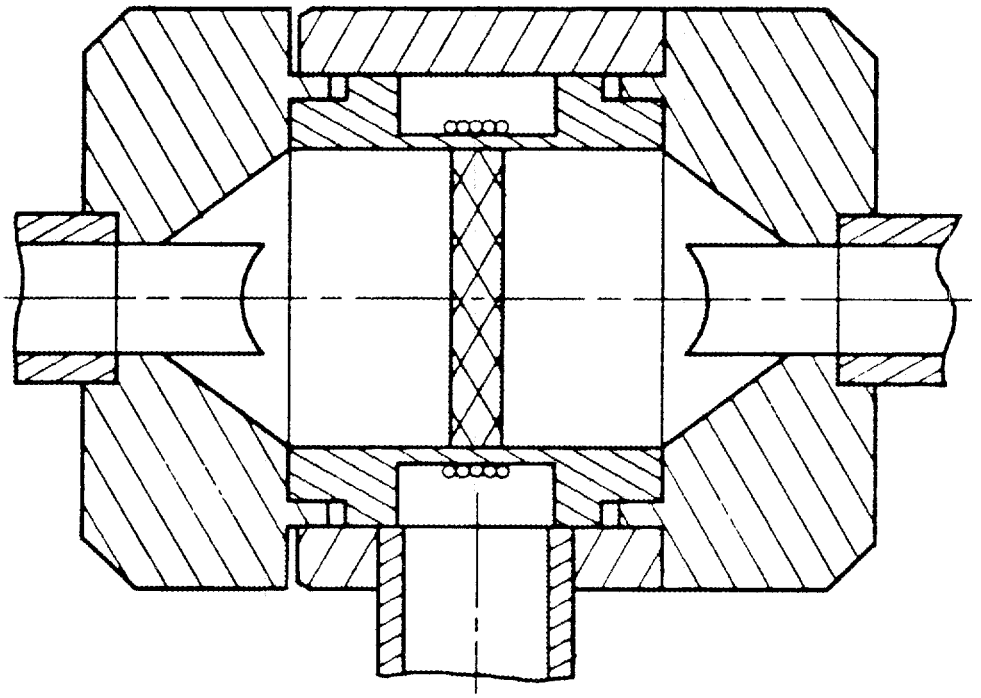

Figure 6. Input Window Assembly

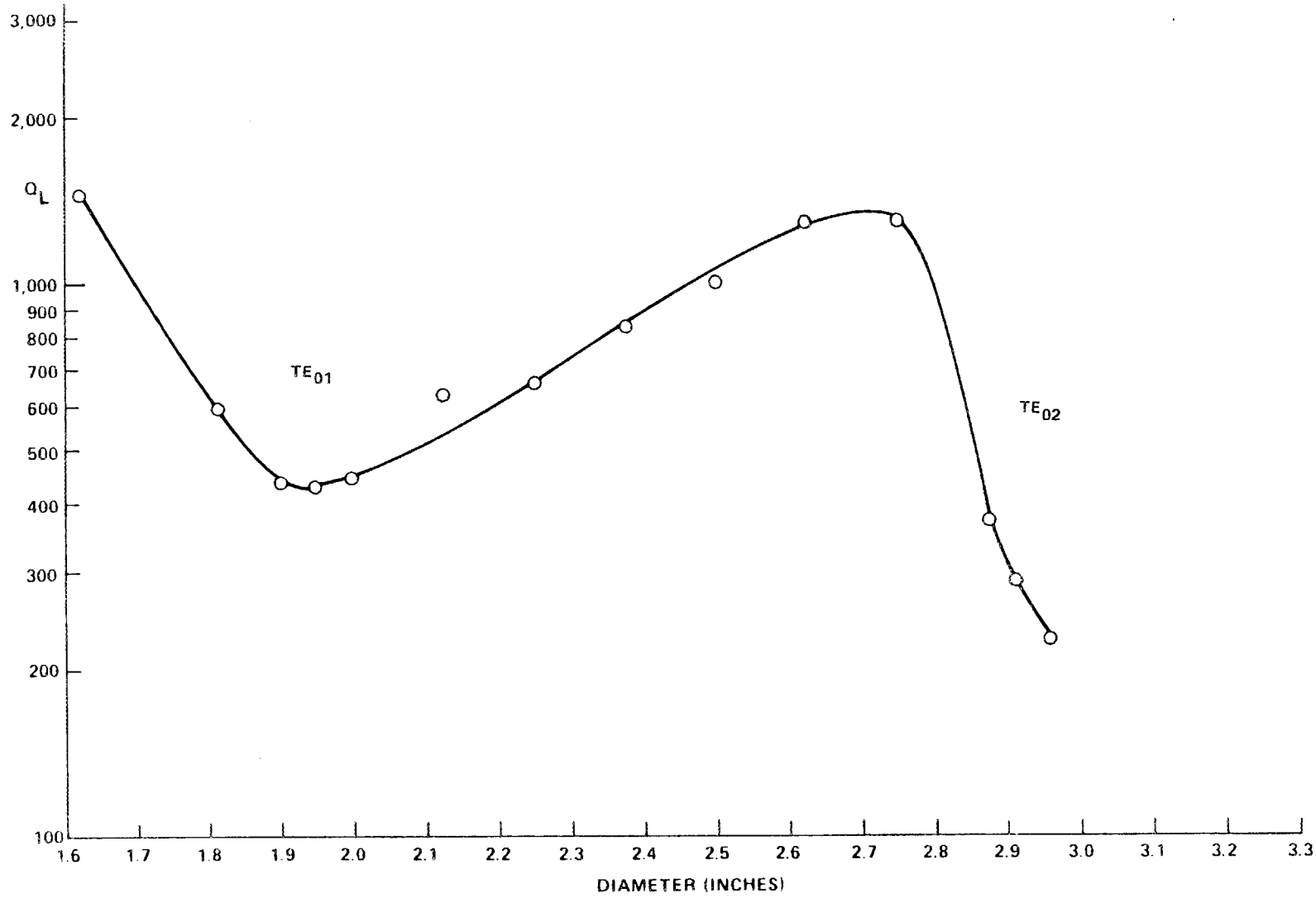

Figure 7. Output Cavity Loading

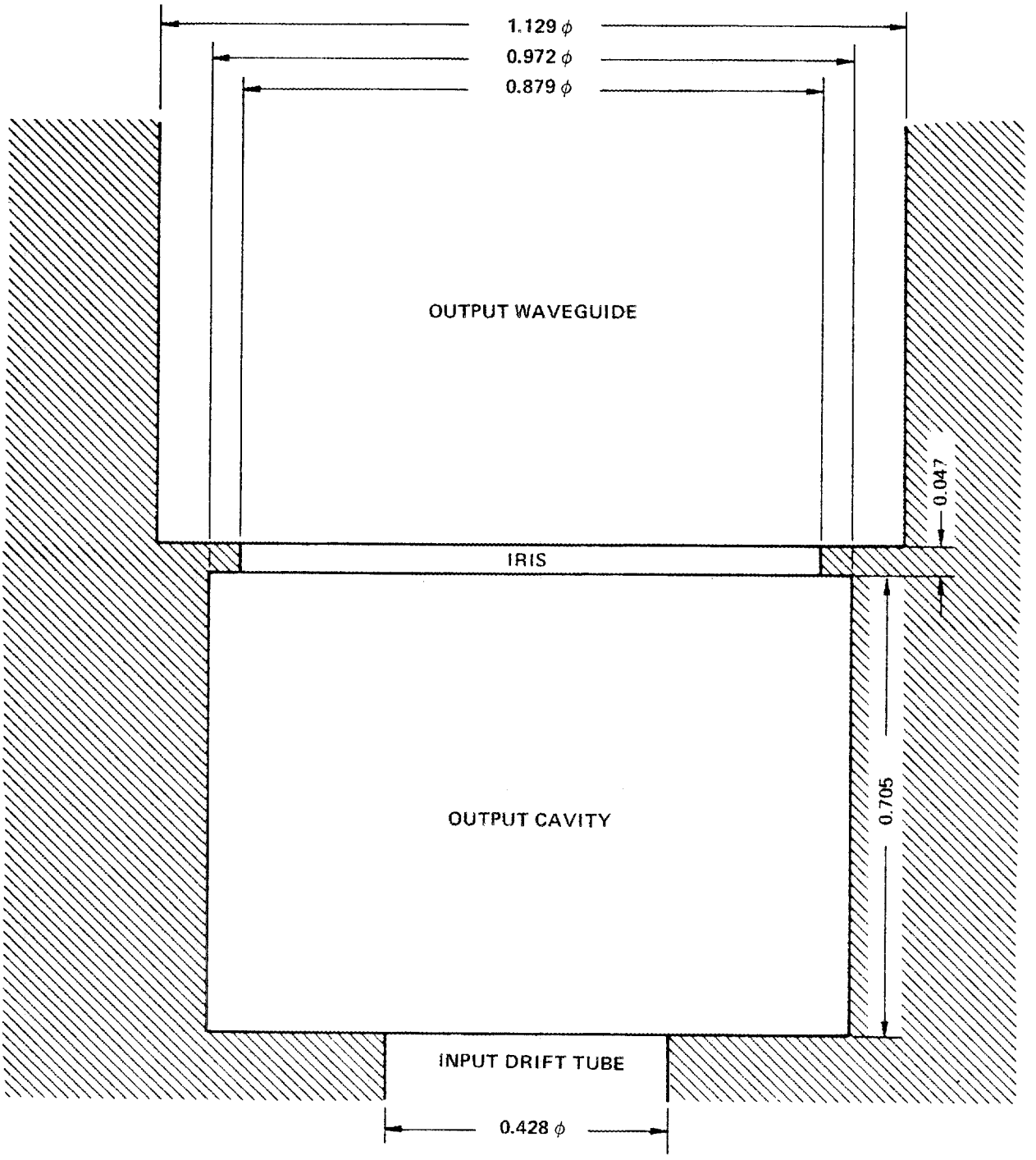

Figure 8. Output Cavity Dimensions

E. OUTPUT COUPLING

Although coupling from the output cavity directly into cylindrical waveguide gave a satisfactory Q_L, the problem of coupling to the outside remained. Two basic systems of output coupling were studied. The first case involved use of the cylindrical collector as an oversized waveguide, with rf output through a window structure beyond. The second case made use of a miter bend and a separate output waveguide immediately following coupling from the output cavity and prior to the collector.

In the first design case, an attempt at extracting rf through the collector used a 6-inch-long 8-inch-diameter collector with 27 degree half angle linear tapers from the waveguide at the output cavity and to the 2.5-inch-diameter output waveguide to the window. A concern for this case was trapped resonances in the collector. A structure the size of the collector could support circular electric modes up to the $TE_{0,18}$. Figure 9 shows a mode chart for circular electric modes up to TE_{06}. The estimated mode spacing for all variety of modes would be about 150 KHz, that for circular electric modes about 9 MHz. Approximately 15 TE_{onm} resonances would exist in the bandwidth obtaining for a Q_L of 195. This order of responses would play havoc with the cavity impedance presented to the electron beam since some coupling of modes by the tapers is unavoidable. These effects were verified by cold test measurements. It was also verified that reduction of collector volume by shortening the length decreased the number of extraneous resonances, and opening up the collector end hole from the original 2.5 inches decreased their amplitudes.

Two approaches were taken to minimize the effects of trapped resonances in the collector. One made use of smooth, long, radiused transitions between diameters. The second employed longer linear tapers. In each case the collector was 8 inches long and 5.75 inches in diameter. The linear tapers proved to be the better approach.

In the second design case, a circular electric waveguide miter elbow with a suitable beam hole was introduced immediately following the output cavity coupling, as shown in Figure 10, allowing output coupling and

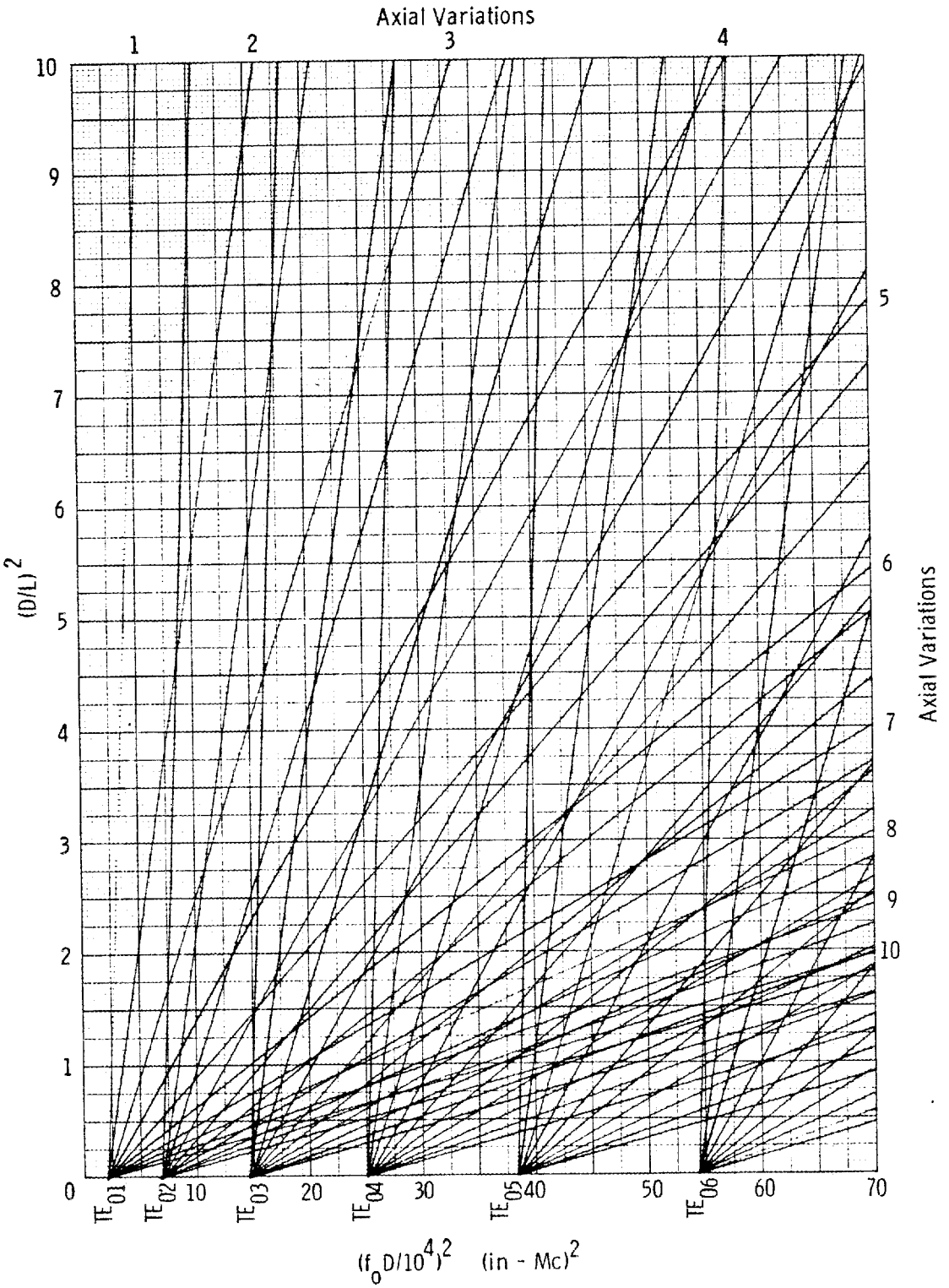

Figure 9. Mode Chart for Cylindrical TE_{om} Modes

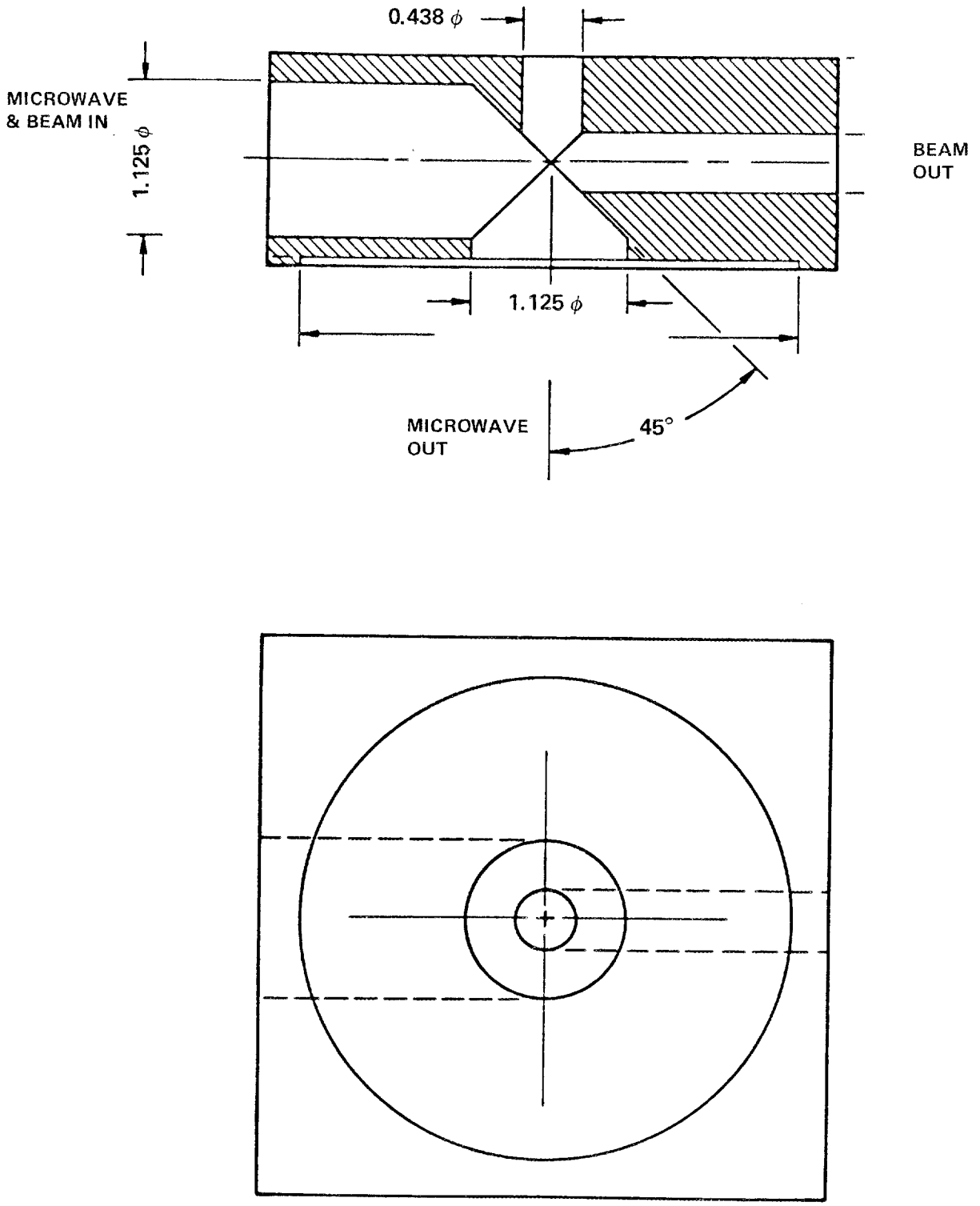

Figure 10. Miter Elbow

collector problems to be treated separately. Preliminary cold tests were encouraging, though they showed sensitity to the angular position of the output waveguide. It was thought that this problem might be minimal with symmetrical excitation of the output cavity.

The magnitude of resonance distortion appeared approximately similar for each of the design cases discussed. Both approaches were pursued.

F. OUTPUT WINDOW

The initial output window design incorporated a half-wavelength BeO ceramic disc brazed to copper cups and surrounded by a stainless steel water jacket. With rf energy transmitted in a circular electric mode, in which wall currents flow circumferentially, it was feasible to interrupt the conducting wall at a plane perpendicular to the axis. The edge of the ceramic window disc protruded into the coolant, providing loading of evanescent modes and giving the best possible window edge cooling. The initial design is shown in Figure 11.

Later in the program, a double-disc window design was used. FC-75 coolant was channeled across the waveguide between the two discs to cool them. Details of this design will be described in a later section.

G. DRIFT TUBE COUPLING AND LOSS

One of the areas of concern in the microwave design is the possibility of feedback from the output cavity to the input cavity by virtue of one of the propagating drift tube modes. Of primary concern, are the TE_{11} and TE_{21} modes. A variety of drift tube configurations, including smooth bores of different lengths, drift tubes with TE loading ports (rectangular waveguide with E-field perpendicular to tube axis) and TM ports (rectangular waveguide with E-field parallel to axis) were tried. None of these proved to give adequate attenuation.

A tunable cavity with a diameter of 2.68 λ in the drift tube was tried. Nulls in drift tube transmission were found for cavity lengths of 0.49 λ,

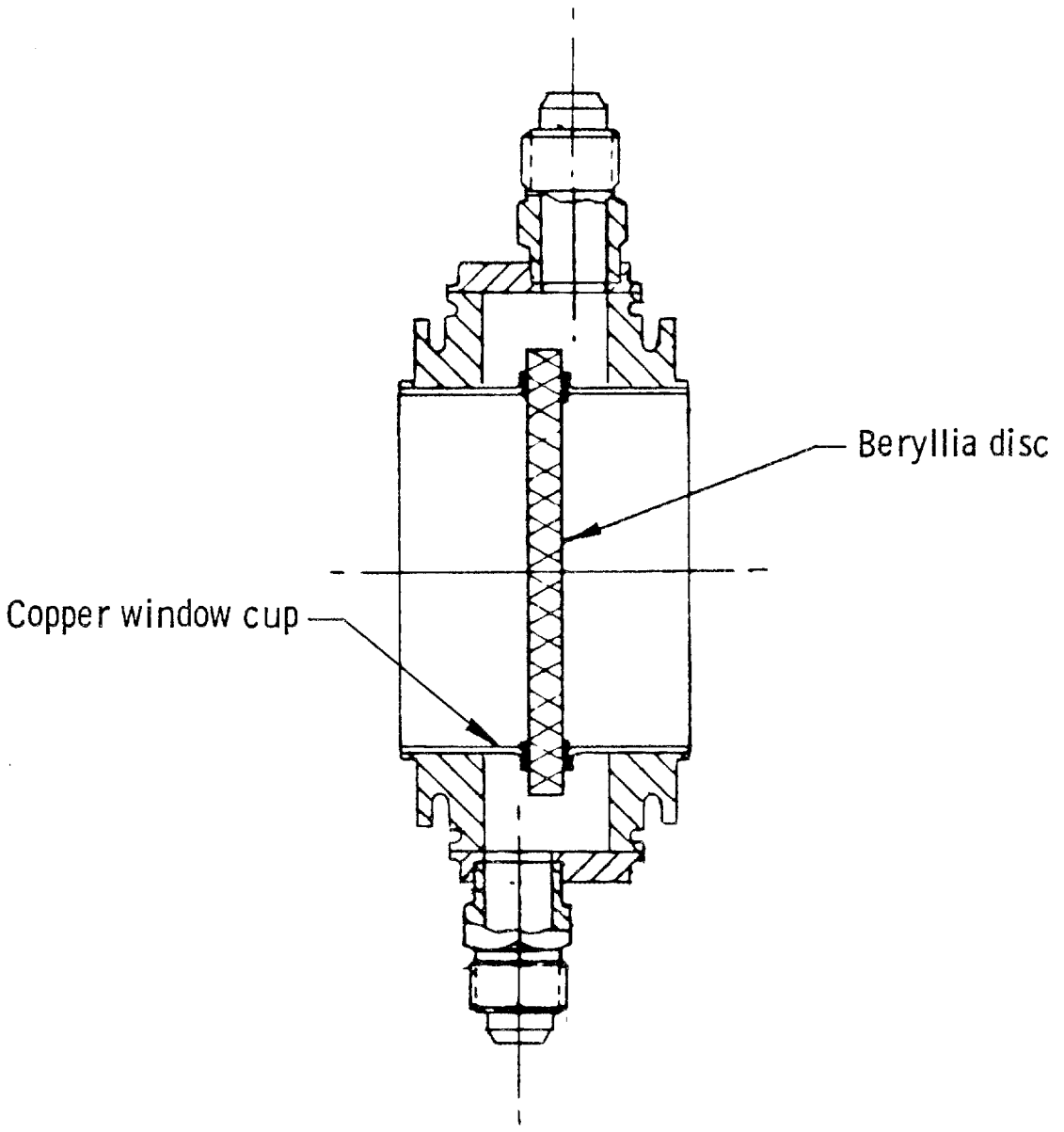

Figure 11. Output Window Assembly

0.60 λ, 0.84 λ, and 1.60 λ. However, performance was sensitive to drift tube end conditions of the system.

The most encouraging results were obtained by breaking the drift tube and allowing a portion of the TE_{11} and TE_{21} modes to radiate into free space. The first experiment consisted of 0.8 λ long drift tubes attached to the input and output cavities. The drift tubes had flat plates on the ends. As the cavities were separated, the relative transmission as a function of gap length was measured as shown in Figure 12. The transmitted power was fairly constant up to a gap of $\lambda/2$, at which point there was a sharp null, too sharp to attempt to utilize. As the gap was increased beyond $\lambda/2$, transmitted power fell as $1/r^2$.

Observation of the radiated angular pattern indicated TE_{21} as the primary mode of transmission. Low gain drift tube antennas were designed by removing the plates from the ends of the drift tubes and making the drift tubes $\lambda_g/2$ long for the TE_{21} mode. This corresponded to a drift tube length of 1.71 λ on each cavity. For a given gap length, this drift tube length gave maximum loss. However, this drift tube length proved to be too long for the 3 λ spacing between input and output cavities determined by amplification calculations. The drift tubes were shortened, keeping the spacing between cavities constant. The loss for an effective 3 λ cavity spacing for different drift tube lengths is shown in Table 2.

TABLE 2

Radiating Drift Tube Loss

Drift Tube Snout Length (λ)	Minimum Loss (dB)
1.45	23.8
1.30	28.1
1.16	29.9
1.01	32.7
0.86	36.4
0.71	>45

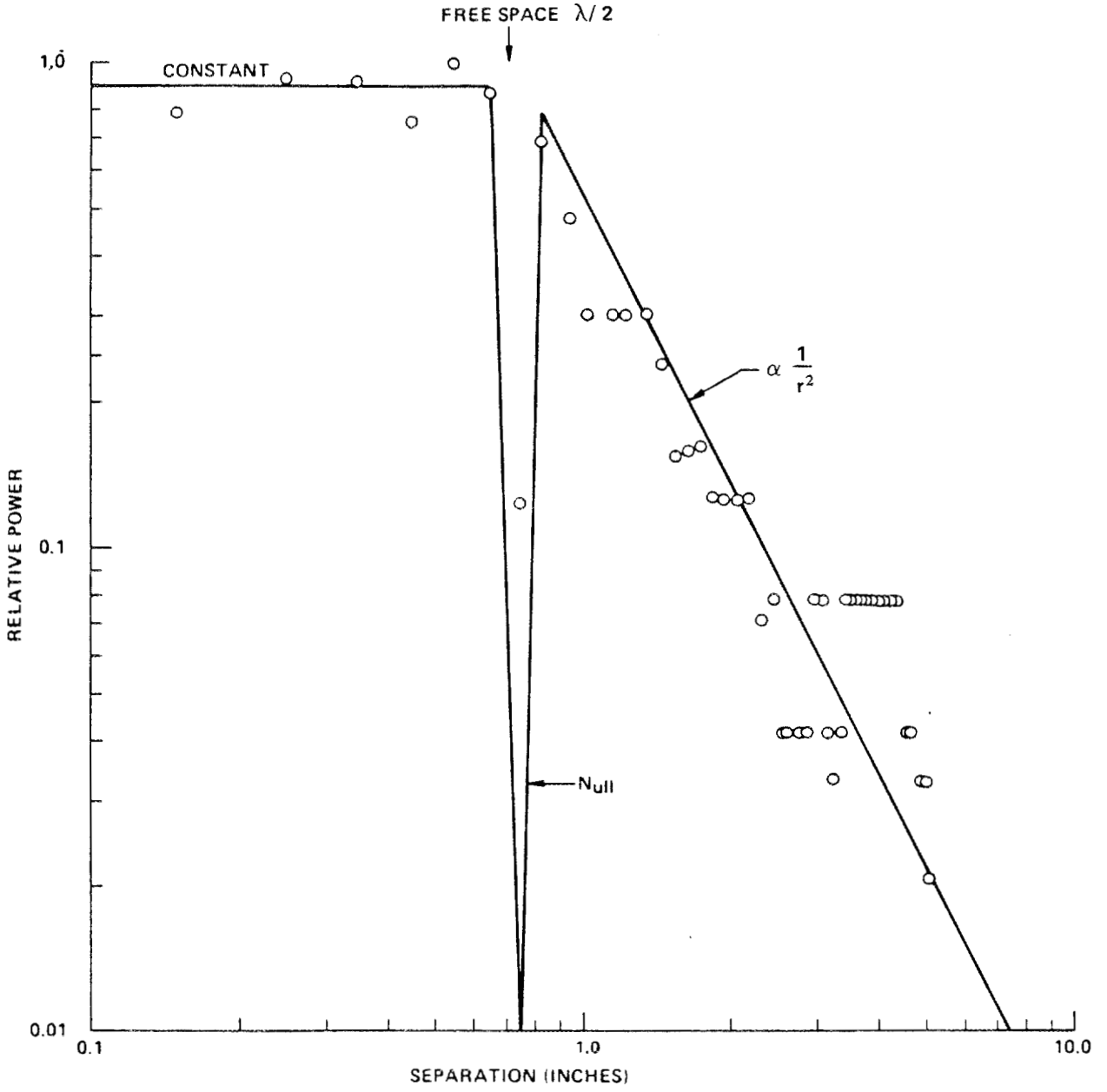

Figure 12. Coupling Between Cavities with Variable Air Gap in Drift Tube

The amount of attenuation measured with the short snout radiating drift tubes appeared promising.

The next step in the drift tube loss procedure was to simulate free space in a vacuum envelope. Several approaches were considered, including a beryllia cylinder water load, a lossy cylinder, lossy plates, and silicon carbide loaded beryllia wedges and pills.

In conjunction with the beryllia cylinder water load approach, the dielectric constant and loss tangent of water as a function of temperature were calculated.[21] The dielectric constant is plotted in Figure 13. The loss tangent is plotted in Figure 14. A reasonable match could probably be made using a 3 $\lambda/4$ thick BeO cylinder. However, it would be frequency and temperature sensitive.

A lossy cylinder was simulated by a cylinder of resistance paper $\lambda/4$ from the cylindrical wall as shown in Figure 15. A resistance of 1500 to 3000 ohms per square gave ~45 dB loss. A resistance of 400 ohms per square gave > 45 dB of loss.

Loss plates were simulated by sheets of resistance paper $\lambda/4$ from the end walls of the drift tube cavity, as shown in Figure 16. A resistance of 8000 ohms per square gave a loss of ~40 dB. A resistance of 1100 ohms per square gave > 45 dB loss.

Lossy wedges were simulated by pleated resistance paper as shown in Figure 17. Twenty-four pleats of 8000 ohms per square paper gave > 45 dB loss.

Loss pills were simulated by a handful of silicon carbide loaded beryllia pieces of random size and shape partially filling one side of the drift tube cavity, as shown in Figure 18. This experiment also gave > 45 dB loss.

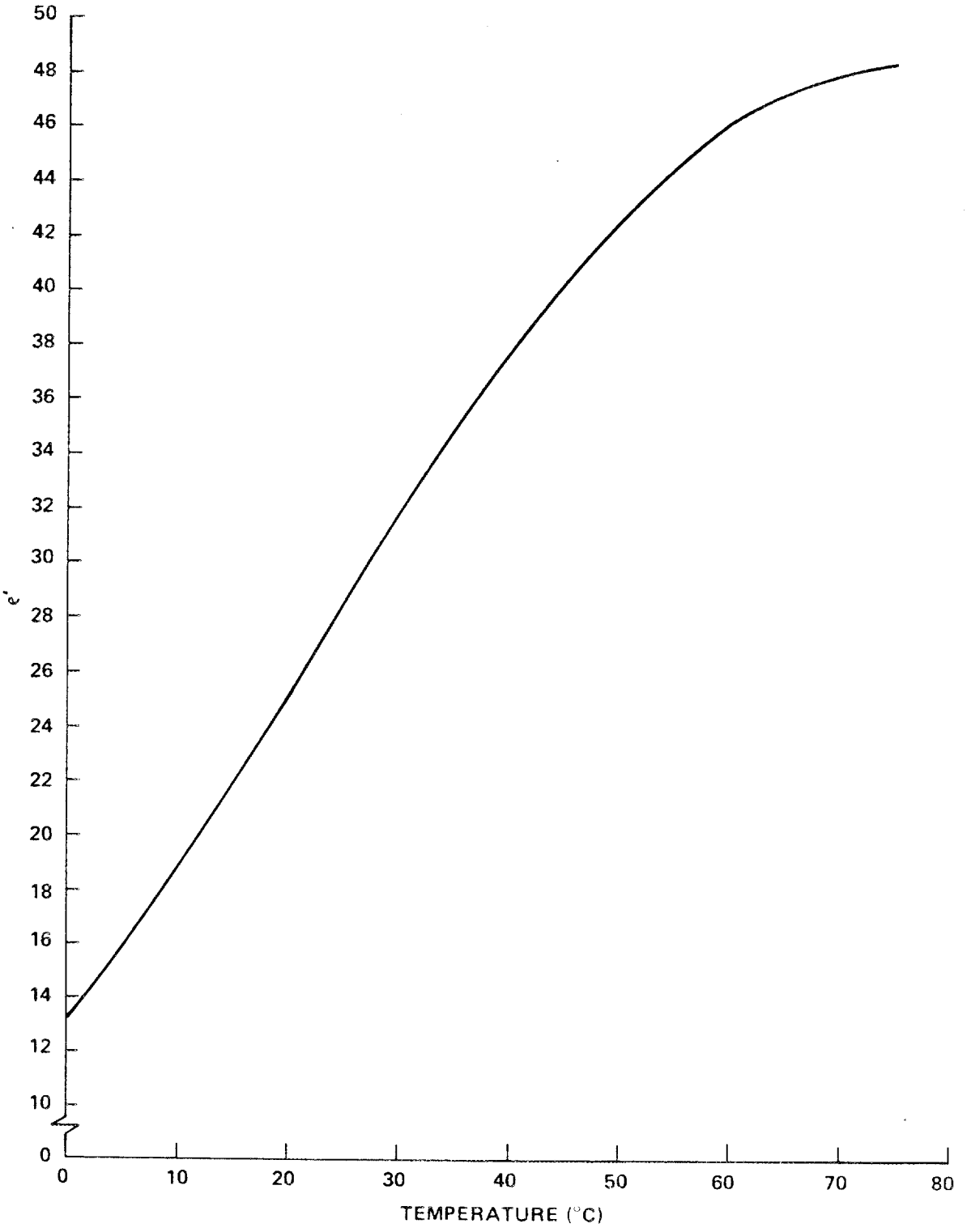

Figure 13. Relative Dielectric Constant of Water at 28 GHz

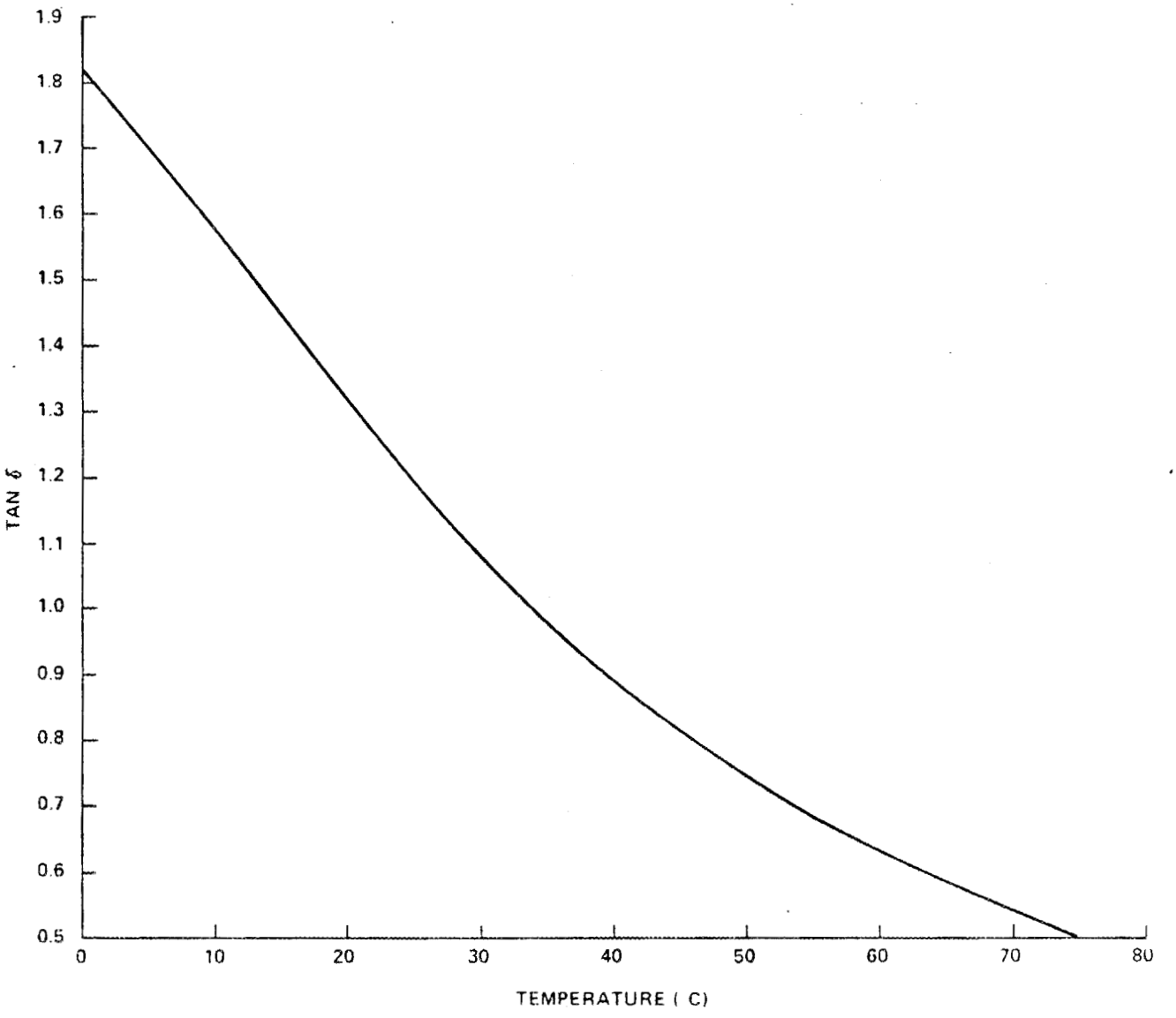

Figure 14. Loss Tangent for Water at 28 GHz

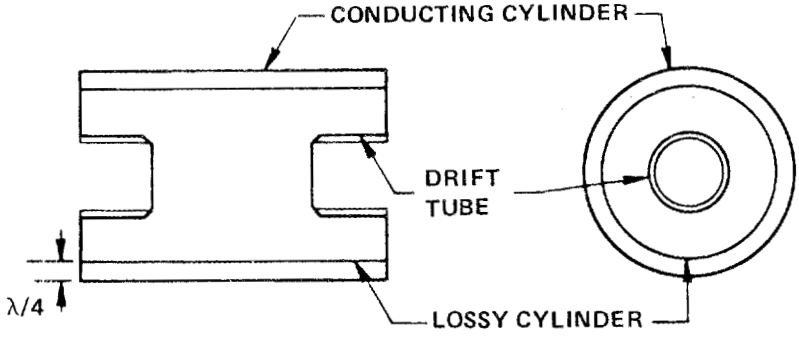

Figure 15. Lossy Cylinder

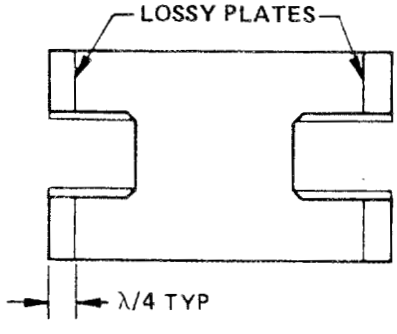

Figure 16. Lossy Plates

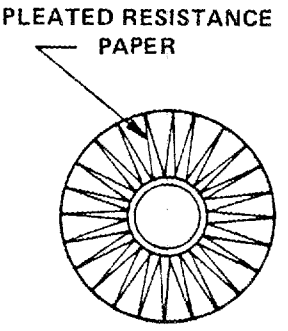

Figure 17. Lossy Wedges

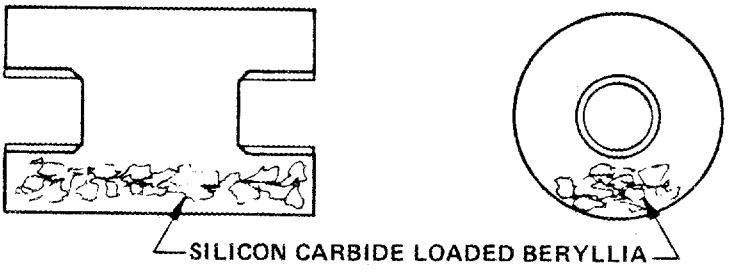

Figure 18. Silicon Carbide Loaded Beryllia Loading

The net result of the drift tube loading experiments is that a reasonable degree of flexibility is shown in how the loss in the drift tube cavity can be attained.

An additional experiment in drift tube loading consisted of coating the conducting cylinder of the drift tube cavity with Kanthal^{tm} (Kanthal is a trademark of Kanthal Corporation for an iron base electric resistance alloy.) The loss for the Kanthal coated cylinder was not much more than the uncoated cylinder and was much less than the silicon carbide loaded beryllia loading.

H. COLLECTOR

The collector design is strongly influenced by the type of output system chosen. If microwave output is separated from the beam immediately following the output cavity iris, greater mechanical design flexibility is possible for the collector. One can choose collector diameter, length, and axial position and the tapers on either end independent of microwave considerations. The collector might also be built without the need for collector focusing coils, though this might require an awkwardly large diameter.

If microwave output is brought out through the collector, a small diameter is desired from a microwave point of view, and tapers are critical. Collector coils are required. High power collectors have been known to deform slightly at high power densities. This might cause undesirable mode conversion.

Electron trajectory calculations were made to determine the beam distribution in the collector region for a variety of conditions with no external collector magnet coils. Variations in transverse energy, simulating rf output conditions, and variations of space charge were analyzed. For a 10-inch-diameter collector, the maximum power density was approximately 900 W/cm^2.

A collector geometry was analyzed for 20 ft/sec velocity water flow at 100 lb/in^2 absolute pressure at 35^oC temperature for power densities of 900, 1200 and 1500 W/cm^2. The collector geometry consisted of a 10-inch-inside-diameter cylinder, 0.713 inch thick with 120 3/16-inch-diameter water passages centered 0.3 inch from the heated surface. The equations used in the analysis are:

$$h = 0.023 \frac{k}{d} \left(\frac{ud}{\nu}\right)^{0.8} P_r^{1/3}$$

for normal convection, where

h = average heat transfer coefficient [Btu/hr ft^2F]

k = thermal conductivity [Btu/hr ft F]

d = diameter [ft]

u = velocity [ft/sec]

ν = viscosity [ft^2/sec]

P_r = Prandtl number = $\frac{\nu}{\alpha}$ where

α = thermal diffusivity [ft^2/hr] = $\frac{k}{wc}$ where

w = weight density [lb/ft^3]

c = heat capacity [Btu/lb F],

$\ln (q/A) = 3.85373 \ln (t_{wall} - t_{water} - t_{subcooling}) - 0.696782$

for film boiling where

q = rate of heat transfer [Btu/hr]

A = area [ft^2]

t = temperature [F],

and

$(q/A) = 4 \times 10^5 u^{1/3} + 4800 (t_{saturation} - t_{water}) u^{1/3}$

for the burnout peak heat flux.

The wall temperatures calculated for 900 W/cm^2 are shown in Table 3. The water channel burnout wall temperature of 199.4^oC makes this case marginal, considering the possible circumferential variations of power density of a beam emitted by a temperature-limited cathode. Further calculations considered variations in water velocity, hole diameter and number of holes.

TABLE 3

Collector Wall Temperatures

Wall	Temperature (^{o}C)
Heated face	351
Hot side of hole	197.7
Cool side of hole	108
Rear face	117

In general, the area of greatest concern in the collector is the point of maximum power density. This usually occurs at the intersection of outer beam edge and the collector cylinder. Further insight to the problem can be gleaned by considering the following approximation, shown in Figure 19. The assumptions made in the approximation are the beam emanates from a point source on the axis, and that the current is uniformly distributed over a spherical segment. The maximum power density on the collector surface is then given by the following equation:

$$P.D. = \frac{P_o \sin^3 \left[\tan^{-1}\left(\frac{R}{\ell}\right)\right]}{2\pi R(2.54)^2 \left\{\cos\left[\tan^{-1}\left(\frac{R}{\ell+L}\right)\right] - \cos\left[\tan^{-1}\left(\frac{R}{L}\right)\right]\right\}}$$

Where P_o = Beam power in kilowatts

R = Collector cylinder radius in inches

ℓ = Axial distance in inches from point source to intersection of outer beam edge and collector cylinder

L = Axial length of beam interception along collector cylinder in inches

$P.D.$ = Maximum power density in kilowatts/cm^2

The above equation was evaluated for different values of R, ℓ and L assuming a beam power of 640 kW. Representative results are shown in Table 4. Some of the cases in Table 4 will be impossible to realize, while others

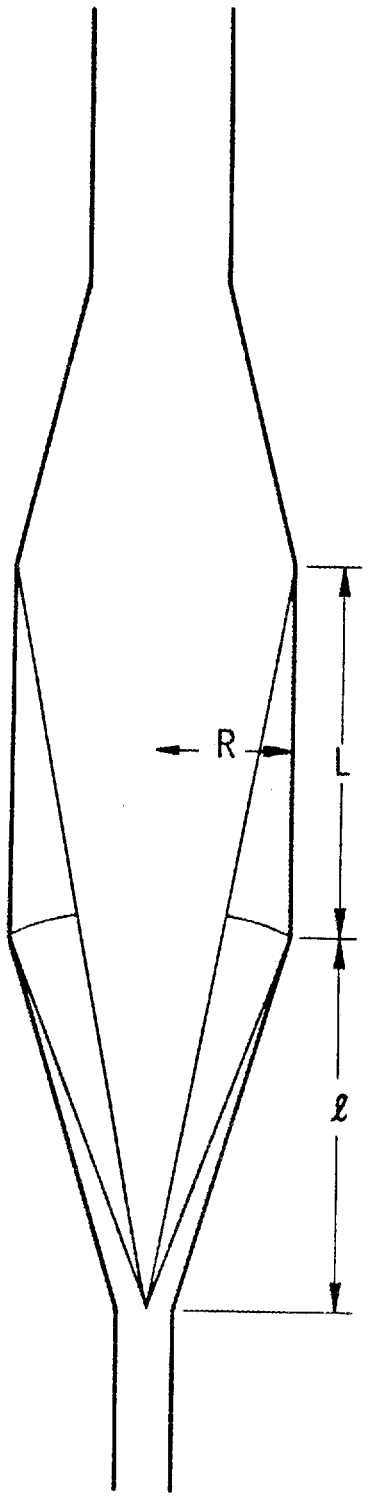

Figure 19. Model for Calculating Collector Dissipation Assuming a Point Source of Electrons

TABLE 4

Approximate Maximum Power Densities for Different Collector Geometries

R (inches)	ℓ (inches)	L (inches)	P.D. (kW/cm^2)
1.250	24	36	1.27
1.250	30	18	1.40
1.250	30	∞	0.85
1.5	8	10	3.26
1.5	8	18	2.88
1.5	12	18	2.10
2.0	8	8	2.58
2.5	4	18	2.62
2.5	8	18	1.66
2.5	10.781	9	1.64
2.5	10.781	18	1.34
2.875	8	8	1.74
2.875	10	8	1.55
2.875	10.781	5.943	1.72*
3	8	6	1.86
4	8	6	1.33
5	3	24	0.86
5	4	5	1.22
5	4	24	0.85
5	6	3	1.59
5	6	24	0.77
5	6	∞	0.72
5	8	3	1.53
5	8	6	1.02
5	8	12	0.78
5	8	∞	0.63

*Case corresponds to Figure 22 of Quarterly Report No. 5 assuming the beam follows the flux lines.

will be difficult because of required shaping of the magnetic field in the collector region.

A special case of no collector coils was studied making the assumption that the beam would follow the magnetic flux lines. The parameters ℓ and L were adjusted as a function of R to match computed flux lines in the collector region due to leakage from the main solenoid. The maximum power density as a function of R is shown in Figure 20. The results of this model are reasonably consistent with the more exact calculation discussed earlier which led to a power density of 900 W/cm^2 with a 10-inch diameter.

It was concluded that the most conservative design for the collector would involve a 10-inch diameter, which would have a tolerable power density with little or no special shaping of the magnetic field. CW operation with smaller collector diameters was feasible but would require careful magnetic shaping.

I. MAGNETICS

Various magnetic circuit approaches incorporating iron pole pieces were evaluated on the computer. The DOE program TRIM was used to evaluate design alternatives for the solenoid. The goal was to achieve a design with less than 0.4% calculated variation in magnetic field in the central 5 inches (of axial length) of the solenoid, with a goal of 1% variation in the actual solenoid. The concentration of ampere turns was chosen to be compatible with the capabilities of hollow-core conductors. The initial thickness chosen for the iron pole pieces was 1.25 inches. The goal was to obtain the desired field with the same value of current in all the coils, with an upper limit of 500 amperes. Two approaches were considered: varying the conductor size and number of turns from coil to coil, and varying the spacing between identical coils. The latter approach was decided upon because of flexibility of the design and coil inter-changeability.

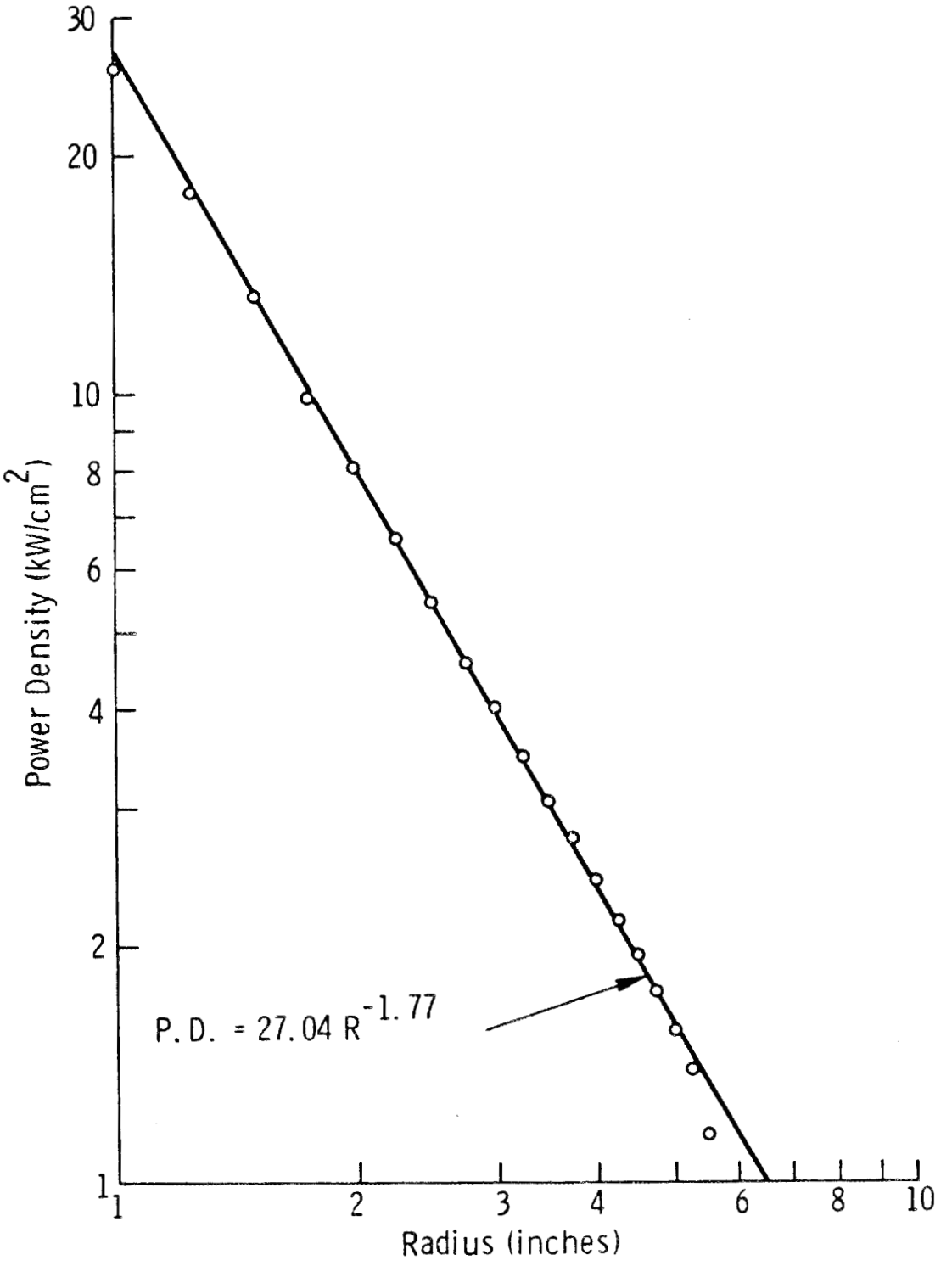

Figure 20. Maximum Collector Power Density with No Collector Coils

In Figure 21, the results obtained for the field on axis in the central region of the solenoid are plotted. The variation is about 40 gauss, or about 0.365%, meeting the design goal. Twelve identical coils of 41 turns each were used, with a current of 488 amperes. However, the peak field in the iron reaches 19.2 kGs, an excessive value if the effects of saturation are to be avoided. Therefore, the iron pole pieces were increased in thickness to 1.75 inch.

The Varian program LAPLACE was used to study design alternatives for producing the desired magnetic field in the regions of the gun and the collector. The best approach seemed to be the use of supplementary coils in those regions, with associated iron shielding. In Figure 22, the results are plotted showing flux tubes and magnetic equipotentials for a radially thin, 5-inch-diameter coil for use in the gun region. The field on the axis in the region of the gun is plotted in Figure 23. Analysis of the beam optics using the two-dimensional field indicated that the off-axis field shape was not optimal with the effective gun coil diameter as small as 5 inches. Calculations were then performed simulating radially thick coils of mean diameter larger than 5 inches. Finally, a configuration was chosen using a 5.5-inch effective diameter and two coils for flexibility of adjustment.

Figure 24 shows a sample of a LAPLACE analysis applied to the collector region. In this case, the intent was to design coils for a collector with a 5-3/4-inch inside diameter. Two coils were used in the calculation, one just above the collector pole piece and one around the upper end of the collector. The 1-3/4-inch thick collector pole piece representing the final design for the main magnet was assumed in the calculation. The flux tubes representing the outer and inner envelopes of the beam in the center of the solenoid are shown as dashed lines. The design limit for mean power dissipation in the collector is 1 kW/cm^2. For the case of Figure 24, the mean dissipation would be 0.924 kW/cm^2, based on the flux tubes threading the envelopes of the beam in the solenoid. The solenoid coils are simulated by fields specified at the mean coil radius, a technique that compares reasonably well with results from TRIM.

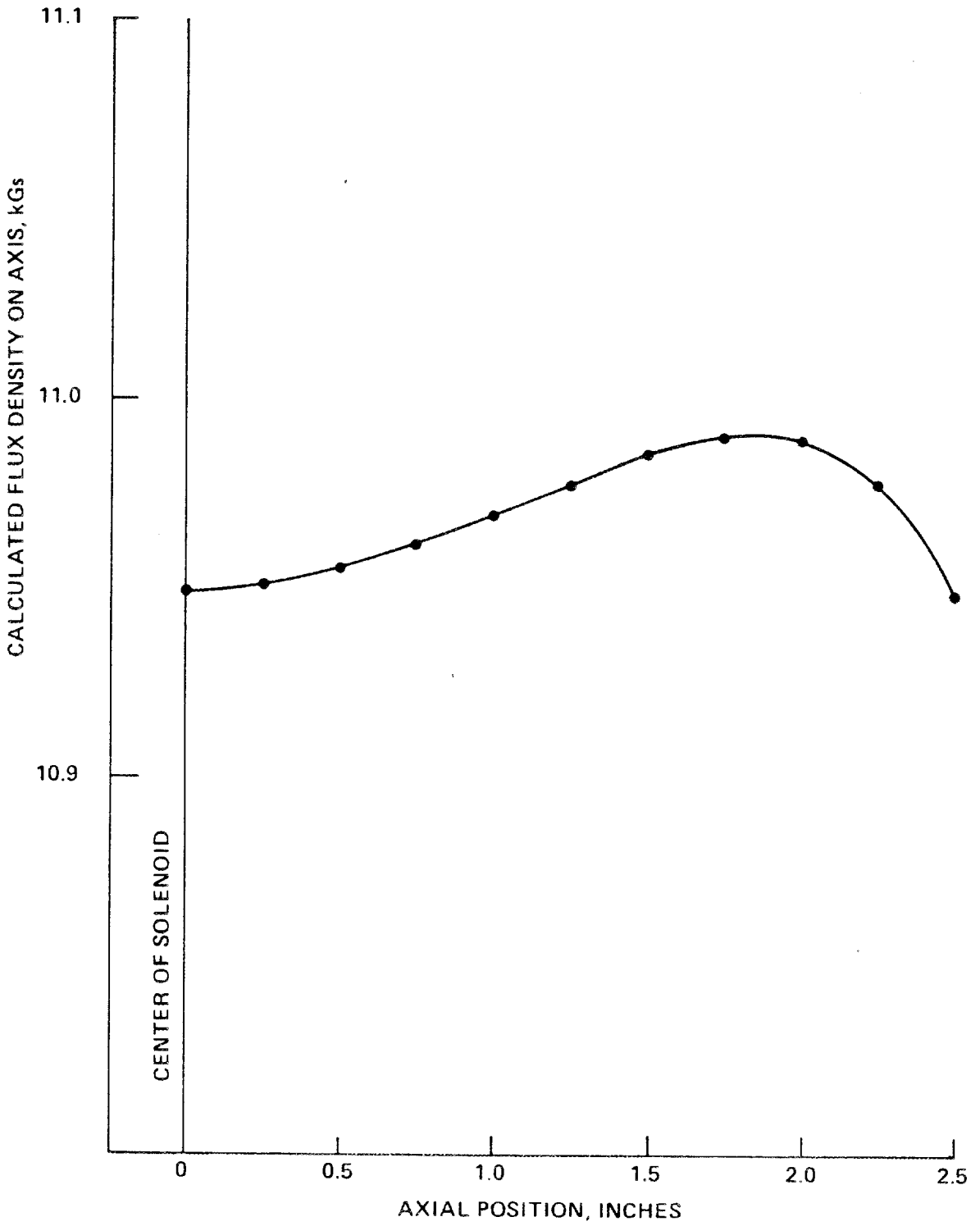

Figure 21. Field on Axis in Center of Solenoid, from TRIM

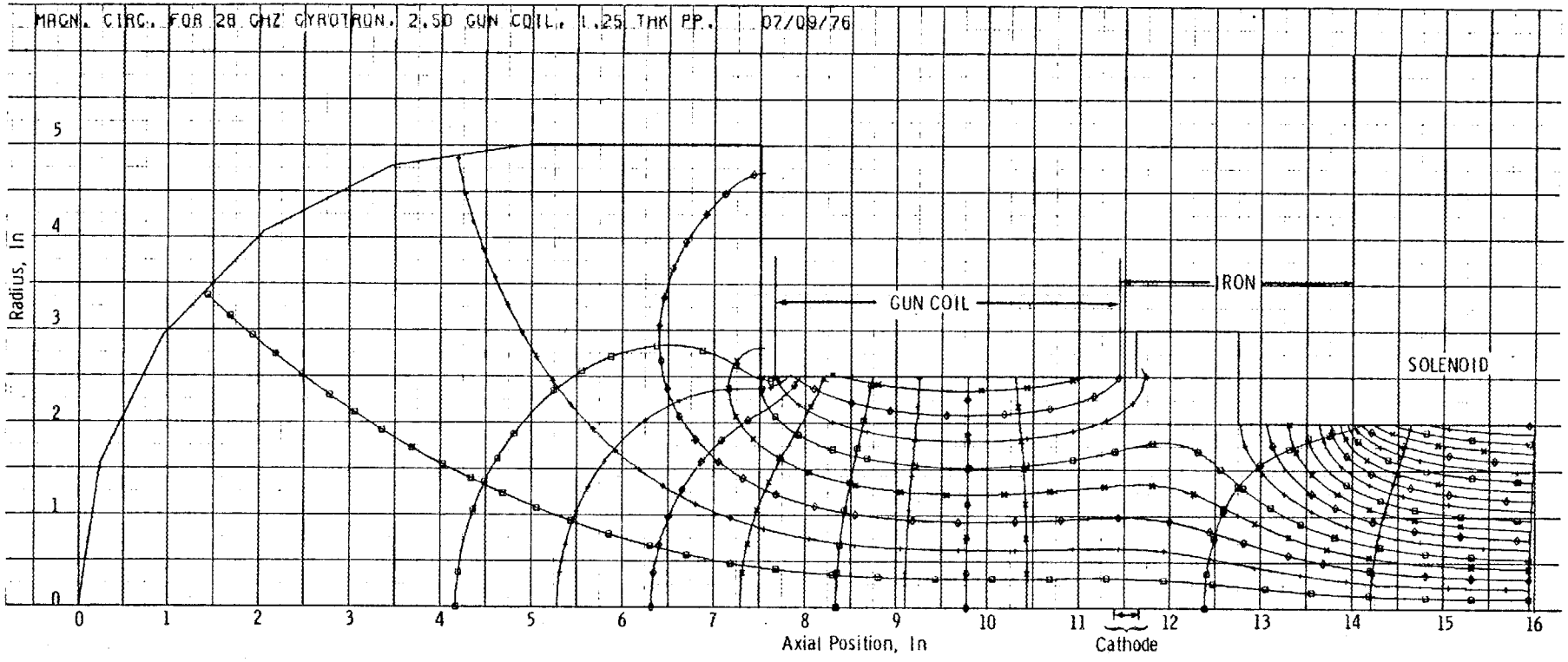

Figure 22. LAPLACE Solution for 5-inch Diameter Gun Coil

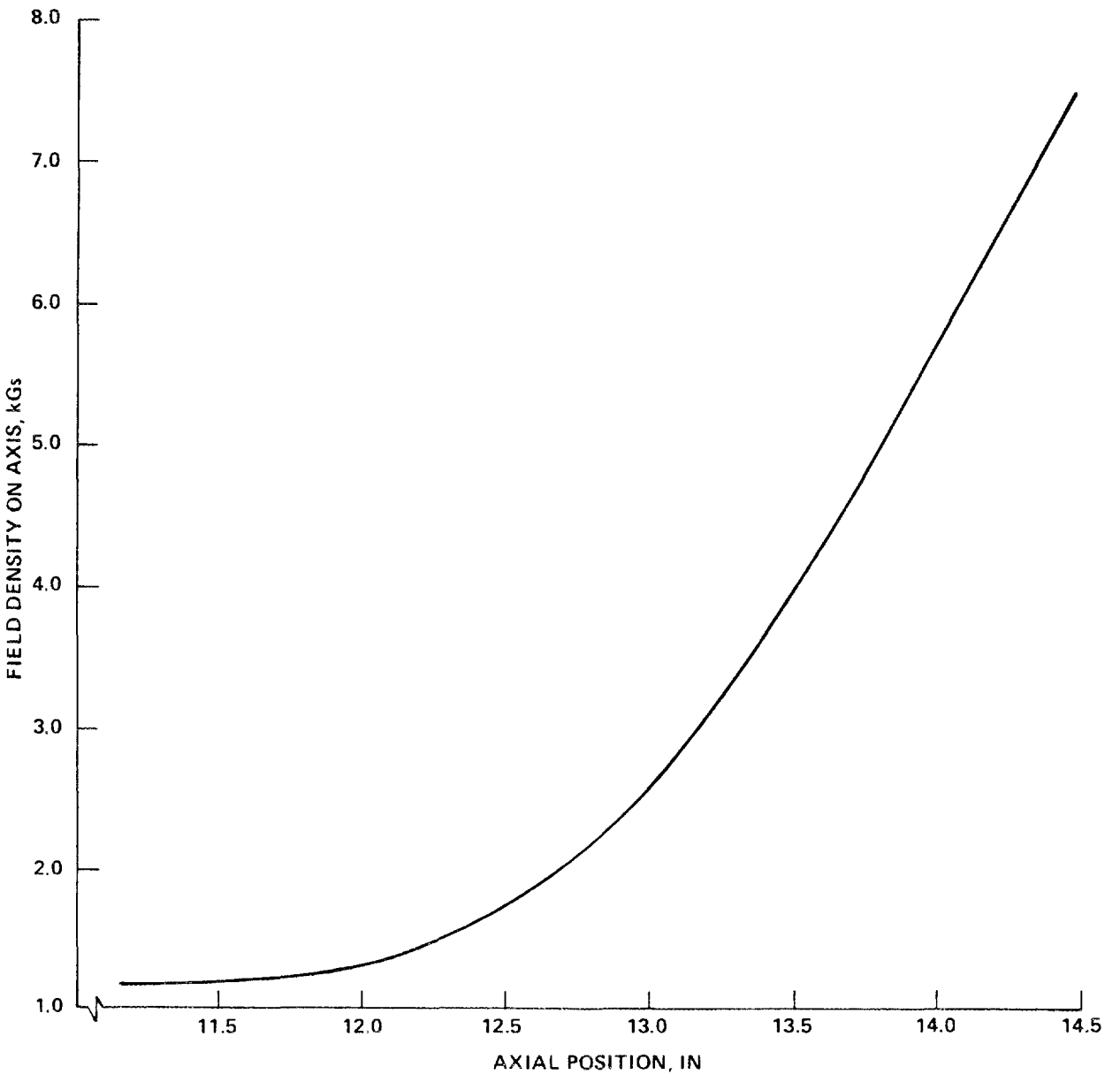

Figure 23. Computed Field on Axis from LAPLACE for Thin 5-inch Diameter Gun Coil

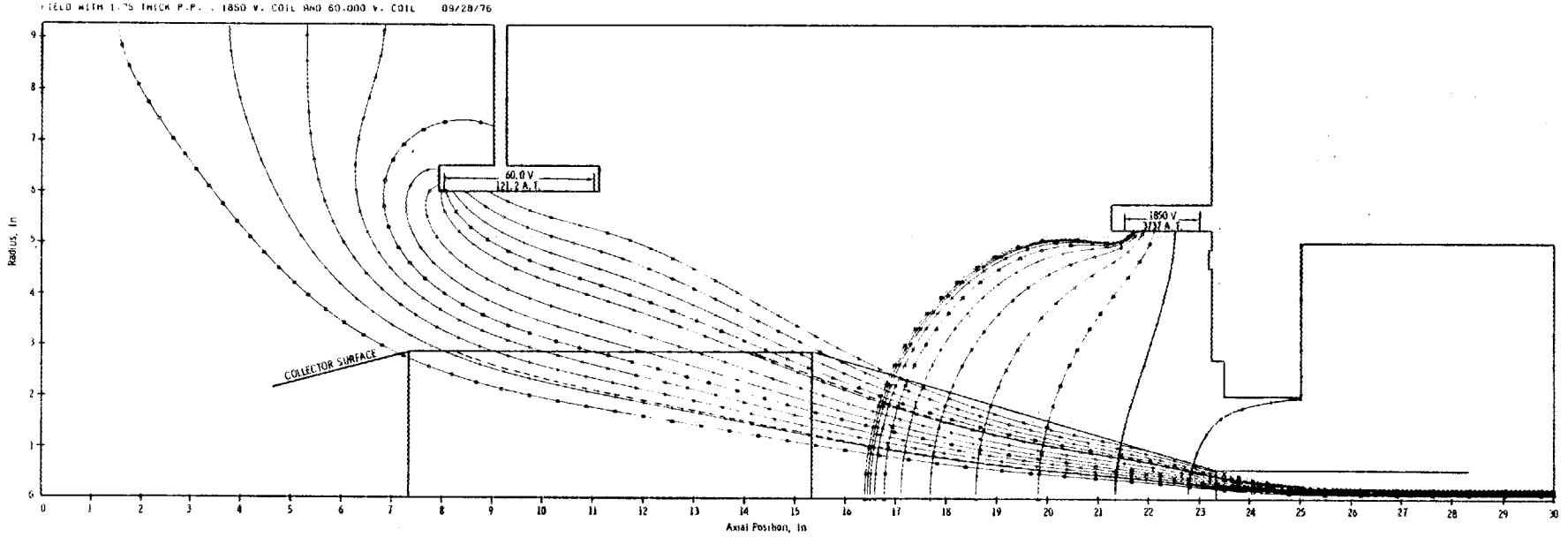

Figure 24. LAPLACE Run for Flux Tubes in Collector with 121 A.T. and 3737 A. T. Coils Simulated with Ideal Return Paths

Computations of the actual beam trajectories in the fields of the solenoid plus collector coils indicated that the collector field needs to be cut off more sharply than indicated by a flux tube analysis because the electrons do not follow flux lines exactly. The calculations also indicated that the vector velocity direction of the electrons on exiting the output cavity may significantly influence their trajectories in the collector.

The magnet frame, as it was finally implemented, consists of a top and bottom pole piece, a three-piece cylindrical outer return path and an inner nonmagnetic cylindrical core. The two pole pieces are 1.75 inches thick with 4-inch diameter center holes. The return path is made up of three 113° sections from a single cylinder 19 inches in outside diameter. These sections are 1.4 inches thick and are bolted to the pole pieces. The material for both the pole piece and the body is a low carbon steel alloy ($\leq$0.22%C).

The inner cylinder core, through which the tube will be inserted, has a minimum inside diameter of 3.85 inches. It is held in place between the two pole pieces. Its purpose is to restrict the coils from shifting radially. It is made from type 304 stainless steel.

The designing, machining, and assembling of the first magnet frame was accomplished at Varian. However, the first set of main solenoid coils and the gun coils were designed and constructed at Oak Ridge National Laboratory and Ogallala Electronics, respectively.

The main solenoid coil design was greatly affected by the two criteria of high field and homogeneity of the near axis field. The three-in-hand, double-pie pancake winding used minimizes the amount of transverse magnetic field produced. The high field, hence high current density requirements, dictated the use of hollow core conductors. This in turn caused the magnet return path to be slotted as mentioned earlier. The slots in the return path allow each conductor to be brought outside the magnet for water connection.

The cooling water for the main solenoid and the two gun coils is distributed from a manifold supported on the magnet frame. The connections between the manifold and the coils are made through lengths of 3/8 inch OD plastic tubing. The design value for total magnet water flow was 17 gallons/minute.

The two gun coils have inside and outside diameters of 5.5 and 11.0 inches, respectively, and are 2 inches long. Each gun coil is enclosed in a return path with 1/8 inch thick walls. The gun coils are supported by a plate attached to the bottom pole piece of the main solenoid. The inch gap between the main solenoid and the gun coils is 0.848 inch.

The magnetic fields on the solenoid axis were measured using a digital gauss-meter and stainless steel probe alignment fixtures. First, each of the four main magnet sections was excited and the fields measured. These are plotted against the axial coordinate in Figure 25. Next, all coils were excited and a measurement was made of axial and transverse field.

Nowhere was the transverse magnetic field greater than 30 gauss. The axial field was in close agreement with that predicted by computer studies. Figure 26 compares experimental and predicted fields in the region between the cathode and the main solenoid with both the main magnet and the gun coils excited.

J. TUBE LAYOUT

Figure 27 shows an early version of a CW amplifier-solenoid assembly. In this case, the rf microwave output was channeled through the collector, which was reduced in diameter to minimize collector resonance effects. At the time of this illustration a 5.75-inch-diameter collector was being considered.

It was intended that the axis of the tube should be vertical during operation, with the electron gun down and immersed in oil. The layout shows a proposed oil tank arrangement. The high voltage coax leads from the supply cabinets are shown terminating in the side of the tank with flexible

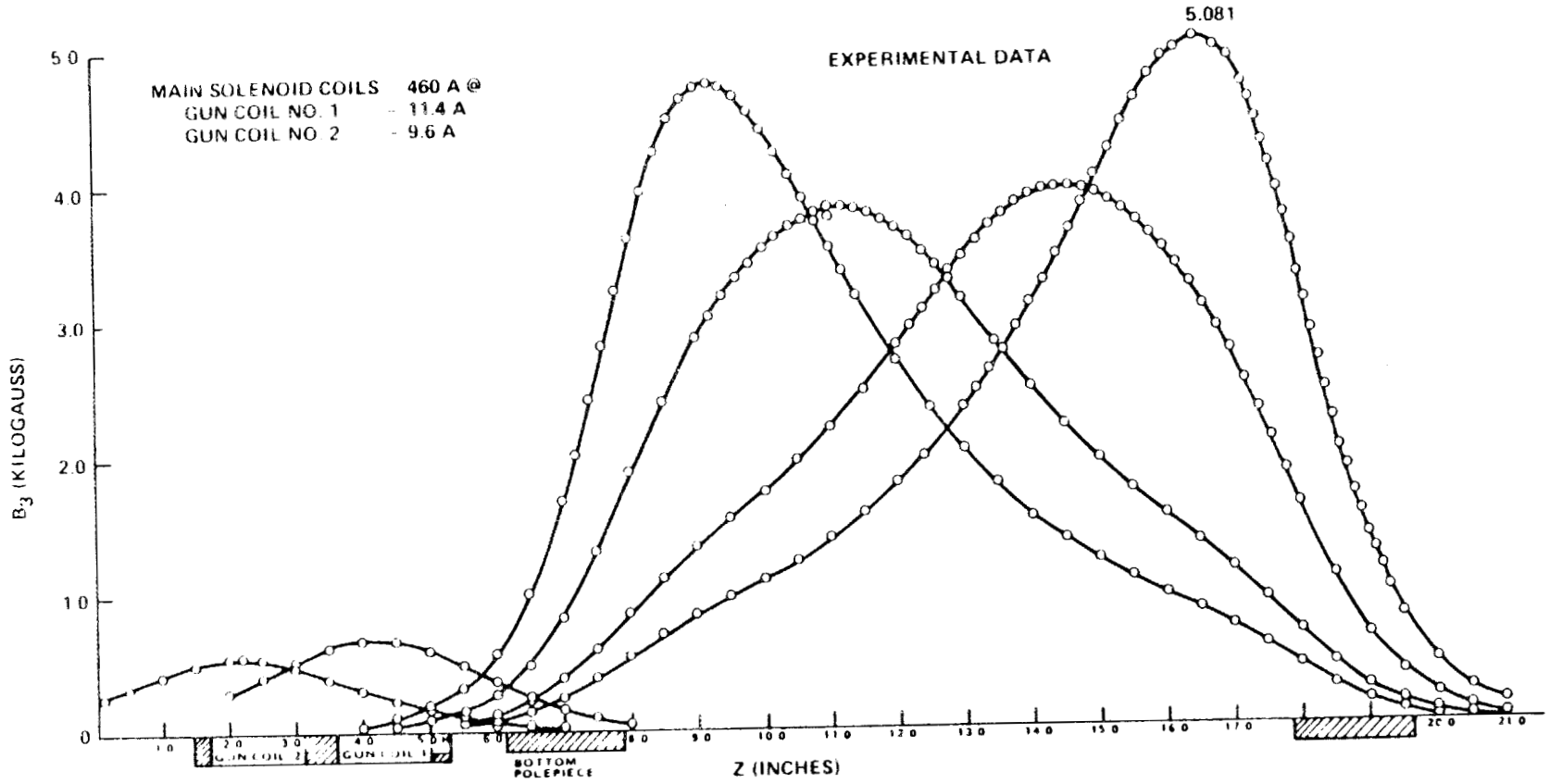

Figure 25. Magnetic Field Contributions of Individual Coil Sets

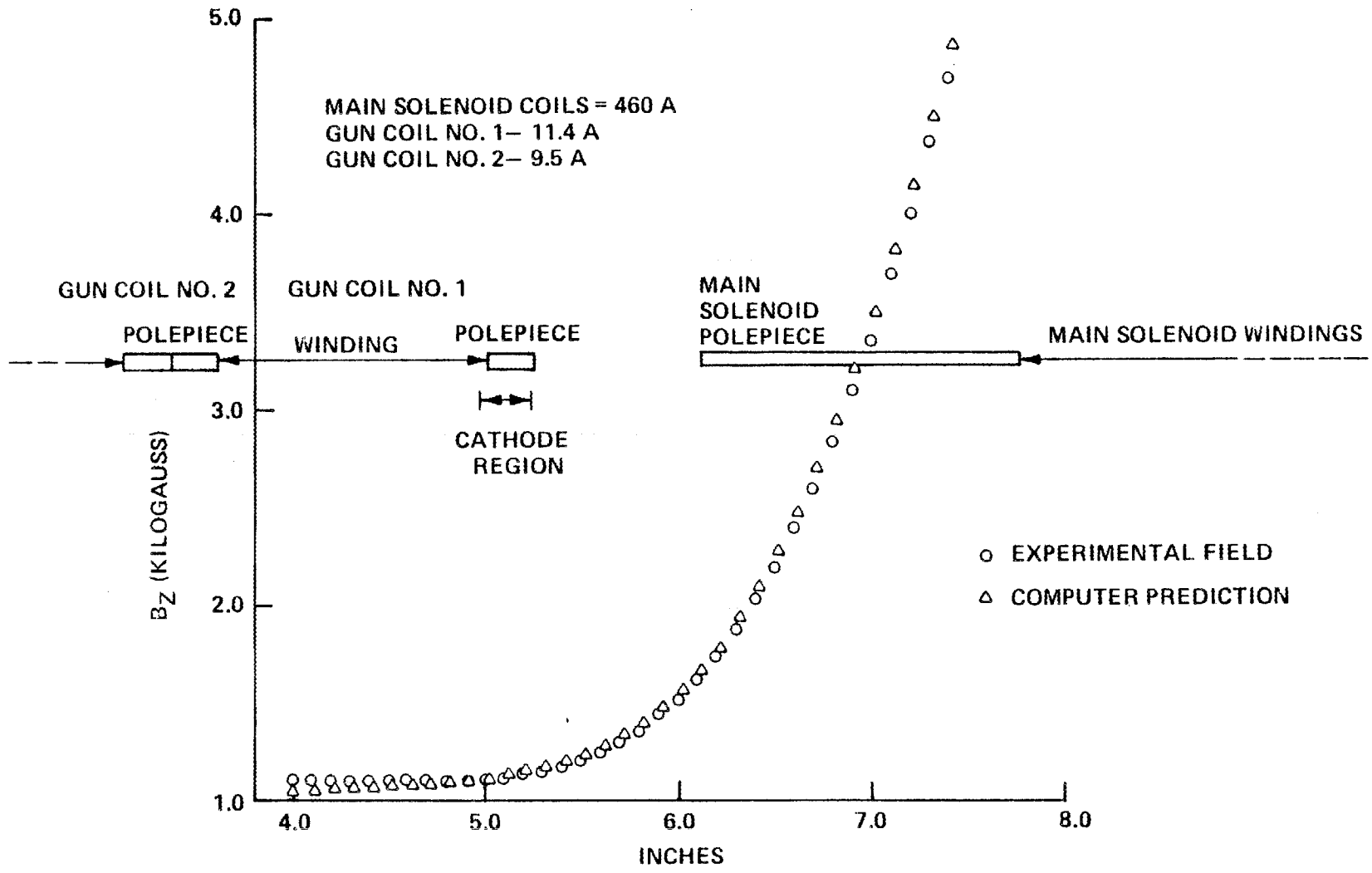

Figure 26. Cathode Magnetic Field

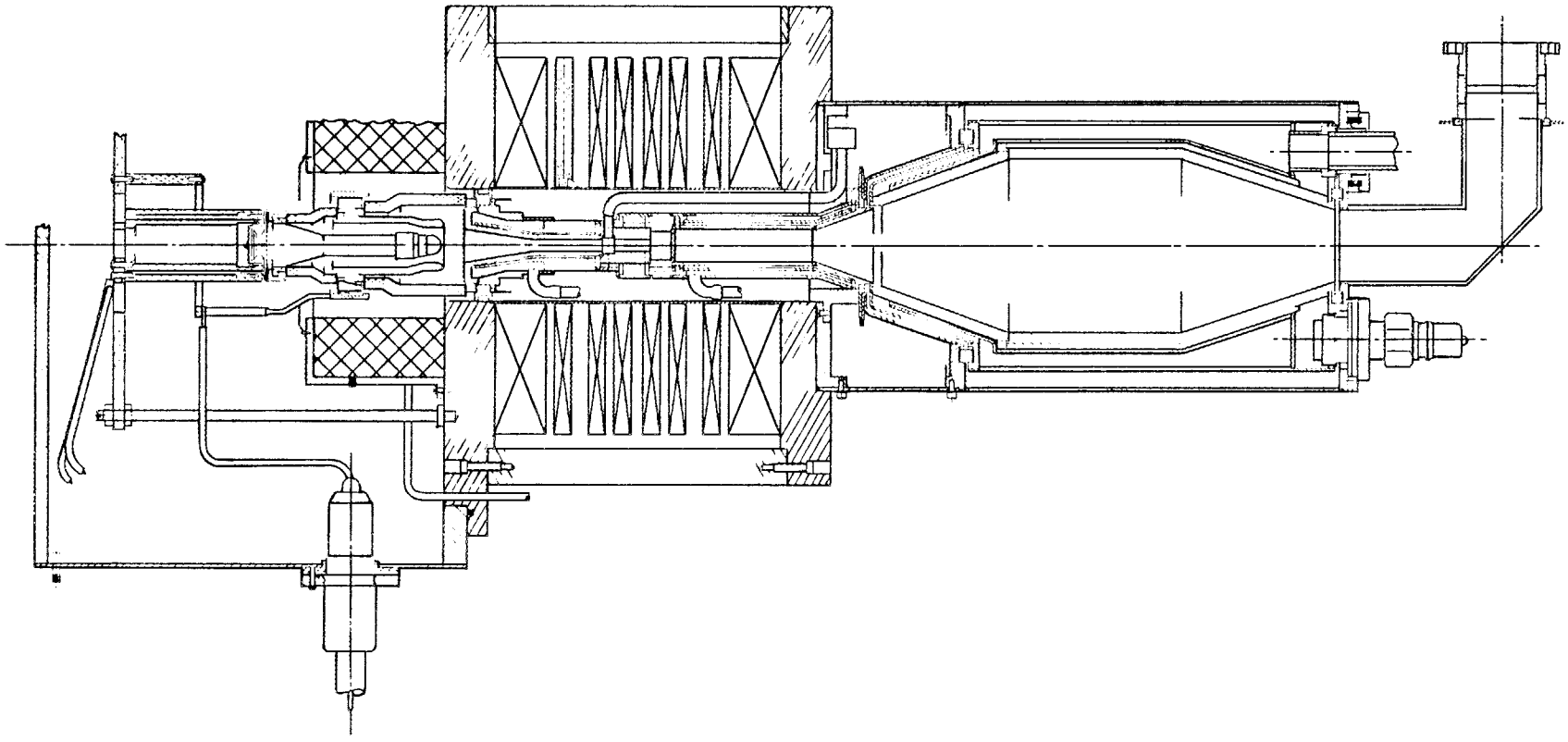

Figure 27. Layout Drawing, Second Revision

leads connecting between these terminals and the tube socket. With this arrangement, the combination of tube, socket, and magnets can be lifted out of the tank for inspection. Alternatively, the tube alone can be lifted out of the magnet and socket assembly. In the latter case, the connections to the gun coil can come out through the lower end plate of the main magnet or, if flexible leads are used, they could go to the side of the tank.

K. OUTPUT WATER LOAD

The rf output waveguide, as envisioned, was to be a 2.5-inch-diameter tubing propagating circular electric modes. Three basic designs were considered for a water load: a long lossy tubing, a quarter-wavelength ceramic disc transformer water load, and conical ceramic load.

A brute force approach would be to provide a long lossy tubing which would be water cooled. The advantage of this approach is that the load would have an excellent match for all modes. The disadvantages are associated with the physical size. Circular electric modes are famous for their low wall losses, resulting in an excessively long length. If bends are required, it is difficult to match all modes. The large surface area would make the calorimetric measurement difficult. It would require avoiding heat losses due to conduction, convection, and radiation between the input and output temperature measurements.

A quarter-wavelength ceramic disc transformer water load would use beryllia as the transformer medium between air and water. Figure 28 shows the required thickness of a 2.5-inch-diameter BeO disc water load window. For a practical system, a $\lambda/4$ window would be too weak, a $3\ \lambda/4$ window would be marginal while a $5\ \lambda/4$ window would be practicable. The $3\ \lambda/4$ and $5\ \lambda/4$ windows would both be narrowband, temperature sensitive, and a poor match for many modes.

A conical ceramic water load which was choosen as the favored approach, used the cone shown in Figure 29. The cone was placed inside the cylindrical guide as a water barrier. Because of its long taper and lack of dependence on thickness, it is a broadband match to all modes. The CW water

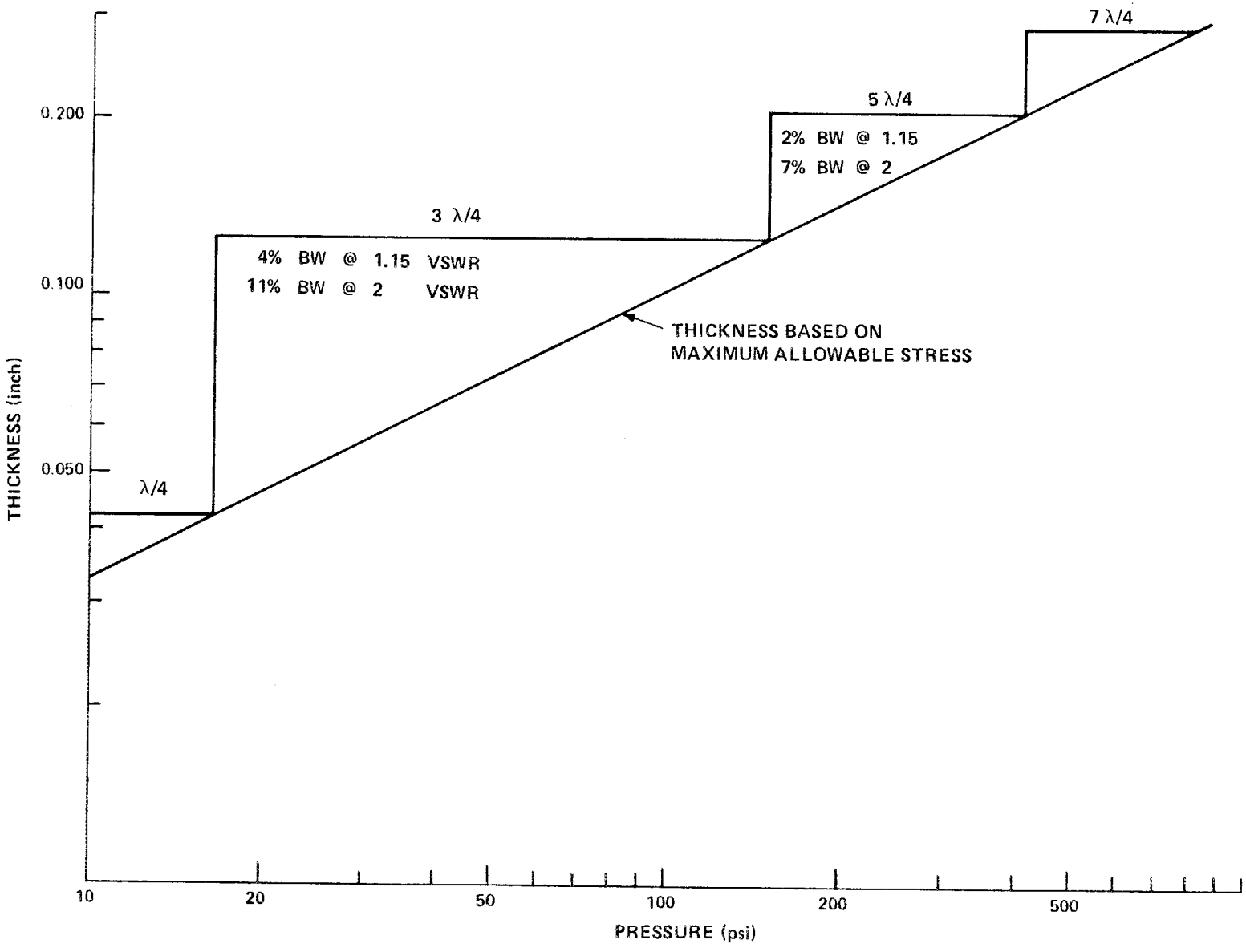

Figure 28. Required Thickness of a 2.5-inch Diameter BeO Disc Water Load Window

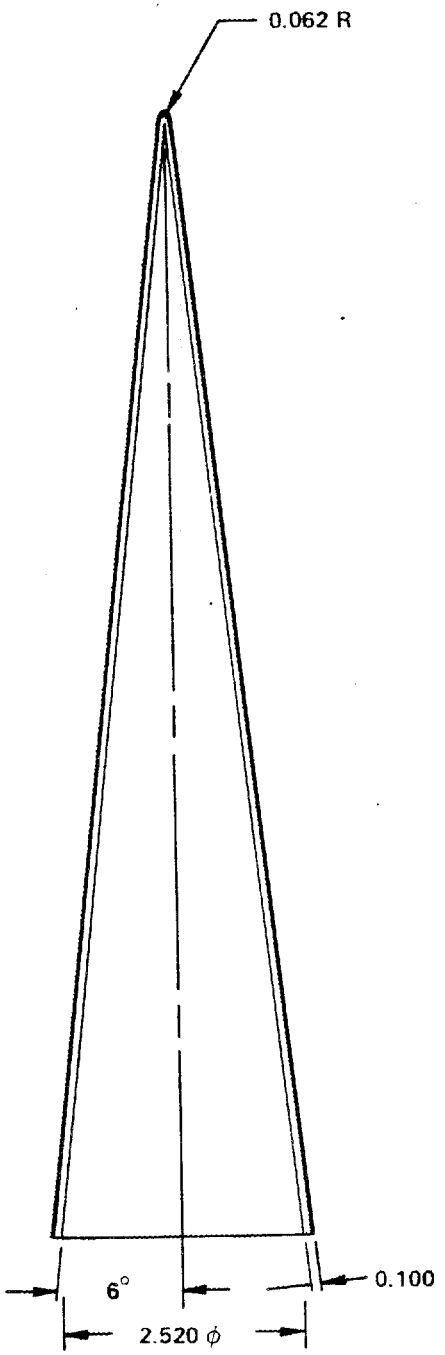

Figure 29. Ceramic Cone

load was designed to pass approximately 75 gallons of water per minute over the cone inside a stainless steel cylinder. See Figure 30.

L. PULSED GYROKLYSTRON AMPLIFIERS

The theory of gyroklystron amplifiers is given in Appendix A. This section of the report gives details relating to gyroklystron pulsed amplifiers No. 1 through No. 4. General design details for the components of these tubes are covered in Sections III-A through III-K. Additional design data, as pertinent to each experimental model tube, are given in the individual sections covering the tubes.

During experimental work with 28 GHz pulsed gyroklystron amplifiers, parallel efforts were carried on in the field of 28 GHz gyrotron oscillators. By the time work was being carried on with gyroklystron pulsed amplifier No. 4, very significant results had been obtained with gyrotron oscillators, and the major thrust of program work was then centered on experimentation with these tubes and the delivery of representative models for use by the customer.

1. Pulsed Amplifier No. 1

The first experimental amplifier was planned as a pulsed tube to test design concepts with minimum construction complication. A pulsed model, for example, with greatly reduced average power, would allow the use of a substantially smaller collector than necessary with a CW tube. The first pulsed tube collector had a 2-inch-inner diameter. Following the collector region, the output guide tapered up to a 2.5-inch diameter to fit the diameter of the CW window. The pulsed tube was built with no 90° bend between the collector and the window. By adding the bend outside the vacuum, the tube could be tested to get a direct evaluation of the effect of the bend on tube performance. Similarly, a structure equivalent to the CW collector could be microwave tested by adding it outside the vacuum. The 2-inch-diameter collector allowed testing at a duty factor of up to 5%.

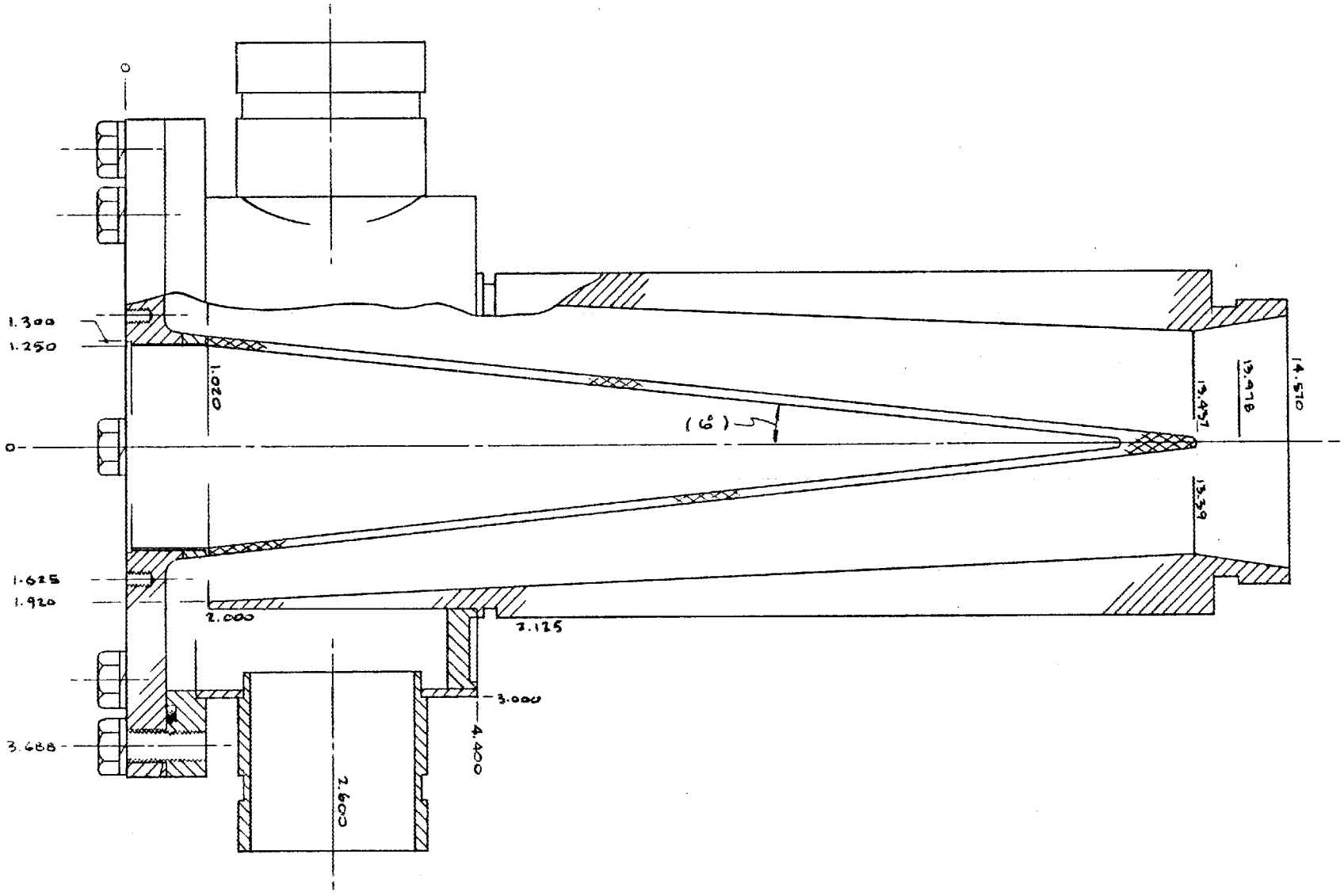

Figure 30. Water Load Assembly

The other difference in the pulsed tube was that the body of the tube did not include integral cooling channels. With this simplification, the tube could be assembled and modified much more quickly.

In other respects, the pulsed tube was similar to the CW design. It used the same basic magnet system, with no collector coils. The initial design used two cavities with a solid metal drift tube separating them. The microwave characteristics of the cavities were the same as planned for the CW tube. The electron gun design was the same. The input window design was the same. A layout of the tube is shown in Figure 31.

a. Output Cavity

The measured values of Q and resonant frequency for the output cavity of the pulsed tube compared to the design values are shown in Table 5.

TABLE 5

Output Cavity Parameters

Parameter	Q	Frequency (GHz)
Design Value	195	28.000
Experimental Tube	192	27.984

b. Input Cavity

The changes in Q and frequency as the input cavity passed through various construction phases are shown in Table 6.

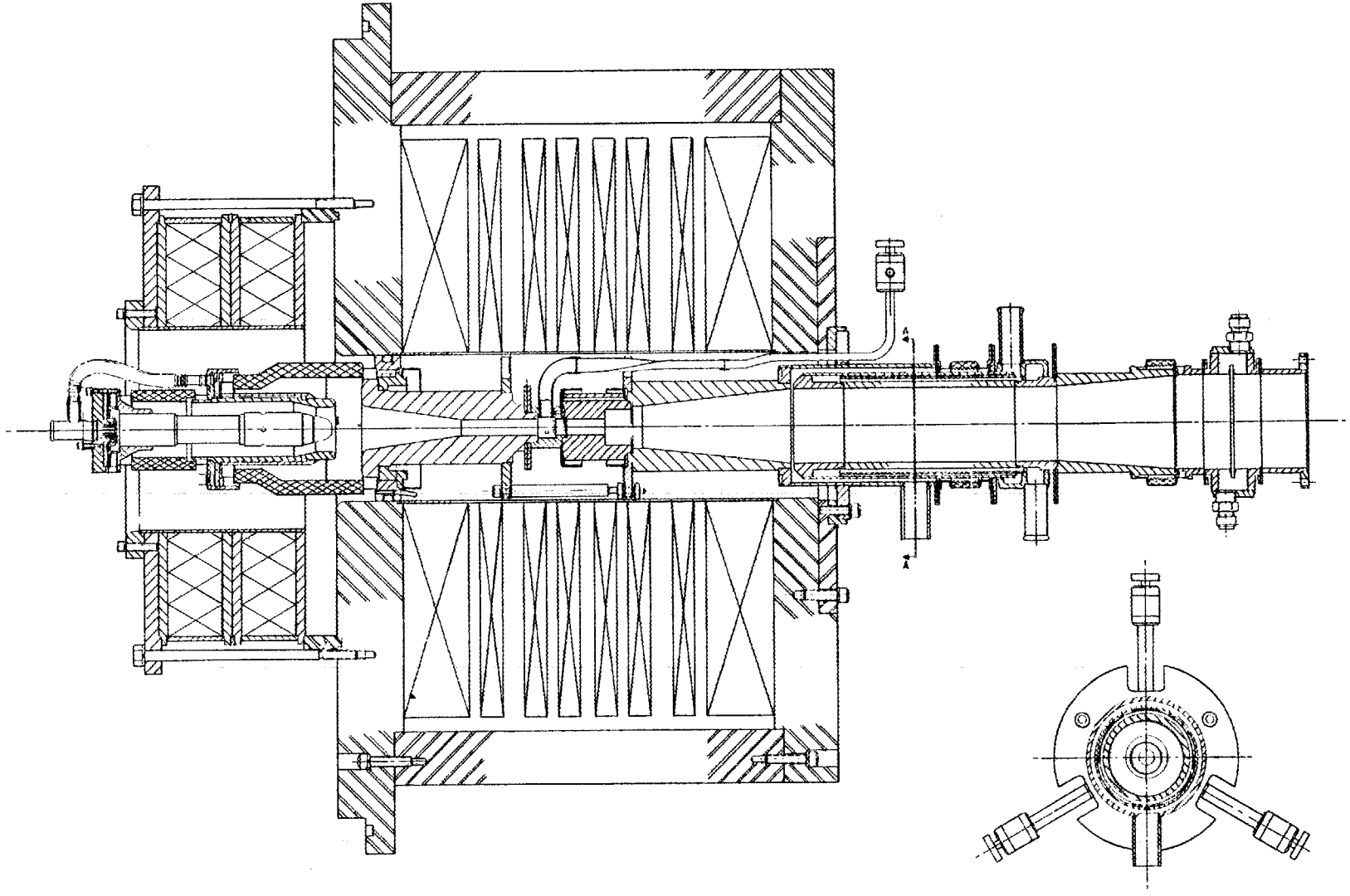

Figure 31. Layout Drawing of Pulsed Tube No. 1

TABLE 6

Input Cavity Parameters

Parameter	Q	Frequency (GHz)
Design Value	333	28.000
Before Braze	346	28.021
After Brazing Two Waveguide Elbows	304	28.010
Before Bakeout	267	28.004
After Bakeout	250	28.010

c. Input Windows

The VSWR of the input windows during construction are shown in Table 7. The bulk of the final window mismatch was caused by the bends which typically have a VSWR of 1.2.

TABLE 7

Input Window Matches

Window	1	2	3
After Window Braze	1.08	1.12	1.09
After Waveguide Bend Braze	1.28	1.34	1.21

d. Drift Tubes

The original design used long lengths of constant diameter drift tubes in the anode, intercavity drift space, and collector regions. There was concern that such long lengths could potentially prove troublesome because resonances at the cutoff frequencies of various modes might result in oscillations. To avoid oscillation, slight tapers were used in the first tube in the three drift spacers mentioned above. The small end of the collector-to-window taper was opened up from 2.00 inches to 2.05 inches diameter. Figure 32 is a photograph of gyroklystron No. 1.

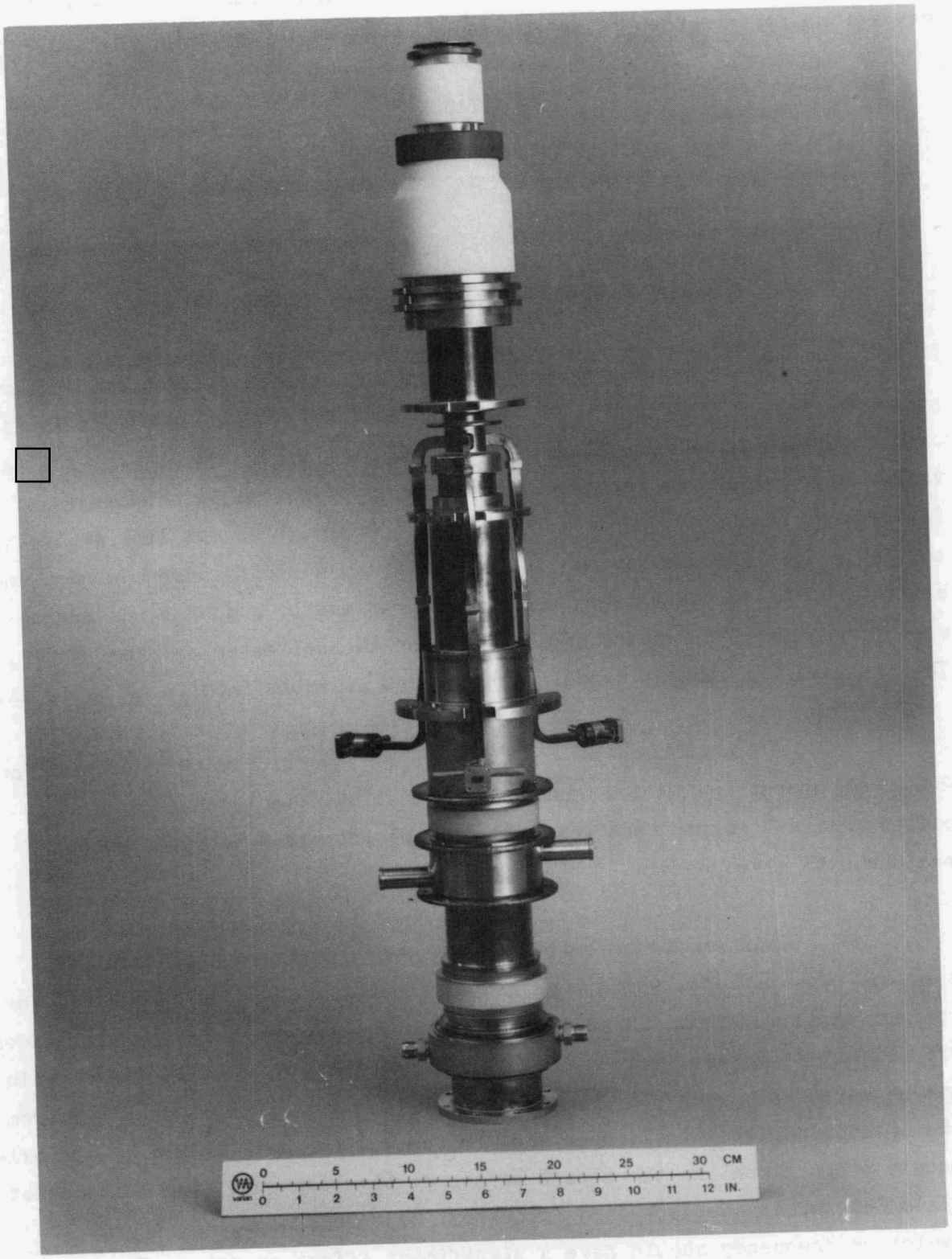

Figure 32. Pulsed Gyroklystron Before Bakeout

Significant performance for a gyroklystron amplifier was demonstrated in tests of No. 1. A summary of the results and standard deviations for a series of measurements is given in Table 8.

TABLE 8

Amplification Results

Peak Power Output	5.81	±0.73	kw
Gain	12.6	±3.1	dB
Cathode Current	2.04	±0.12	A

These results were obtained after overcoming problems in early stages of test. The first problem was that of stray beam electrons landing on the output window resulting in the window cracking. This created a small vacuum leak, which was repaired with Vacseal^{tm} (Vacseal is a Space Environment Laboratories, Inc., trademark for a high vacuum leak sealant.) sealant. The test problem was solved by adding a second output window and evacuating the volume between the two windows and by adding a transverse magnetic field of 630 gauss applied between the collector and the window. This reduced the current reaching the window assembly from 16 mA to 18 μA.

A second problem was the mass of the calorimeter designed for 200 kW CW operation. A low mass load consisting of polyethylene tubing coiled inside a copper tube was used for the calorimetric power output measurements given herein.

Gain and power output levels were limited by the onset of spurious oscillations, which occurred as tube parameters were adjusted for optimum amplification. Three parameters were observed to have a significant effect: beam current, main magnet field, and gun coil field. Stable gain was achieved only when one or more of these parameters was backed off from the optimum design value. According to theory, the gain should be approximately proportional to the square of the dc beam current. The main magnet field determines the cyclotron frequency. A change of a few percent in cyclotron frequency should have a significant effect on gain. The gun coil

field affects the gain by changing the ratio of transverse to axial beam velocity.

The results in Table 8 represent the situation where beam current was reduced to about 25% of design value, and transverse beam velocity was reduced from the design value by operating with higher gun coil field. The main magnet field appeared to be slightly off the optimum value, as well. Operation at increased beam current, for example, required further backing off of main magnet or gun coil fields to maintain stability, and the resulting stable gain was essentially the same.

The results of Table 8 were very encouraging when it was considered that gain should be proportional to the square of beam current. An increase in beam current by a factor of 4 to the design value should increase the gain by 12 dB. This would be reasonably close to the calculated and design values for gain.

The gain-limiting spurious oscillations occurred primarily at frequencies near 26 and 27 GHz. However, by varying beam current, main magnet field, and gun coil field over a fairly wide range of values, it was possible to observe oscillations at other frequencies. To gain as much information as possible about spurious oscillations, a study was made of all detected oscillations. These oscillation frequencies are summarized in Figure 33. Cutoff frequencies for the 0.428-inch-diameter drift tube are shown for comparison.

It is believed that the oscillations were of two general classes. In the first class were modes which could exist in the input cavity, not loaded by the input waveguides or drift tubes. The TE_{212} mode was observed in cold test at 26.705 GHz. This could account for at least part of the problem in the 26.495 to 26.967 GHz range. The TM_{111} mode was observed in cold test from 27.419 to 27.460 GHz. This could account for the oscillation at 27.466 GHz.

In the second class were modes that may involve the entire tube length from the gun to the output waveguide system. These may be influenced

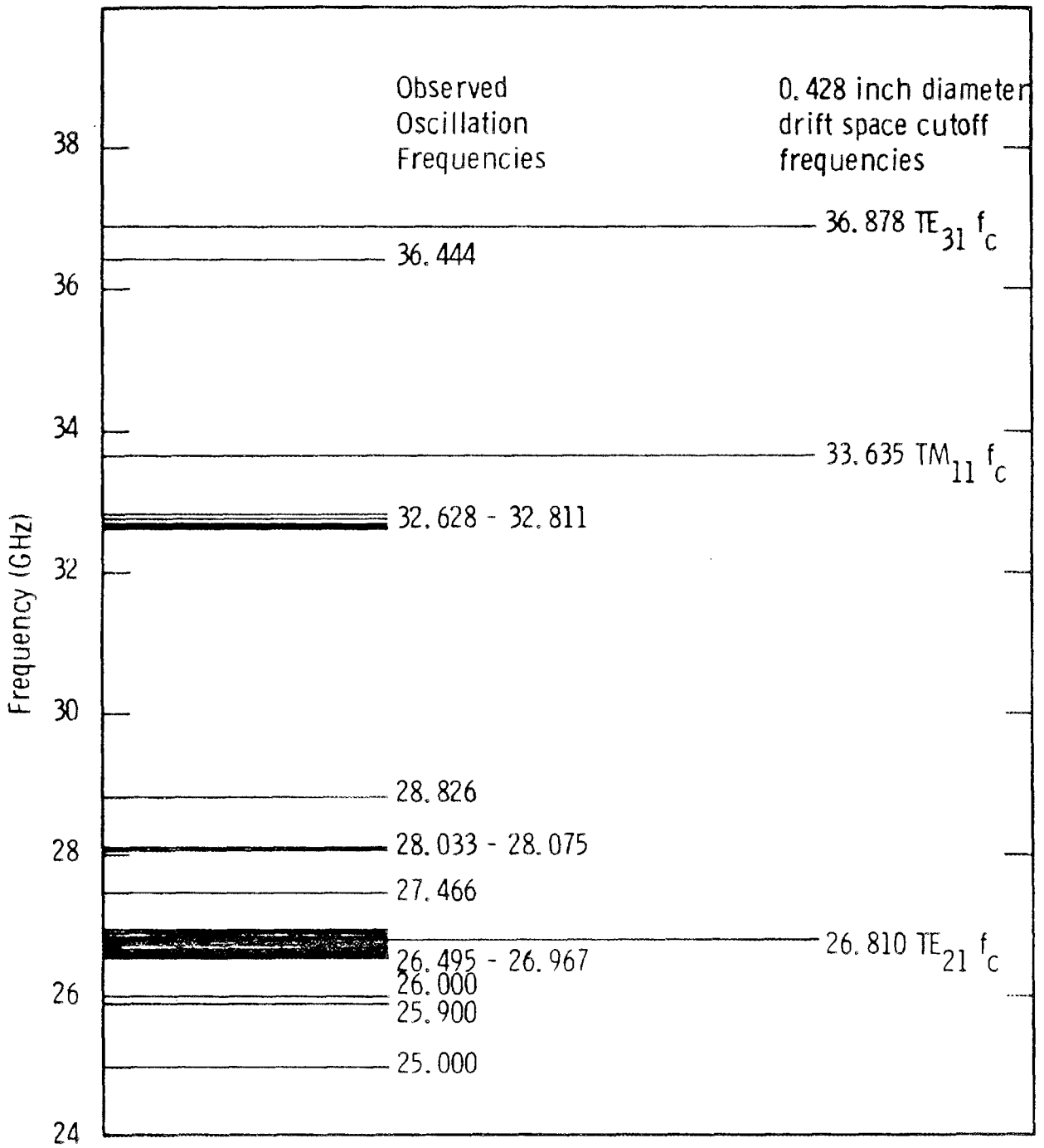

Figure 33. Oscillation Frequencies

by the tube surroundings through the gun ceramics. This may explain the narrow frequency spacing of some of the modes.

These two general classes of modes suggest two general solutions. The first would be to interrupt and load radial and axial wall currents at the corner of the input cavity. The second would be to load the drift tube bore, which must play an essential role in any overall tube resonance.

It was concluded from the tests on No. 1 that the beam quality and performance were quite good and very close to design expectations. This was an important achievement since the characteristics of the beam were radically different from those of typical linear beam microwave tubes. Amplifier performance appeared to be reasonably close to design predictions except for limitations due to spurious oscillations. The interfering oscillations appeared to be the main problem requiring solution to obtain full amplifier performance.

2. Pulsed Amplifier No. 2

Two general design changes were made to the second pulsed amplifier, both directed at improving stability. The first was the addition of Kanthal to the inside surface of the anode tunnel and the tunnel between input and output cavities. Kanthal is a resistance alloy that is flame sprayed onto copper surfaces. Its composition is given in Table 9.

TABLE 9

Kanthal Composition

Iron	72%
Chromium	22%
Aluminum	5.5%
Cobalt	0.5%

It is commonly used as a lossy microwave coating in high power microwave tubes. The details of the bore with Kanthal are shown in

Figure 34. The Kanthal was intended to provide loss for resonances in any geometric configuration that includes the bore. The second change directed at improving stability was the addition of a lossy ring to the input cavity structure. This design feature was discussed in section III-B, "Input Cavity", and was illustrated in Figure 5.

The pulsed amplifier No. 2 was tested in two configurations. The first was a conventional amplifier driven by the klystron driver tube. The second was an amplifier driven by a sample of its own output through a feedback loop, resulting in an oscillating system. The highest powers obtained for these two conditions are shown in Table 10.

In the case of the klystron drive, input power was limited by driver protective circuitry monitoring back power reflected from the input cavity. The input cavity voltage reflection coefficient as a function of frequency is shown in Figure 35. Although the starting current for unwanted oscillations was four times higher than in the first pulsed amplifier, the gain was limited again by oscillations, this time from 26.2 to 27.62 GHz, from 41.445 to 41.455 GHz, and from 43.565 to 43.6 GHz. These oscillations, although in undesirable modes, produced some fairly respectable output powers as shown in Table 11.

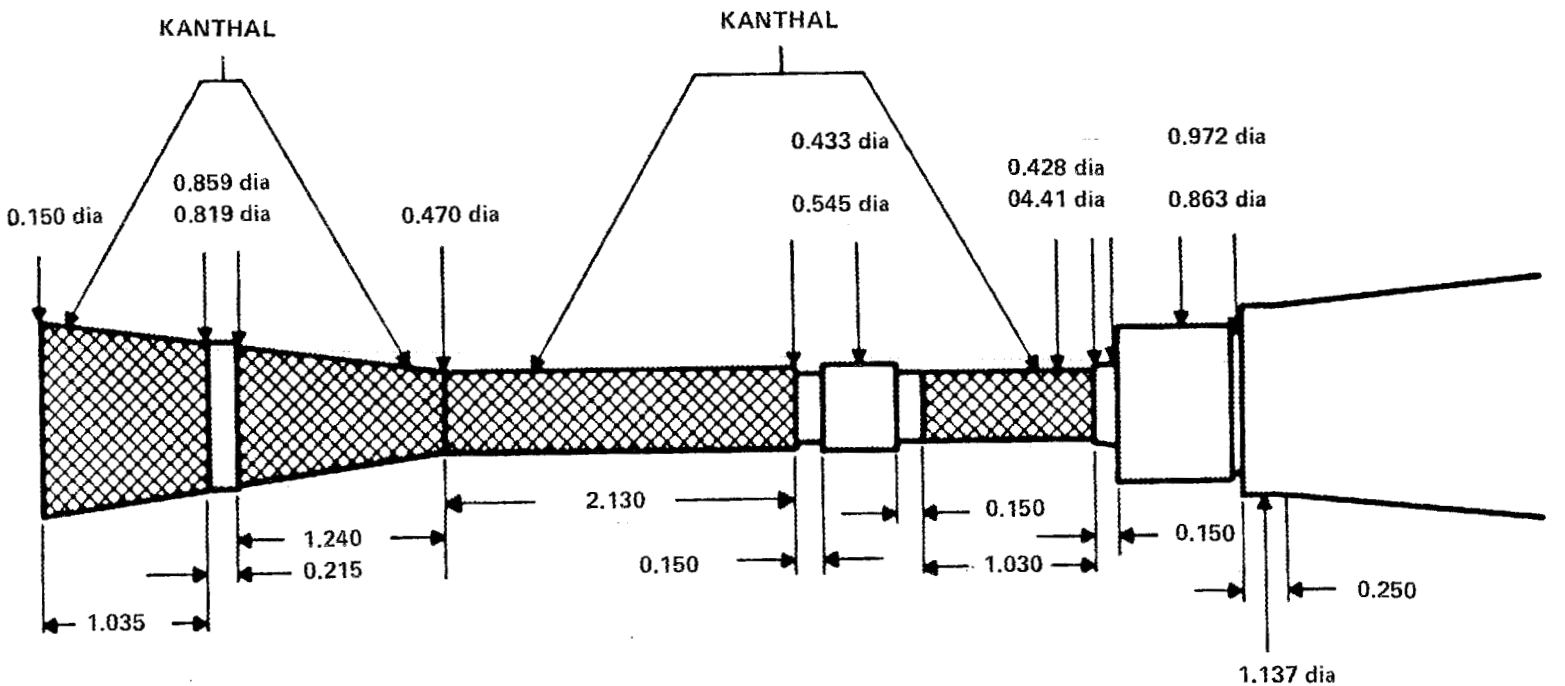

Figure 34. Bore Details of Second Pulsed Amplifier:. Dimensions Assume 0.020-inch Diameter Change of Kanthal

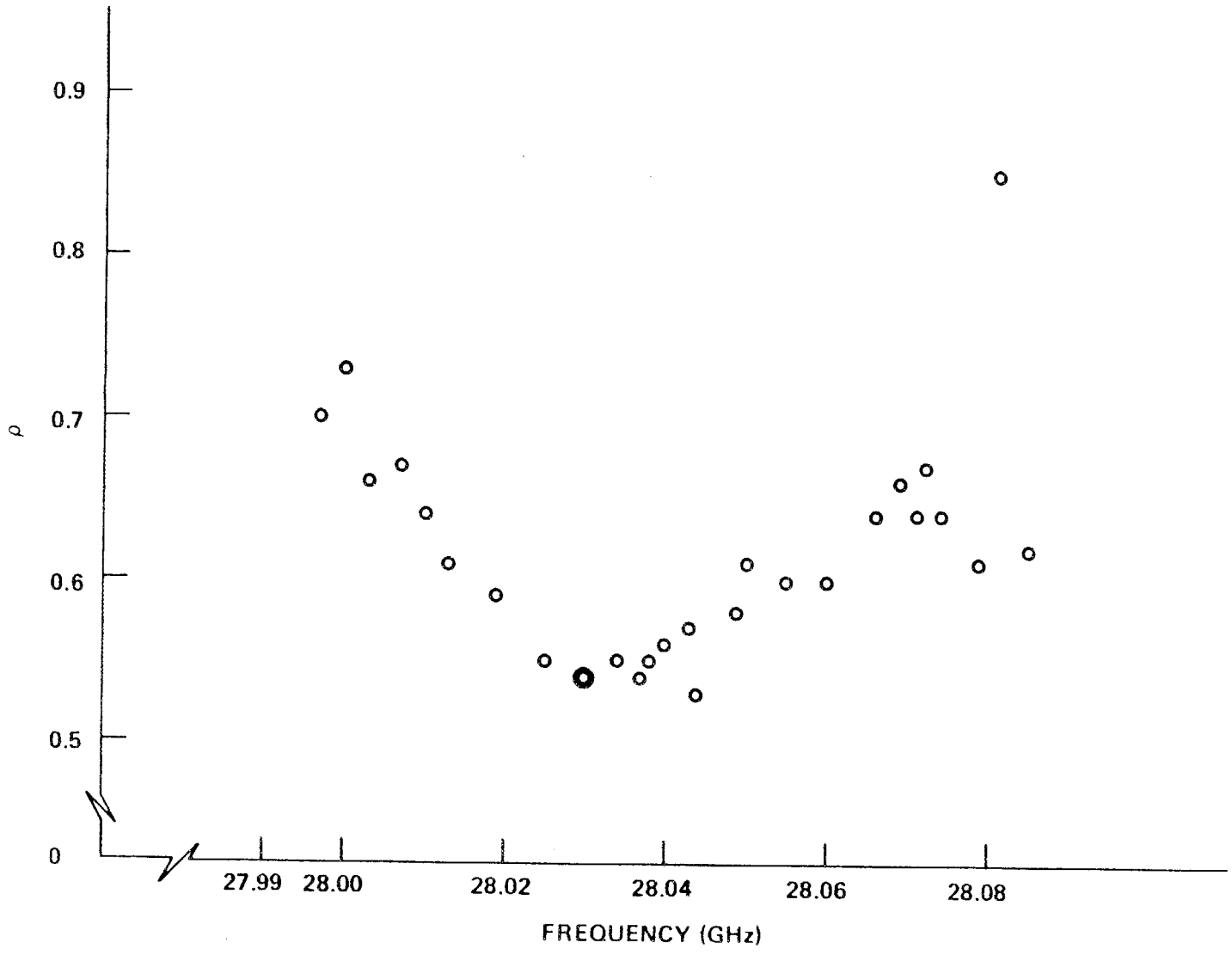

Figure 35. Input Cavity Voltage Reflection Coefficient (Second Pulsed Amplifier)

TABLE 10

Best Test Results for the Second Pulsed Amplifier

	Klystron	Feedback Loop
Peak Output Power (kW)	24.9	65.4
Peak Drive Power (W)	305	3885
Gain (dB)	19.1	12.3
Beam Voltage (kV)	80.5	80.7
Beam Current (A)	7.8	8.6
Efficiency (%)	3.97	9.42
Gun Anode to Cathode Voltage (kV)	20.4	21.2
Magnet Coil Currents (A)		
Main 1	405	403
2	512	510
3	480	489
4	440	410
Gun 1	12.2	13.5
2	10.0	10.1

TABLE 11

Undesired Oscillations

Frequency (GHz)	Power (kW)
26.960	167
41.450	18.4
43.565	31.0

With reference to Table 10, it should be noted that the peak power of 24.9 kw for the case with klystron drive is not saturated, but rather is limited by the available drive power and gain. In the case of the feedback loop driven amplifier, it is not clear whether the tube was saturated or not. The tube in this configuration operates with a gain equal to the loss of the feedback loop. This loss of 12.3 dB was not readily adjustable. Referring to Figure 36, our visibility is limited to the 12.3 dB line. The real performance of the tube could be anywhere from a small-signal gain of 12.3 dB to a saturated gain of 12.3 dB. The parameters used to obtain the

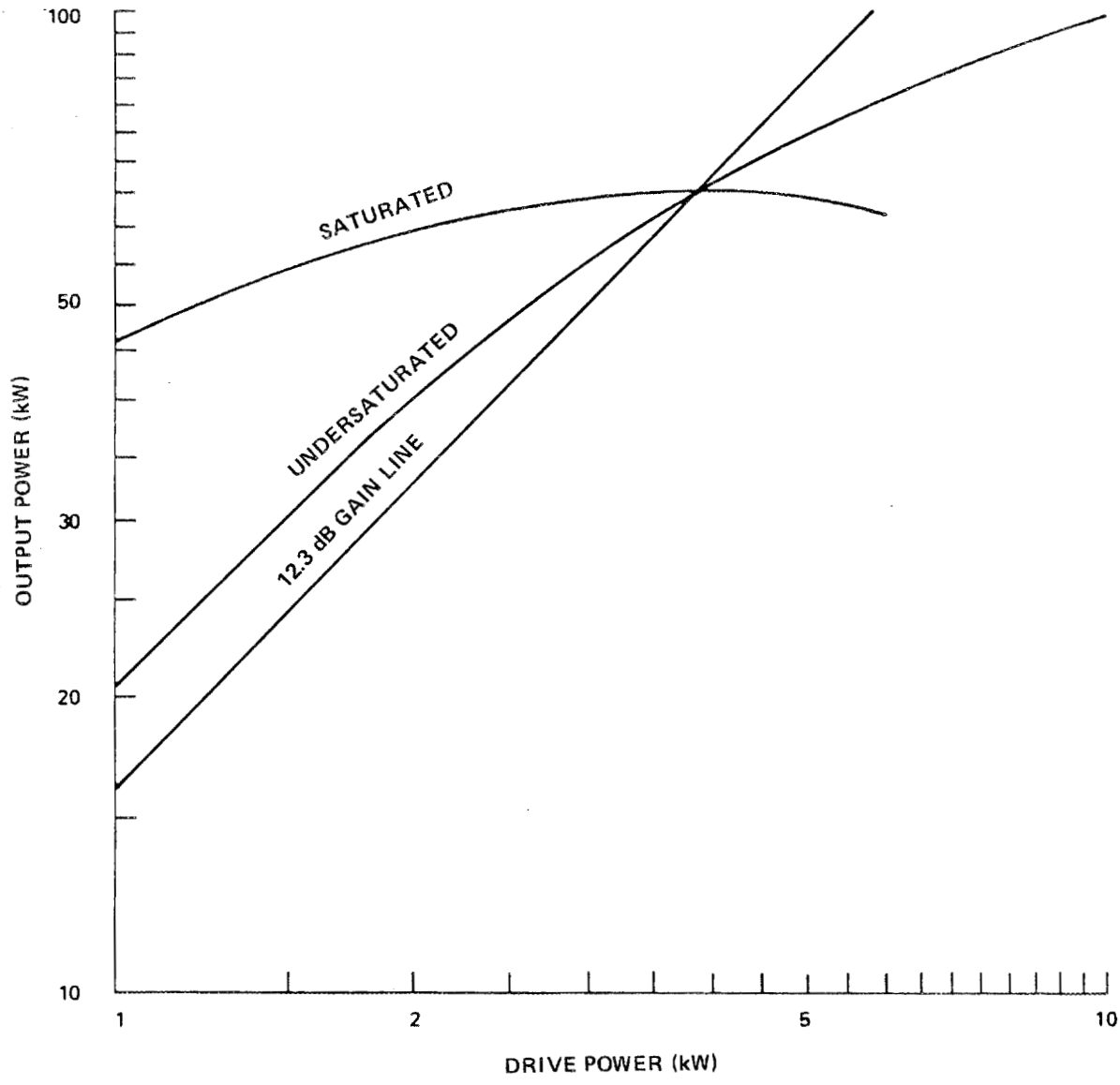

Figure 36. Uncertainty of Saturation for Feedback Loop Driven Amplifier

65.2 kW number may not be the optimum paratmeters were the 12.3 dB gain restriction lifted. Additional measurements of the performance of the second pulsed amplifier are included in the Fifth Quarterly Report[8].

The emission characteristics of the gun were studied. Figure 37 shows cathode current as a function of heater power with beam voltage as a parameter. In the test set used for these measurements, gun anode voltage was derived from the beam voltage through a potentiometer. Therefore, beam and anode voltage varied proportionally except for bias voltage and a small series resistance drop. These same data are plotted in a different format in Figure 38, where cathode current is shown as a function of gun voltage with heater power as a parameter. It can be seen that the cathode was neither space-charge-limited ($I = kV^{3/2}$) nor temperature limited (I = constant), but was operating in a transition region.

3. Pulsed Amplifier No. 3

Design work on the third pulsed amplifier considered two alternatives. One approach was to add additional lossy elements in the tube to try to achieve stability with the design value of beam perpendicular energy. The other was to accept beam parameters as they were with stable operation of the second amplifier, and to add a third cavity to achieve the required gain. To determine the beam parameters at the maximum stable gain condition, the measured beam and gun voltage and measured magnetic fields were used with the gun simulation code. The results indicated a $\beta_\perp$ of 0.4 and a β_z of 0.3 compared to the respective design values of 0.45 and 0.225. As a further check on these beam parameters, the expected gain for the configuration of the second amplifier was calculated using the small-signal ballistic analysis. The result was a predicted gain of 18 dB, which agreed well with the measured gain.

One concern with the proposed three-cavity amplifier was the probable reduction in efficiency due to reduced effective length of the output cavity, caused by the high β_z. Because of this concern, it was decided that work should proceed on a two-cavity amplifier with added loss.

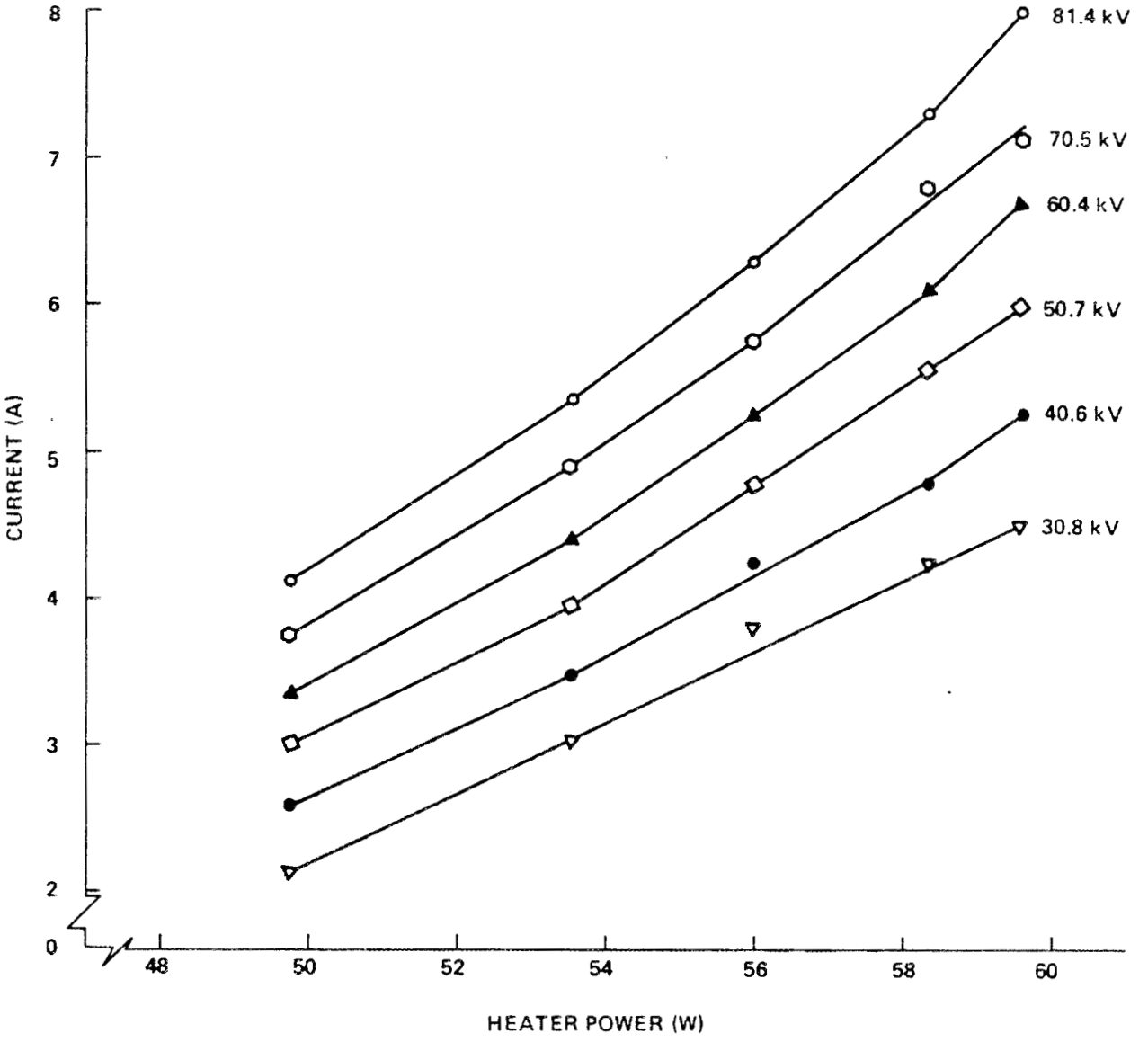

Figure 37. Beam Current as a Function of Heater Power (Second Pulsed Amplifier)

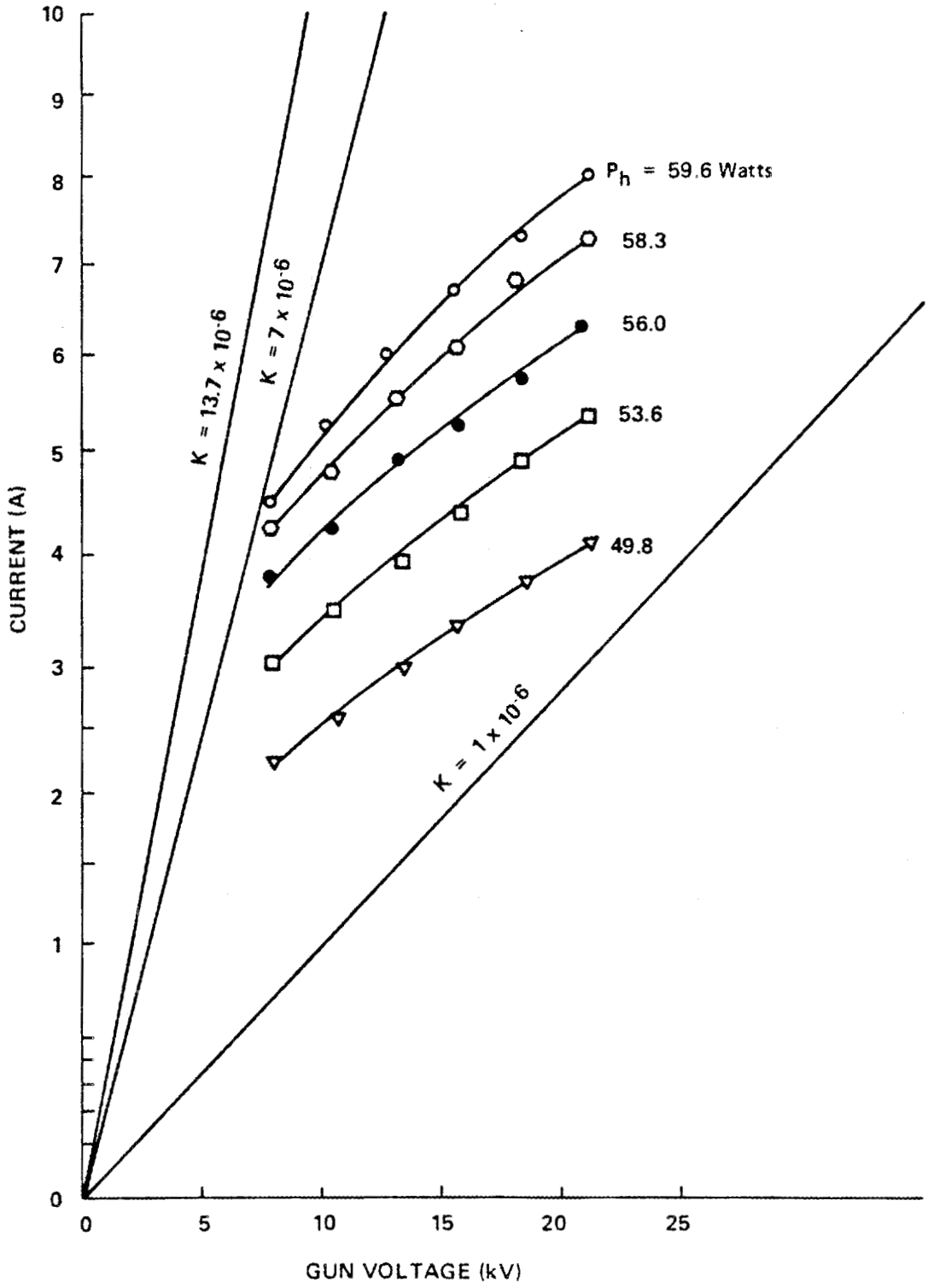

Figure 38. Beam Current as a Function of Gun Voltage (Second Pulsed Amplifier)

In the meantime, large-signal calculations were performed on a three-cavity amplifer design.

Accordingly, attention was centered on schemes to produce loading at locations in the tube where energy is stored in undesired modes. Cold test work on models of the rf circuitry showed that some energy storage occurred in the straight drift regions at the cutoff for the TE_{21} mode. It was hypothesized that this long region (approximately 7.5 wavelengths) formed a single-cavity oscillator, the cause of one of the more persistent oscillations encountered in test.

At 28 GHz, the 0.428 diameter drift tube can support only the TE_{11}, TE_{21}, and TM_{01} modes. The first attempts at loading these modes considered lossy wall coatings, as used in the second amplifier. To evaluate various coatings, sample measurements were performed using coated sections of WR-28 rectangular guide, 2 inches in length. The insertion loss for the dominant mode was measured for each section. The results are shown in Table 12. Compare these values with a theoretical attenuation of about 0.02 dB/in for copper guide.

TABLE 12

Attenuation In Lossy Rectangular Guide at 28 GHz

Loss Material	Coating Method	Attenuation
Nichrome[tm]	Vacuum Deposited	0.05 dB/in
Kanthal	Vacuum Deposited	0.32 dB/in
Kanthal	Flame Sprayed	0.37 dB/in

(tm Nichrome is a Driver-Harris Co. trademark for a special nickel chromium alloy material used for resistance wire and strip.)

The next experiments used lossy rings in circular guide with 0.428-inch inner diameter. Test sections were constructed from aluminum rings alternated with lossy (in this case 40% SiC) rings. The purpose was to provide a structure which would break up the longitudinal wall currents

inherent in non-$TE_{0,n}$ modes. The lossy rings had a slightly larger inside diameter (0.435 inches) than the aluminum rings. This was intended to shadow the lossy rings from beam interception in a real device. A TE_{11} wave was excited in this guide by tapering directly from a TE_{10} rectangular guide, and the insertion loss was measured as before. Table 13 gives the results. These may be compared to a theoretical attenuation of about 0.007 dB/in for copper.

TABLE 13

Attenuation In Lossy Circular Guide

Frequency	Attenuation
27.5	1.52 dB/in
28.0	2.72 dB/in
28.5	3.67 dB/in

It was decided that the third pulsed amplifier would utilize this kind of drift tube loss, but that in other respects it would be like the second amplifier. Thus, the most significant change in No. 3 concerned the method by which rf loss was accomplished in the drift regions of the device. The third pulsed amplifier contained lossy rings, (40% SiC, 60% BeO) alternated with copper rings, in the constant diameter regions between cavities and preceeding the input cavity. The bore details can be seen in Figure 39. This is in contrast to the second pulsed amplifier, which utilized Kanthal in these regions.

During hot tests, No. 3 gave a peak output power of 76.3 kw at saturation with a gain of 41.1 dB. With different operating parameters, a saturation gain of 45.4 dB was obtained. Although adequate gain was available, the tube was lacking in efficiency. Many test experiments were directed at investigating this shortcoming. Oscillations, which were less of a problem with this tube, were also investigated.

The tube was initially set up with the parameters used to obtain 65.4 kW from the previous amplifier when driven with the feedback loop. The

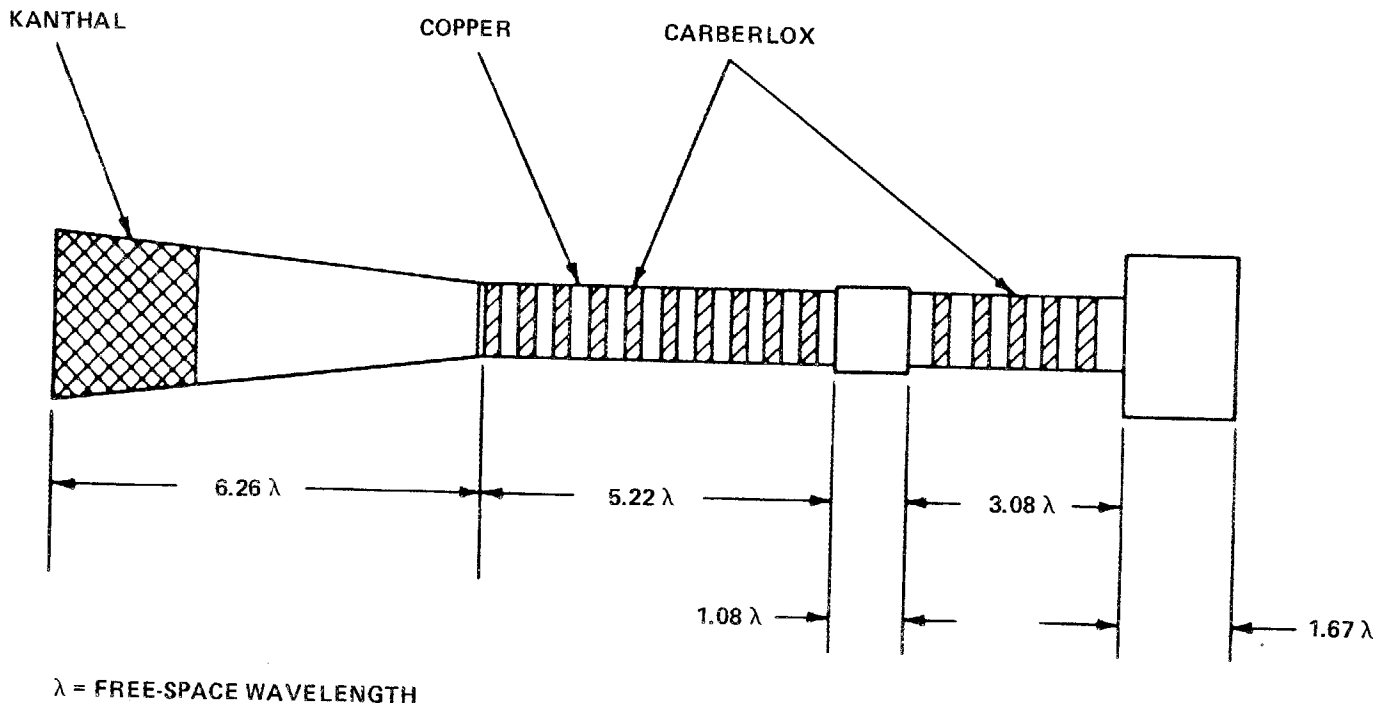

Figure 39. Bore Details of Third Pulsed Amplifier

result was 19.7 kW, limited by oscillations. With the parameters used to obtain 24.9 kW from the previous amplifier when driven by the klystron driver, 5.5 kW was obtained. Investigation of output power and gain as a function of frequency revealed maximum output power at 28.068 Ghz and a broad maximum in gain higher in frequency, as shown in Figures 40 and 41. The input cavity prior to test was at 28.000 GHz. A VSWR calculation based on measurement of forward and reflected power in the test socket indicated that this was still plausible, as shown in Figure 42. Based on the results of Figures 40 and 41 the output cavity resonance may have been higher in frequency than expected.

A comparison of the best performance of the three amplifier tubes built to date is shown in Table 14. In addition to the increasing power levels and gains, one can obtain an approximate indication of the improved stability and increased transverse power available for interaction from the normalized $(E/B)^2 i_o$ factor. For this relative comparison, E is taken as the gun anode voltage, B as the magnetic field at the cathode, and i_o as the cathode current.

In an effort to understand the low efficiency, the following curves were plotted: relative small-signal gain as a function of gun anode voltage (Figure 43), saturated power output and gain as a function of gun anode voltage (Figure 44), power and power divided by the square of the beam current (Figures 45 and 46), and output vs input power (Figure 47).

The small-signal gain has an optimum gun anode voltage (transverse energy) at low beam current as shown in Figure 43. Simple ballistic theory would predict that gain would monotonically increase as transverse energy increased. The observed peaking of gain is presumably caused by velocity spread effects which may come from aberrations in the gun or from space charge effects in the drift length between cavities. These measurements were made at very low beam currents to avoid spurious oscillations, which would appear for curve (a), for example, at a gun anode voltage near 23 kV at normal beam current.

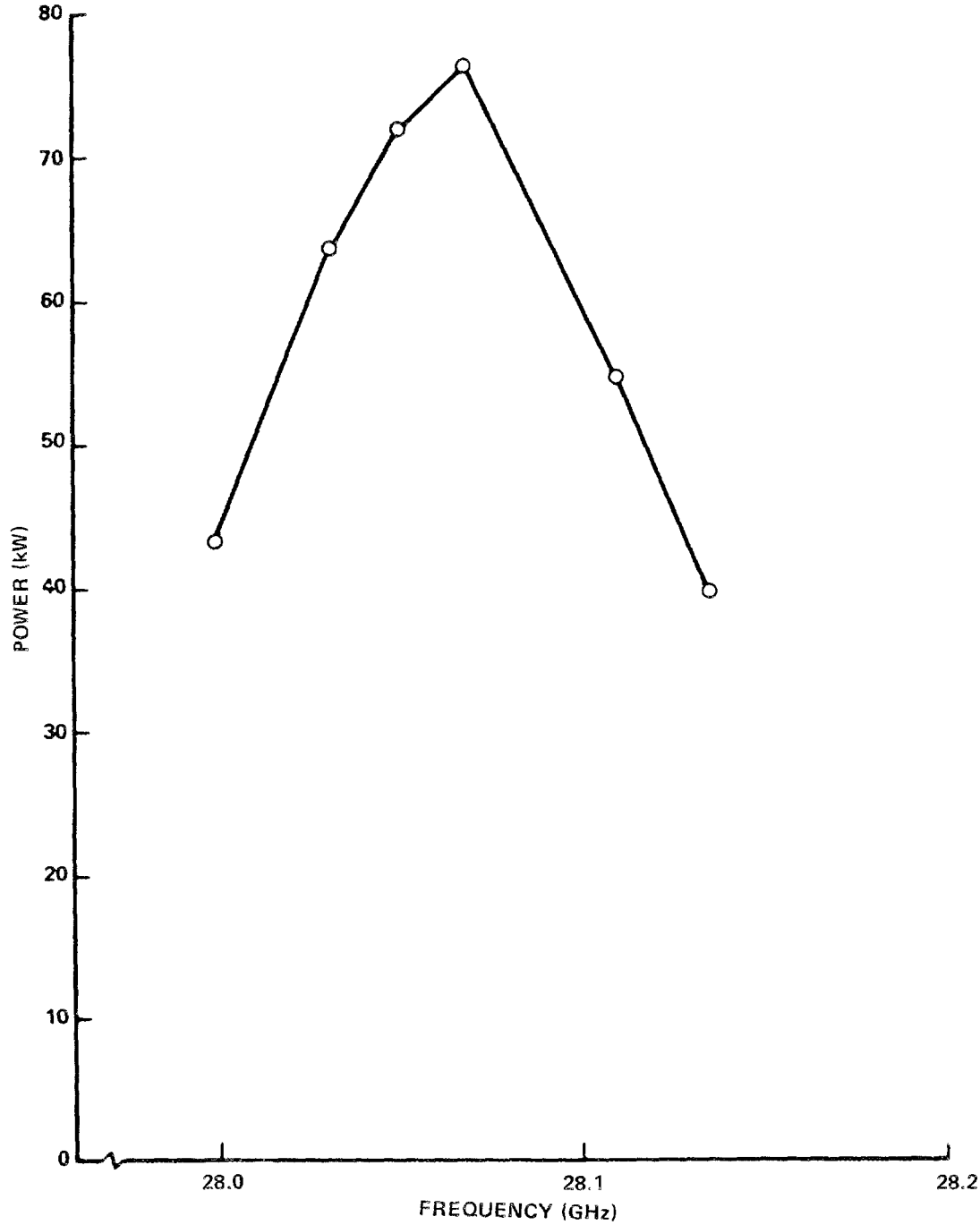

Figure 40. Third Pulsed Amplifier Peak Output Power vs Frequency with Operating Parameters Optimized at Each Point

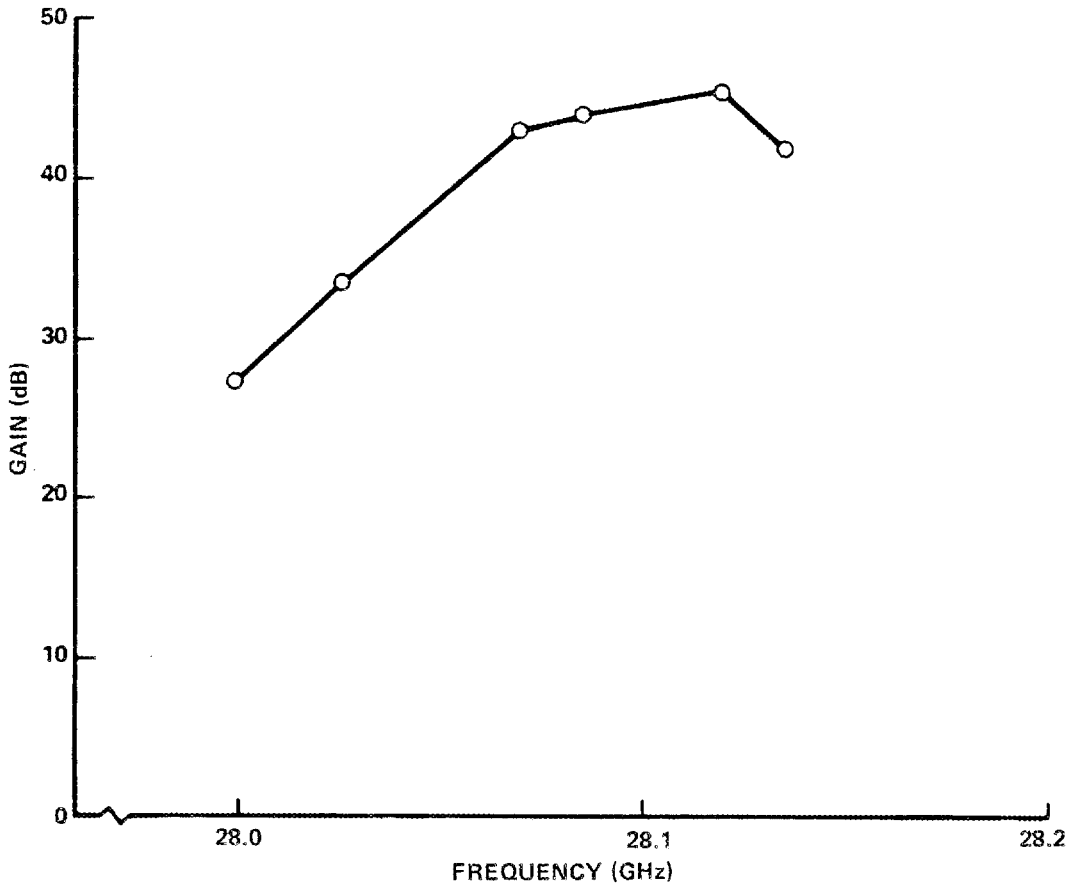

Figure 41. Third Pulsed Amplifier Gain at Saturation vs Frequency with Operating Parameters Optimized

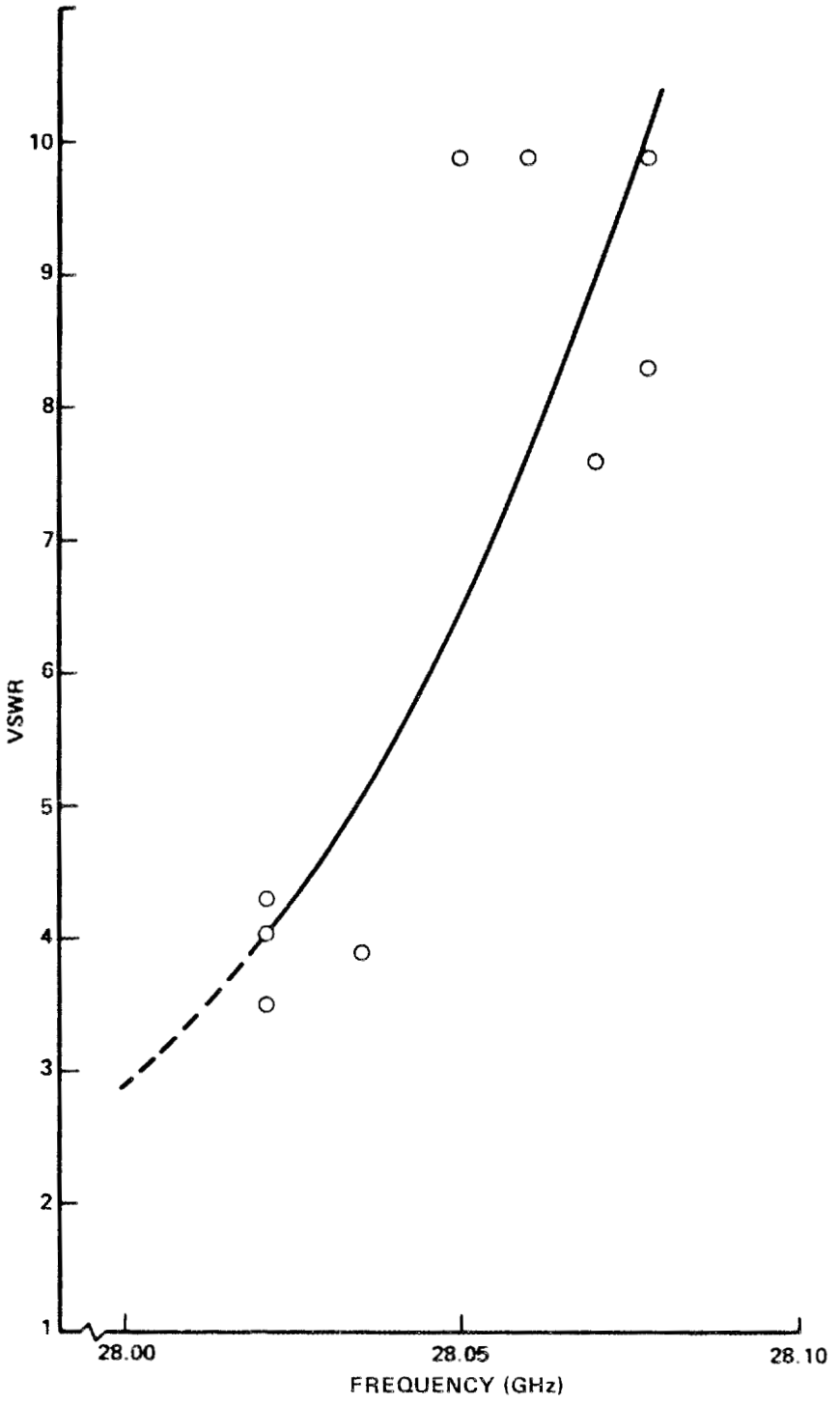

Figure 42. Third Pulsed Gyroklystron Amplifier Input Cavity VSWR

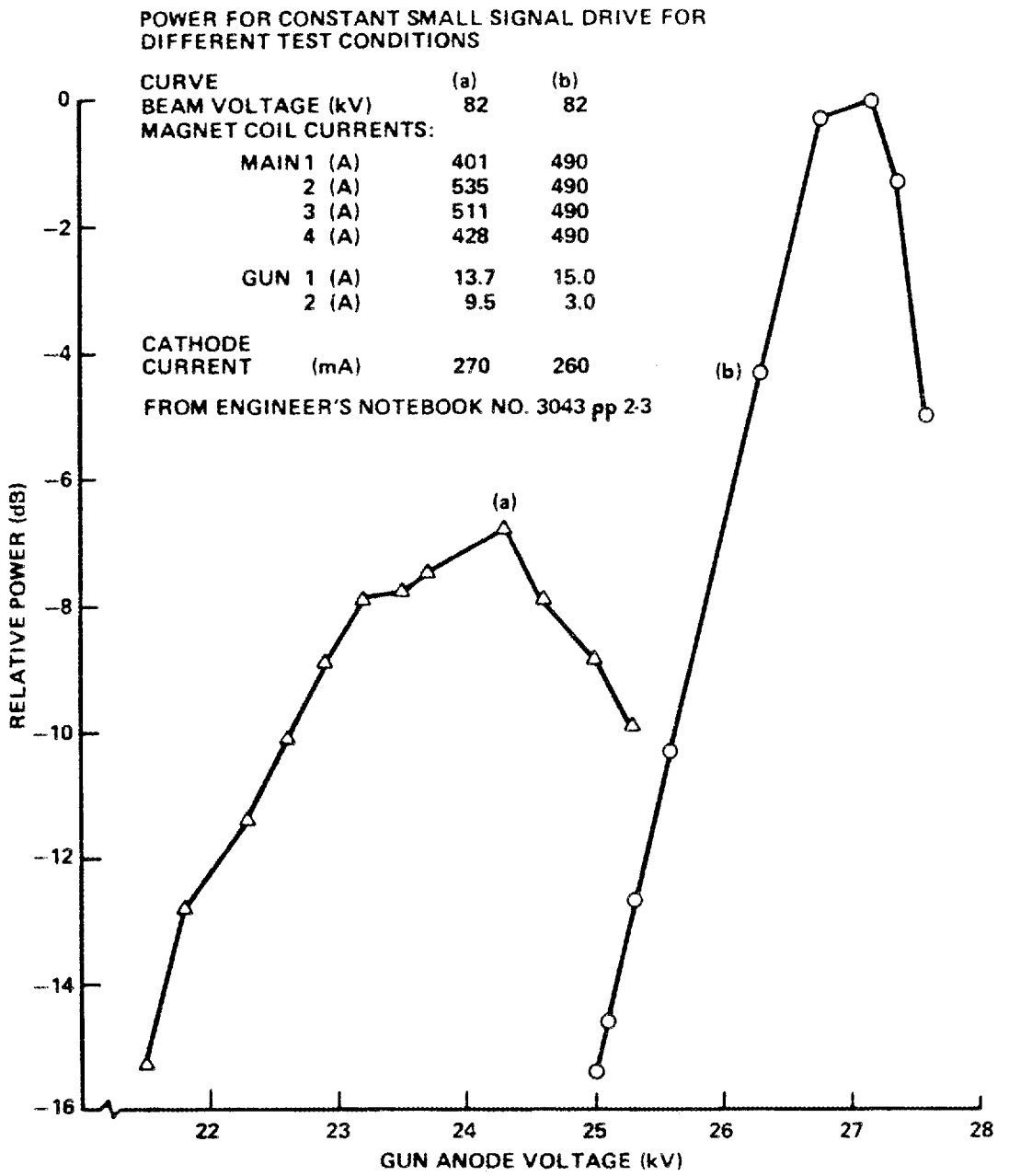

Figure 43. Third Pulsed Gyroklystron Relative Peak Output Power for Constant Small-Signal Drive for Different Test Conditions

Figure 44 shows that saturated power and gain at saturation vary oppositely with respect to anode voltage or transverse energy. It was concluded that even in the region where increases in gun anode voltage

TABLE 14

Best Performance of First Three Gyroklystrons

Driver	First Klystron	Second Klystron	Feedback	Third Klystron
Peak Output Power (kW)	5.81	24.9	65.4	76.3
Beam Voltage (kV)	81.0	80.5	80.7	78.4
Beam Current (a)	1.95	7.8	8.6	11.2
Efficiency (%)				9
Gun Voltage (kv)	24.7	20.4	21.2	24.4
Gain (dB)	12.6	19.1	12.3	41.1
Magnet Coil Currents (A)				
Main 1	408	405	403	477
2	529	512	510	582
3	481	480	489	448
4	465	440	410	420
Gun 1	11.0	12.2	13.5	15.2
2	11.5	10.0	10.1	2.9
Normalized $\left(\frac{E}{B}\right)^2 i_o$	1.00	2.64	2.82	4.95

produce increases in gain, there is a mechanism in effect which causes a decrease in efficiency.

Figures 45 and 46 are limited on the low cathode current side by insufficient gain, and by high reflected power in the input waveguide as well as by oscillation on the high current side. However, there was enough range to indicate that space charge effects could cause the reduced

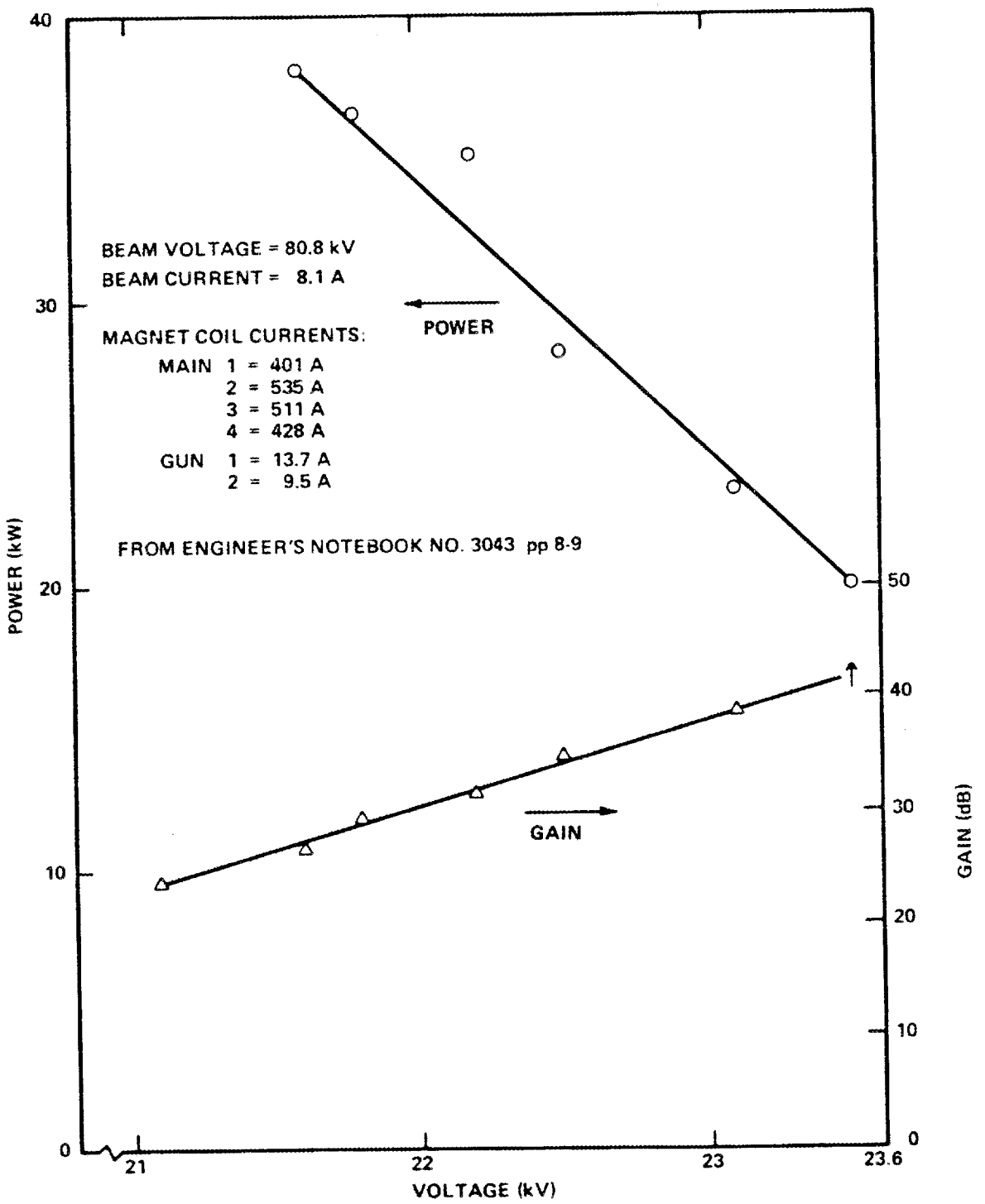

Figure 44. Third Pulsed Gyroklystron Saturated Power and Gain Sensitivity to Gun Anode Voltage

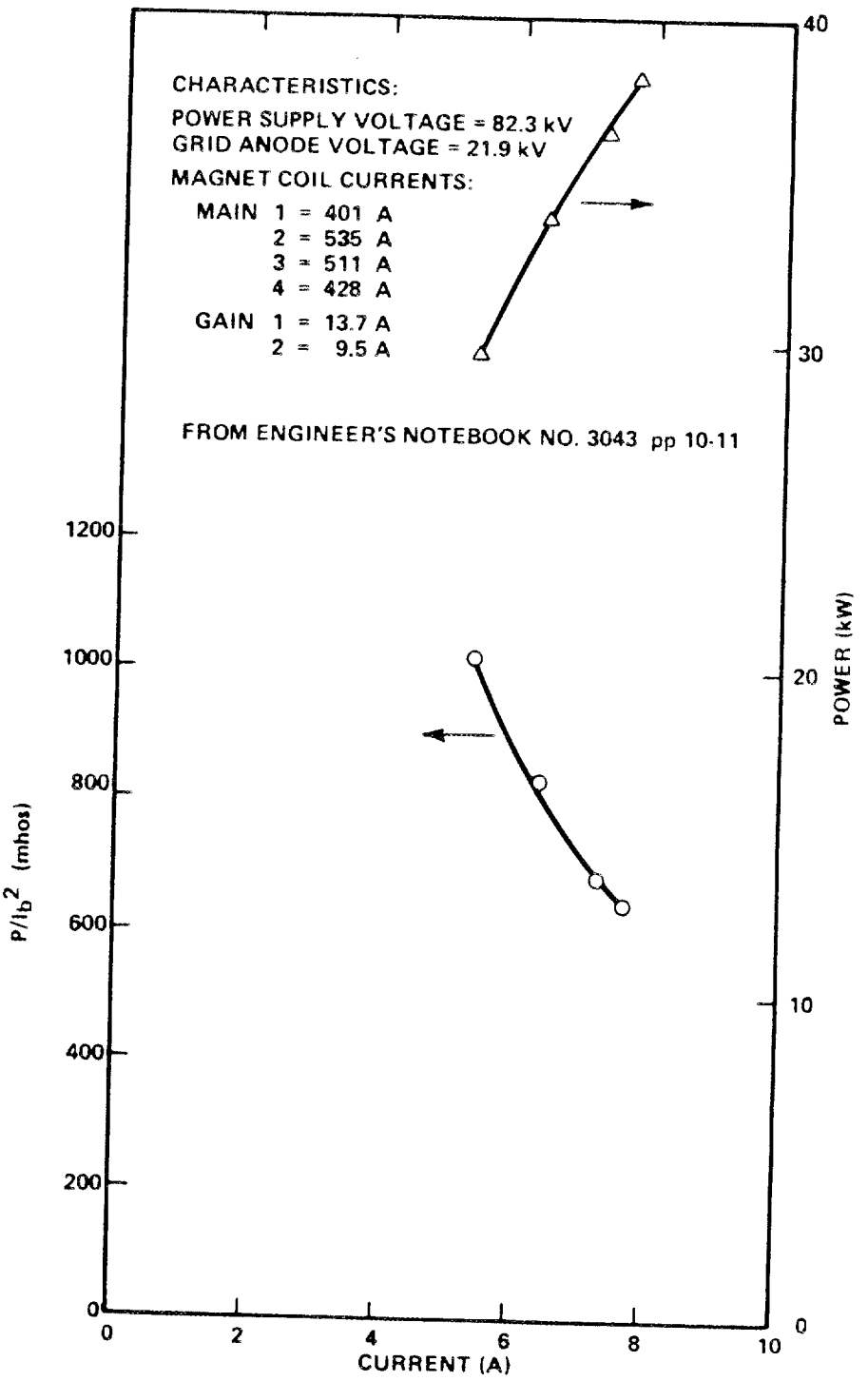

Figure 45. Third Pulsed Gyroklystron Power Current Characteristics

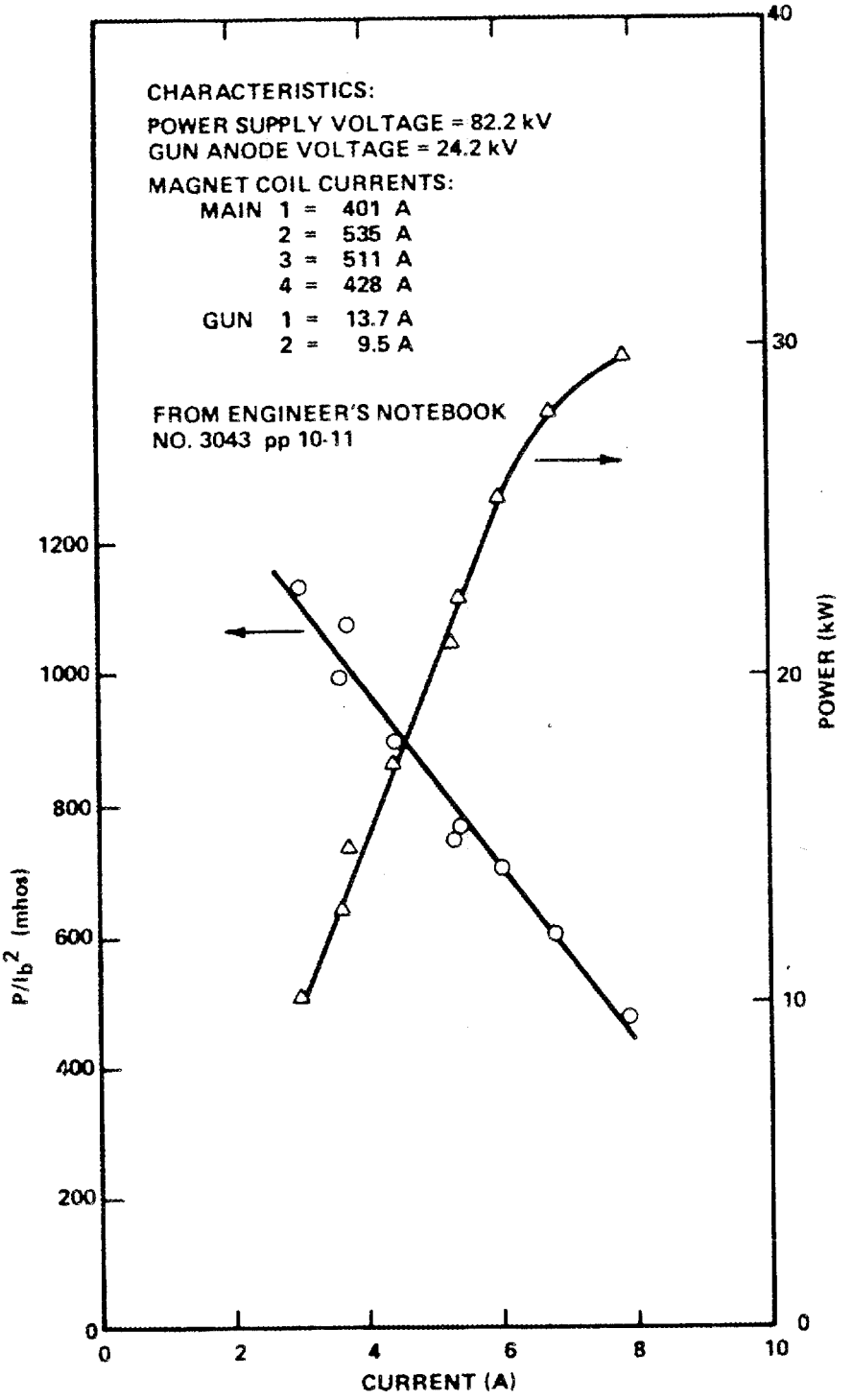

Figure 46. Third Pulsed Gyroklystron Power Current Characteristics with Increased Anode Voltage

efficiency by making the drift length between the cavities too long for optimum performance. Stated simply, output power, P, may be expressed in terms of rf current, I_1, beam current, I_b, and a constant output cavity impedance, R.

$$P = I_b^2 \left(\frac{I_1}{I_b}\right)^2 R$$

$$\frac{P}{I_b^2} \propto \left(\frac{I_1}{I_b}\right)^2$$

Normally the depth of modulation should be constant so the P/I_b^2 should be constant, independent of I_b. However, it can be seen from Figures 45 and 46 that rf current modulation decreased as the beam current increased. This strongly suggested that a space charge effect was casuing the problem.

A gain compression of 5 to 6 dB from small-signal to saturation is shown in Figure 47. This is a fairly typical number for microwave tubes.

The effect of load conditions on output power and operating parameters was studied. The load tried included a 0.030-inch thick Teflon^{tm} (Teflon is an E.I. DuPont de Nemours and Co., Inc., trademark for a fluorocarbon resin) disc with VSWR ~ 1.6, the same load displaced one-quarter wavelength, and a 0.062-inch thick Teflon disc, VSWR ~ 2.2. The results are compared to a reference condition with no intentional mismatches in Table 15. It can be seen that there was a general tendency for the output power and gain to fall off with increasing mismatch.

During testing, oscillations were observed from 21.243 GHz to 21.503 GHz, from 21.796 GHz to 21.952 GHz, and 24.792 GHz. These are believed to be non-TE_{0n} interactions. Additional loading would be required to eliminate them. In addition, with very high values of transverse energy amplifier No. 3 self-oscillated at 28.066 GHz, apparently using the TE_{02} mode in the output cavity. The output power was 113 kw. Small-signal

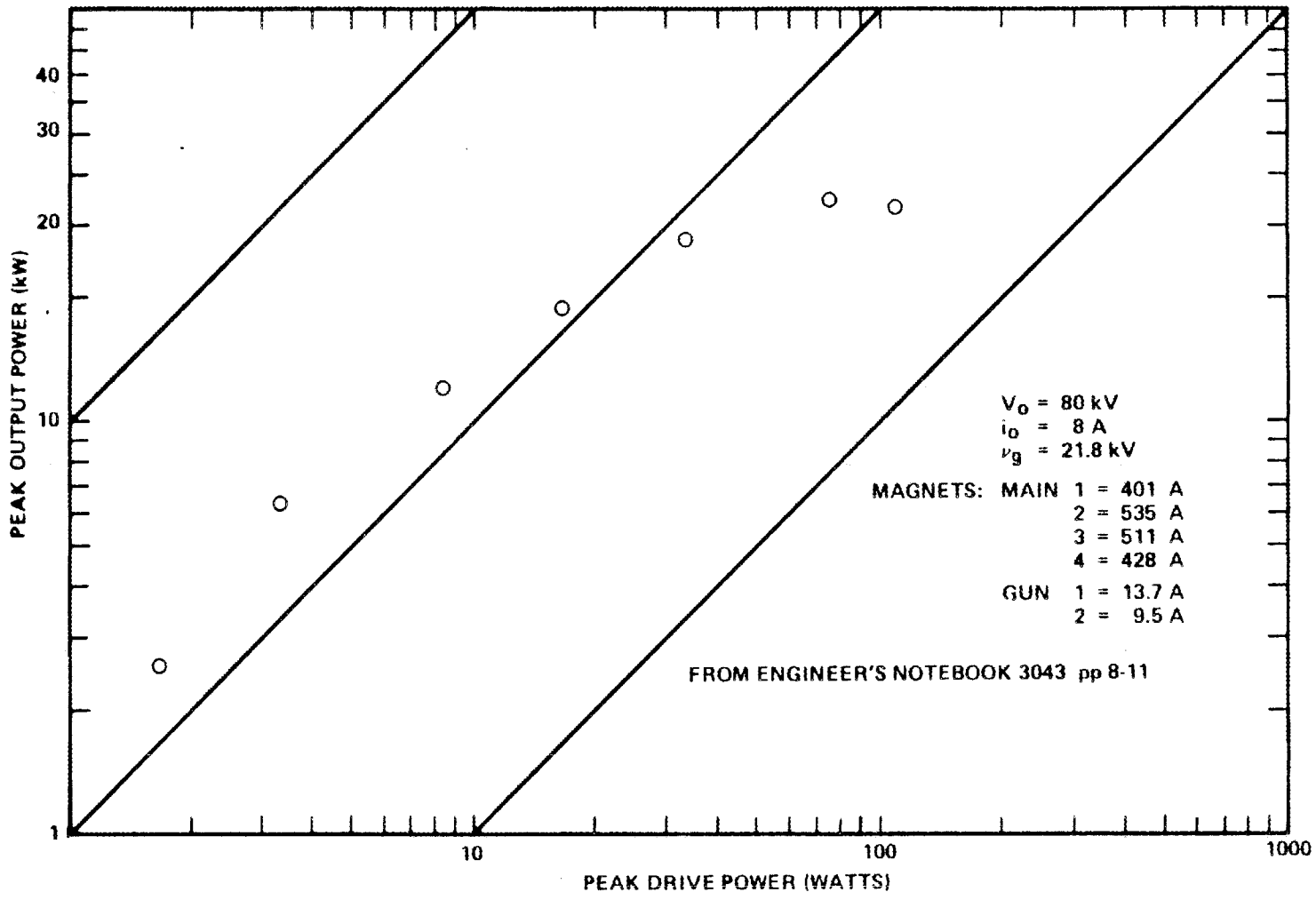

Figure 47. Third Pulsed Gyroklystron Amplifier Input-Output Characteristics

calculations predict oscillation in the output cavity when the transverse energy is somewhat above the design value.

In a final experiment amplifier No. 3 was raised 0.055 inch in the solenoid to determine the effect of axial translation of the cathode in the magnetic field. A peak output power of 61.1 kW with 39.2 dB gain was obtained. This was comparable to the 76.3 kW, 41.1 dB gain best performance obtained in the lower position.

TABLE 15
Effect of Load on Amplifier Operation

Load	Reference	0.030" Thick Teflon Disc	0.030" Thick Teflon Disc plus λ/4 Spacer	0.062" Thick Teflon Disc
Peak Output Power (kW)	63.8	56.5	50.7	45.7
Frequency (GHz)	28.068	28.068	28.068	28.068
Beam Voltage (kV)	80.9	80.8	80.3	80.8
Beam Current (a)	12.1	13.6	13.4	13.7
Efficiency (%)	7	5	5	4
Gun Anode Voltage (kV)	22.1	21.4	21.2	21.2
Gain (dB)	37.5	30.1	28.7	24.4
Magnet Coil Currents (A)				
Main 1	481	476	476	476
2	586	581	585	585
3	444	443	447	447
4	416	418	414	414
Gun 1	15.2	15.4	15.0	15.0
2	2.9	2.9	2.9	2.9

4. Pulsed Amplifier No. 4

A pulsed amplifier No. 4 was designed with an additional cavity between the input and output cavities and with shorter drift lengths between all cavities. The added cavity was chosen as a TE_{021} cavity with a length of 1.33 λ and a total Q of 700. Intercavity drift lengths were designed to

be 1.2 λ. Assembly of the pulsed amplifier No. 4 was stopped when the program was redirected to develop only gyrotron oscillators. More design details of the fourth amplifier are given in Quarterly Report No. 7[10].

IV. GYROTRON OSCILLATORS

Work on gyrotron oscillators was undertaken initially as a backup to efforts in the gyroklystron amplifier portion of the program. Notable success with oscillators and relative lack of it with amplifiers led to concentration on gyrotron oscillators. Two general types of CW oscillator models were designed and constructed. The first type extracted rf microwave energy immediately following the oscillator cavity, prior to the collector, using three miter bends in series. Hence, these tubes became known as "triple miter bend" models. The second type employed straight through collector routing of rf microwave energy, in which the collector per se was treated as a component of the output coupling system. Tubes using the straight through collector structure became known as "axisymmetric" models. Prior to the CW oscillators tests were conducted with two pulsed models having 2-inch-diameter axisymmetric collectors.

In general, sections IV-A through IV-H discuss theoretical considerations, design features, tests of pulsed oscillators, operational problems, and subsequent design modifications. Sections covering experience with the CW tube models are

IV-I "Triple Miter Bend Models"
IV-J "Axisymmetric Models"

Twelve CW tube models are covered in the discussion, six of each type. Many of the models were rebuilt several times with modifications. The identifying serial numbers express these changes by the addition of R1, R2, etc. after the regular serial number. A number of model tubes were shipped to ORNL for further tests and operation with the EBT system. Reference, in some cases, is made to this experience.

A. OSCILLATOR CAVITY DESIGN

Oscillator design studies led to the choice of a 5-wavelength long resonant cavity for the first experimenal tube. This corresponded to a cavity length of 2.108 inches. For the TE_{021} resonance, a 0.946-inch-

diameter cavity was required. Cutoff diameters for TE_{22}, TE_{02}, and TE_{61} modes are shown in Table 16. A coupling iris diameter exceeding 0.900 inches would be required to avoid trapping the TE_{22} mode.

TABLE 16

Cutoff Diameters at 28 GHz

Mode	Diameter
TE_{22}	0.900
TE_{02}	0.941
TE_{61}	1.007

With long oscillator cavities it is generally difficult to achieve a low enough loaded Q. The lower limit on Q is given approximately by the diffraction Q:

$$Q_{diff} = 4\pi \left(\frac{L}{\lambda}\right)^2$$

For $L = 5\lambda$ the diffraction Q has a value of 314. Russian literature[22] has suggested tapered diameter oscillator cavities. If the diameter is reduced below 0.941 inch, the fields may be expected to decay exponentially. If the diameter is increased much above 1.007 inches, a trapped TE_{61} resonance may be expected.

Design of the oscillator cavity was influenced by a determination of the interaction length required to achieve an rf output power of 200 kW. Figure 48 shows the results of a calculation of output power as a function of normalized cavity field for a 5λ cavity. The loaded Q required to achieve a given field amplitude is also plotted. The calculations show that a loaded cavity Q of 225 would yield 260 kW of rf output power. A similar calculation for a 2λ cavity indicated poorer results and was not given further consideration.

The horizontal line in Figure 48 represents the theoritical minimum Q achievable with a constant diameter. From the same figure, it is clear

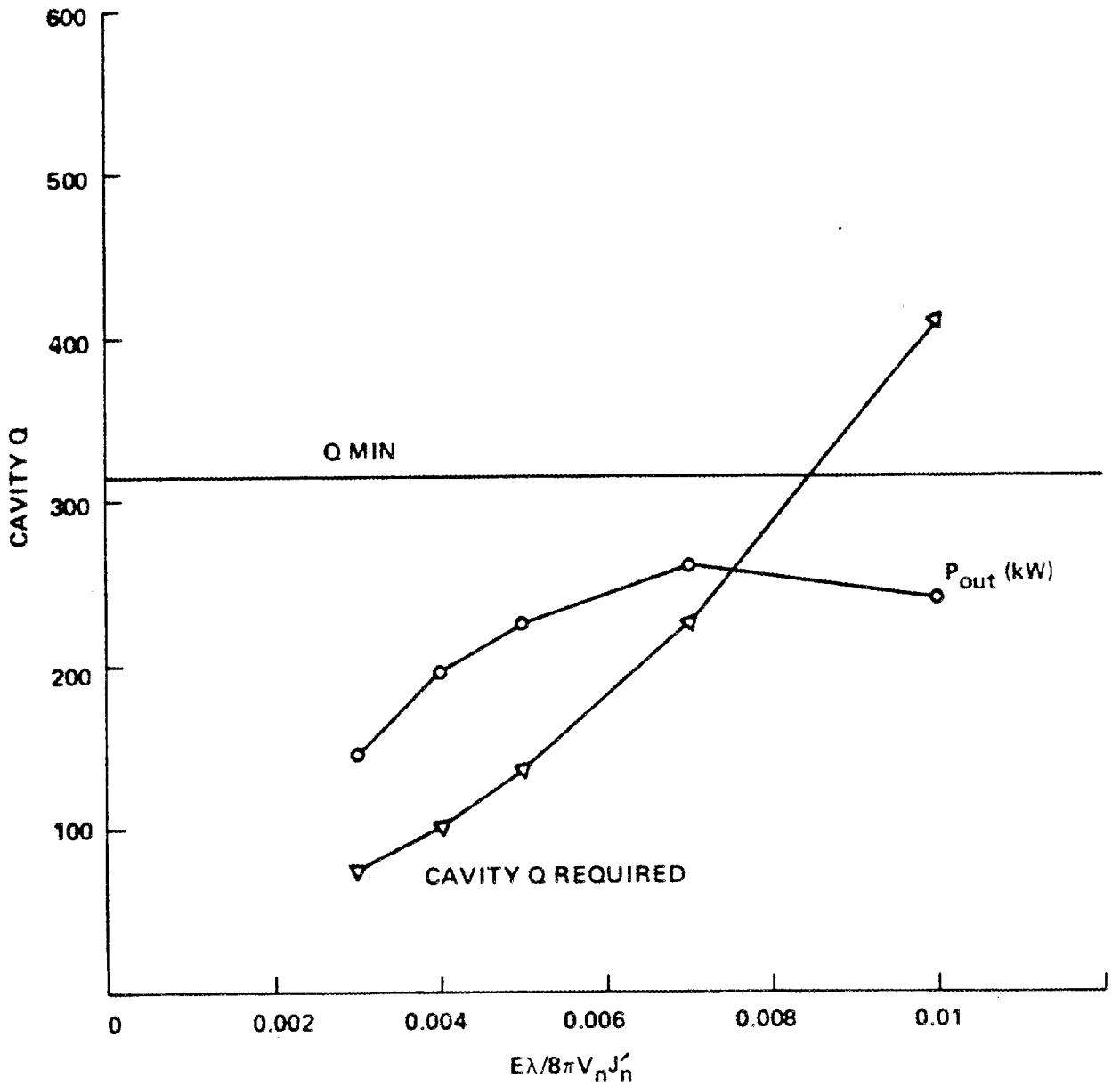

Figure 48. Oscillator Power and Cavity Q vs Normalized Cavity Field for L = 5λ, TE_{021} Mode, Beam = 80 kV, 8A

that a Q in the range of 100 to 400 should result in over 200 kW of rf output power. To ensure a Q this low, cold test models were built with a taper as indicated in Figure 49. The addition of the taper was also intended to increase beam efficiency, as discussed by Bykov and Gol'denberg[22]. Five cold test models were built and the results are shown in Table 17. Model No. 5 was chosen as a satisfactory design.

In the analysis of the cold test models, primary consideration was given to axial energy distribution. Efficiency considerations determined that the axial field profile should extend approximately 2.1 inches (5λ) and also that the peak field should be off center as much as possible towards the output iris. This would give an extended low-amplitude region at the beginning of the cavity. The energy distribution was measured by drawing a dielectric perturbation axially through the cavity and observing the change in resonant frequency. Figure 50 shows the result. The downward shift in frequency is proportional to E^2 in the cavity.

TABLE 17

Oscillator Cavity Dimensions, Frequency, and Q

Trial	A	B	C	D	E	F	Frequecny	Q
1	0.850	1.59°	1.800	0.950	0.700	0.920	28.189	479
2	0.860	1.43°	1.800	0.950	0.700	0.920	28.030	480
3	0.920	0.48°	1.800	0.950	0.700	0.920	27.941	490
4	0.928	0.48°	1.300	0.950	0.700	0.930	27.961	453
5	0.927	0.45°	1.400	0.950	0.720	0.940	28.010	430

B. FIRST EXPERIMENTAL PULSED OSCILLATOR

A pulsed oscillator tube was assembled to check out the design. The first model was a pronounced success, producing 248 kw peak rf power output at 28.020 GHz with an efficiency of 35%. Operating parameters for this test are given in Table 18.

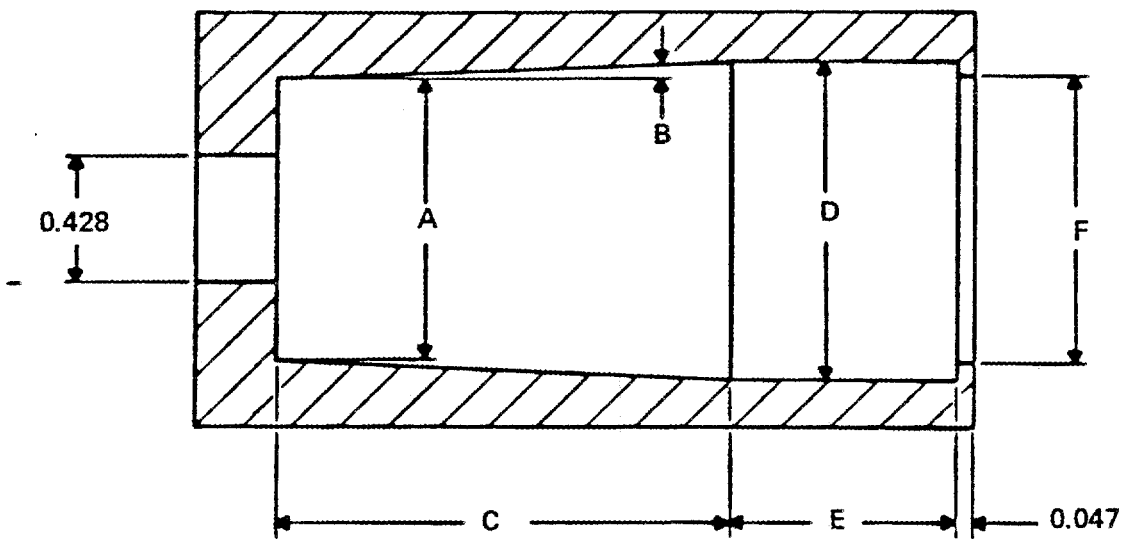

Figure 49. Oscillator Cavity

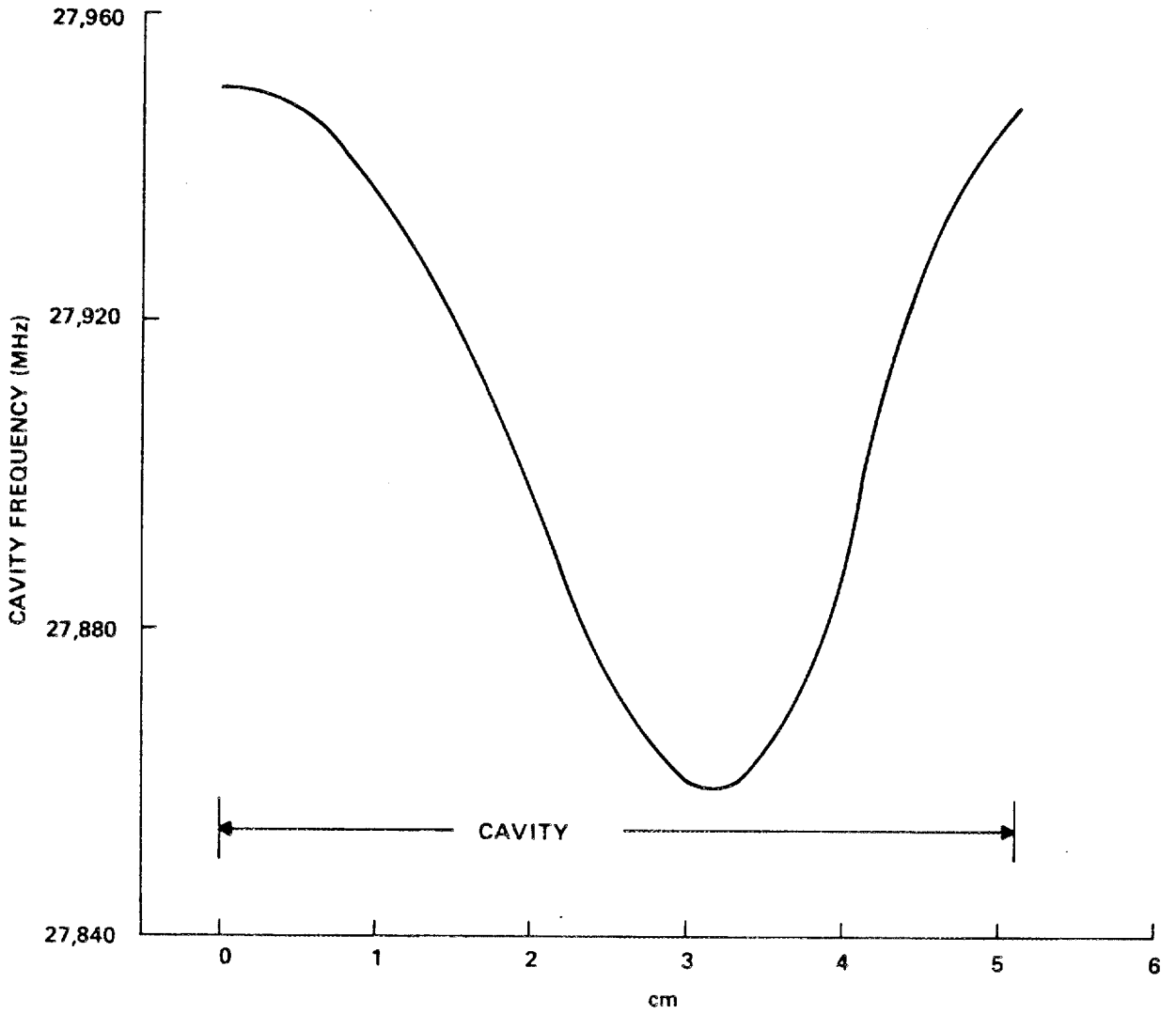

Figure 50. Cavity Frequency of TE_{021} Mode vs Axial Position of Dielectric Perturbation

TABLE 18

Best Test Results for the First Pulsed Oscillator

Peak Output Power	248 kW
Frequency	28.020 GHz
Beam Voltage	81.5 kV
Beam Current	8.7 A
Efficiency	35%
Gun Voltage	23.6 kV
Rf Pulse Duration	27.5 μs
Pulse Repetition Rate	60 pps
Rf Duty	1.65×10^{-3}
Average Power	410 W
Magnet Coil Currents	
Main 1	401 A
2	535 A
3	511 A
4	428 A
Gun 1	13.7 A
2	9.5 A

Many trade-offs were possible among gun voltage and magnet coil currents, all giving nearly the same output power.

In an effort to optimize parameters, efficiency was plotted as a function of gun anode voltage, Figure 51. For each point, all magnetic fields were reoptimized. The optimization in gun magnet field was particularly notable. In general, it appeared that efficiency was increasing as a function of gun voltage up to 31.6 kV, at which point the limit of current capability of one of the gun coil magnets was reached. In spite of the trend of increasing efficiency with gun voltage, highest efficiency was obtained at 23.6 kV. If the magnetic field were held constant, efficiency dropped rapidly with decreasing gun voltage, as seen in Figure 52.

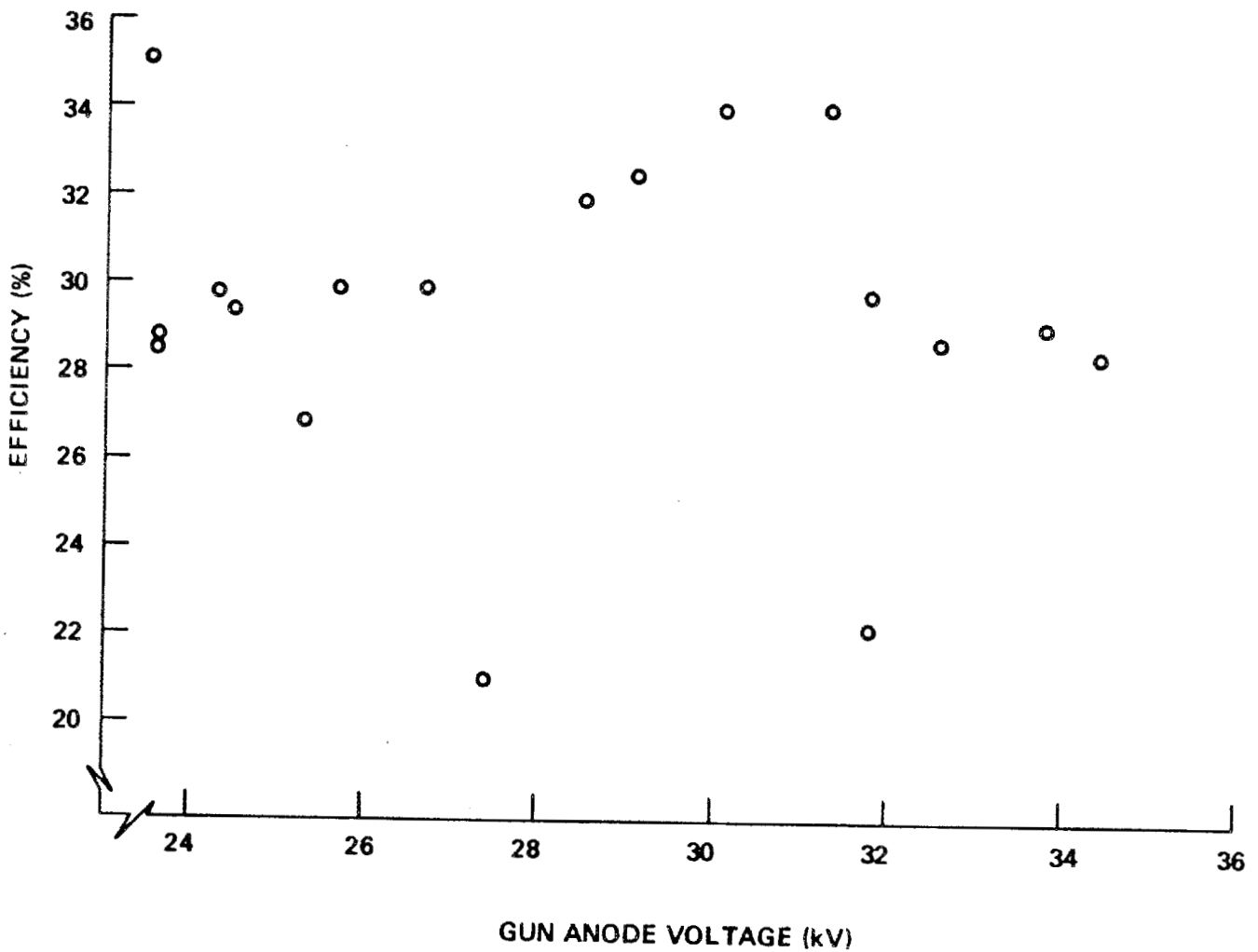

Figure 51. Pulsed Oscillator Efficiency Sensitivity to Gun Anode Voltage, Magnetic Fields Optimized

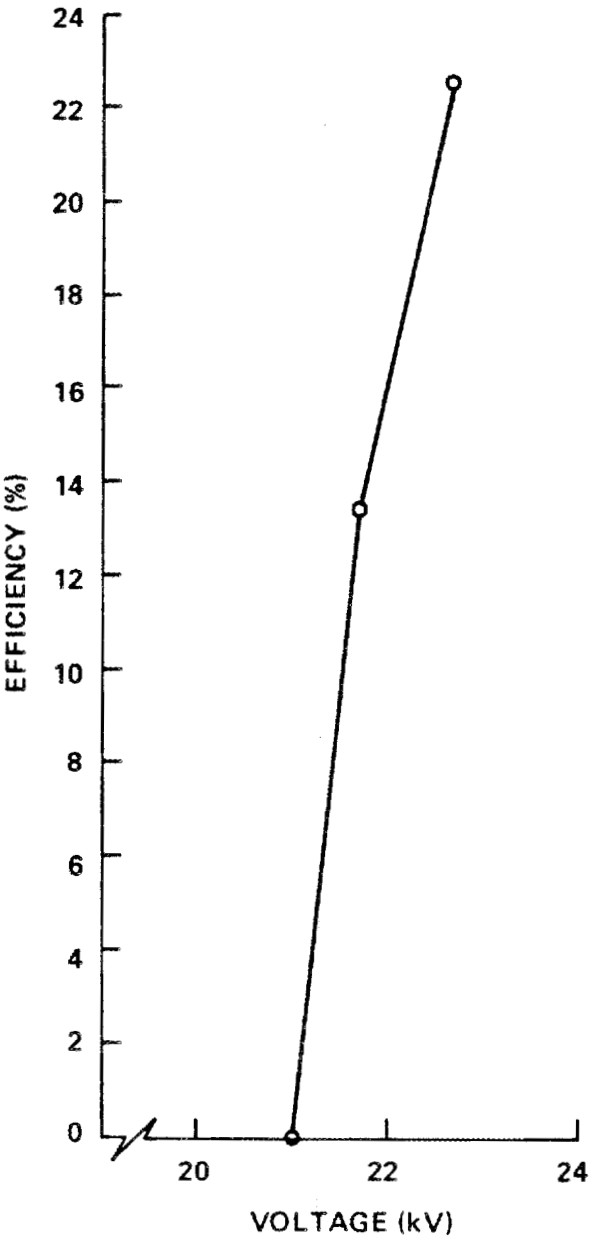

Figure 52. Pulsed Oscillator Efficiency Sensitivity to Gun Anode Voltage, Magnetic Fields Constant

Another area of investigation was the dynamic range of oscillator output power. Two variables studied in detail were cathode current and gun No. 1 coil current. Variation of output power with cathode current is shown in Figure 53. The graph indicates less than 4 dB dynamic range before the gyrotron drops out of TE_{021} mode oscillation. Variation of output power with gun No. 1 coil current, shown in Figure 54, proved to be a much better method, easily providing 10 to 15 dB dynamic range.

An average rf power output of 10.7 kW was demonstrated in one experiment, and one millisecond pulse duration operation was achieved in another. Still other experiments involved sensitivity to various operating parameters, oscillation behavior for different load conditions, and spurious oscillation suppression.

Parameters used in the high average power and long pulse duration experiments are shown in Table 19, along with the high peak power result obtained in earlier tests. As the pulse duration was increased, power supply pulse droop became a problem. Quantities based on average values and pulse duration yielded "average peak" values rather than true peak values. This shows up in the peak output power and efficiency numbers. At the higher average power levels power dissipation in the oscillator cavity heated the cavity, enlarging it and lowering its frequency. A plot of oscillation frequency as a function of average power is shown in Figure 55. A corresponding temperature rise can be calculated and a cavity temperature as a function of average power can be generated, also shown in Figure 55. At the higher average powers, it was necessary to readjust the main magnetic field downward to track the reduction in frequency.

At low duty, a series of experiments was performed to determine the sensitivity of output power to gun magnet coil current, heater voltage, gun anode voltage, beam voltage, and main magnet coil current. The results are tabulated in Table 20. These data show the main magnet coil current to be the most sensitive and the gun magnet coil currrent to be the least sensitive. In previous tests it was found that this latter parameter could be used to obtain a wide dynamic range of output power. Although the output power was quite sensitive to the absolute value of the magnetic field in the

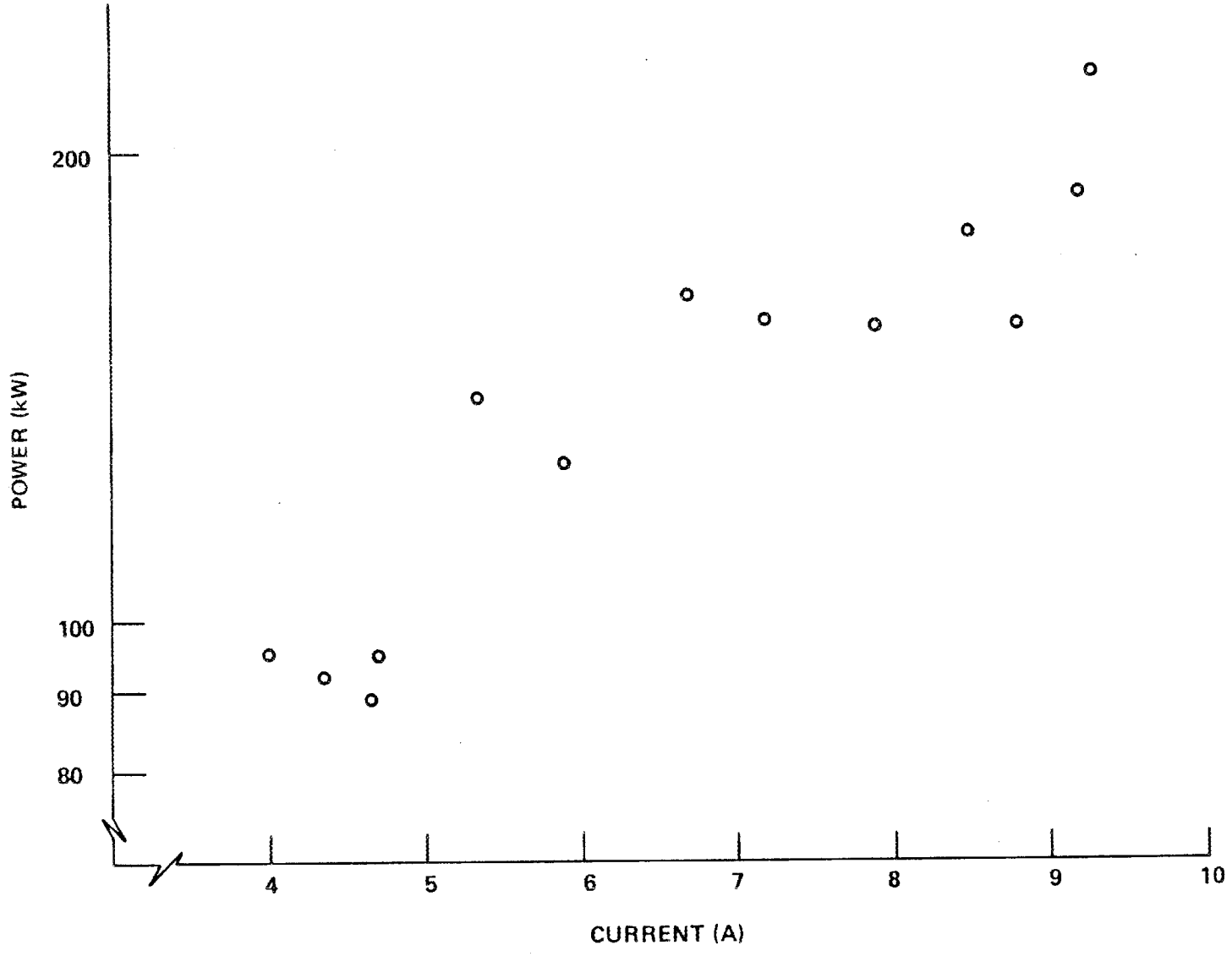

Figure 53. Pulsed Oscillator Peak Output Power Sensitivity to Cathode Current

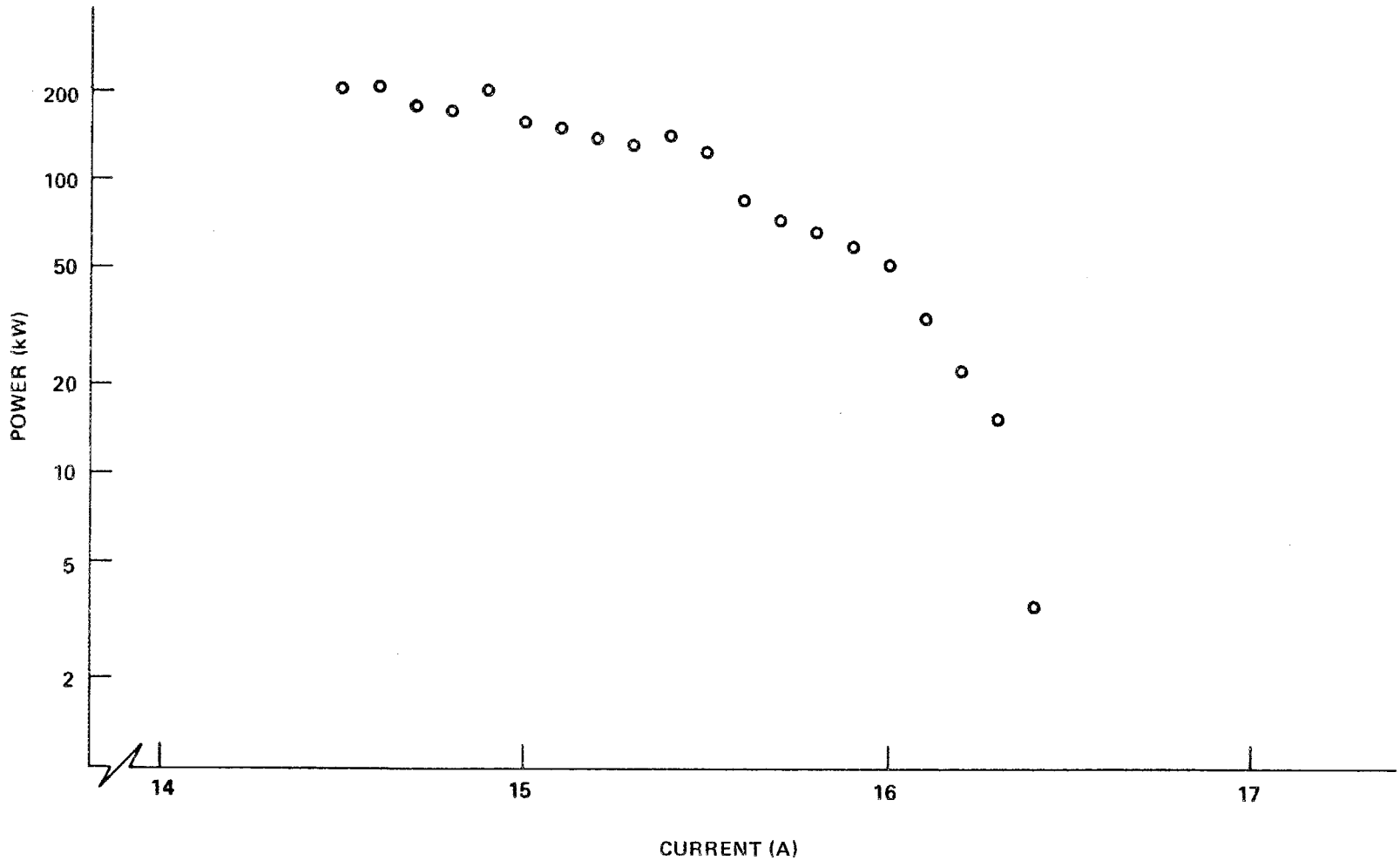

Figure 54. Pulsed Oscillator Peak Output Power Sensitivity to Gun No. 1 Coil Current

TABLE 19

Best Average Power Test Results for the First Pulsed Oscillator

		High Peak Power	High Average Power	Long Pulse
Peak Output Power	(kW)	248	223	160
Frequency	(GHz)	28.020	27.908	27.980
Beam Voltage	(kV)	81.5	83.7	81.2
Beam Current	(a)	8.7	8.5	7.55
Efficiency	(%)	35	31	26
Gun Voltage	(kv)	23.6	27.7	26.3
RF Pulse Duration	(μs)	27.5	400	1000
Pulse Repetition Rate	(pps)	60	120	15
RF Duty	(%)	0.165	4.8	1.5
Average Power	(W)	410	10,700	2400
Magnet Coil Currents	(A)			
Main 1		401	398	398
2		535	533	540
3		511	498	490
4		428	389	389
Gun 1		13.7	14.4	14.5
2		9.5	9.0	9.0

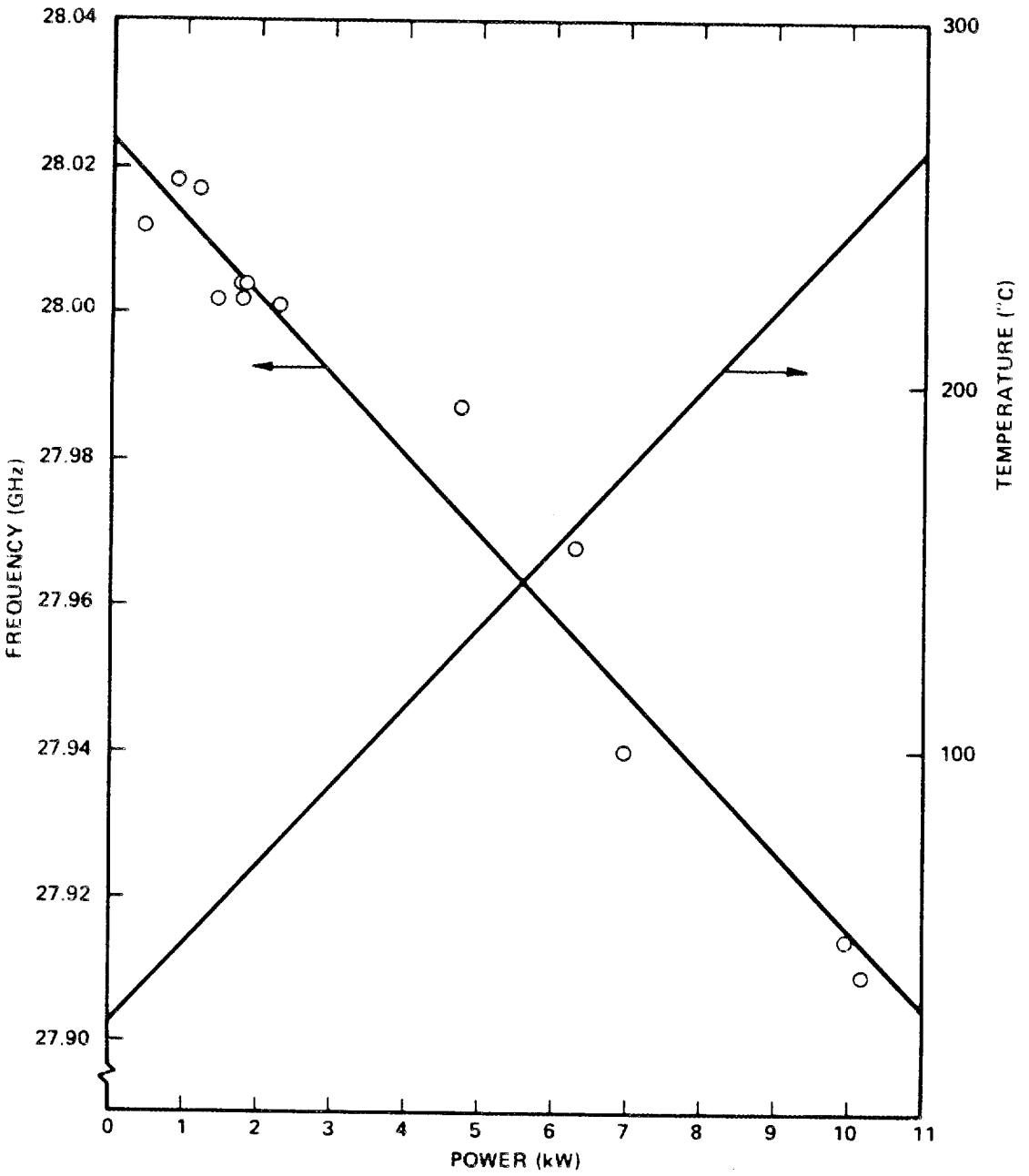

Figure 55. Pulsed Gyrotron Frequency and Calculated Cavity Temperature as a Function of Average Power

TABLE 20

Output Power Sensitivity to Variation of Parameters

Parameter	Sensitivity (dB/%)
Gun Magnet Coil Current (2 supplies together)	-0.11
Heater Voltage	0.32
Gun Anode Voltage	0.39
Beam Voltage	0.54
Main Magnet Coil Current (4 supplies together)	-1.21

oscillator cavity, there appeared to be a relative insensitivity to field shape. Figure 56 shows the extremes of magnetic field shapes which yielded over 200 kw of peak rf output power.

The reaction of the oscillator to changes in the output guide was tested with two configurations. These included a double miter bend and Teflon discs of two thicknesses inserted in the output waveguide run. With magnetic fields set up for typical operation, installation of a double miter bend resulted in a non-TE_{On} oscillation at 26.872 GHz. In an effort to suppress this oscillation, believed to be associated with TE_{21} mode in the anode tunnel, a magnetic perturber in the form of an iron cylinder was placed around the anode. With the presence of the iron cylinder it was necessary to readjust the magnet coil currents to obtain high output power. With the magnet coil currents readjusted, 230 kw peak rf power output was obtained without the double miter bend. Reintroduction of the double miter bend reduced the output to 196 kw but with parameter readjustment output recovered to 239 kw.

With the double miter bend removed and a 0.030-inch thick Teflon disc (VSWR ~ 1.6) installed, output power snapped back and forth between 28.007 GHz and a non-TE_{On} oscillation at 26.902 GHz. With readjustment of parameters, 214 kw peak output power was obtained free of interfering oscillations. However, at lower values of transverse energy an oscillation appeared at 28.5 GHz, possibly the TE_{022} resonance. Effect of the

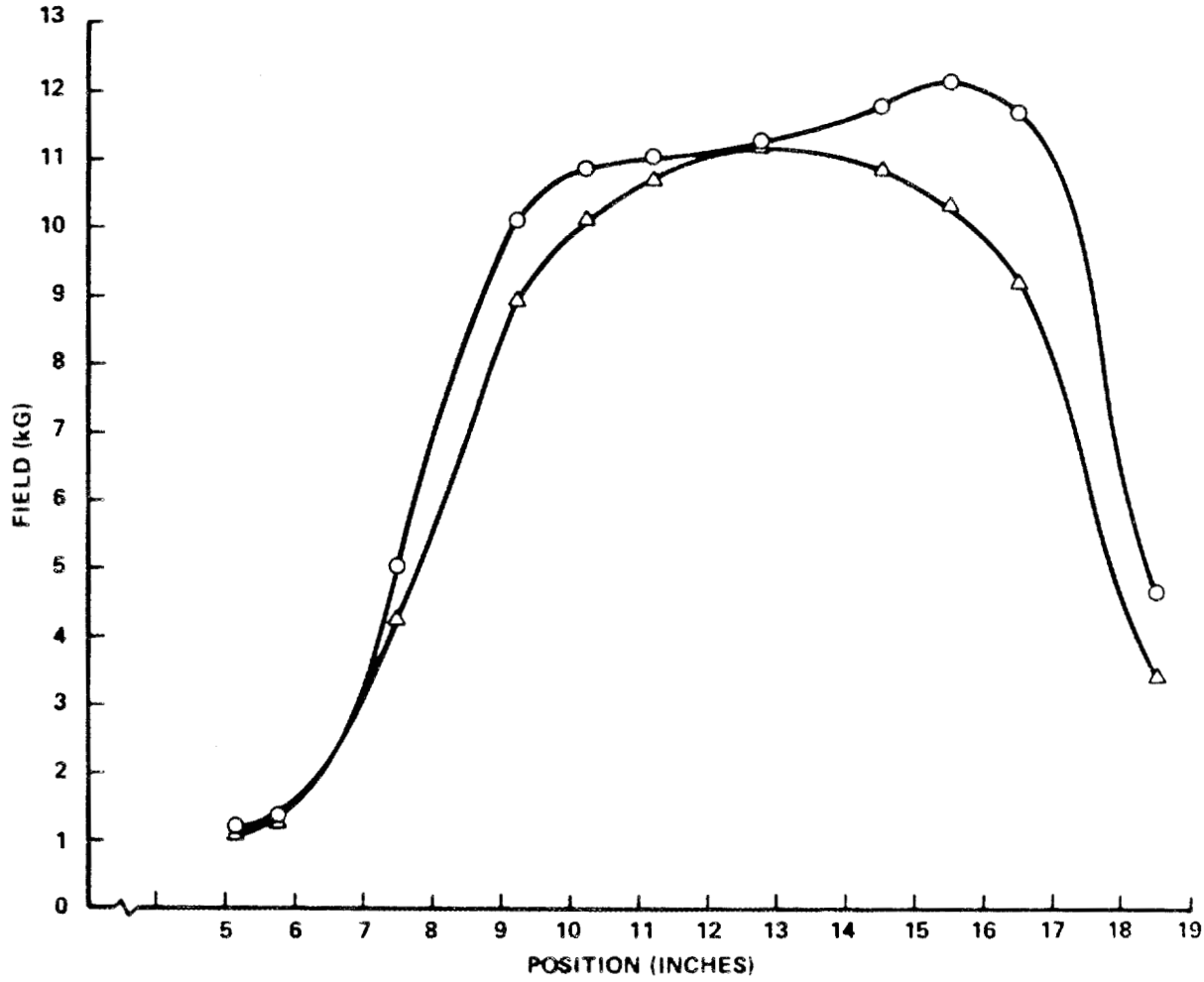

Figure 56. Pulsed Gyrotron Oscillator Magnetic Field Extremes

oscillation is shown in Figure 57, which plots efficiency as a function of gun magnet No. 1 coil current. Note that high values of gun coil current result in lower transverse energy. In this case, the interfering oscillation limits the dynamic range of the desired oscillation. With readjustment of parameters, wide dynamic range free of the 28.5 GHz oscillation was restored although at a lower power output, as indicated in Figure 58.

With a 0.062-inch thick Teflon disc (VSWR ~ 2.2) installed, power output dropped to 100 kw but with parameter adjustment was restored to 164 kw. However, at this power level the first 6 microseconds of the pulse were at 28.038 GHz, the next 8 microseconds at 28.020 GHz, and the remaining 17 microseconds at 28.057 GHz, presumably all variations of the TE_{02} mode. Again, with parameter adjustment single frequency pulses could be obtained over a wide dynamic range at lower power levels, as shown in Figure 59. Adjustment of parameters for best output power under different load conditions are summarized in Table 21.

The spurious oscillations observed during operation of the pulsed oscillator were in three ranges: from 26.822 GHz to 26.899 GHz, near 27.212 GHz, and from 28.498 GHz to 28.528 GHz. Additional mode suppression was desirable to suppress these spurious frequencies.

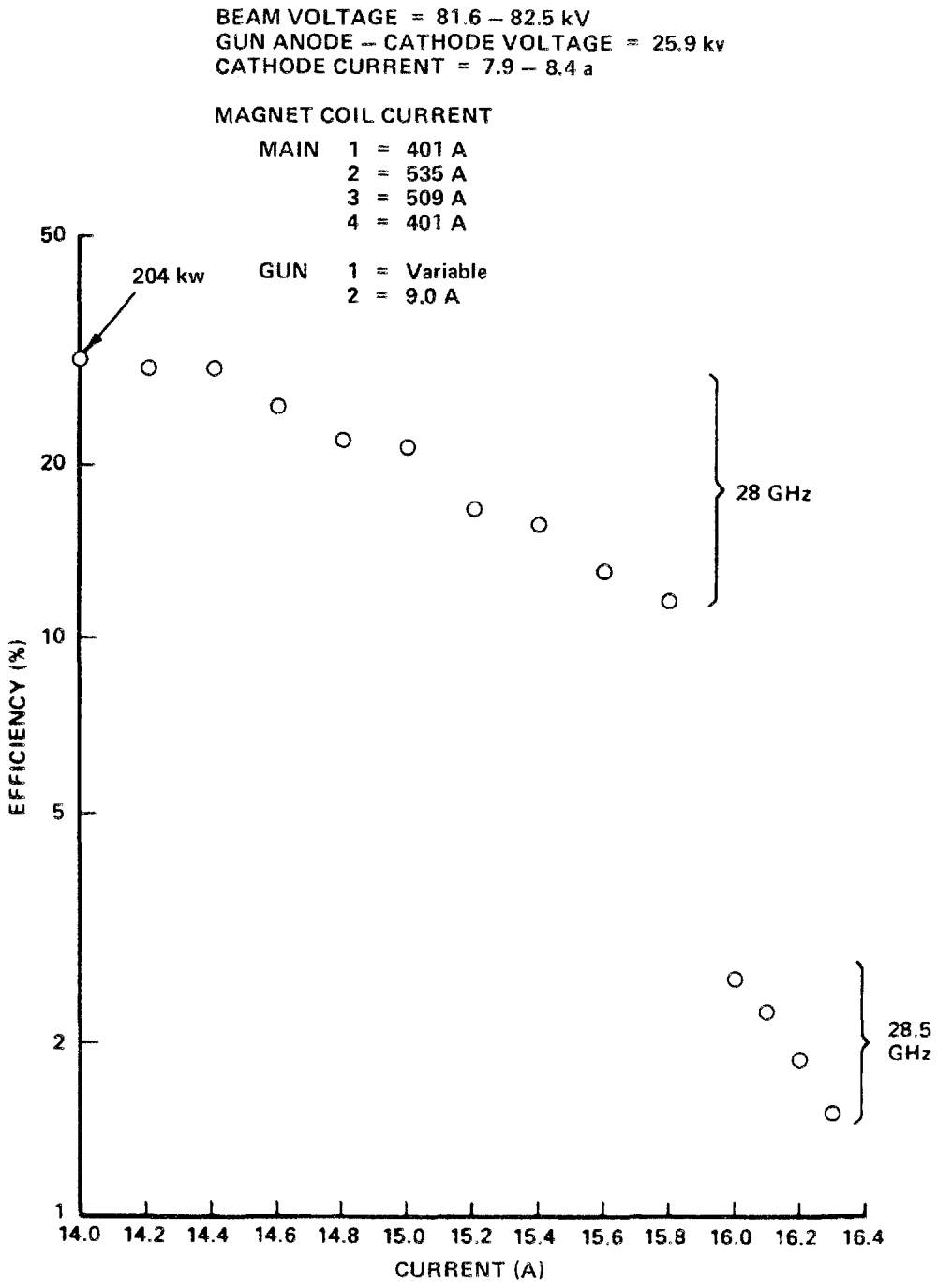

Figure 57. Pulsed Gyrotron Oscillator Efficiency as a Function of Gun No. 1 Coil Current with 0.030-inch Thick Teflon Disc in Output Guide

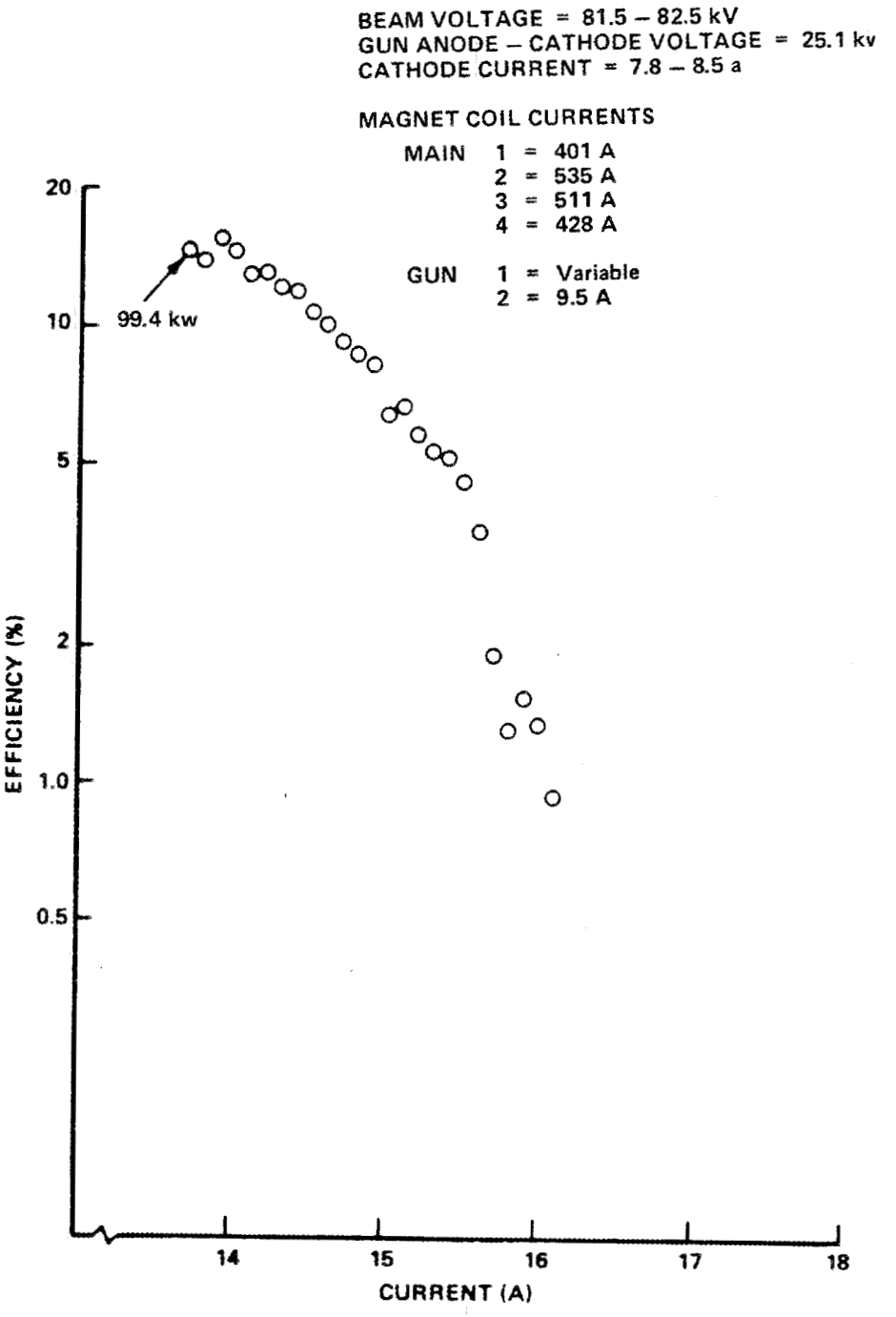

Figure 58. Pulsed Gyrotron Oscillator Efficiency as a Function of Gun No. 1 Coil Current with 0.030-inch Teflon Disc

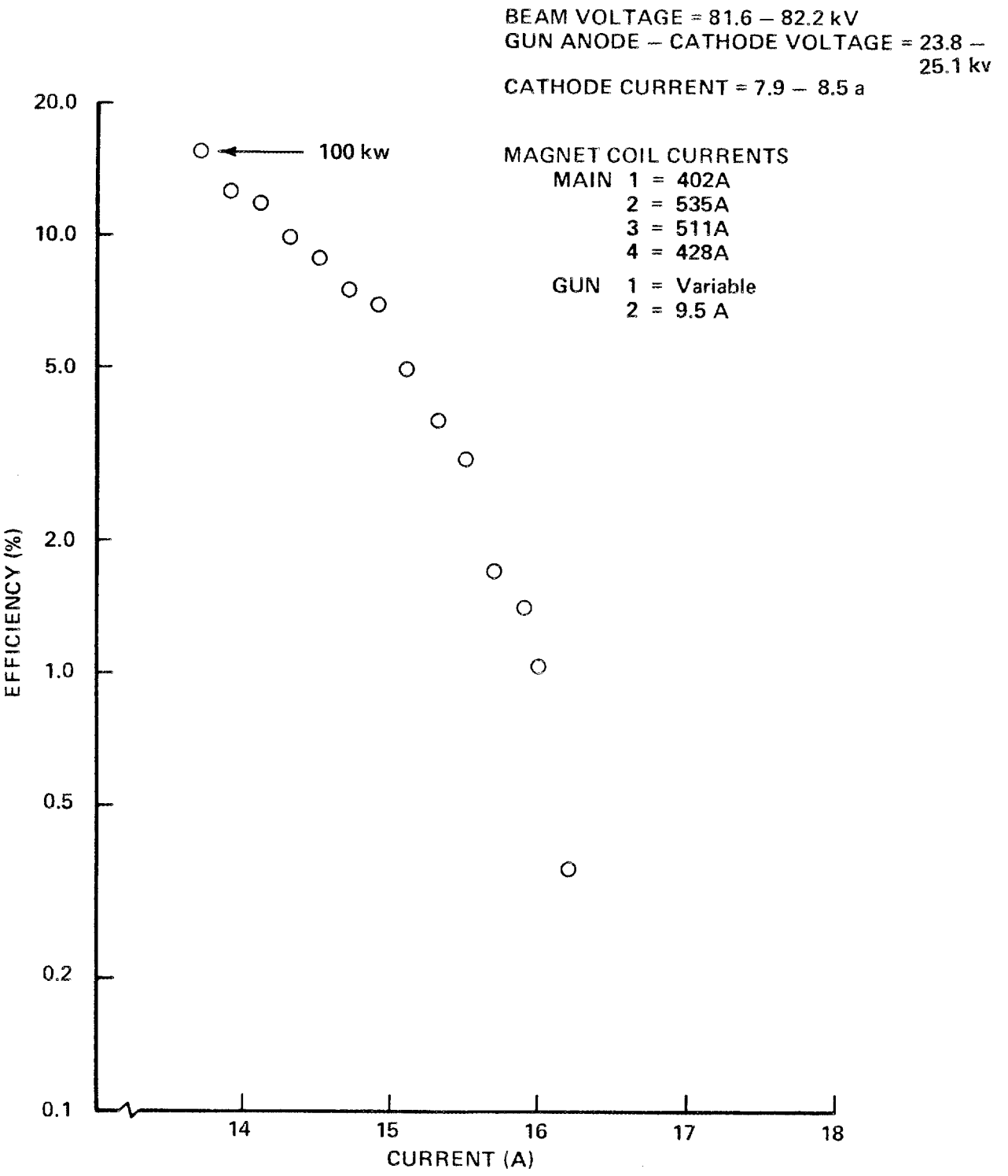

Figure 59. Pulsed Gyrotron Oscillator Efficiency as a Function of Gun No. 1 Coil Current with 0.062-inch Thick Teflon Disc

TABLE 21

Effect of Load on Oscillator Operation with Magnetic Perturber

Load	Reference	Double Miter Bend	0.030" Thick Teflon Disc	0.062" Thick Teflon Disc
po (kW)	230	239	214	164
f (GHz)	28.020	28.030	28.038	28.057
V_o (kV)	80.1	79.8	80.7	81.2
i_o (a)	8.5	8.7	8.2	8.3
η (%)	34	34	32	24
v_g (kv)	26.0	25.3	25.7	24.2
τ (μs)	36	36	34	31
PRR (pps)	60	60	60	60
rf Duty (%)	0.216	0.216	0.204	0.186
Po (W)	498	517	436	304
I_1 (A)	401	401	401	401
I_2 (A)	535	535	535	535
I_3 (A)	500	499	504	514
I_4 (A)	401	401	401	400
I_{g1} (A)	13.7	13.7	14.4	13.7
I_{g2} (A)	9.0	9.0	9.0	6.5

C. SECOND EXPERIMENTAL PULSED OSCILLATOR

Chronologically, the second pulsed oscillator was built following work with the first two CW oscillators, discussed in Section IV-H. The tube was designated VGA-8050 S/N 2, and the main purpose of the device was to test a beam tunnel diameter change under consideration for use in the third CW oscillator. Beam transmission and undesirable spurious oscillations were areas of concern. The new beam tunnel incorporated alternate copper and SiC-BeO rings. The inside diameter of the copper rings was 12% smaller than that of the lossy SiC-BeO rings, which had the normal 0.43-inch inside diameter. The arrangement represented a substantial change from the Kanthal-coated anode of the first pulsed oscillator.

The second pulsed oscillator resonant cavity was water cooled to stabilize dimensions with varying duty factor. The first pulsed oscillator, which had no cavity cooling, had shown relatively large lowering of resonsant frequency with increasing average power.

The first set of experiments performed with S/N 2 involved investigation of how various parameters could be altered while maintaining operation in the desired mode. Each parameter was varied independently of the others, which were kept at baseline values given in Table 22.

TABLE 22

Baseline Experimental Operating Parameters

Magnet Coil Currents		
Main 1	410	A
2	530	A
3	530	A
4	490	A
Gun 1	12.0	A
2	9.0	A
Beam Voltage	81.0	kV
Beam Current	8.0	A
Gun Anode Voltage	26.0	kv
Rf Pulse Duration	100	μs
Pulse Repetition Rate	60	pps
Rf Duty	0.60	%
Average Output Power	~0.69	kW
Peak Output Power	~115	kw
Efficiency	17.7	%
Frequency	28.065	GHz

Figures 60 through 63 show the change in rf output power observed for changes in the currents of the four main magnet sections. As the magnet currents were decreased, the output power increased linearly, until a point was reached where the oscillator jumped modes. For the two sections nearest

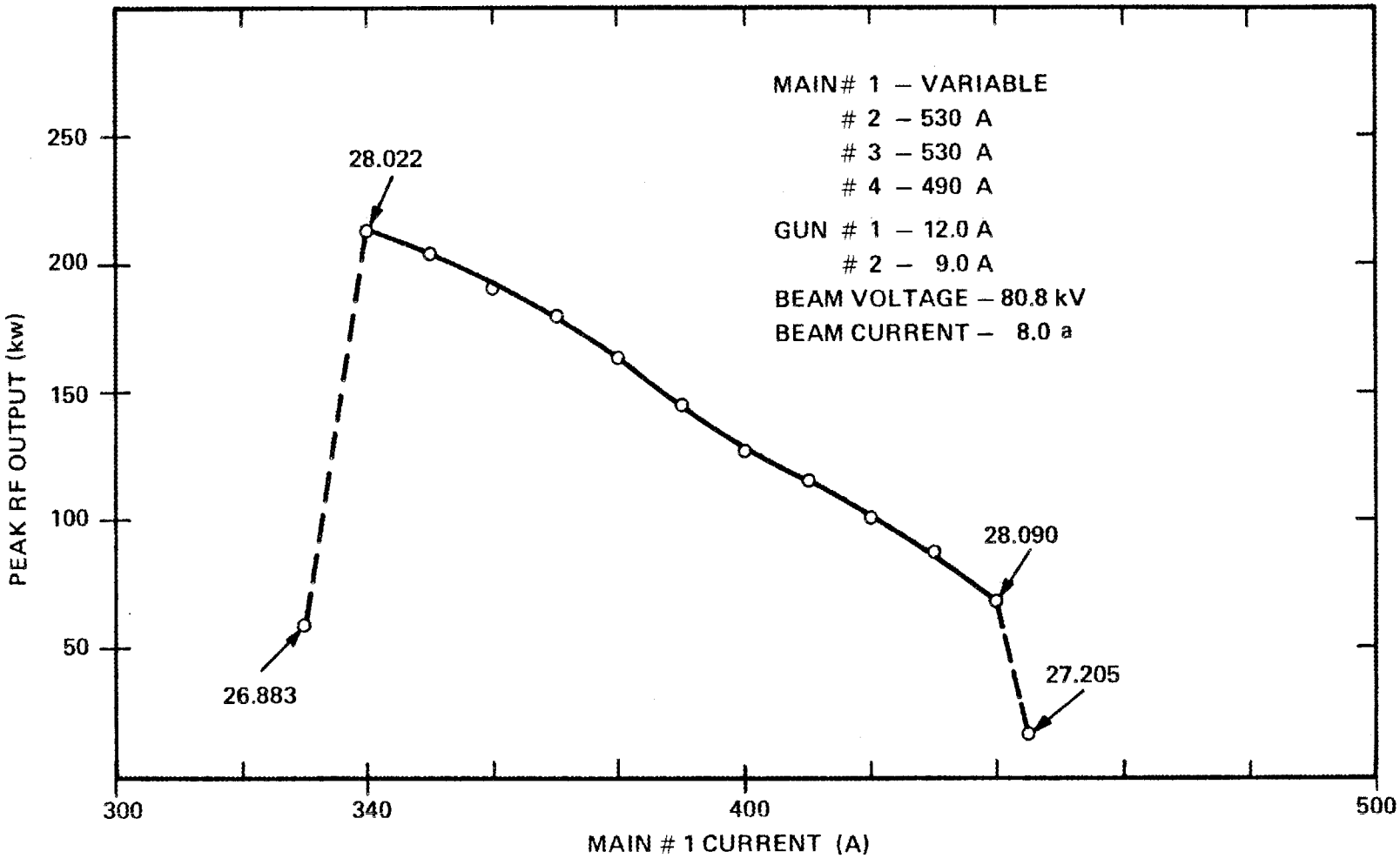

Figure 60. Peak RF Output vs Focusing Solenoid Current No.1

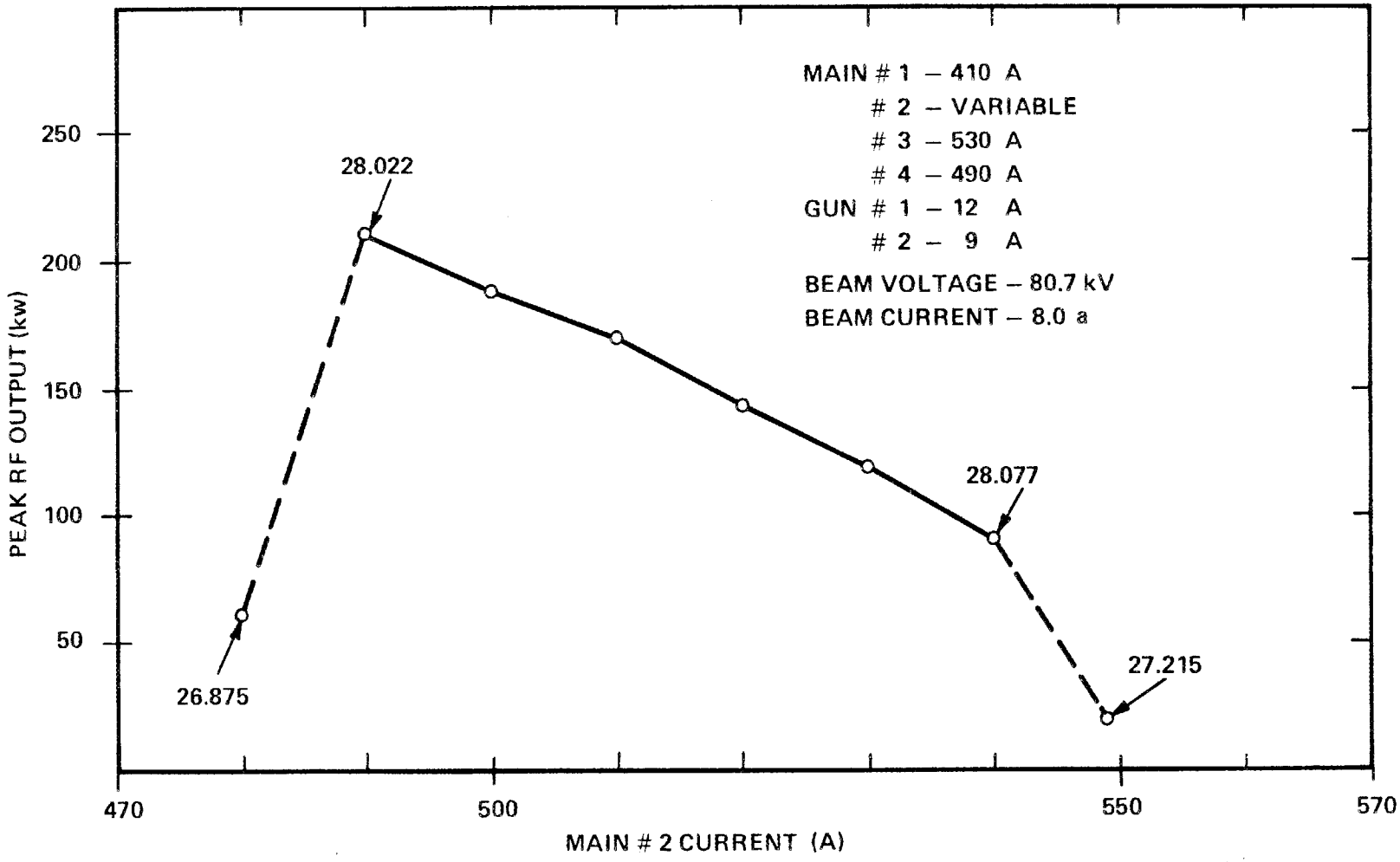

Figure 61. Peak RF Output vs Solenoid Current No. 2

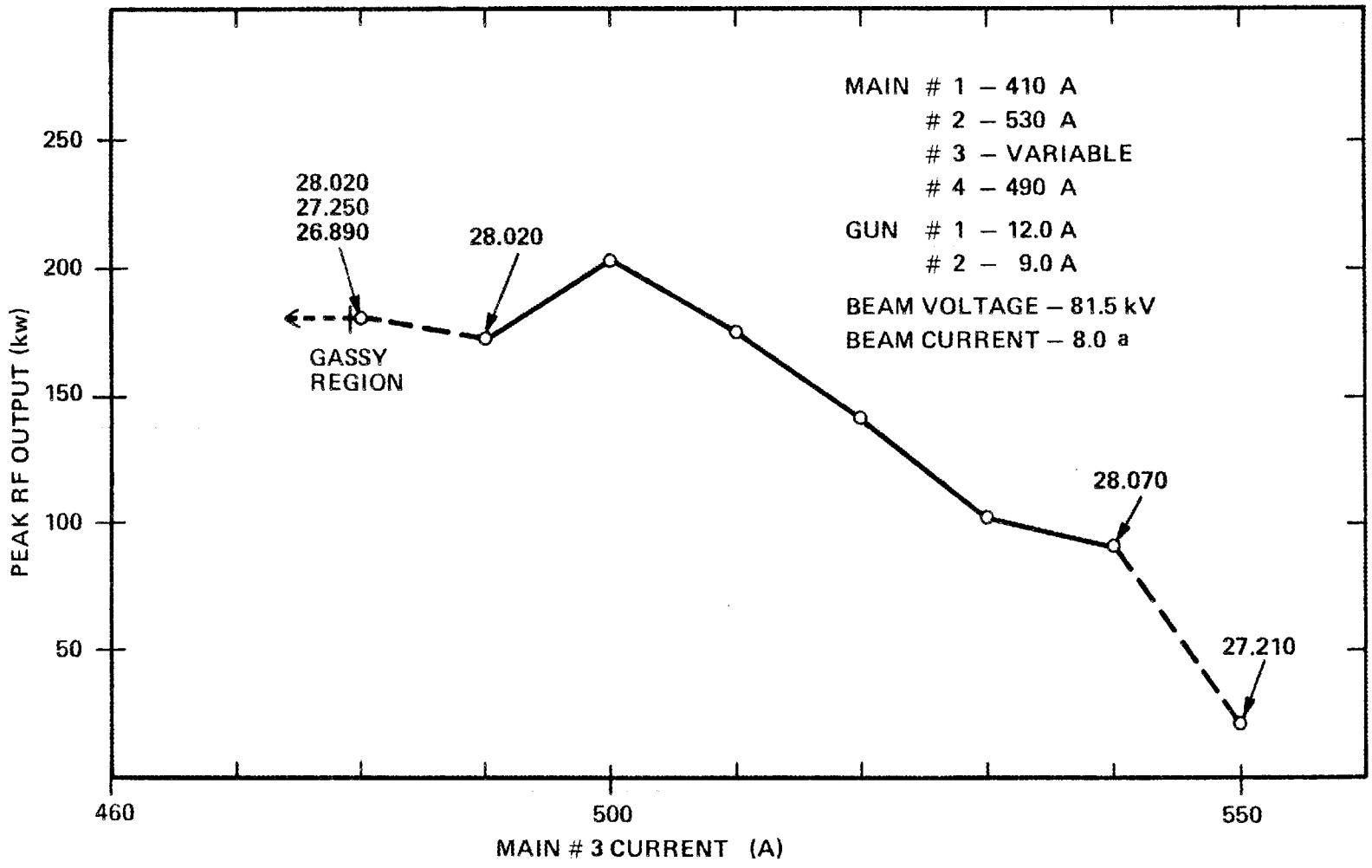

Figure 62. Peak RF Output vs Focusing Solenoid Current No. 3

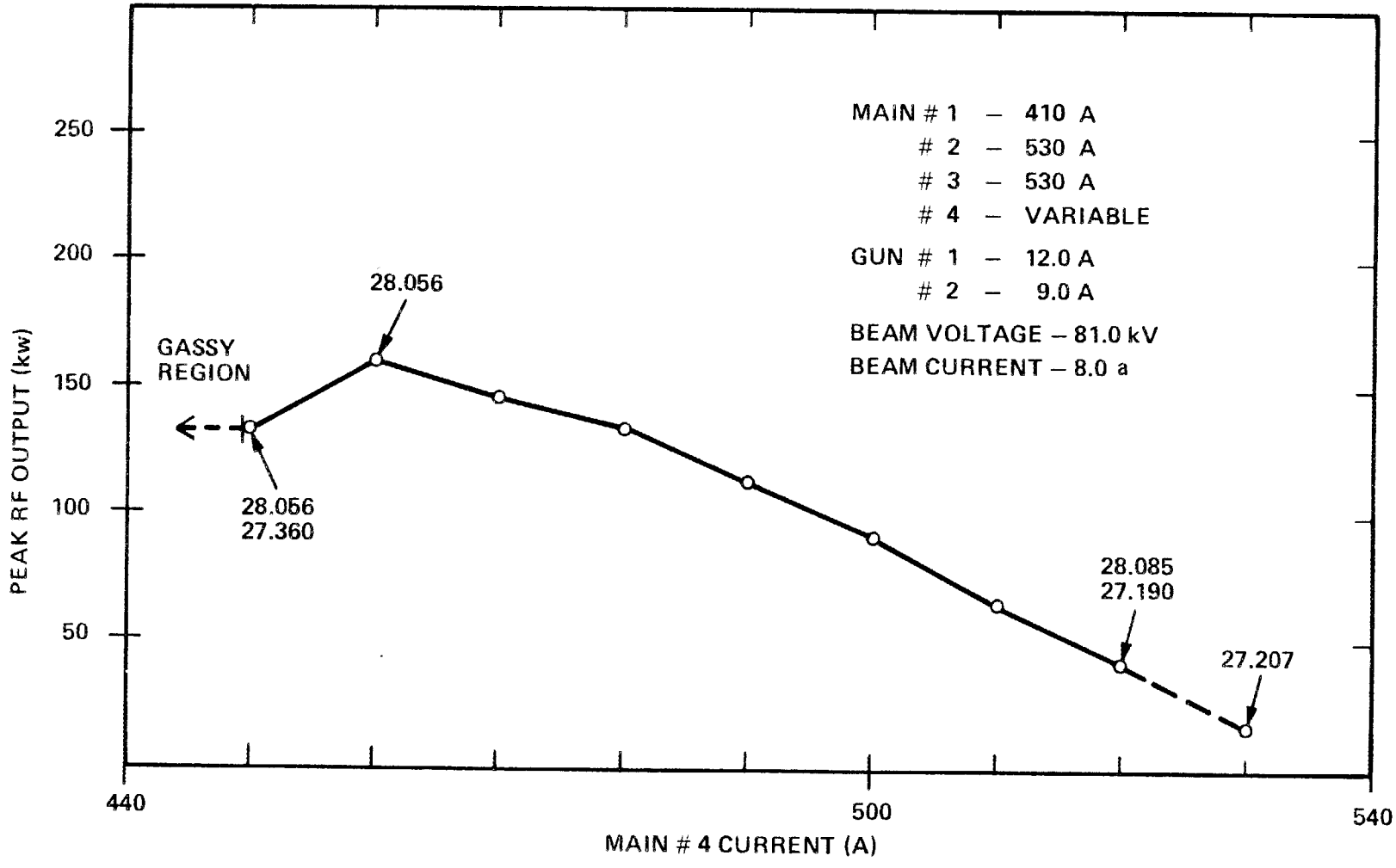

Figure 63. Peak RF Output vs Solenoid Current No. 4

the collector (Figures 60 and 61), the alternate mode produced approximately 60 kw of peak power at 26.8 GHz. For the two sections nearest the anode, the alternate mode caused excessive gas pressure which turned the tube off, making frequency identification difficult. Increasing the current of each coil from the baseline value results in a decrease of rf output power and finally a jump to a mode which gave 10 kw of peak power output at 27.2 GHz. In main-mode operation, the output frequency varied directly with magnet current between the two end point values shown in the figures.

Variations of other parameters such as gun coil currents, beam voltage, and beam current did not introduce any new spurious frequencies. The spurious frequencies near 26.8 and 27.2 GHz were similar to those observed previously. It was concluded that the dimensional change in the beam tunnel diameter did not create any new spurious microwave outputs.

It was also noted that the peak body current did not exceed 15 ma during normal operation, indicating good beam transmission through the reduced diameter beam tunnel. Therefore, the diameter change was considered satisfactory for use in the third CW oscillator.

In the course of making the measurements described, a peak rf output power of 255 kw was achieved. The appropriate operating parameters for this output are listed in Table 23.

TABLE 23

Best Test Results for the Second Pulsed Oscillator

Magnet Coil Currents		
Main 1	350	A
2	530	A
3	530	A
4	490	A
Gun 1	12.0	A
2	9.0	A
Beam Voltage	80.8	kV
Beam Current	8.8	a
Gun Anode Voltage	26.0	kv
RF Pulse Duration	100	μs
Pulse Repetition Rate	60	pps
Rf Duty	0.60	%
Average Output Power	1.53	kW
Peak Output Power	255	kw
Efficiency	35.8	%
Frequency	28.025	GHz

D. CW OSCILLATOR DESIGN

The early success of the experimental pulsed gyrotron oscillator led to a decision to make the first CW tube an oscillator. Work on pulsed gyroklystron tubes up to this point had not yielded the desired results, and it appeared that a long and difficult development period might be required before satisfactory amplifiers would be possible. Further, work on CW oscillators, it was felt, would in fact give many results later applicable to gyroklystron design. Major differences in design of the CW tube from its predecessors are listed below.

1. The beam tunnel between the gun and the oscillator cavity used Kanthal in the tapered region near the gun and alternate rings of copper and SiC - BeO in the main untapered portion.

2. The water cooled resonant cavity was electrically the same as used in the pulsed gyrotron oscillator but had increased water cooling.

3. The output waveguide incorporated a triple miter bend to extract microwave power prior to the collector. See Figure 64. The output waveguide was water cooled.

4. Provision was made for passage of the electron beam through a suitable hole in the first miter bend and into a water cooled tunnel of increasing diameter leading to a 10.2-inch diameter collector. Maximum collector power density was expected to be close to 1000 watts per square centimeter. The collector was electrically isolated to permit monitoring of body current.

The first CW oscillator built with the foregoing design features was designated VGA-8000 S/N 1. Test results are described in Section IV-I, "Triple Miter Bend Models", Subsection 1 and a layout drawing of the tube is shown (Figure 64).

E. CW OSCILLATOR DESIGN CHANGES CONSIDERED

Chronologically, interest in the design changes considered in this section of the report came after construction and test of the first two CW oscillators, VGA-8000 S/Ns 1 and 2. In effect, these changes reflected the need for improvements indicated by experience with these tubes. They are listed as follows:

1. Reduction in Power Output: Loss of power output and efficiency in CW tubes, as compared to pulsed oscillators, suggested an interference problem in the microwave circuit design. Microwave cold tests of individual elements making up the rf output system; cavity, miter bends, tapers, etc. indicated that the desired microwave characteristics were being achieved. However, more extensive measurements with the components of S/N 2 indicated rather complex microwave intercoupling effects among various elements; including the oscillator resonant cavity, miter bends, output waveguide, collector, and electron gun. Such intercoupling effects may cause splitting

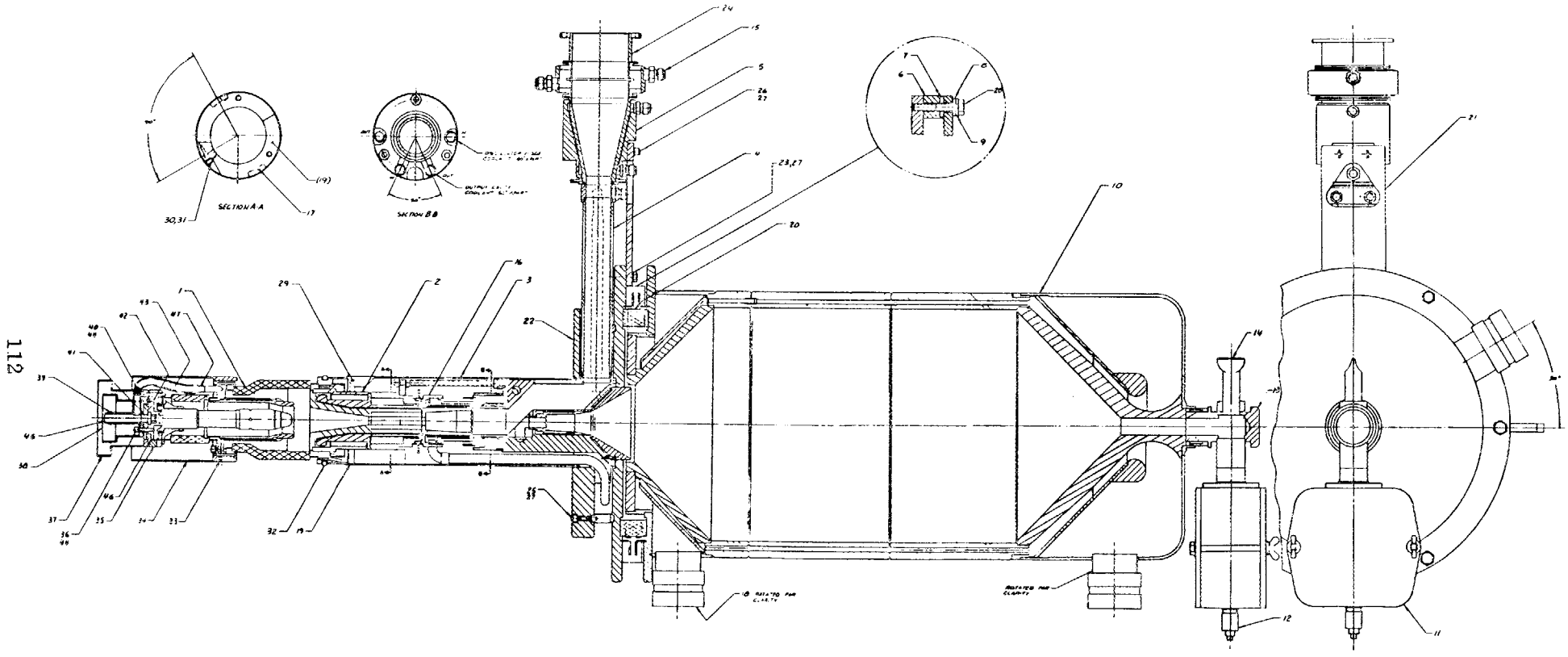

Figure 64. Layout Drawing of CW Gyrotron Oscillator

and lack of resonance symmetry in the oscillator cavity, thus altering the effective Q. This would explain loss in power output and efficiency. To obtain improvement, it appeared desirable to pursue design changes involving the collector, the method of coupling rf power out, and a possible means of decoupling the electron gun region from the oscillator resonant cavity. Decoupling the gun region would not only enhance efficiency, but would also reduce microwave heating of the cathode.

2. Output Window: A window failure at 18 kW average power output was probably significantly affected by trapped energy in the output waveguide. Yet sufficient concern existed to warrant investigation of alternate designs. One possibility considered was the use of a double disc arrangement, two ceramic discs separated suitably to allow passage of a low loss dielectric cooling liquid such as the fluorocarbon FC-75^{tm}. (FC-75 is a trademark of Minnesota Mining and Manufacturing Co. for a flourocarbon liquid.) Losses in this liquid at 28 GHz were found to be about 1% for a length of 0.080 inch. A second possibility was face cooling of a single window by means of a forced draft of gas. Calculations were undertaken to determine the relative merits of this technique.

3. Open-Ended Cavity: Work was started on an open-ended oscillator cavity, with no end wall at the electron gun end. This was done to avoid trapping unwanted modes, which could propagate in the cavity itself, but which were cut off in the beam tunnel leading toward the electron gun. Ideally, unwanted modes would radiate out of the open end of the cavity and into free space. In a practical tube, however, it is necessary to close the vacuum envelope. Two approaches considered in attempting to approximate a free-space termination were the use of a metal cylinder coated with lossy material and the use of a ceramic cylinder with water outside as a load.

The coated metal arrangement proved rather ineffective. However, the ceramic with water behind it gave fair results. A cold test was performed using simulated tube parts; the power going toward the gun was reduced by a factor of five. Further, the cavity resonance curve was much less sensitive to changes in orientation of the miter bend and output waveguide. Additional investigation of this system was planned.

4. Collector Resonance Effects: Extensive work was carried out to document microwave effects of the collector. It was observed that the addition of loss resulted in reduced splitting of the oscillator cavity resonance curve. Further, it was determined that dimensional details of the pumpout tubulation at the top of the collector had considerable effect on cavity resonance. A collector auxiliary microwave loading port was given some consideration.

5. Output Coupling System: It had been observed in cold test that line lengths between the various miter bends in the output waveguide system had noticeable effect on cavity resonance. Additional tests were planned to optimize these lengths. A symmetrical output waveguide coming out through the large collector volume was now under consideration as an alternative output system. The arrangement could take the form of tapers going up to the collector diameter and then back down to the desired output guide diameter. Another alternative was the use of spherical mirrors to focus the output power through the collector region. Cold tests were carried out to evaluate these approaches.

Work on the output window and on output coupling systems is covered in greater detail, as the efforts progressed in

Section IV-F "Output Window"
Seciton IV-G "Output Coupling Systems"

F. OUTPUT WINDOW

Output window work reported in this section began as the result of a window failure in VGA-8000 S/N 2, touched upon in Section IV-E, Subsection 2. The design growing out of this effort made use of two ceramic discs separated by a small distance to permit the passage of coolant between. The coolant is a low loss fluorocarbon, FC-75. The arrangement gives direct face cooling at the source of window heat. The requirement for a closed FC-75 coolant circulating system is a disadvantage, to be sure, but the design makes for very high power capability in the output window.

Calculated VSWR for the new double-disc window showed a near perfect match at 28 GHz and low VSWR over substantial bandwidth above and below. Calculations were done for both alumina and beryllia windows. The calculations for two beryllia windows, shown in Figures 65 and 66, indicated improvement in bandwidth over those for an alumina window, given in Figure 67. This result was not unexpected, since beryllia has a lower dielectric constant than alumina. On the other hand, alumina is a much stronger material. Beryllia window discs with their wider bandwidth lead to improved loading of unwanted modes through the window structure.

Some comparisons have been made of the various tube windows and their respective losses. Of the measurable losses, very little is in the ceramic itself. With the Alumina window, 93% of the total loss is in the FC-75. With the Beryllia window, 98% of the losses are in the FC-75. Therefore, looking at the FC-75 dissipation will be a good indication of window performance.

The Alumina window has a smaller FC-75 gap than the Beryllia window, 0.032" and 0.050", respectively. The Alumina window would then be expected to have lower losses. Figure 68 shows a comparison of Beryllia and Alumina windows. Tube No. 5R2 shows the lower FC-75 dissipation achieved with the Alumina window. With the beryllia window, the FC-75 in the gap does dissipate more rf, but the FC-75 has a higher flow at a given pressure, and therein lies the trade-off. In Figure 68, tube No. 12M shows a curve which starts off with a slope as would be predicted by calculation, and tube No. 6 has a steeper slope than predicted. Tube No. 6 is an axisymmetric tube, and No. 12 is a miter bend tube. There is no evident answer for why No. 6 has more dissipation. It does appear that the dissipation could be as low as that of No. 12M and future windows will provide more data. The curve upward of the dissipation in tube No. 12M is explained by the multi-moding of the miter bend tube output worsening with the increase in output power. Figure 69 shows tube No. 5R window dissipation with and without a slightly mismatched load. It clearly shows an increase in FC-75 dissipation due to a mismatched load. It appears that the window dissipation can be affected by the load applied to the tube.

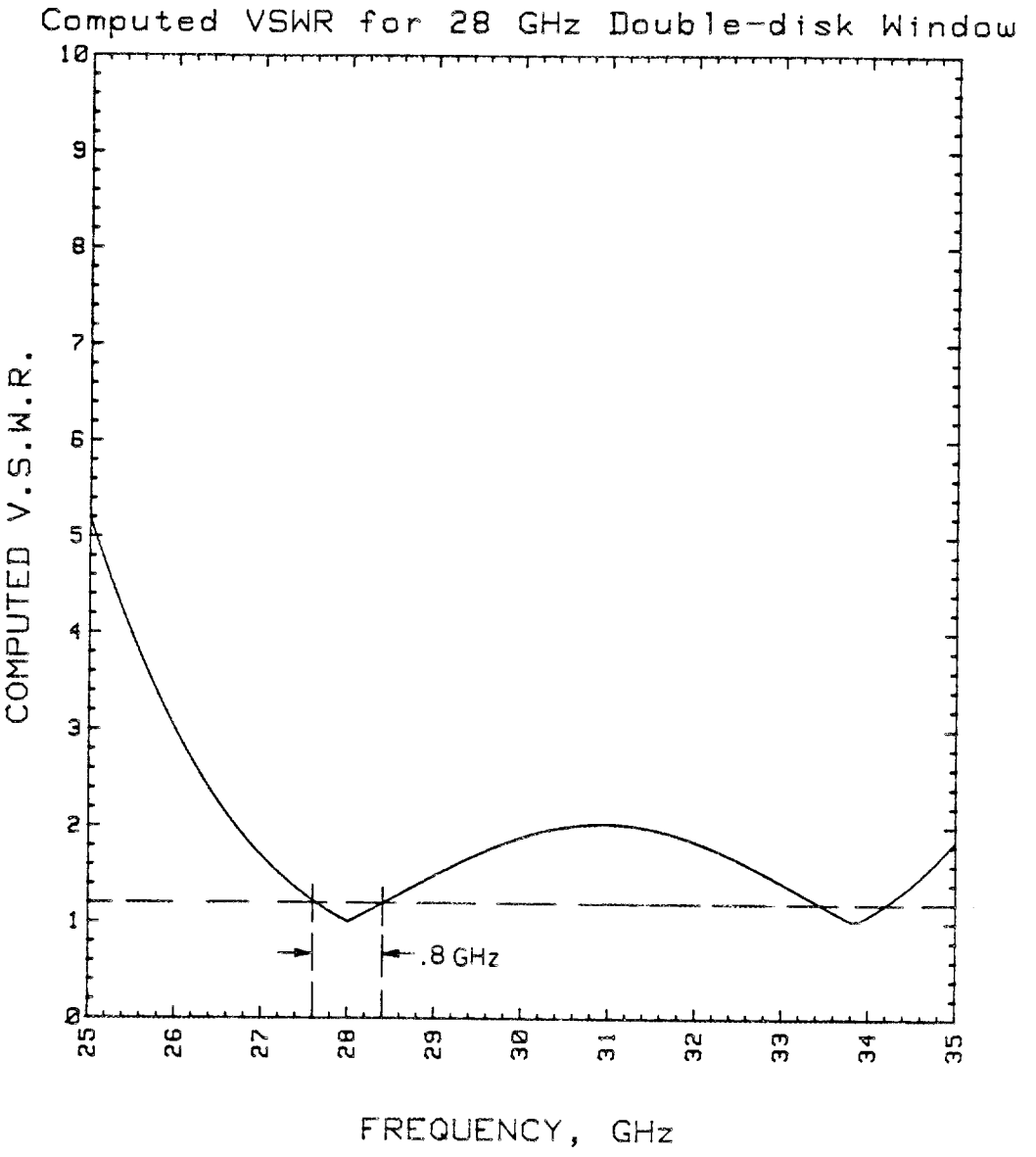

Figure 65. Tube No. 8 Beryllia Window

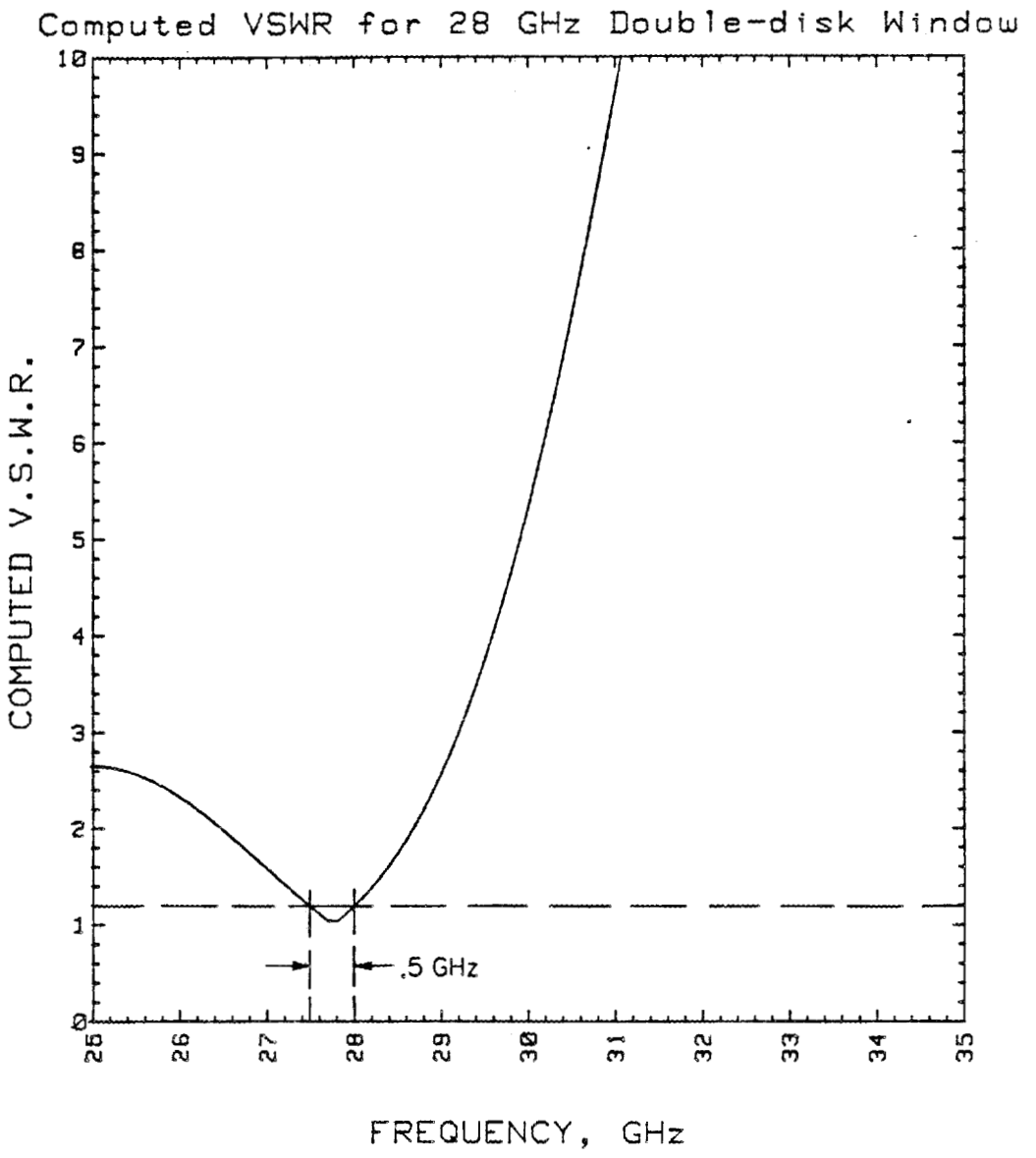

Beryllia Window

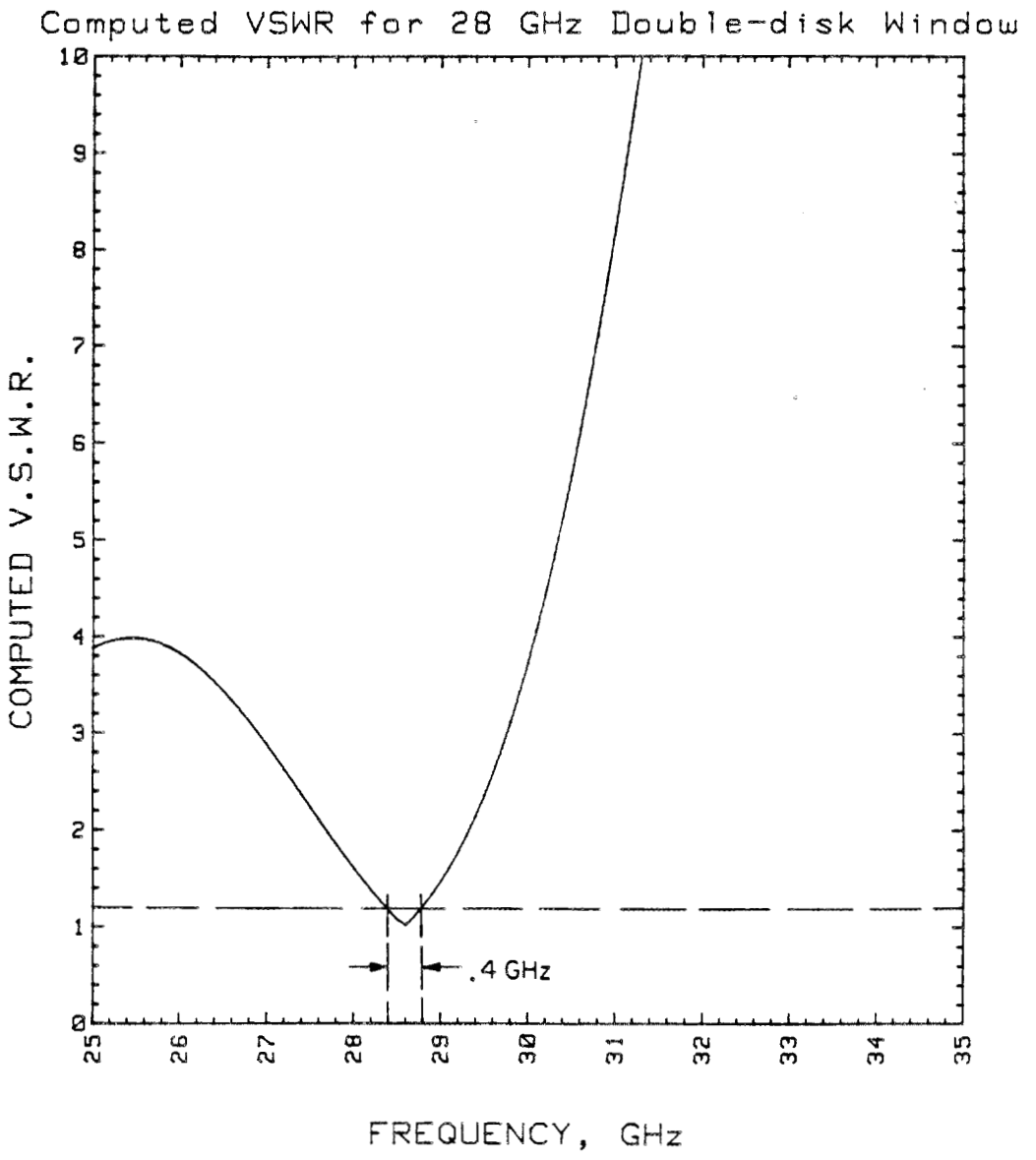

Figure 67. Tube No. 5 Alumina Window

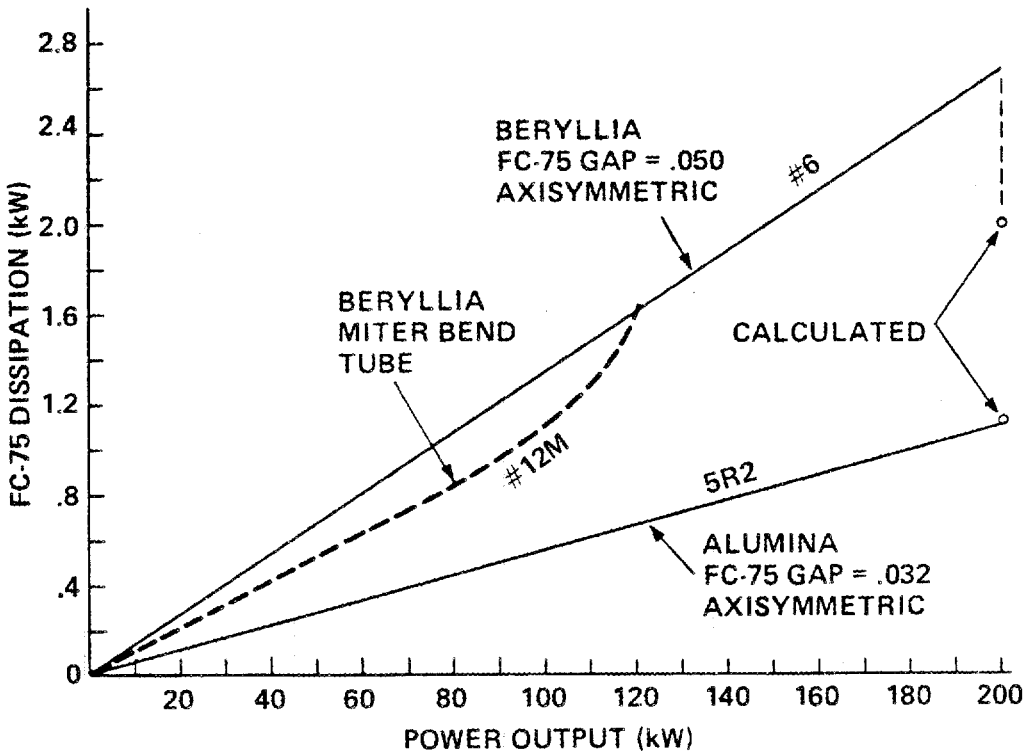

Figure 68. Output Power vs FC-75 Dissipation

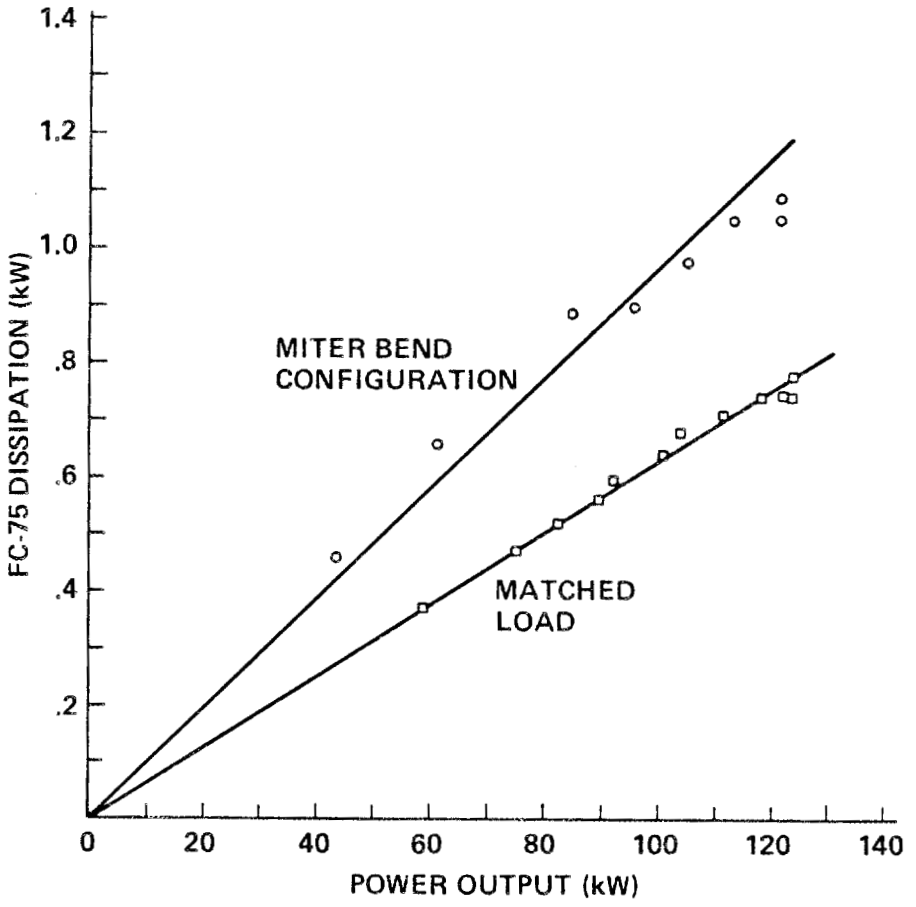

Figure 69. FC-75 Dissipation S/N 5R2

G. OUTPUT COUPLING SYSTEMS

The subject of this section was introduced in Section IV-E, "CW Oscillator Design Changes Considered", Subsection 5. Output coupling systems that came to be of interest in the program were:

1. Triple miter bend
2. Spherical mirror
3. Straight through collector

The triple miter bend output coupling system came under close scrutiny when test of CW gyrotron oscillator tubes, VGA-8000 S/Ns 1 and 2, showed rf power output lowered from earlier pulsed tubes, apparently because of intercoupling effects both in the microwave output circuitry and also involving the electron gun and collector. The spherical mirror system, a possible alternative, attempts to transmit the microwave signal across the collector region by means of optical techniques. Straight through collector systems treat the collector as a microwave waveguide element of the output waveguide. Three possible straight through collector systems were studied, each incorporating different size combinations of collector, output waveguide, and window.

1. Triple Miter Bend

Calculations based on the analyses of both Marcatili and Katsenelenbaum for TE_{01} mode conversion in single miter bends were sufficiently disconcerting to prompt further study. The analyses deal chiefly with the TE_{01} loss and the fraction of loss converted to TE_{02}. Of immediate interest, was loss in a TE_{02} propagating wave and degree of conversion to modes other than TE_{on}. Much of the power in these modes is wasted if a mode filter is used. Their presence places an unnecessary burden on the window.

Calculations showed that for the 1.125-inch-diameter guide at 28 GHz, TE_{01} loss is 1.7 dB, i.e., more than 30% of power is transferred to

other modes. The fraction converted from TE_{01} to TE_{02} was calculated to be 10%. A TE_{02} mode incident on the miter would be expected to fare even worse.

Measurements of mode purity were made by probing the radiation patterns with a rectangular WR-28 waveguide and a crystal. The waveguide was mounted on a carriage inside a small wedge, minimizing the reflection from the holder. The reflection at the discontinuity between the end of the cylindrical guide and free-space was negligible at 28 GHz for TE_{01} and TE_{02} modes. In other words, the radiating guide behaved like a matched guide. Figure 70 shows the main elements of the arrangement. The rectangular guide was translated across a diameter of the circular guide usually at a distance of 0.3 inch from the plane of the end of the guide. Voltages corresponding to position and crystal current were fed to an X-Y recorder. The validity of the technique was demonstrated for simple TE_{01} and TE_{02} modes propagating in a 2.5-inch-diameter waveguide. Some loss of resolution was experienced in measurements at the end of a 1.125-inch-diameter waveguide, but nevertheless the technique's simplicity had much to commend it. Gross perturbation of TE_{on} modes by the sampling guide was negligible for practical purposes. Measurements were made with diametric scans in orthogonal directions AA' and BB', and each scan was carried out twice, once with the narrow dimension of the guide parallel and once perpendicular to the scan direction.

The resulting X-Y plots, then, corresponded closely to E_θ^2 and E_r^2 along the two scan lines at a single plane of the beat pattern of the modes in the guide. Sometimes more extensive measurements were made for different lengths of guide and at different locations across the guide aperture. In principle, a complete analysis is facilitated in this manner. In the presence of more than two or three significant modes, however, the analysis presents a formidable problem.

Figure 71 shows the modal output (E_r^2 and E_θ^2) along a single diameter of a 1.125-inch-diameter guide excited in the TE_{02} mode. This diameter is close to that of the guide used in the triple miter. Note the absence of radial electric field across the diameter. Adding a single miter

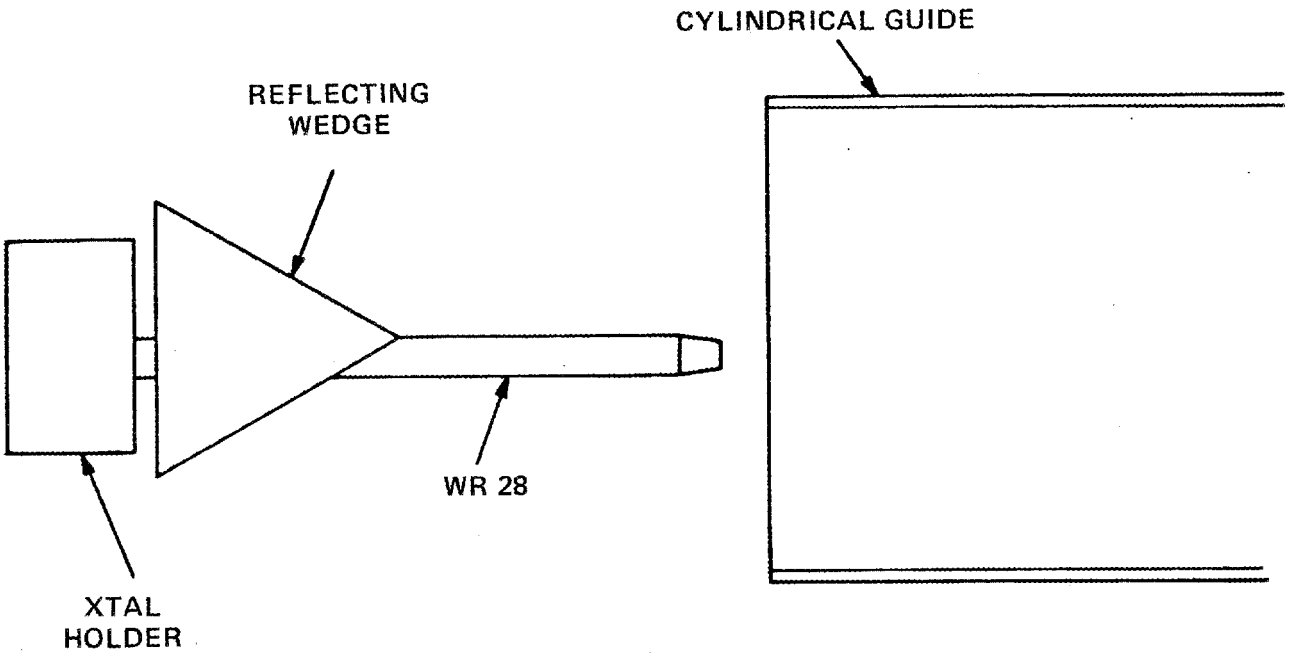

SIDE VIEW

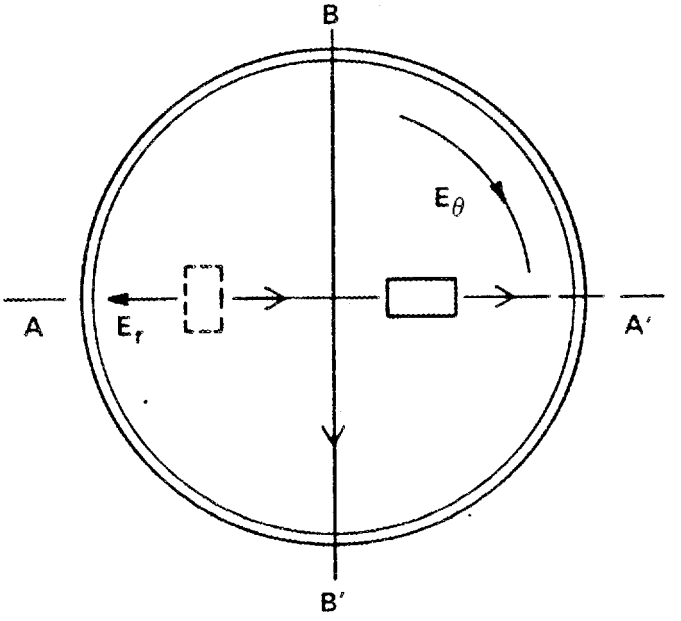

END VIEW

Figure 70. Mode Probing Arrangement

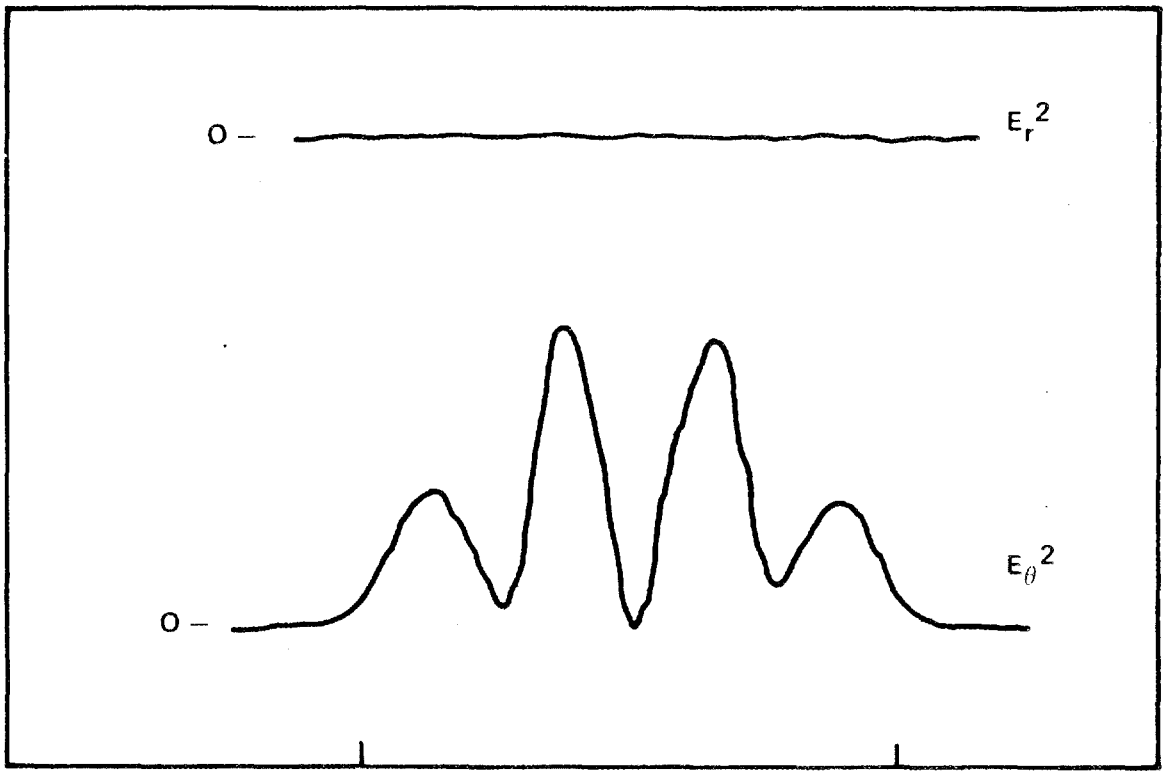

Figure 71. Modal Output Along Diameter of 1.125-inch Diameter Guide (Guide Wall Position Indicated)

in the same diameter guide gave rise to a considerable change in the pattern, consistent with some conversion into TE_{11} and TE_{12}. For the TE_{01} incident mode, the output appeared to be primarily TE_{01}, TE_{02}, TE_{11}, and TE_{12}. Theoretically, mode conversion is less for the TE_{01} than for the TE_{02}. Lower conversion occurs as the diameter of the guide or the frequency is increased. For example, at 28 GHz, a miter in a 2.5-inch guide results in a calculated power conversion of about 11% for the TE_{01} and 36% for the TE_{02}. At 120 GHz, values for the same 2.5 inch guide become 1.2% and 4%, respectively.

When the single miter is replaced by the triple miter, the modes from TE_{02} excitation measured in scans parallel to and perpendicular to the axis of the first guide are shown in Figures 72 and 73, respectively. Note the emergence of significant E_r field. The dominant modes appear to be TE_{02}, TM_{01} and TM_{02}. It is roughly estimated that at least 30% of the power is converted by the triple miter into non-TE_{on} modes.

For TE_{01} excitation, the conversion is less but nevertheless significant. In terms of tube performance, the results of mode conversion are: added window stress, a few percent added transmission loss between tube and load, extensive mode conversion at subsequent miters, and considerable output power monitoring difficulty. On the other hand, if the proper efficiency can be achieved, the window can be adequately cooled, and multimode coupling to the plasma is satisfactory, the compact mechanical design of the triple miter output has much to commend it.

2. Spherical Mirrors

In cooperation with work at ORNL, an investigation was carried out on the use of spherical mirrors located in the collector to transfer the microwave power in semi-optical fashion from the input aperture across the collector to the output waveguide. Microwave power is radiated from the aperture A_1, Figure 74, towards mirror 2. Separation of the mirrors is chosen such that with a given aperture at A_1 and a given cavity mode (TE_{01} or TE_{02}), the angle subtended by the 2.5-inch-diameter aperture in the second mirror contains only a few percent of the initially incident wave.

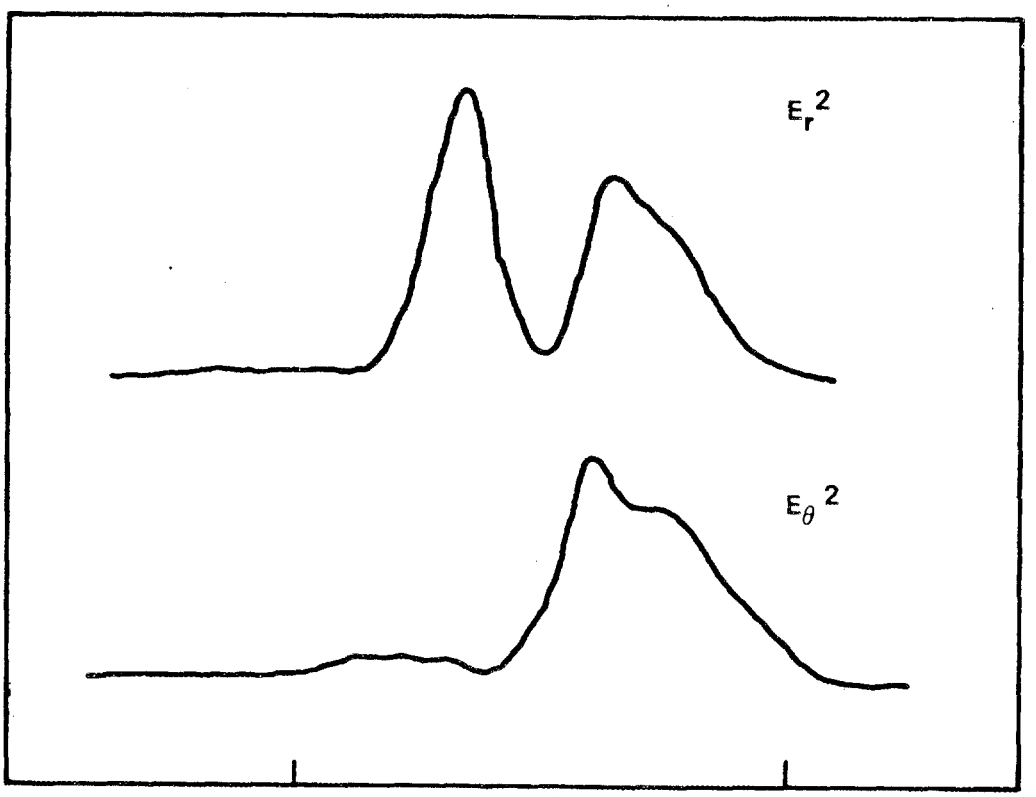

Figure 72. Modal Output After Triple Miter Scan Parallel to Axis of Gyrotron

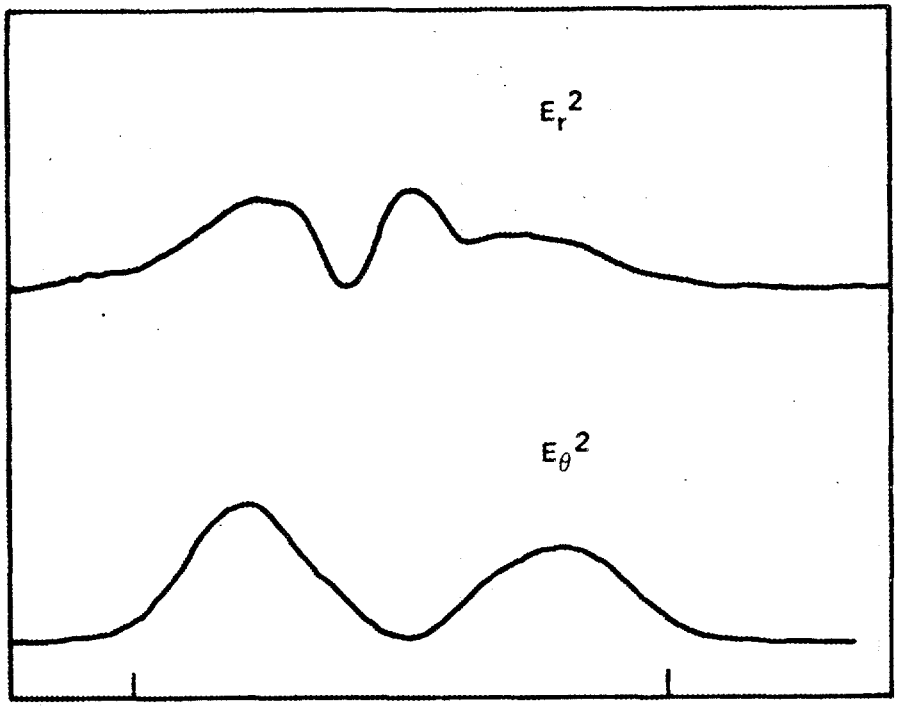

Figure 73. Modal Output After Triple Miter Scan Perpendicular to Gyrotron Axis

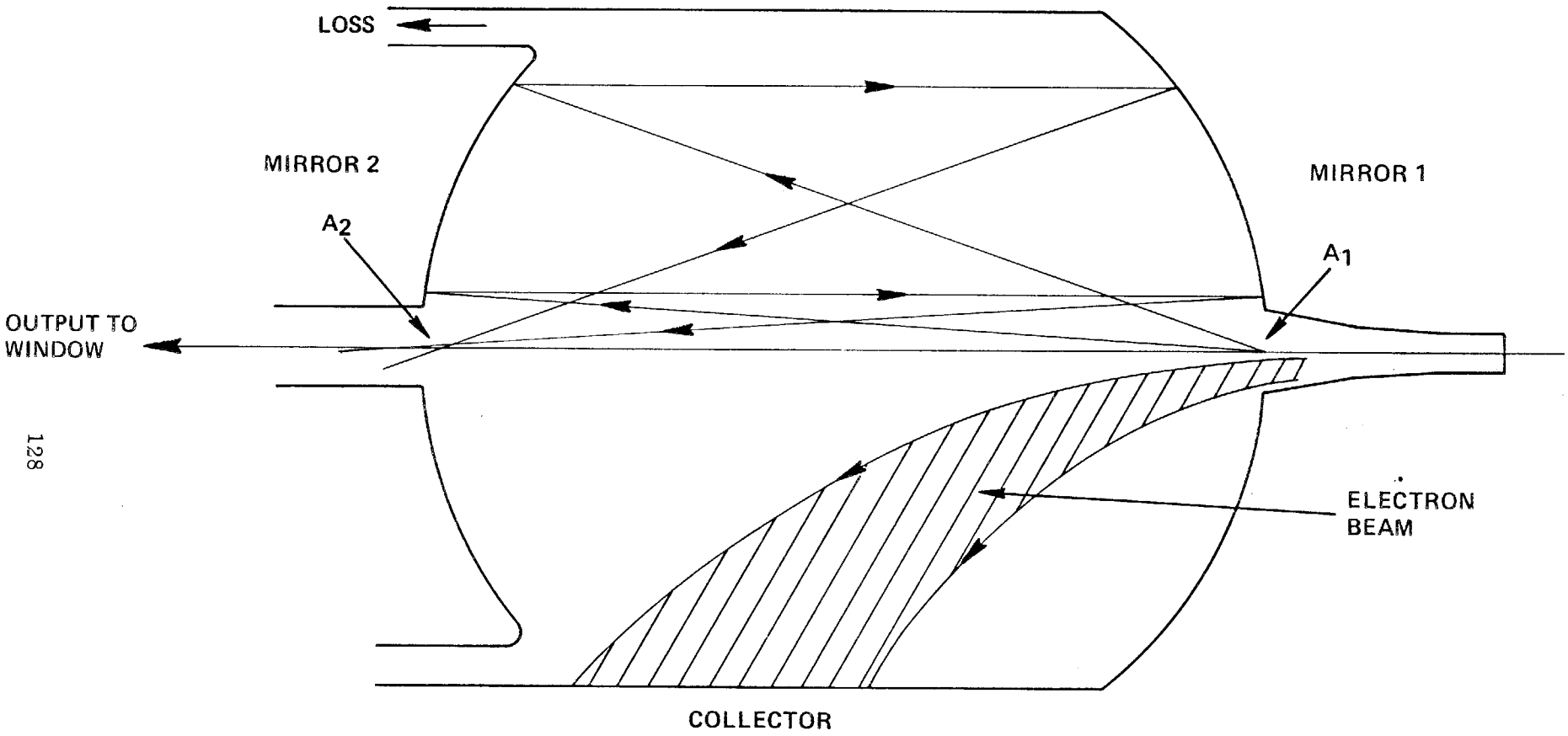

Figure 74. Schematic of Mirror Output (Upper Section Idealized Microwave Path, Lower Section Electron Beam; Both are in Form of Figures of Revolution About Axis)

Since the radiating beam has a hollow core, this may be done with relatively small mirror separation, about 16 inches for a 2.5-inch-diameter aperture at A_1. The reason for minimizing the interruption of the initally incident wave at the second aperture is that the boundary conditions there may result in high order axisymmetric modes. Some of these would be reflected and lost to the output; the remainder would interfere and beat with the wave reflecting from the mirrors. The radius of curvature of a mirror is chosen such that for an effective source at or near A_1, a spherical wave front becomes planar after reflection at mirror 2; i.e., A_1 should be at the focus of a paraboloid mirror 2. For a paraboloid approximated by a spherical surface the radius of curvature is twice the axial distance to A_1. The plane wave then falls on mirror 1, which may have the same radius of curvature as mirror 2, thus producing a spherical wave which converges on the aperture A_2.

The diameter of the mirrors should be such that there is only a small amount of overspill from the initially incident wave since, in general, that too will be lost from the output. "Overspill" and reflection of the incident wave at the aperture will result in trapped modes, which may give rise to undesirable resonances unless they are suitably loaded. The lower half of Figure 74 shows a portion of the intended path of the axisymmetric electron beam. The upper half shows geometrical optical rays through the system. For 12-inch-diameter mirrors with a 32-inch radius of curvature spaced 16 inches apart, the path difference Δp between an axial ray and one which transits via the periphery of the second mirror is such that $\Delta p/\lambda = 0.149$, measuring to the plane perpendicular to the axis at the intersection of mirror 2 with the axis. The path difference Δp would be zero for parabolic mirrors. The maximum difference in axial position between the ideal paraboloid and the sperical surface is only 5 mil at the circumference. At a 5-inch radius, it is only 2.4 mil. In the case of the TE_{01} mode, only a few percent of the power lies outside the 5-inch radius. Thus, the spherical approximation seems justified. Purely from output circuit considerations, the TE_{02} mode is less desirable than the TE_{01} because of its increased divergence for a given aperture A_1 and for a given incident interruption at A_2. In fact, the central lobe of the TE_{02} mode diverges in a very similar fashion to the <u>complete</u> TE_{01} beam. Thus, for the

TE_{02} mode, larger diameter mirrors become necessary. These would then require closer parabolic form.

Figure 75 shows the locus of the maxima and minima of E_Θ^2 as a function of axial distance from the aperture for the TE_{01} mode. For reference, a 12-inch-diameter mirror subtends a semi-vertical angle of 20.56° at the 16 inch distant focal point. Figures 75 and 76 were obtained as the result of a series of scans made perpendicular to the axis of the 2.5-inch-diameter aperture in a 12-inch-diameter mirror fed by a 0.62-inch-diameter circular guide and a taper section. Some higher-order mode fields were detected, particularly TE_{02}. The presence of these modes influenced the details of the distribution. In addition, if higher-order modes were present, a short section of circular guide between the taper and mirror would change the relative phase at the aperture. Therefore, the field distribution would also be changed. Figure 76 shows E_Θ^2 distributions at selected planes.

A TE_{011} cavity whose diameter corresponded to the inner modal surface of the TE_{02} cavity was also excited and used to feed the mirror system. The effect of the system on the cavity frequency response curve was examined, particularly as a function of the second mirror position. As the second mirror was moved axially over a half wavelength, the response curve is changed as indicated in Figure 77. Note that a change in separation of 30 mils may produce a marked change in the response. A series of Q measurements was made for mirrors separated by a distance corresponding to that of the upper and lower curves of Figure 77 and for other separations of a half-wavelength increment. A minimum Q, corresponding to minimum coupling back to the cavity, was obtained at a mirror separation of the focal distance, Figure 78. The resolution of the measurement was the half-wavelength step. Unsurprisingly, this mirror separation was also found to be optimum from the point of view of mode purity at the output guide aperture of the second mirror.

Figure 79 shows the $(E_\Theta)^2$ and $(E_r)^2$ fields measured at the mouth of the output guide. Note that in none of these particular experiments was the cylindrical collector simulated. The effect of such a simulation is to

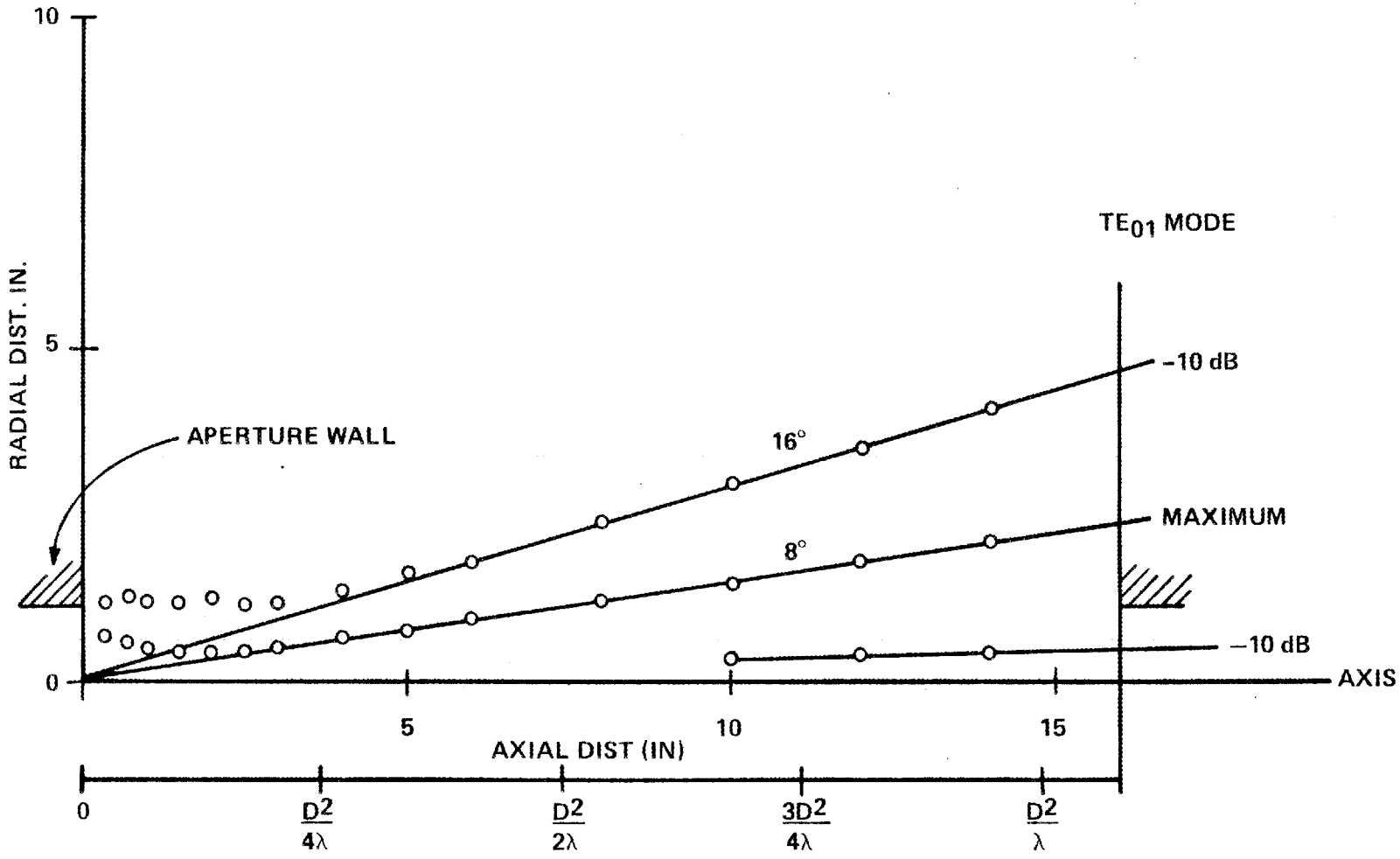

Figure 75. Radiation Pattern from 2.5-inch Diameter Aperture, TE_{01} Mode

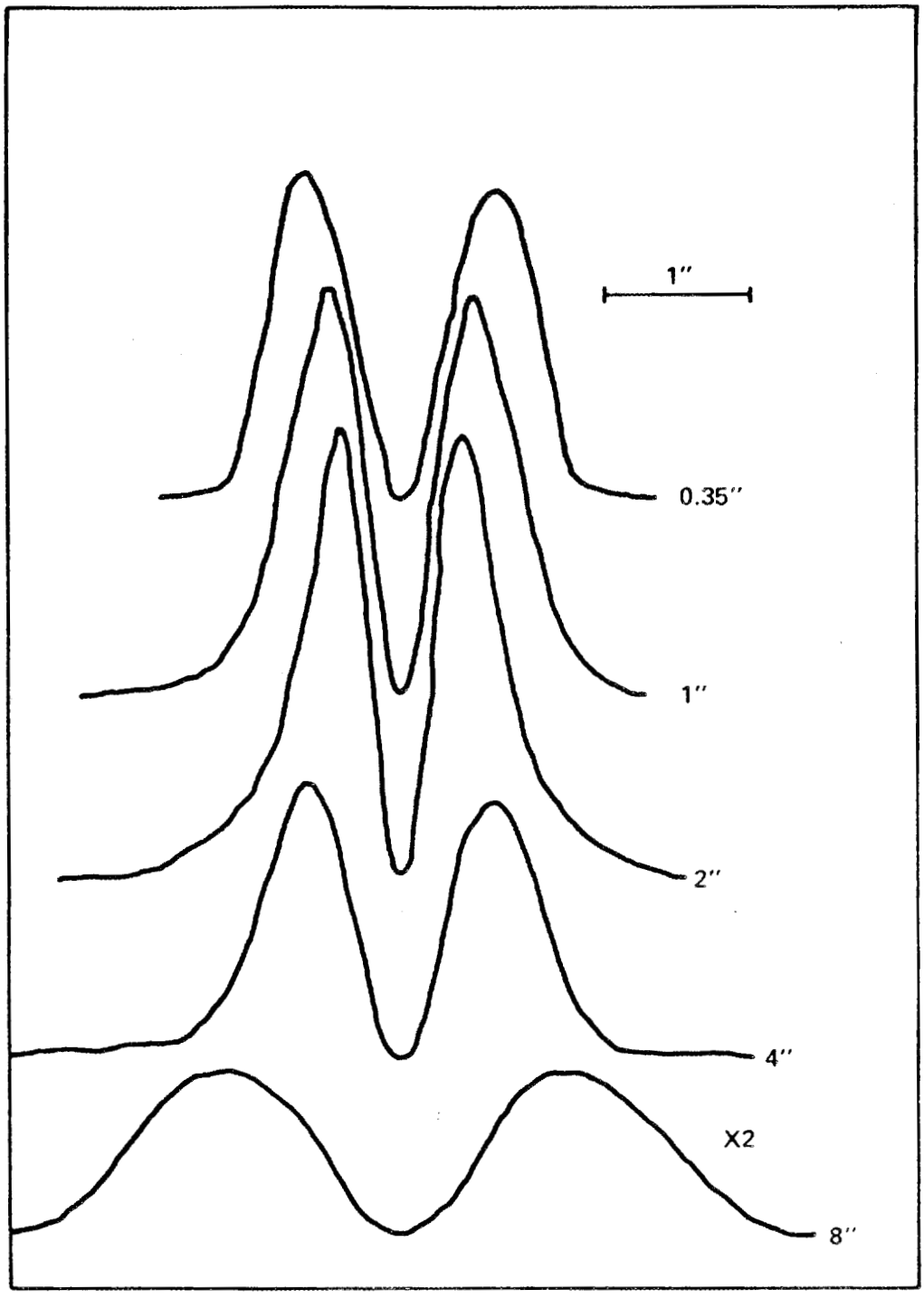

Figure 76. E_θ^2 Perpendicular to and Across the Axis of the Aperture as a Function of Distance from the Aperture

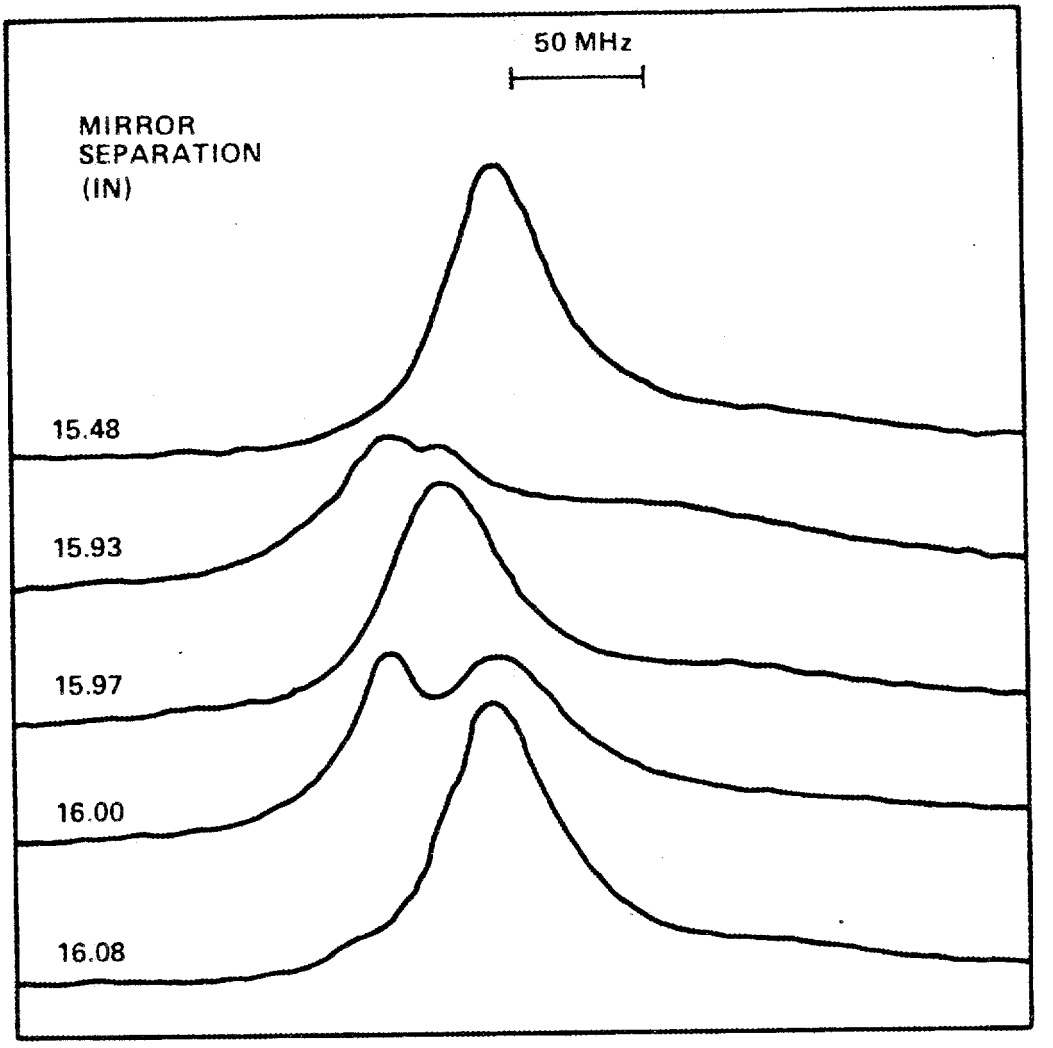

Figure 77. Cavity Resonance Curve as a Function of Mirror Separation, TE_{01} Mode

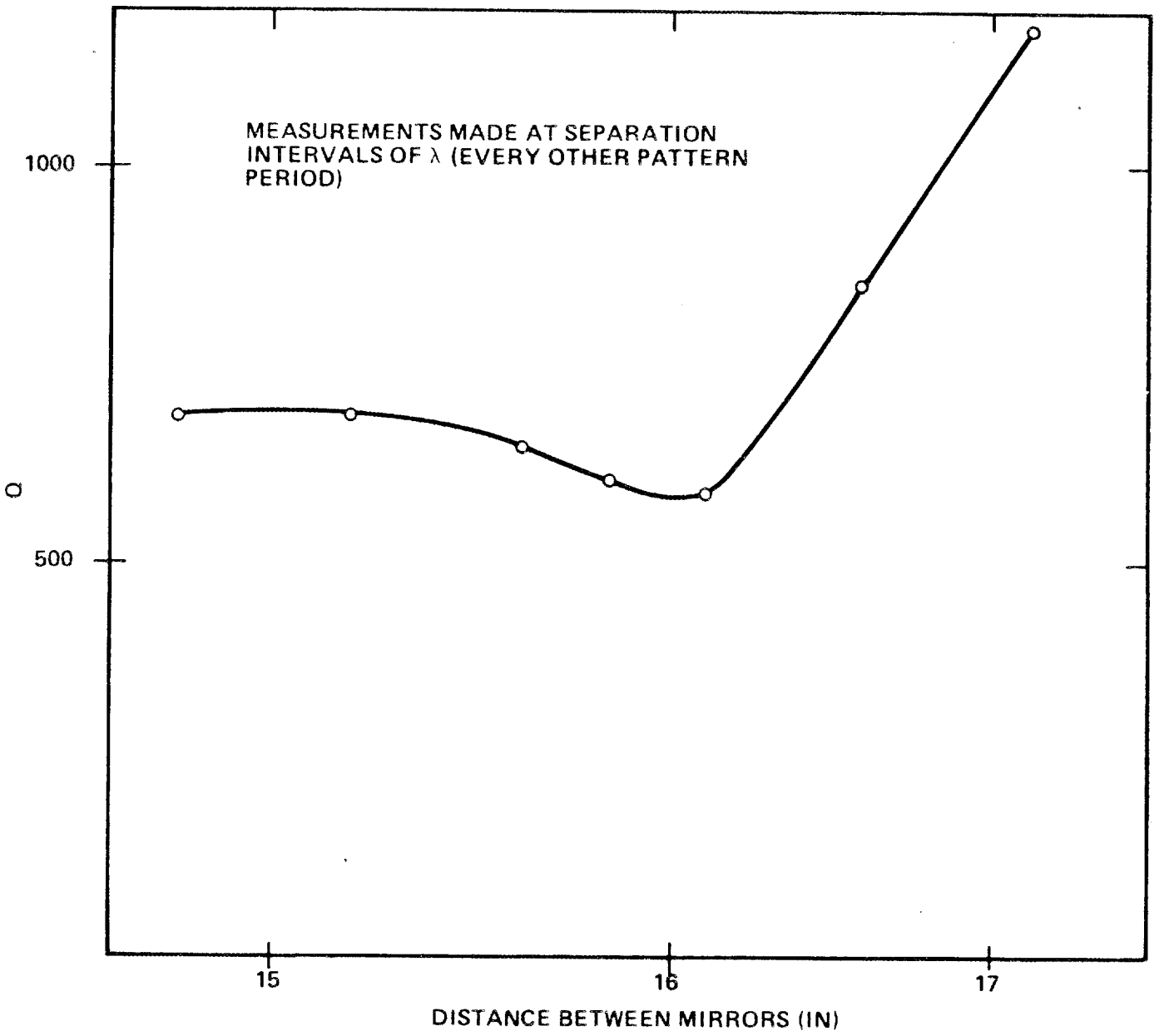

Figure 78. Q as a Function of Mirror Separation

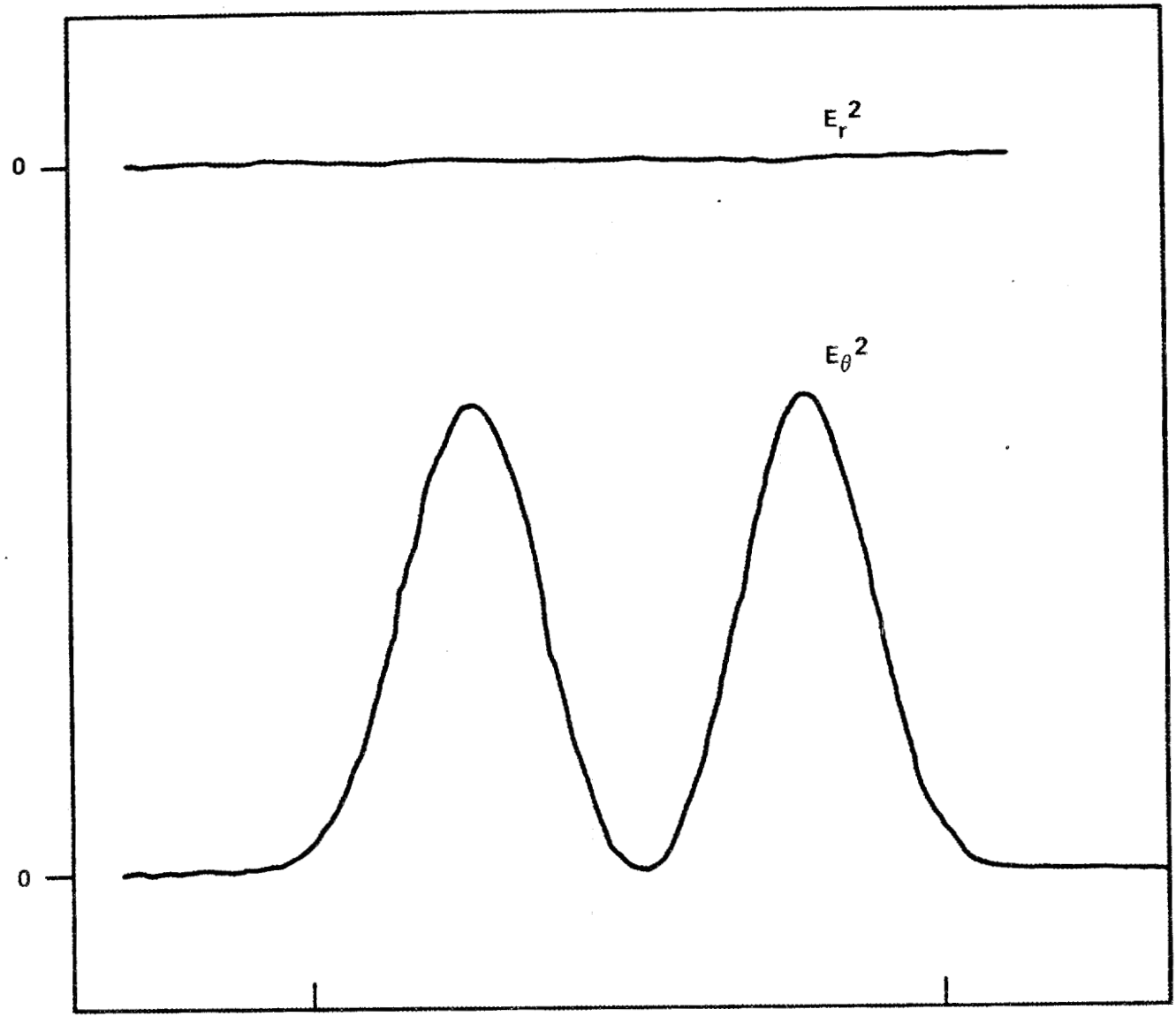

Figure 79. Output from 2.5-inch Diameter Guide After Reflection Through Mirrors

produce a spiked response because of trapped modes. As was found at ORNL, a gap of 1/2 inch between the cylinder and a mirror caused sufficient loss in these modes to reduce them to a possibly tolerable level. In practice, this might be accomplished by a large diameter ceramic window and a water load.

It is of interest to note that the addition of a single miter in the 2.5-inch-diameter output guide produced an undetectable effect on the resonance curve but modified the fields at the output of the miter to those shown in Figure 80. This is consistent with our expectation that the mode conversion excites predominantly forward propagating modes.

Most of the measurements discussed above apply to the TE_{01} mode. TE_{02} operation requires the use of larger diameter (15 inches) parabolic mirrors, the second of which must be water cooled because of electron beam collection. A separation of 16 inches and a focal length of 32 inches should result in a 3% or 4% loss or mode conversion due to the direct path at the second aperture and an estimated 5% to 10% loss at the periphery. Further, a similar loss or conversion would be expected in coupling back into the output guide. Alignment and proper separation are critical. The separation must be set to about 1/2 mm, tilt must be less than about 0.1°. The former primarily affects cavity response when the mirrors are close to their optimum separation. The latter is evidenced by increased mode conversion and transmission loss. The preceding tolerance statements are estimates based on measurements such as those of Figure 80. Obtaining and holding such close dimensional tolerances would require careful consideration of collector thermal distribution during tube operation. Changes in collector temperature would have a noticeable effect on rf power output unless mirror separation were made thermally independent.

Further work on spherical mirrors was deferred at this point in the program, while studies of straight through collector systems were undertaken. Careful evaluation of the spherical mirror system suggested that while dimensional constraints were probably tolerable in laboratory cold test experiments, they would likely be extremely difficult to maintain in practical tubes.

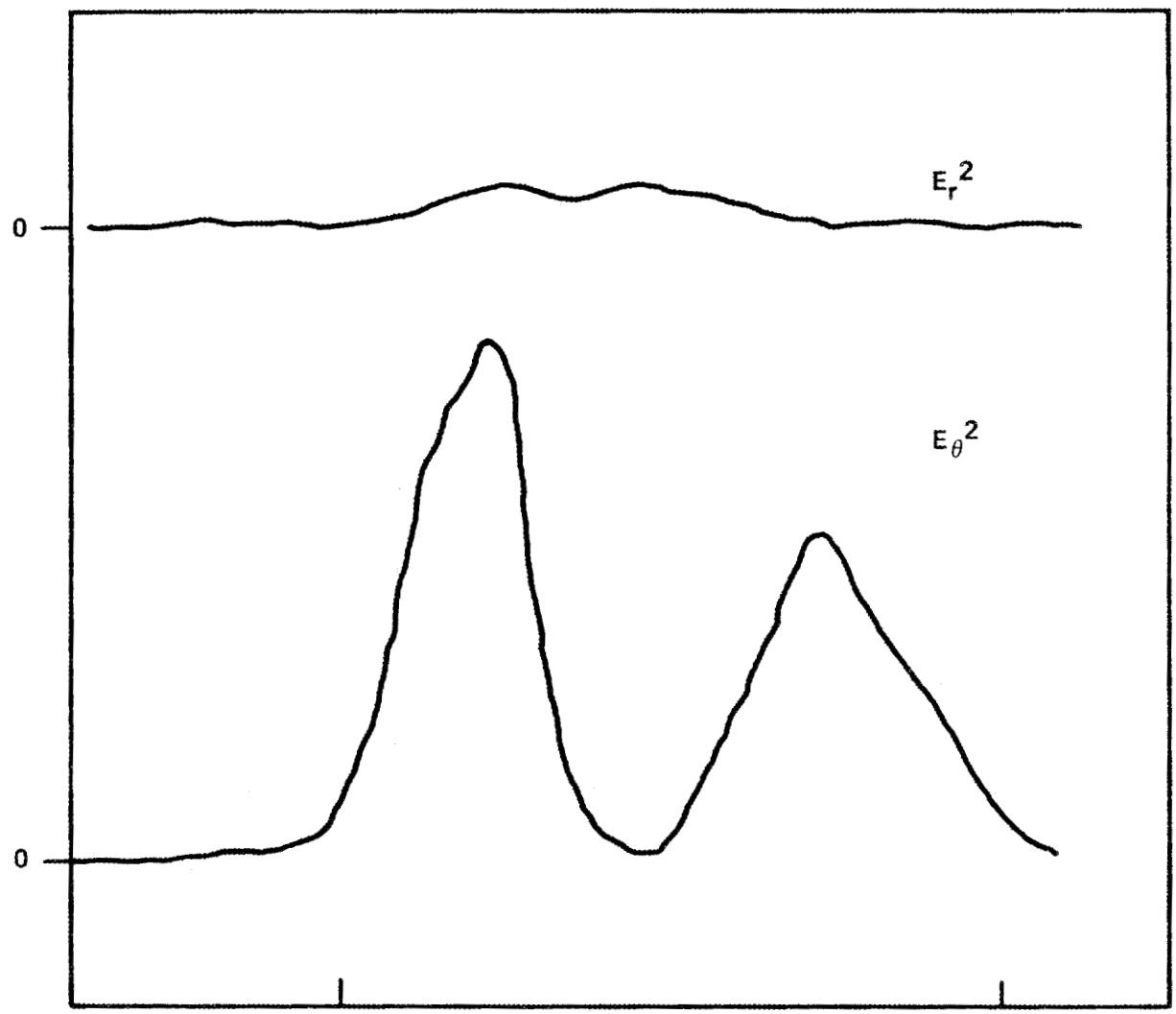

Figure 80. Effect on Output of a Single Miter Bend Following a Mirror System

3. Straight Through Collector

The straight through collector output coupling system, as the name suggests, treats the collector as an element of the overall microwave output system. Suitable tapers are employed between differing component diameters. The name "axisymmetric output" came to be applied to this type of output coupling system. Tubes incorporating it came to be known as "axisymmetric" models. Three possible arrangements of collector, window, and output waveguide were considered. The differences among them concerned component diameters. Table 24 identifies these areas of interest and indicates the report subsection in which each is discussed.

TABLE 24

Straight Through Collectors

Report Subsection	Collector Diameter	Window Diameter	Output Diameter
a.	5.0"	5.0"	5.0"
b.	2.5"	2.5"	2.5"
c.	5.0"	2.5"	2.5"

It was recognized, or at least suspected, at the outset that the 5-inch window diameter of Subsection a. would likely prove to be too large, that the 2.5-inch collector diameter of Subsection b. would probably be too small, and that the arrangement of Subsection c. probably represented the best compromise. Nevertheless each of the three designs was pursued closely to determine electrical and mechanical limitations.

a) Collector, Window, and Output All 5-inch Diameter: A paper design for this type of collector/output is shown schematically in Figure 81. An 8 degree taper is used between the TE_{021} oscillator cavity and the 5-inch-diameter collector. Beam trajectory calculations showed that the addition of a short magnet coil would shift the maximum of the beam power density to the region of the junction of the taper and cylinder. The beam would thus be spread over a larger area, reducing power density at the wall by at least a factor of about two compared to a 2.5-inch diameter. A

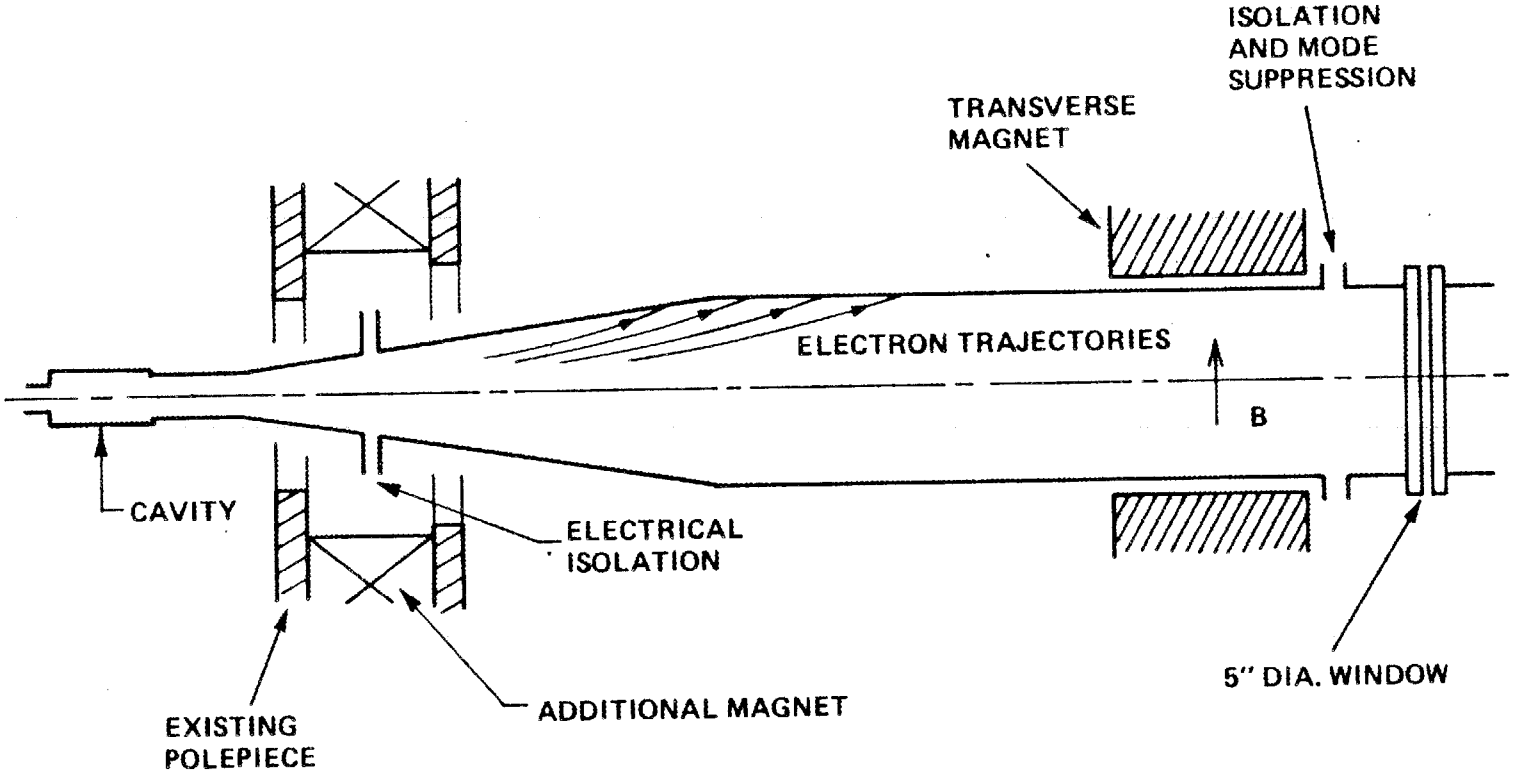

Figure 81. 5-inch-Diameter Collector, Window, and Output Guide

transverse magnet provided a field greater than 300 gauss to protect the window from electron bombardment. The length of the output section from the top of the existing pole piece to the window was 40 inches. A paper design was also completed for a double FC-75 face-cooled 5-inch-diameter window. The thickness of each of the 5-inch-diameter windows had to be increased to at least one guide wavelength to enable the windows to withstand the atmospheric and coolant pressures. The increased window thickness would lead to proportionately larger microwave power loss. With respect to thermal conductivity to the face, the larger power loss, because of the increased thickness, are more than offset by an increased area available for face cooling. The obvious advantage of this approach would be the large collector diameter, which would make beam spreading less critical. The window would have increased power loss but reduced coolant interface power density. The 5-inch output guide could be used, but there would clearly be practical inconveniences and difficulties because of the large size. Overall, the approach did not appear to be optimum.

b) Collector, Window, and Output All 2.5-inch Diameter: Obvious advantages of this type of design are the elimination of the down taper and freedom from the mode density inherent with a large diameter collector. However, design of a 2.5-inch-diameter collector is critically dependent upon electron beam control. Knowing cathode magnetic flux, magnetic field, and interaction region electron velocity components; one may show that adequate magnetic flux is available at the collector for beam control. The electron beam expands adiabatically into the collector if reduction of the magnetic field is suitably gradual.

In the interaction region, the maximum space-charge force associated with the dc beam is less than 0.4% of the magnetic force. At the collector wall, the space-charge force on the outer electrons increases to about 10% of the radial magnetic force. This means that for a real beam, outer electrons will be interceped by the collector earlier than they would be with zero space-charge. Inner electrons would arrive at the collector at points closer to space-charge-free calculated values. Thus, the effect of

space-charge is to give a modest reduction in the power density at the collector wall. Calculations based on space-charge-free conditions are conservative.

Trajectory calculations were carried out in the collector region using analytic magnetic fields that could be syntheszied by long low-power solenoids. The fields had the form $B_z = a/(b + Z)$, where a and b are constants.

Figure 82 shows the interception of inner trajectories at the collector wall. Nine equispaced electrons were introduced around a circular cross section of a cycloidal orbit. Their transverse and axial energies corresponded to the magnetic field at the plane of introduction. Similar trajectories for outer electrons are intecepted in a shorter distance translated by about 6 inches towards the cavity. The current density at the collector may be determined from the summation of such sets of trajectories. This takes the form shown in Figure 83. The magnetic field for this case is shown in Figure 84. Note that the maximum dc condition power density into the collector would be ~1 kW/cm^2. Collector power density distributions were estimated for a variety of operational modes. In all cases, the maximum power density was less than 1.25 kW/cm^2. To prevent excessive movement of the beam in the collector as the gun coil currents were adjusted, it was planned to program the collector magnet such that collector magnet current $I_c \propto 9 + I_{G1}$, where I_{G1} is the current of gun coil No. 1.

The complete collector is shown in Figure 85. A 3.5° taper extends from the oscillator cavity to the 2.5-inch diameter. This is followed by an insulated gap, which enables body current measurement and acts as a mode suppressor for TE_{on} modes. The collector is cooled by 36, 0.187-inch-diameter cylindrical channels with a water flow of 200 gpm at a pressure head of 180 psi. A transverse magnetic field of greater than 600 gauss provides a barrier for high energy secondary electrons. The window would be mounted in line so that external mode suppression (external to the vacuum tube) could be provided between the window and the first miter bend of the output waveguide. Mode conversion from the TE_{02} to other circular-electric modes would be less than 5% on a power basis.

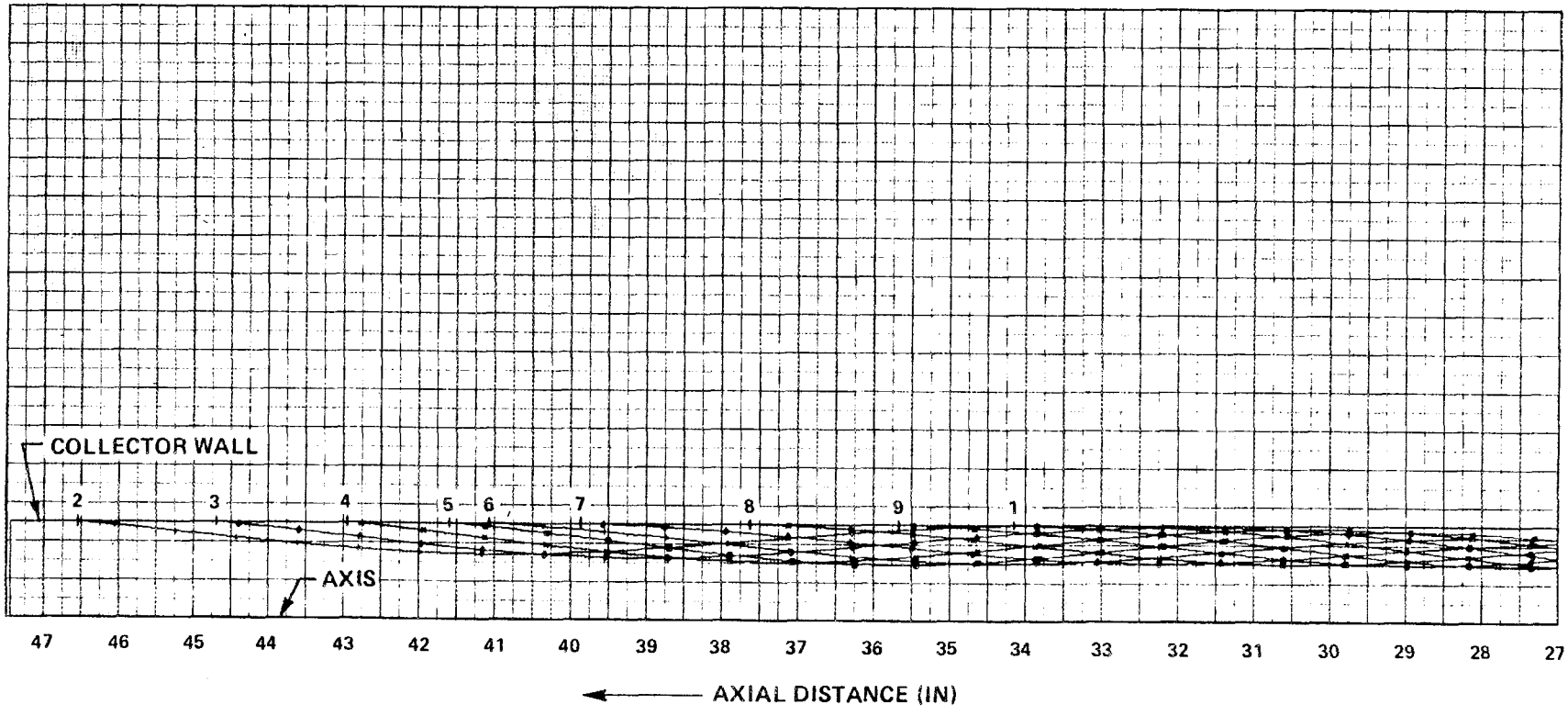

Figure 82. Distribution at 2.5-inch Diameter Collector Wall of Electrons from Front of Cathode

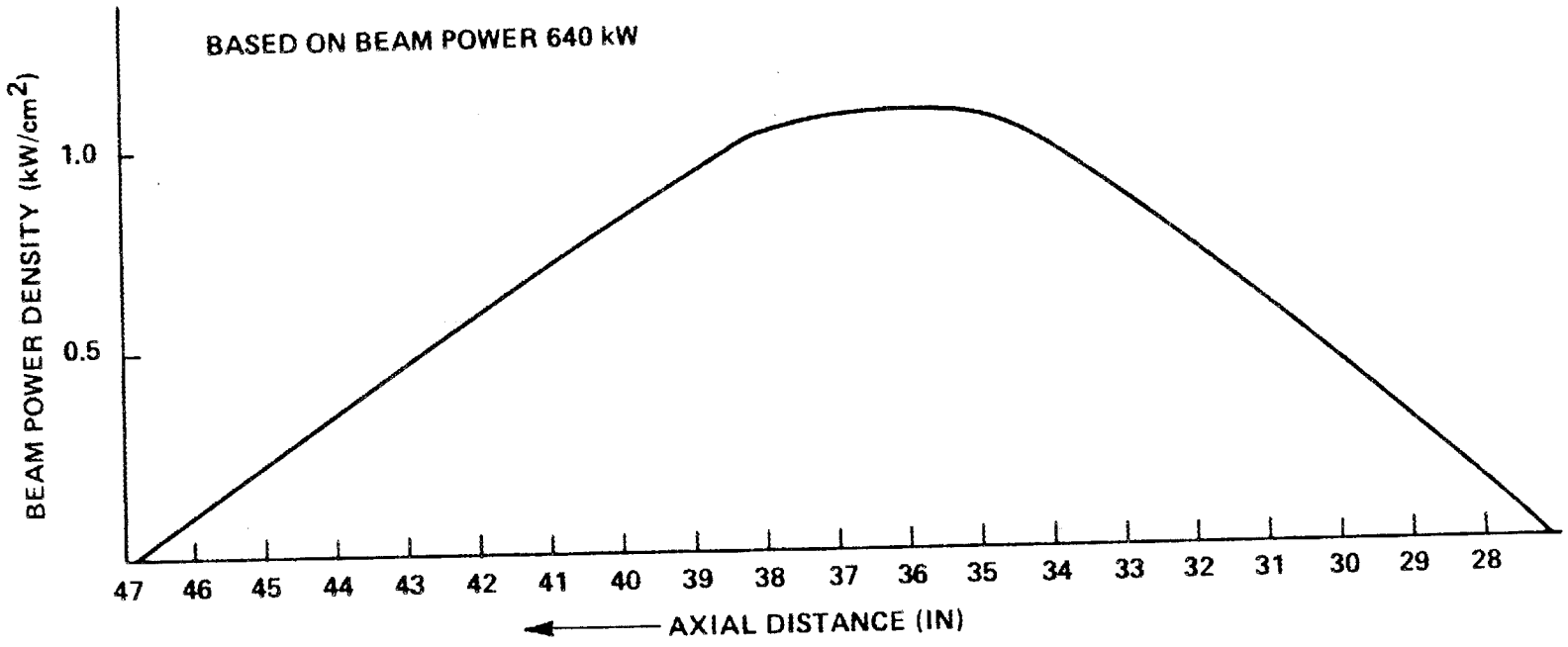

Figure 83. DC Beam Power Density as Function of Distance Along Collector

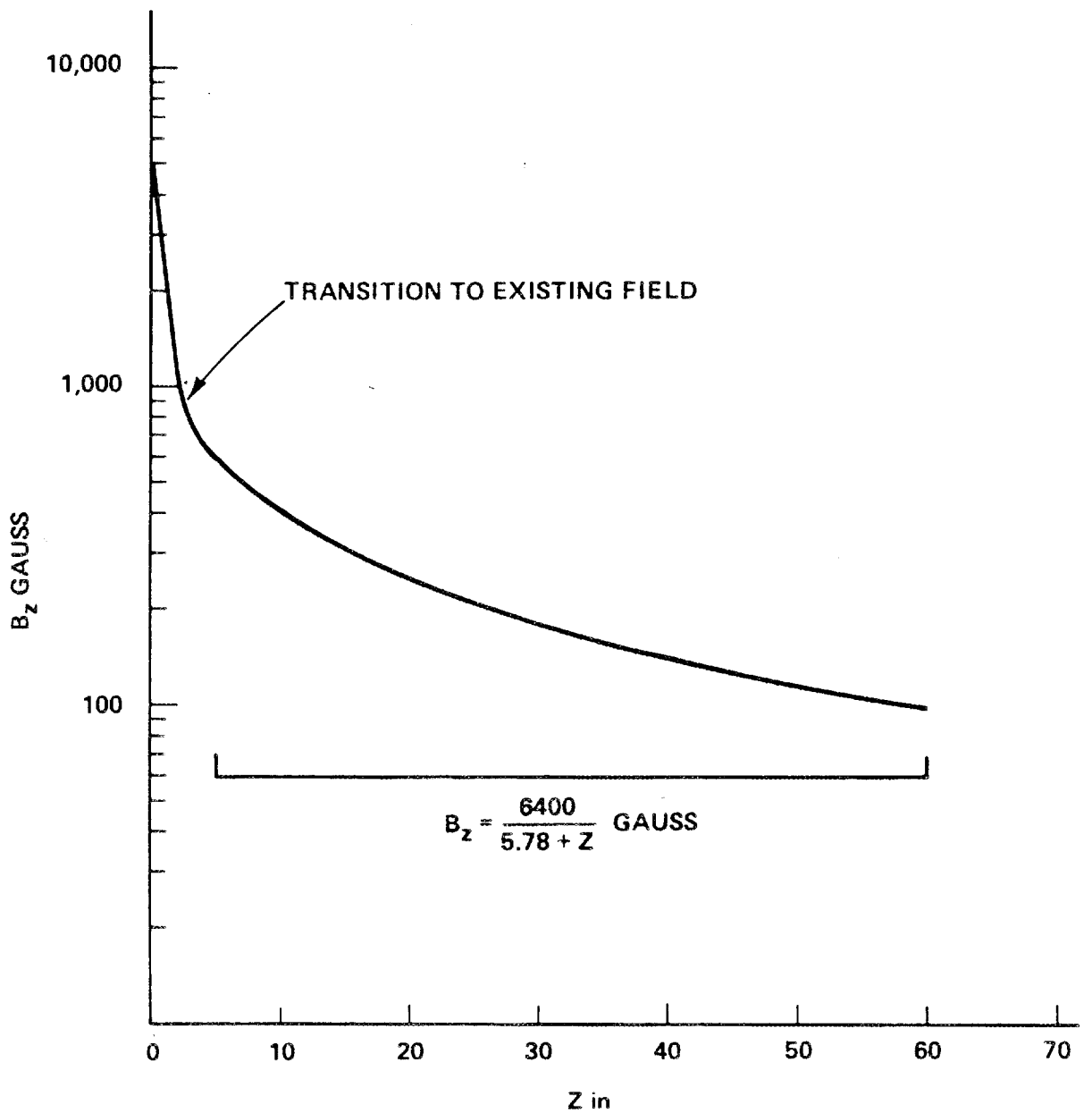

Figure 84. Magnetic Field for Trajectories of Figure 83

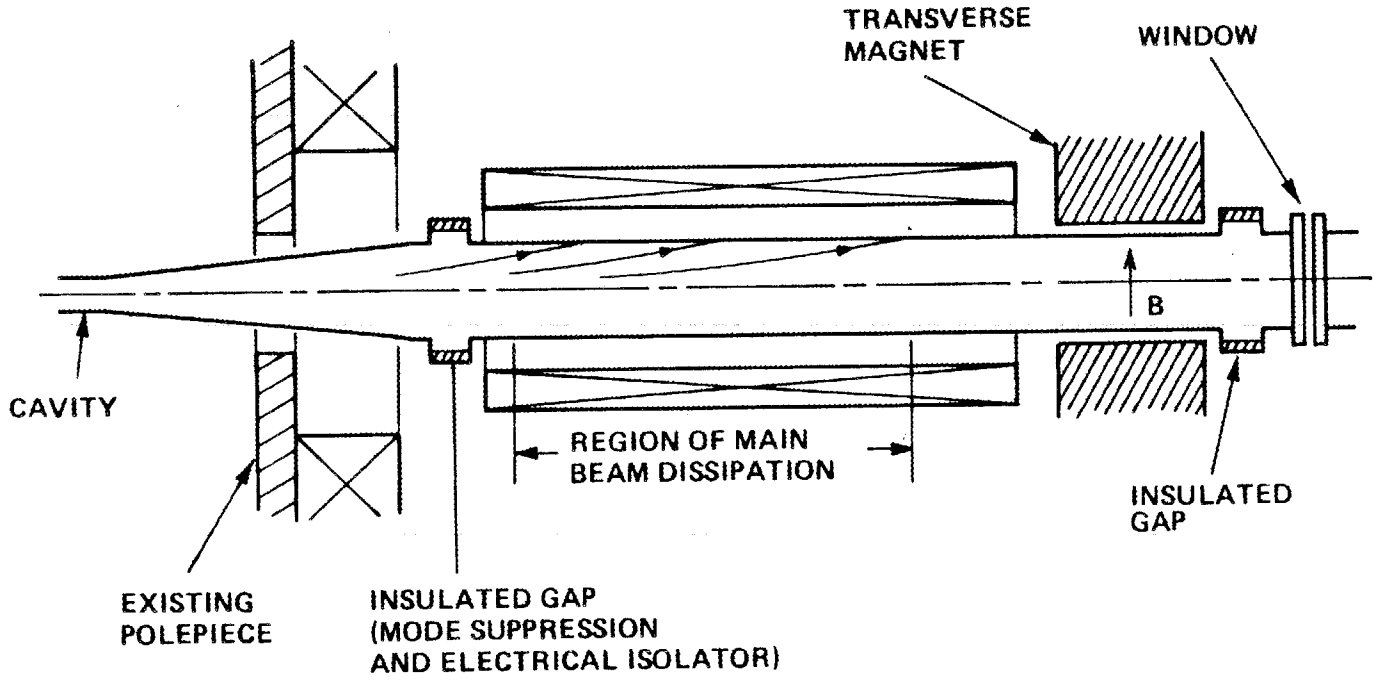

Figure 85. 2.5-inch Diameter Collector, Window, and Output Guide

Estimates were made of the required tolerances on collector alignment with the beam containing flux tubes. These were practical. However, the recent examination of minor beam damage in a 10-inch-diameter collector indicates considerable lack of axial symmetry in the guiding flux tubes of the main magnet at ORNL. While detailed calculations have not been made for such an asymmetry in the 2.5-inch-diameter collector, it is clearly undesirable and must be greatly reduced to make this approach practicable.

c) Collector 5 inch; Window and Output 2.5-inch-diameter: With appropriate magnetic field distribution the 5-inch-diameter collector allows a maximum electron beam dissipation under 1 kW per square centimeter. Further, the design leads to readily achievable tolerances acceptable with respect to both dissipation and dimensional effects on the oscillator cavity resonance.

The design is illustrated in Figure 86. A smooth taper extends from the cavity to the 5-inch-diameter guide, which becomes the collector. Prior to the collector region, there is an annular gap bound by a ceramic window and a water load. This provides selective suppression of both non-axisymmetric modes and, to a degree, of higher-order axisymmetric modes, allowing the lower-order axisymmetric TE modes to pass with negligible loss. The mode suppressor also provides electrical isolation of the collector. The dissipation region of the collector is beyond. It extends from about 6 inches from the suppressor to halfway down the far taper. This taper is the same as the entrance taper. A transverse magnetic field exists at the 2.5-inch-diameter guide, extending over a 6 inch length of the waveguide to act as a barrier for secondary electrons produced at the collector wall. Then follows an insulated gap serving primarily to electrically isolate the window from the collector. The window uses two ceramic discs with facing surfaces cooled by FC-75. The structures similar to the window are described in Section IV-F. Because of the axial symmetry of the system and the reduced mode conversion, the maximum power density at the window for a given power output should be less than that in early CW tubes. The power coupled out radially from the window into the FC-75/water load should also be less.

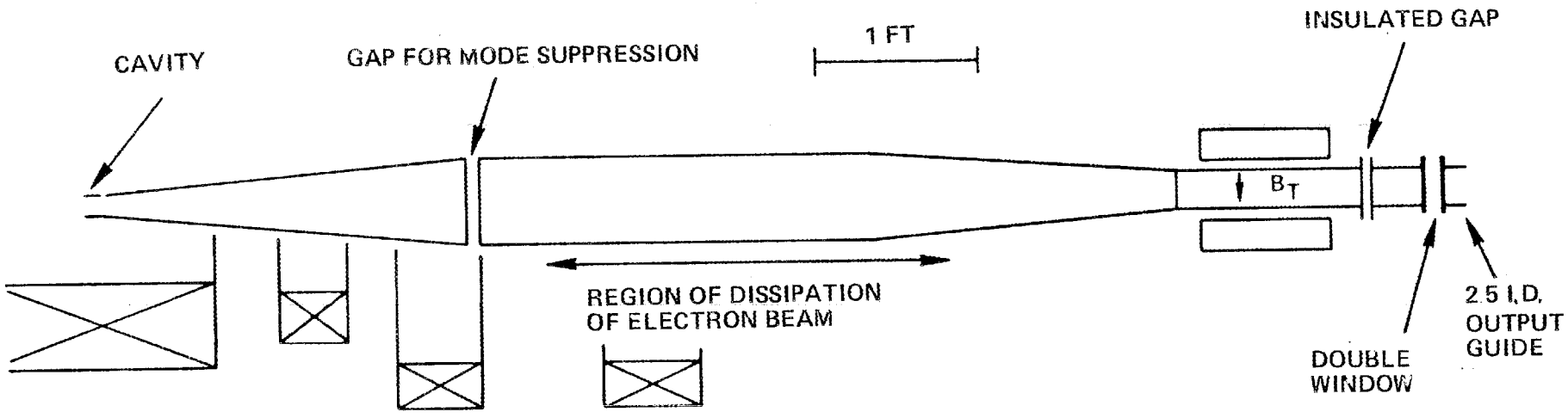

Figure 86. Collector/Output Circuit

The tapers are designed for less than 25% mode conversion. Less than 1% is converted into higher-order axisymmetric modes which could be trapped between the tapers. At 28 GHz, all TE_{on} modes, up to and including TE_{05}, are transmitted by the 2.5-inch output guide. It is important, therefore, that coupling to the TE_{06} and higher modes is kept as small as possible. An approximate calculation indicates that the conversion to the TE_{06} mode is less than -30 dB. The effect of the gap on this mode could produce an attenuation of -0.25 dB, thus a relative insertion loss of -0.5 dB. This would amount to ~10% power loss in the TE_{02} mode, if the resonant condition were satisfied for the TE_{06} mode in the region between the two tapers[5]. With conversion to TE_{06} less than -40 dB, power loss in the TE_{02} mode would be under 2%. The actual conversion to TE_{06} lies between -30 dB and -40 dB; thus, one might expect power loss to the TE_{02} in the range of 10% to 2%. The conversion to higher-order axisymmetric modes is negligible, and while precautions must be taken to minimize conversion to non-axisymmetric modes by maintaining good axial alignment in the collector, any small conversion that does occur is prevented from reaching a seriously resonant and lossy condition by the attenuation of the annular gap.

The system shown in Figure 85, constructed of aluminum for cold testing, was exited from a cavity operating in the TE_{021} mode. The cavity resonance and the power at the exit of the 2.5-inch-diameter guide were monitored. The cavity resonance was examined first with the cylindrical collector section and second taper removed. The later sections were then added and found to produce negligible effect on the resonance curve, provided that a small (~1/4") gap was maintained at the location of the proposed mode filter. Moreover, the resonance curve was insensitive to longitudinal translation of the cylinder and second taper and to tilt and radial displacement considerably greater than that which would occur in a complete tube. With the gap closed, some high Q resonances were observed in the cavity resonance curve with dips on the order of 5%. These resonances were more pronounced in the transmitted power. With the gap again opened, the transmitted power then showed resonant dips of less than 3%. The

addition of a double window containing FC-75 and water in the proper compartments and tubes, had negligible effect on the relative amplitude of the dips.

This situation was markedly changed, however, when a 2.5-inch miter bend was added to the 2.5-inch waveguide after the second taper. It was then found that ~25% dips in the resonance curve and almost 100% dips in the transmitted curve could be obtained due to strong reflection and mode resonances for which the collector walls and gap produced insufficient attenuation. A mode filter of alternating SiC-BeO and copper rings placed between the 2.5-inch guide and the miter bend smoothed both the cavity resonance curve and the transmission curve to variations of less than 3% and 6%, respectively. Initially, it had been planned to place the window after the miter for added isolation from collector secondary electrons. The desirability of placing additional mode filtering between the miter bend and the tube strongly suggested that the window should be placed in line with the tube so that the mode filter need not be part of the tube and, therefore, not subject to vacuum and initial tube processing.

To increase the isolation from secondary electrons of the window positioned on axis, the length of the region over which the transverse field was applied was increased threefold over that in previous pulsed tubes. Thus, a transverse field of 500 gauss was provided over a 6-inch length.

The goal of trajectory calculations was to determine a magnetic field configuration that would spread the dc beam into the collector in such a manner that the maximum power density would be less than 1 kW/cm^2. A satisfactory distribution was ascertained by first expanding the beam adiabatically to a point three quarters of the distance along the first taper and then removing the field more drastically, at the same time maintaining flux in the collector at roughly the same magnitude as that threading the front of the gun. The actual field over the cylindrical portion of the collector varied from 50 gauss to 30 gauss. Further calculations were aimed at determining if the extent of the field could be reduced somewhat without serious effect on the extent of the distribution.

As in previous designs, the maximum pressure of the cooling water and, therefore, maximum dissipation capability is at the gun end of the collector where maximum power density occurs. A water flow rate of 350 gpm with a maximum pressure of 180 psi is indicated for collector cooling.

H. VFA-8000-A3 MODE FILTER

The VFA-8000-A3 mode filter was developed during the program to provide a means of selectively attenuating non-circular modes in a waveguide. The filter has 2.5-inch inner diameter, it mates directly to the waveguide flanges. Attenuation is provided through use of eleven concentric slots at the inner conductor wall. These open to a ceramic cylinder and through to circulating cooling water, which provides dissipation. Table 25 lists important characteristics of the filter.

TABLE 25

Characteristics of VFA-8000-A3 Mode Filter

Attenuation:	Non-circular Modes	4 - 6 dB
	Circular Modes	.3 - .5 %
Power:	Mode Dissipation	50 kW
	Flow Through	>200 kW
Cooling:	Water Flow	5 GPM
	Pressure Drop	120 PSI
	Temperature ΔT	$9^{\circ}C$

Figure 87 is a photograph of the VGA-8000-A3 mode filter.

I. TRIPLE MITER BEND MODELS

Triple meter bend models incorporated output coupling systems introduced immediately following the oscillator cavity output iris, prior to the collector. Typically, three waveguide miter bends were used in routing microwave power to the outside. Six models of this type were built, VGA-8000 s/N's 1, 2, 3, 4, 7 and 12.

Figure 87. VFA-8000-A3 Mode Filter

The identifying serial number of a model was modified whenever a change or repair requiring rebuild was introduced. A tube identification, therefore, might go through a series of changes such as those following:

VGA-8000 S/N 1	Initial Construction
VGA-8000 S/N 1R	First Rebuild
VGA-8000 S/N 1R2	Second Rebuild

and so on.

Preliminary testing of tube models was frequently accomplished using pulse techniques. CW tests followed once basic tube characteristics were established. The practice is common in test of experimental microwave tubes.

1. VGA-8000 S/N 1

Tube S/N 1 was rebuilt three times following initial construction, each change was the result of the need for modification or repair. The final version of the model still did not meet rf expectations, although dc behavior was adequate. The tube was shipped to the customer for use in checking mechanical and electrical compatibility with the system.

a. S/N 1, Initial Results

Initial testing was limited to pulsed operation. A peak output power of 145 kw was achieved. Early testing was hampered by high voltage breakdown problems outside the vacuum envelope. Peak rf output was apparently limited by undesired modes interfering with the main cavity resonance. Average power performance was limited by rf heating of the VacIon (VacIon® is a Varian Associates, Inc., trademark for an ion pump.) Pump.

Arcing occurred between the gun anode connector and the gun coil inner support cylinder. This resulted in damage to the upper high voltage ceramic, as shown in Figure 88. Water had been trapped

Figure 88. VGA-8000 S/N 1 Arc Damage after Pulse Operation

inadvertently at the base of the upper high voltage ceramic. A drain hole was added to the corona sleeve to prevent future accumulation of water. To further guard against breakdown, sheets of Teflon, with a dielectric strength greater than that of transformer oil, were added between the gun anode connector and the gun coil case. The tube ceramic was repaired by covering the damaged area with epoxy.

TE_{01} mode oscillations were observed from 28.000 GHz to 28.050 GHz. Peak power output as a function of frequency is shown in Figure 89. The output power curve was discontinuous, with a gap between 28.019 and 28.040 GHz. Under some conditions two closely spaced frequencies occurred during the pulse. Beam parameters varied as a function of intrapulse time. A comparison of the performance for the pulsed CW oscillator and for the earlier pulsed oscillator is given in Table 26. Competing oscillations were detected from 26.804 GHz to 26.847 GHz, from 26.897 GHz to 26.900 GHz, and from 27.145 GHz to 27.180 GHz and at 26.950 GHz.

Operation of the tube at rf duties higher than 1.8% was limited by rf heating of the copper exhaust tubulation pinch-off and VacIon Pump. An attempt was made to water cool these hot spots. Pinch-off cooling was successful. The internal "egg-crate" structure of the VacIon pump could not be cooled. High gas pressure limited rf operation.

Using an oscillation inhibiting magnetic field, beam duty was run up to obtain high duty information. The modulator duty limit was found at 9.6%, 240 pps at 400 μsecs for a flat top pulse. When beam duty was increased to 20%, 510 pps at 390 μsecs, a 45 degree ramp occurred over the last 160 μsecs of the pulse. Peak body current was 30 mA.

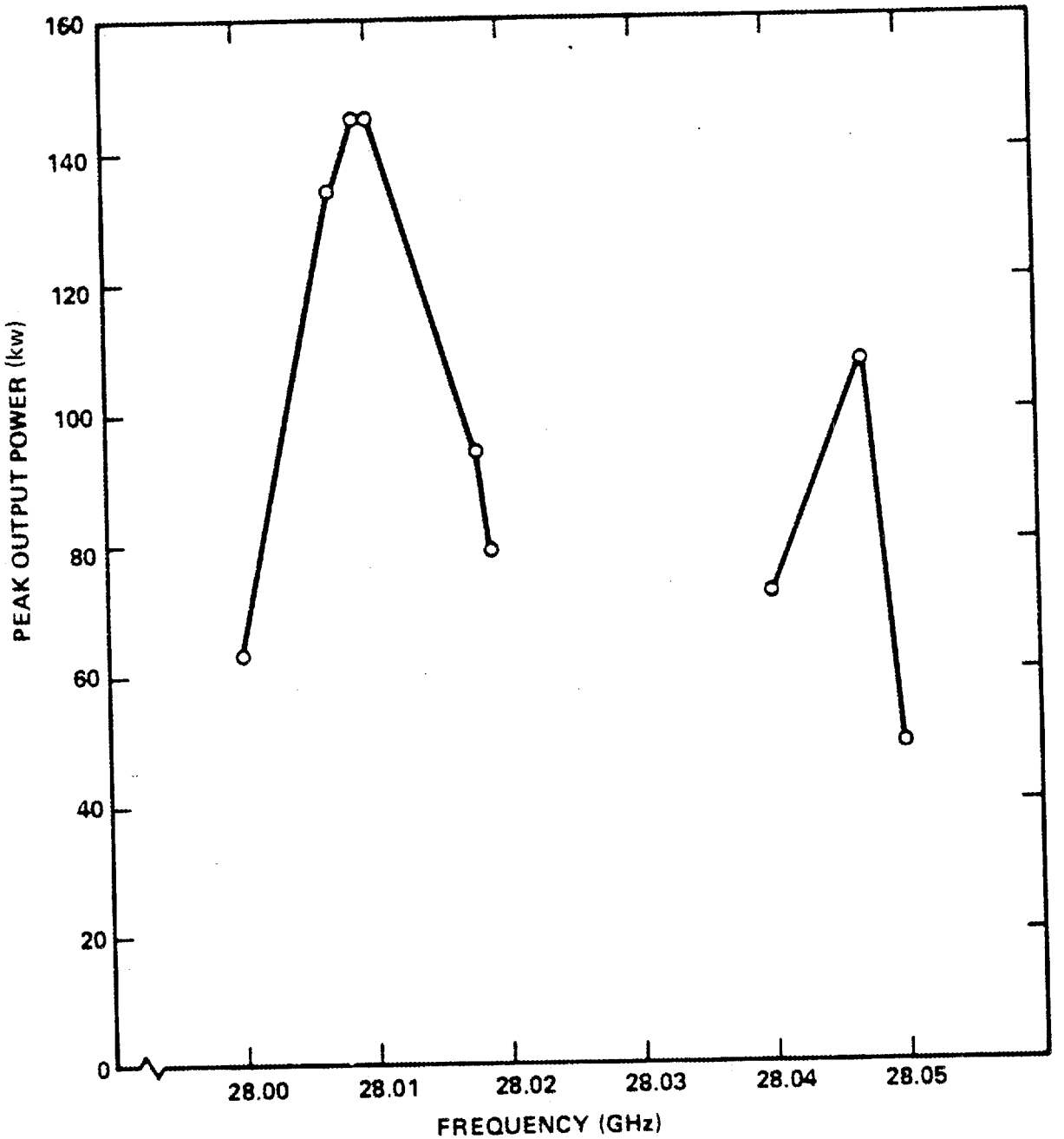

Figure 89. CW Oscillator Peak Output Power as a Function of Frequency
VGA-8000 S/N 1

TABLE 26

Comparison of the First Pulsed CW Oscillator and the First Experimental Pulsed Oscillator Performance

		Experimental Pulsed Oscillator	Pulsed CW Oscillator
Peak Output Power (kw)		248	145
Frequency (GHz)		28.020	28.010
Beam Voltage (kV)		81.5	80.7
Beam Current (a)		8.7	8.8
Efficiency (%)		35	20
Gun Voltage (kv)		23.6	24.3
Magnet Coil Currents (A)			
Main	1	401	394
	2	535	534
	3	511	511
	4	428	425
Gun	1	13.7	12.4
	2	9.5	11.3

b. S/N 1R, Changes and Test Results

Five modifications were made, as listed below:

1. New electron gun ceramics
2. New VacIon pump
3. VacIon pump rf screen
4. Output sleeve rebored to 0.428 inch
5. Addition of 40-60% SiC-BeO ring

The SiC-BeO ring was installed between the collector and the VacIon pump to reduce mode competition with the oscillator cavity resonance.

A peak power output of 168 kw was observed during test, substantially higher than obtained during initial tests, when the model was

not provided with the lossy Sic-BeO ring. Peak output power is shown as a function of frequency in Figure 90. Peak output power and efficiency are shown as functions of peak cathode current in Figure 91. Again, under some conditions closely spaced competing modes were detected across the pulse at 26.742 GHz, 26.858 GHz, 26.865 GHz, and 26.878 GHz.

When average rf power was increased to 11.8 kW, the BeO disc ceramic output window separated at the metalizing on the air side of the window. The output waveguide filled with water. The leak was repaired with epoxy and tests were continued. An average rf power of 19.0 kW was reached momentarily. However, increasing gas pressure prevented taking a complete set of data. The tube was then operated continuously at 18.3 kW average power. At this point, the output window failed showing the Y-shaped crack typical of thermal failure. The tube and waveguide filled with water. Best peak and average power performance of S/N 1R is shown in Table 27.

Flow-pressure data were obtained for the collector and body circuits before tube failure. Collector flow vs pressure drop is shown in Figure 92. Body flow vs pressure drop is shown in Figure 93.

Upon disassembly, minor damage was noted on one edge of the beam hole in the first miter bend of the output guide system, apparently caused by beam interception. The inner surface of the collector showed slight indications of oxidation. In other respects, tube condition was fairly good.

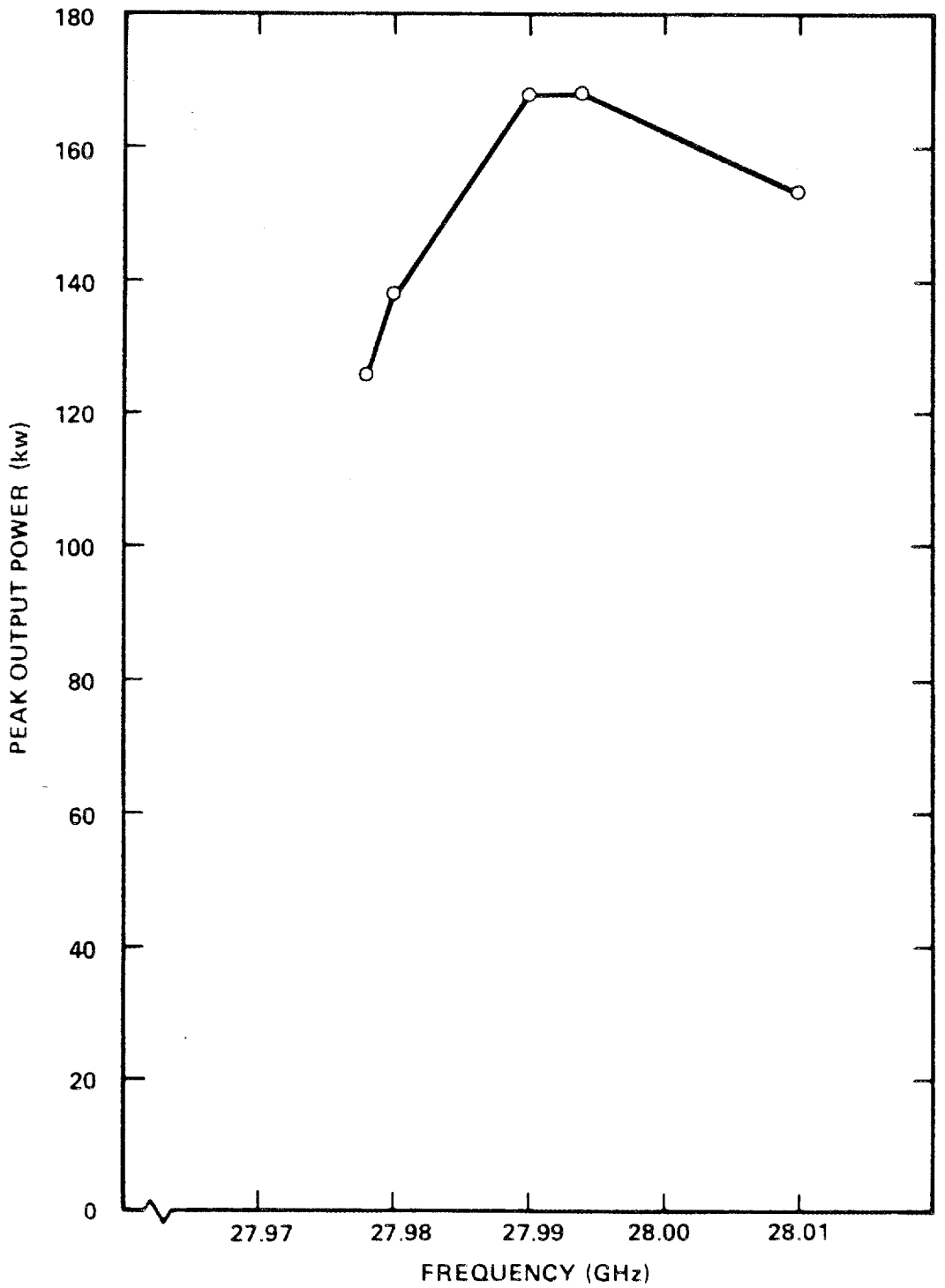

Figure 90. CW Oscillator Peak Output Power as a Function of Frequency VGA-8000 S/N 1R

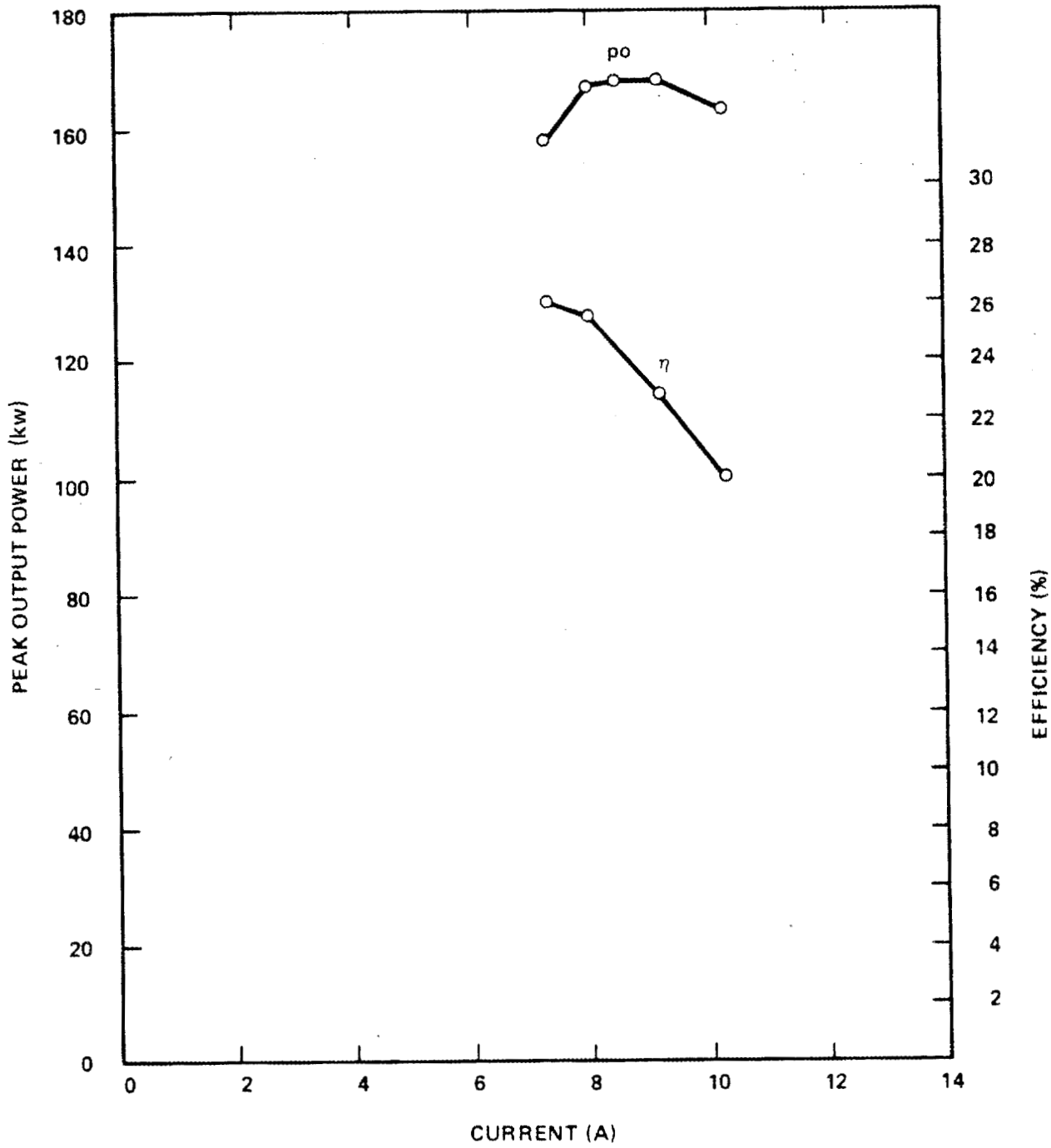

Figure 91. Pulsed CW Oscillator Peak Output Power and Efficiency as Functions of Peak Cathode Current VGA-8000 S/N 1R

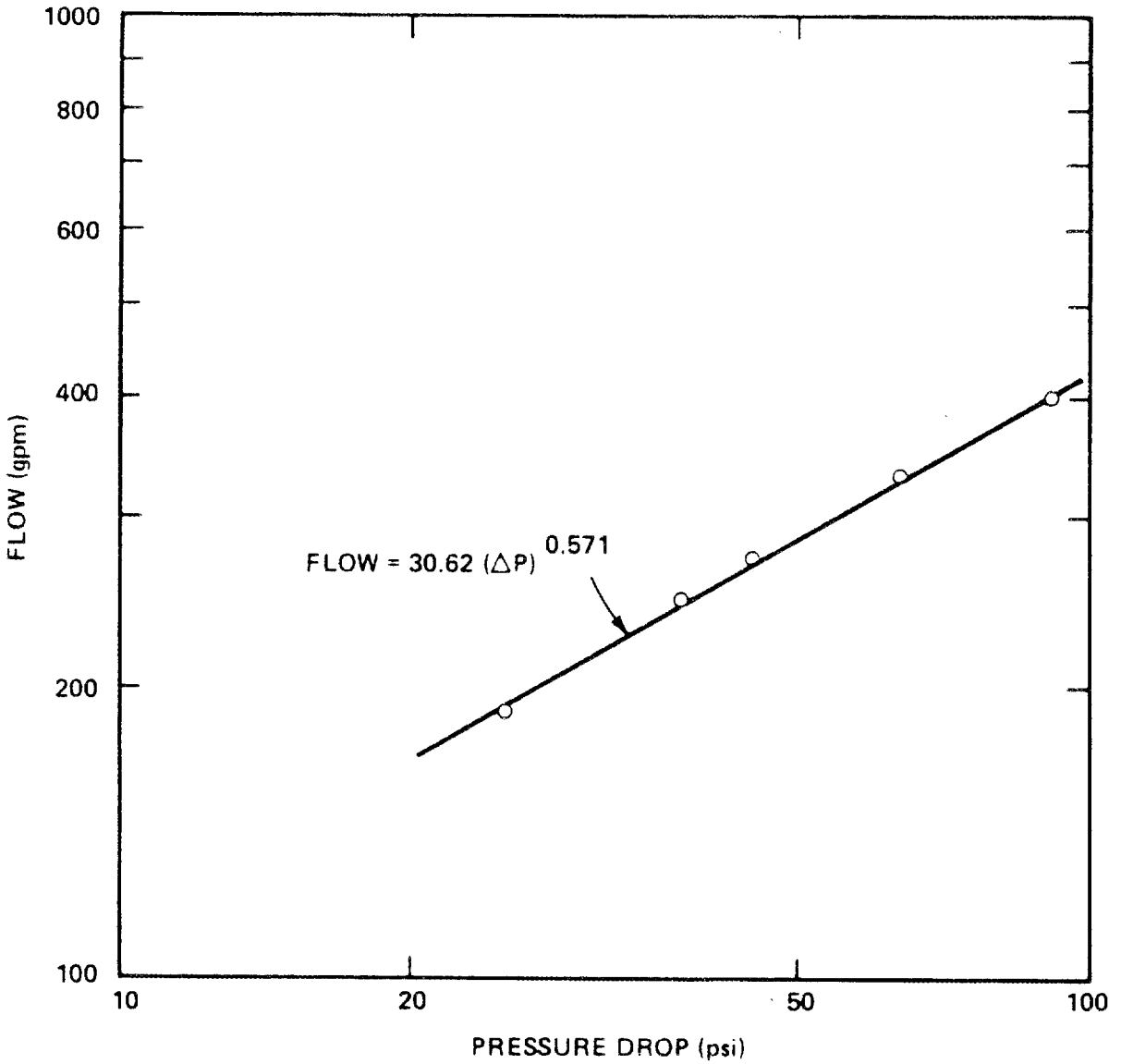

Figure 92. Collector Flow Characteristics VGA-8000 S/N 1R

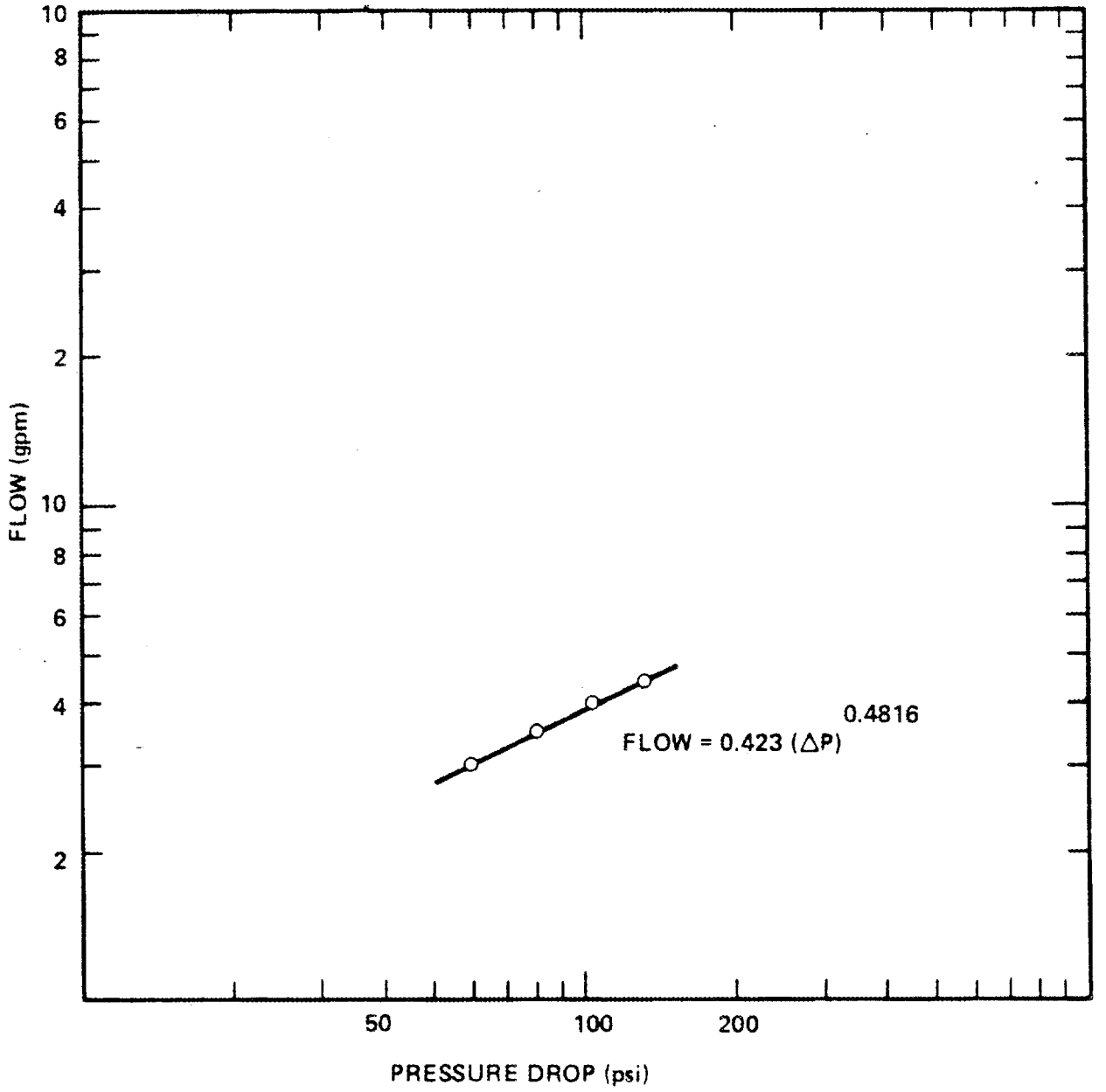

Figure 93. Body Flow Characteristics VGA-8000 S/N 1R

TABLE 27

Best Peak and Average Power Performance of the Rebuilt CW Oscillator

		High Peak Power	High Average Power
Peak Output Power (kw)		168	157
Frequency (GHz)		27.990	27.990
Beam Voltage (kV)		80.9	79.1
Beam Current (a)		8.5	10.0
Efficiency (%)		24.4	19.8
Gun Voltage (kv)		22.4	21.4
RF Pulse Duration (μs)		172	390
Pulse Repetition Rate (pps)		60	299
RF Duty (%)		1.03	11.7
Average Power (kW)		1.73	18.3
Magnet Coil Currents (A)			
Main	1	496	492
	2	472	470
	3	468	460
	4	482	497
Gun	1	10.6	10.1
	2	8.5	9.6

c. S/N 1R2, Test Results

Cold tests indicated that S/N 1R had suffered window failure because of microwave reflections in the external output waveguide. It was, therefore, decided to rebuild that model with no basic changes per se and to build a mode filter to load extraneous resonances in the output line. First tests were accomplished without the mode filter, which was not yet available. But the external output waveguide was simplified by removal of a miter bend, thought to be contributing to the mode resonance problem.

During pulse testing, a peak power output of 167 kw was obtained, and after aging an average power output of 20.4 kW was reached at the modulator limit. Peak power output vs frequency is shown in Figure 94. Peak power output and efficiency vs cathode current are shown in Figure 95. The data of Figure 95 may be compared to that for the pulsed gyrotron oscillator VGA-8000 S/N X-1R3, shown in Figure 96. Despite promising pulsed test behavior, S/N 1R2 showed gassing and arcing during CW operation, even at low levels of power output. The power output reached was at the 15.2 kW level. Table 28 compares pulsed and CW operation.

Returning to pulsed operation, additional experiments were conducted. In one, an attempt was made to determine regions of high power dissipation. Temperature differentials were observed across individual body water cooling circuits with reduced coolant flow. With reduced coolant flow, however, rf behavior changed. The oscillator frequency shifted within a region near 28 GHz. Higher rates of coolant flow in anode and oscillator cavity were accompanied by higher VacIon pump currents. This suggested a contact problem between the SiC-BeO mode loading rings and the copper parts. The nuts on the support rods between the anode and output waveguide block were tightened to more tightly clamp the SiC-BeO to copper joints. The first time the tube was run following this procedure it ran well. But after the rf was turned off and another attempt was made to run with rf, the tube again gassed. This sequence suggested that the copper deformed when heated by rf, and joints re-opened when rf was removed and the tube cooled.

In a second experiment it was found that use of gun coil No. 1 to control output power required working through gassy modes. Adjusting gun anode voltage to increase rf output proved to be less troublesome. The test set was converted to CW operation again to try this method of turning on the oscillator. Operation with CW output was still excessively gassy. The test set was converted back to pulsed operation for further experiments.

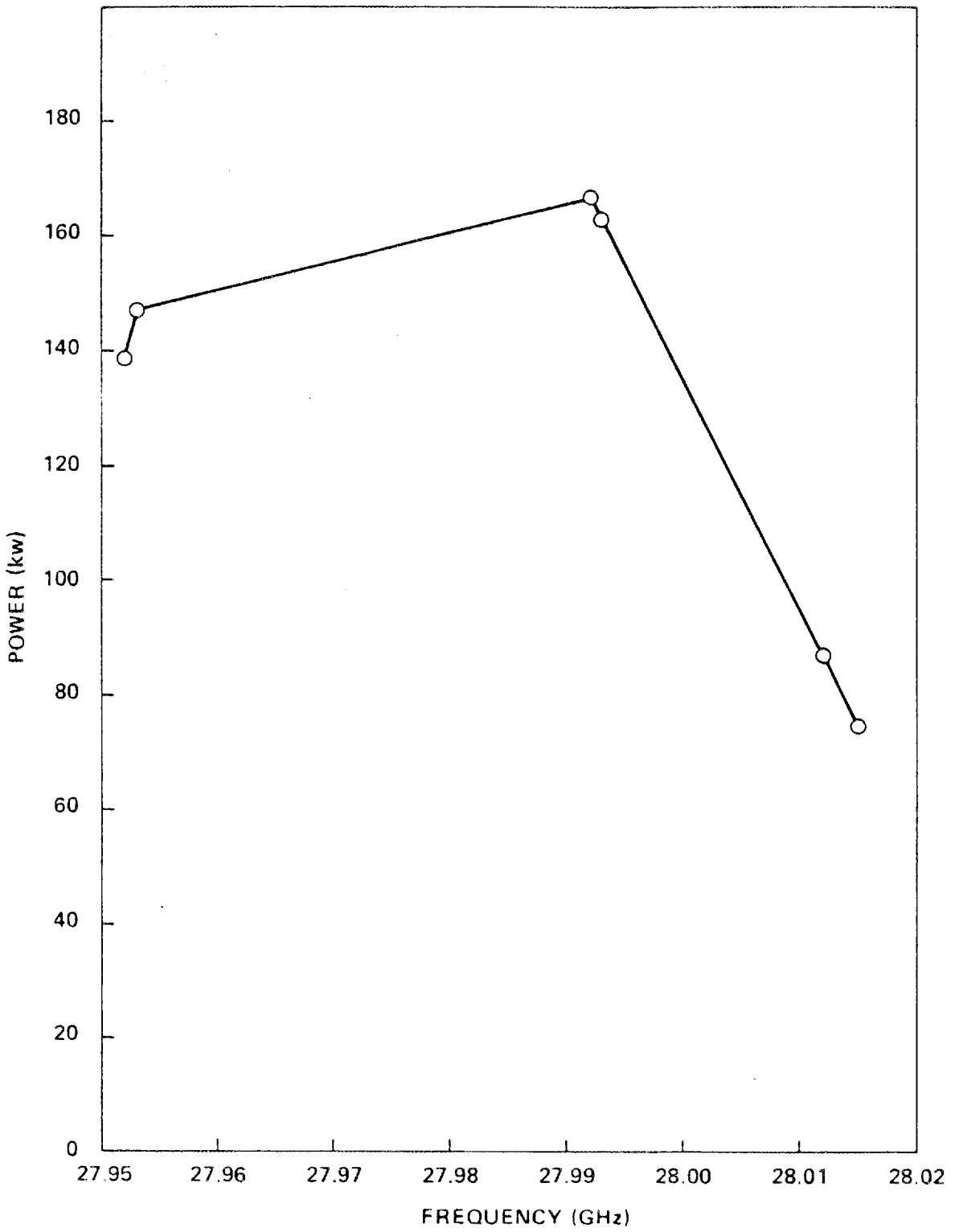

Figure 94. VGA-8000 S/N 1R2 – Peak Output Power vs Frequency

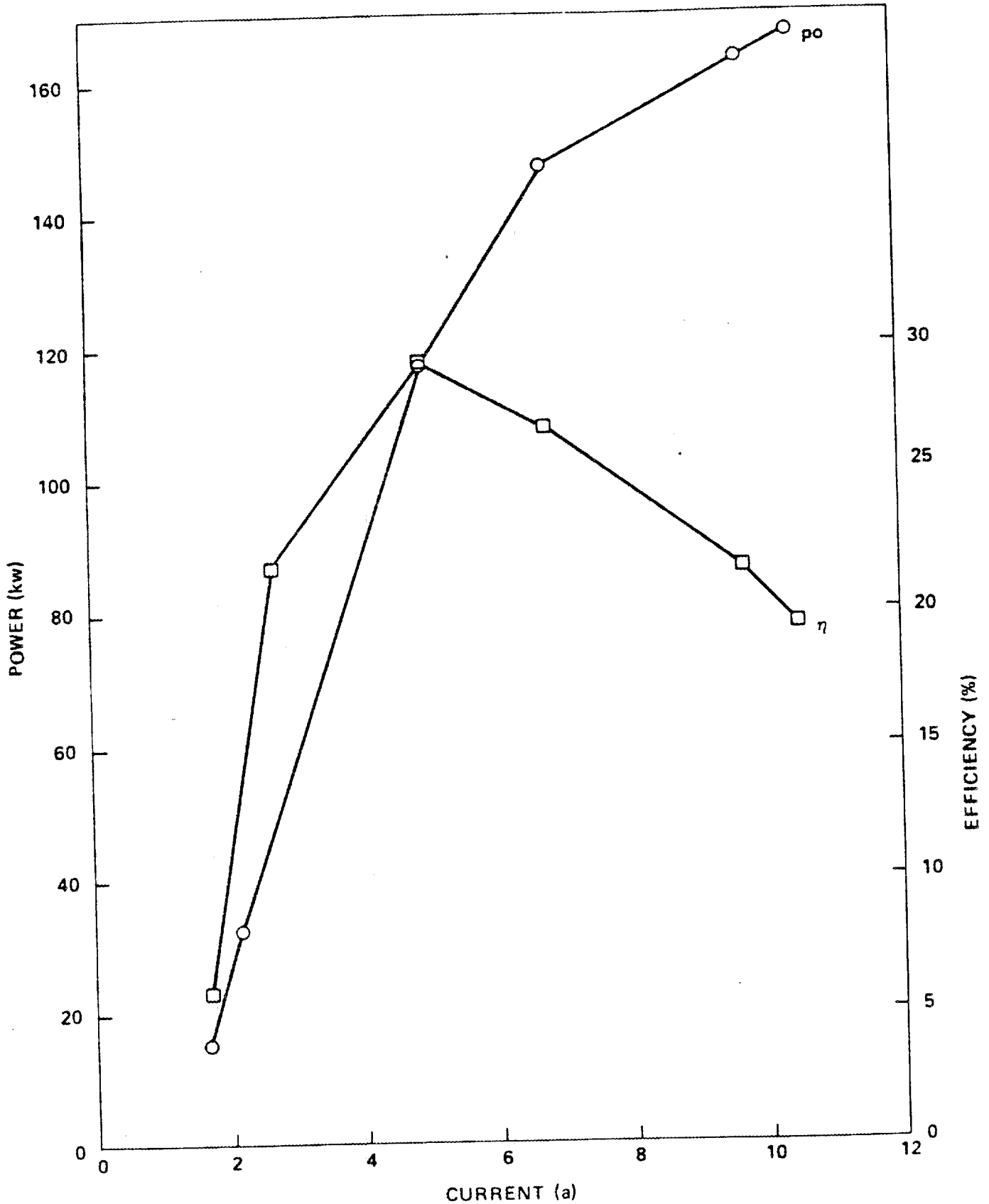

Figure 95. VGA-8000 S/N 1R2 – Power (Peak) and Efficiency vs Cathode Current

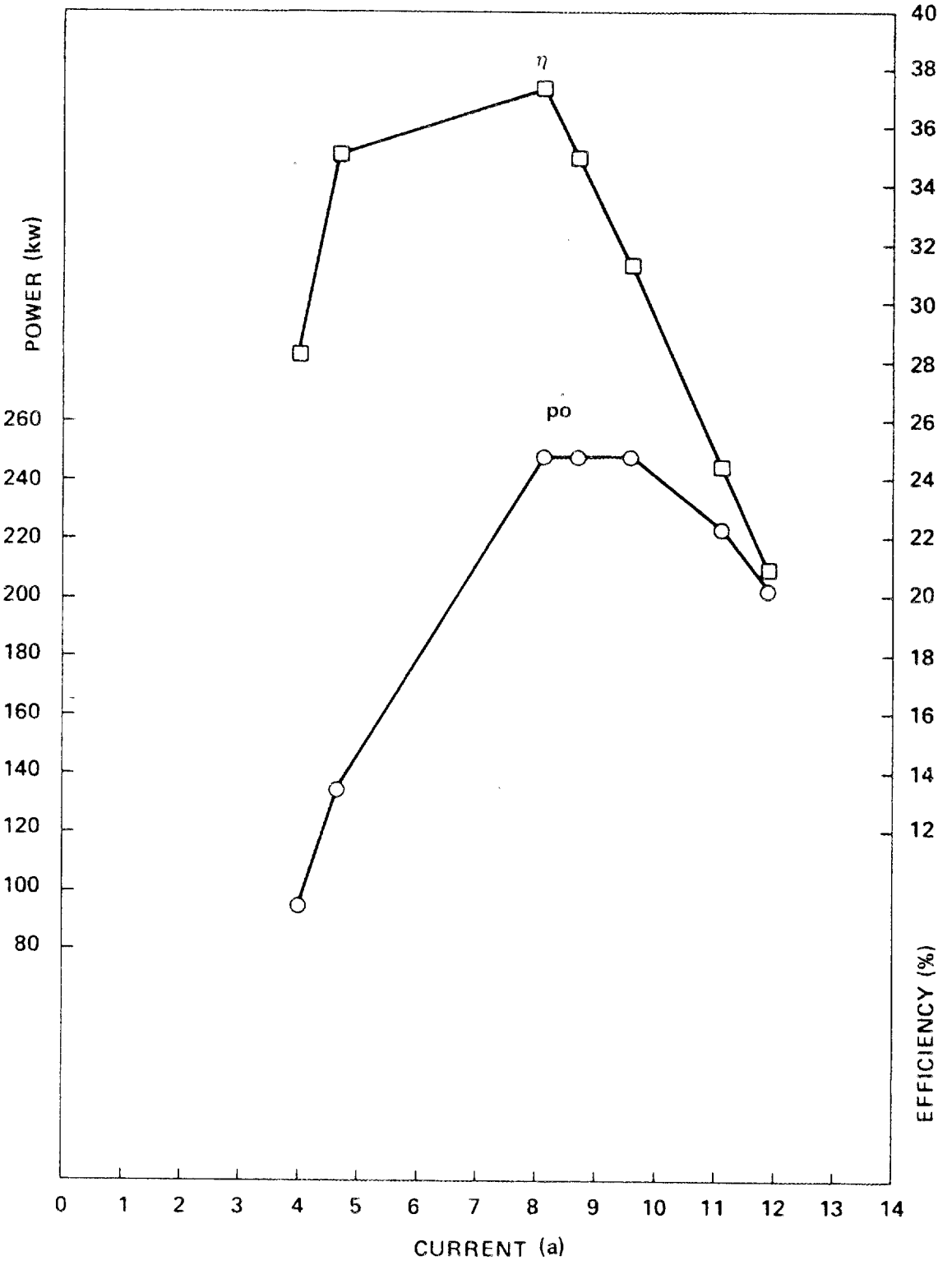

Figure 96. Peak Output Power and Efficiency vs Peak Cathode Current for Pulsed Gyrotron Oscillator VGA-8000 S/N X-1R3

TABLE 28

Best Power Performance of Serial Number 1R2

		Highest Peak Power Pulsed	Highest Average Power Pulsed	Highest CW Power
Peak Output Power (kw)		167	147	15.2
Frequency (GHz)		27.992	27.953	27.992
Beam Voltage (kV)		79.9	80.1	79.5
Beam Current		10.5 a	6.8 a	4.2 A
Efficiency (%)		19.9	27.0	4.6
Gun Voltage		21.5 kv	23.6 kv	20.0 kV
RF Pulse Duration (μs)		200	300	CW
Pulse Repetition Rate (pps)		60	461	CW
RF Duty (%)		1.2	13.8	CW
Average Power (kW)		2	20.4	15.2
Magnet Coil Currents (A)				
Main	1	491	453	480
	2	479	508	511
	3	462	486	470
	4	480	470	460
Gun	1	10.1	10.7	12.6
	2	8.2	9.0	6.0

Tests to identify spurious oscillations showed competition from modes in the frequency ranges 26.802 to 26.845 GHz and 27.223 to 27.236 GHz and also at 26.538 GHz.

A number of other miscellaneous tests were carried out with S/N 1R2, but in no case was satisfactory gas free operation obtained. In view of the good dc beam performance of the model, however, it was decided to ship the tube to the customer for use in checking electrical and mechanical compatibility with the system.

2. VGA-8000 S/N 2

Experience with S/N 1 indicated the need for a number of design modifications. The changes made in S/N 2 are detailed in Quarterly Report No. 8, January - March 1978[11]. S/N 2 was rebuilt nine times, finally failing at the collector ceramic insulator during CW operation at about 60 kW power output.

a. S/N 2

The tube developed an open heater during bakeout.

b. S/N 2R, Test Results

After heater repair, S/N 2R was processed without further incident. The model was first tested under pulsed conditions. A peak power output of 175 kw was obtained at an average power output of 7.6 kW. The data are shown in Figure 97. Peak power output and efficiency vs peak cathode current are shown in Figure 98.

Extensive CW operation was never attempted on this tube, because such operation was accompanied by excessive gun arcing, cathode backheating and heating of the collector seal weld flange. The brazed waveguide joints were successful in keeping those joints cool, but the change in the collector seal was clearly detrimental.

Interfering oscillations were detected from 26.695 to 26.725 GHz, from 16.927 to 27.230 Ghz, and between 50 and 60 GHz. As with the first CW oscillator, as magnetic field was continuously changed, the frequency and mode of oscillation would discontinuously change. An example of this is shown in Figure 99.

The best power performance parameters for S/N 2R are shown in Table 29.

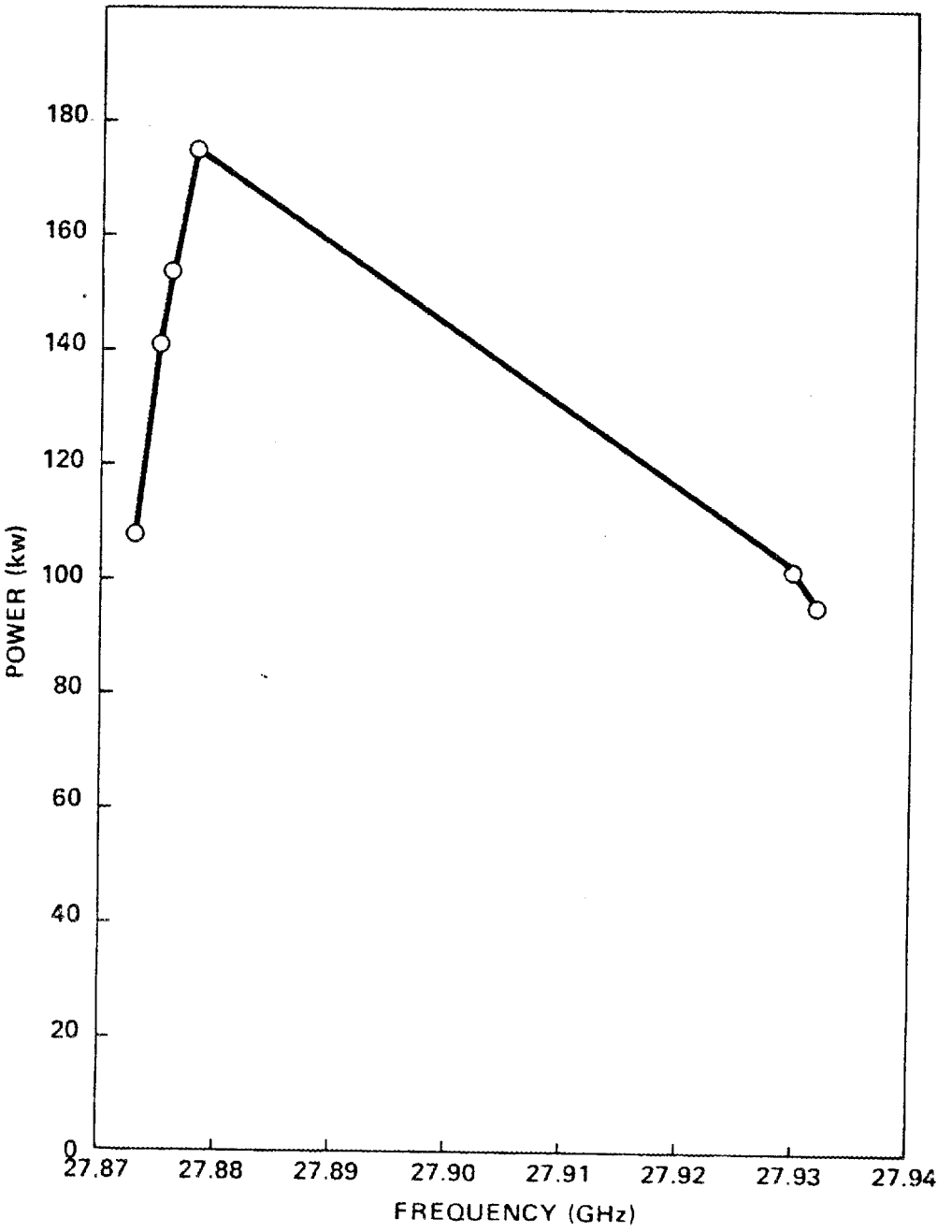

Figure 97. Peak Output Power as a Function of Frequency for S/N 2R

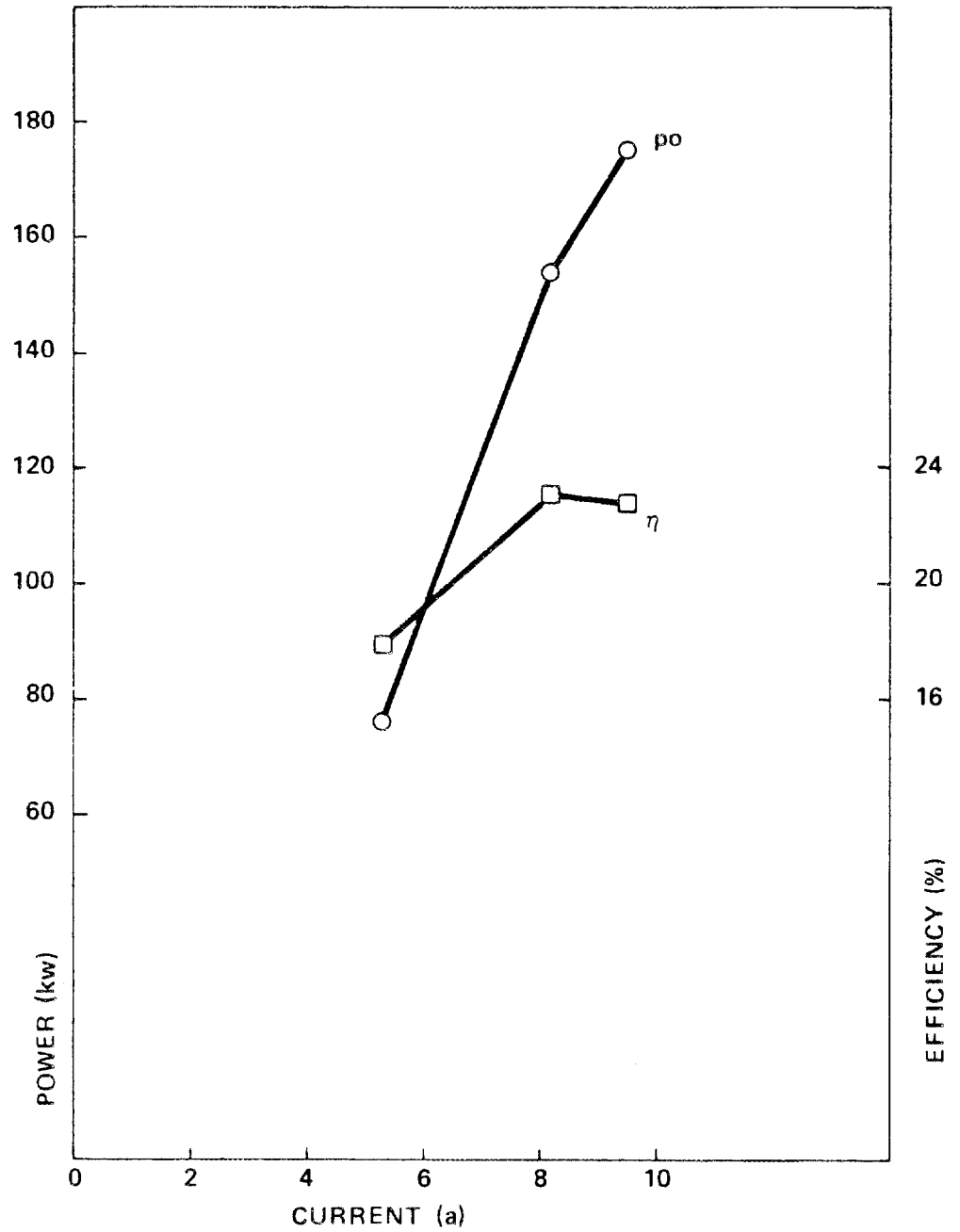

Figure 98. Peak Output Power and Efficiency as a Function of Peak Cathode Current for S/N 2R

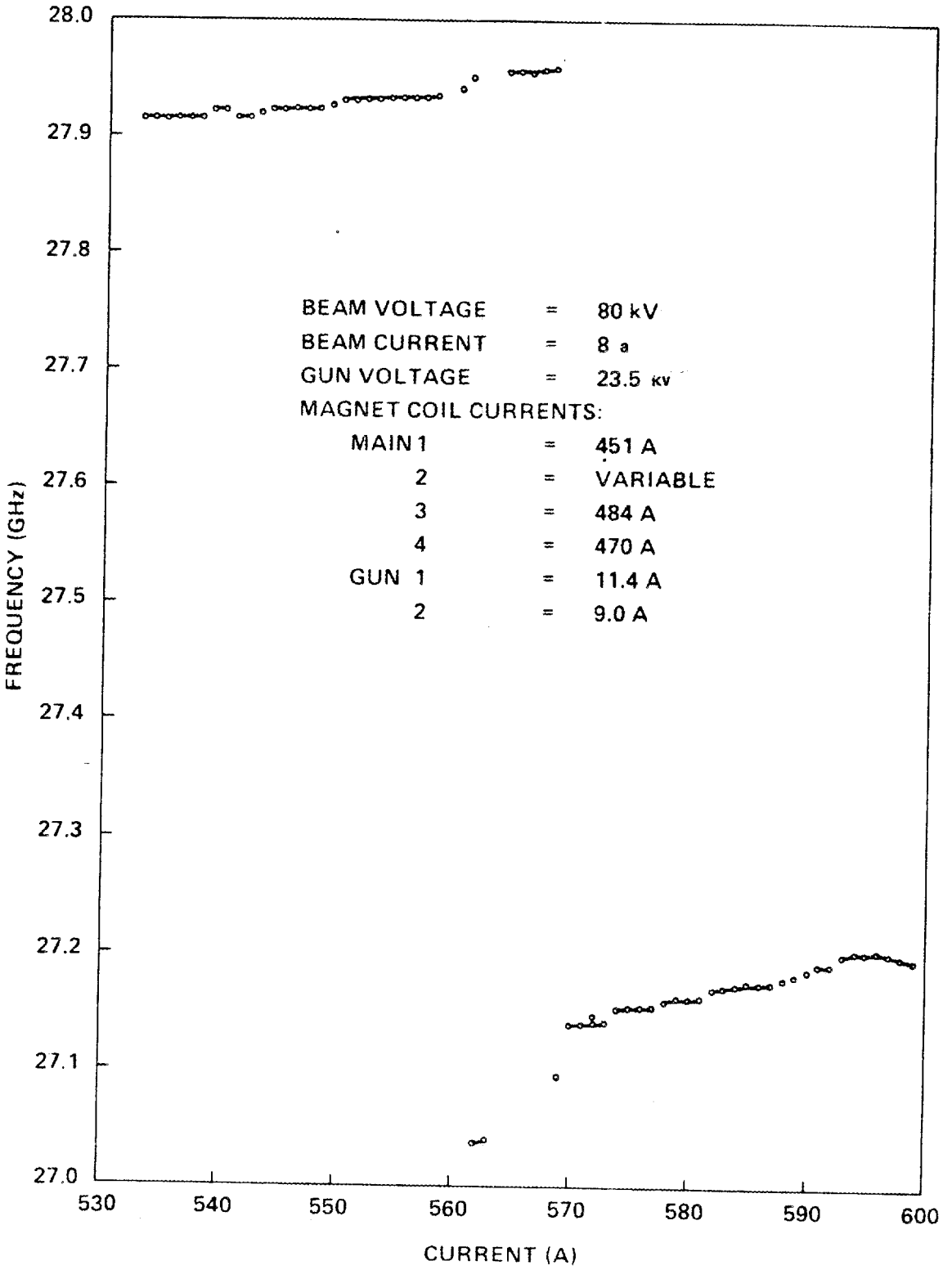

Figure 99. Frequency vs Main Magnet Coil No. 2 Current

TABLE 29

Best Power Performance of Serial Number 2R

		Highest Peak Power	Highest Average Power
Peak Output Power (kw)		175	80.1
Frequency (GHz)		27.878	27.877 & 27.889
Beam Voltage (kV)		80.8	78.0
Beam Current (a)		9.5	6.0
Efficiency (%)		22.8	17.1
Gun Voltage (kv)		23.0	23.0
RF Pulse Duration (μs)		195	395
Pulse Repetition Rate (pps)		60	240
RF Duty (%)		1.2	9.48
Average Power (kW)		2.05	7.6
Magnet Coil Currents (A)			
Main	1	410	403
	2	490	502
	3	495	497
	4	498	502
Gun	1	9.0	7.9
	2	10.3	10.3

c. S/N 2R2, Changes and Test Results

It was decided to rebuild S/N 2 using the original collector seal geometry, which had shown lower temperature increase in the presence of microwave output. Further, lossy SiC-BeO rings were brazed into the anode. and new high voltage ceramics were used. It was expected that these changes should permit CW operation up to about 100 kW power output. It was obvious at this point that additional microwave changes would be needed in a 200 kW tube.

S/N 2R2 produced 105 kW, CW power output, when the output window failed, evidently because of excessive temperature gradient between window center and edge, about 126°C. Best power performance for S/N 2R2 is shown in Table 30.

Spurious oscillations were detected for some magnetic field conditions. These were found from 26.460 to 27.070 Ghz, at 28.981 Ghz, and between 50 and 60 GHz. Tube behavior was improved with respect to cathode rf heating, though for CW operation at over 50 kW power output, heater voltage required constant attention to maintain constant cathode current.

TABLE 30

Best Power Performance of Serial Number 2R2

		Highest Peak Power	Highest CW Power
Peak Output Power (kw)		132	105
Frequency (GHz)		27.863	27.872
Beam Voltage (kV)		83.3	74.9
Beam Current		7.6 a	8.0 A
Efficiency (%)		20.9	17.5
Gun Voltage		22.2 kv	20.9 kV
RF Pulse Duration		285 μs	CW
Pulse Repetition Rate		541 pps	CW
Rf Duty		15.4 %	CW
Average Power (kW)		20.4	105.0
Magnet Coil Currents (A)			
Main	1	410	400
	2	492	500
	3	493	490
	4	494	490
Gun	1	9.6	10.7
	2	10.8	10.7

d. S/N 2R3, Test Results

The tube was rebuilt without change. A 28 GHz microwave power source was needed at ORNL and the existing design would give useful CW performance at up to 50 kW power output.

A CW power output of 50 kW was reached at a beam input of 70 kV at 8 Amperes. Power output sensitivity to gun coil No. 1 current is shown in Figure 100, to gun anode voltage in Figure 101. Tests were conducted with a mode filter in the rf output line. Mode filter and window losses observed are listed in Table 31.

TABLE 31

Mode Filter and Window Losses for VGA-8000 S/N 2R3

Power Delivered To Load (kW)	Mode Filter Power (kW)	Mode Filter Loss (dB)	Window Power (W)	Window Center Temperature (°C)
* 4.04	0.792	0.8	145	21
* 9.84	1.58	0.6	290	21
* 11.0	2.16	0.8	145	—
* 12.8	1.85	0.6	290	—
14.8	3.25	0.9	—	—
19.3	3.96	0.8	435	62
19.7	3.25	0.7	—	—
19.7	5.41	1.1	—	—
21.0	5.41	1.0	725	—
30.6	8.45	1.1	870	60

* Three of the ten silicon carbide loaded beryllia rings in the mode filter were replaced with copper rings for these tests.

The tube was delivered to Oak Ridge National Laboratory, where 45 kW, CW was demonstrated on 29 June 78. The tube lost vacuum on 30 June 78 and was shipped to Varian for analysis and rebuild.

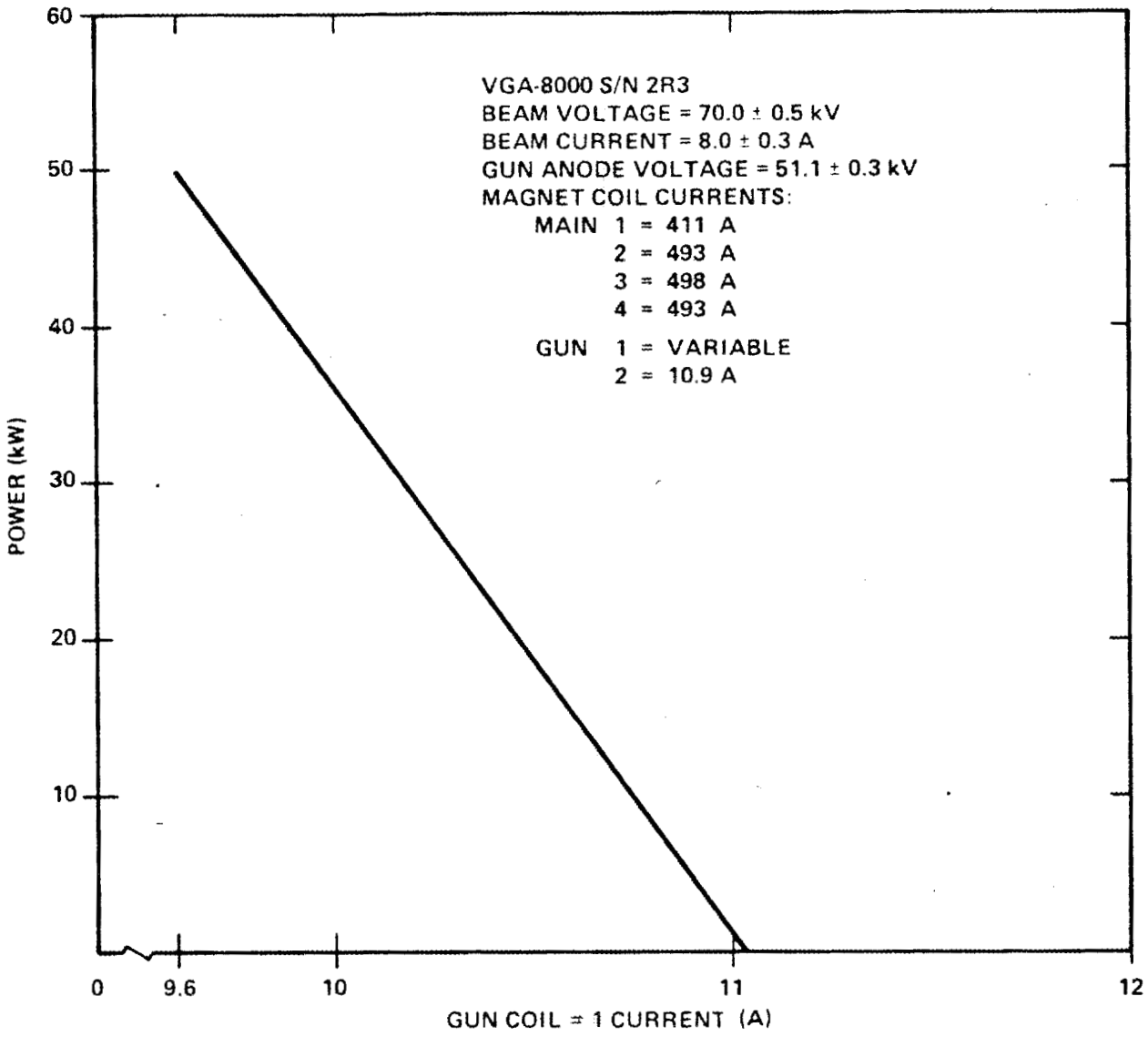

Figure 100. CW Power Output Sensitivity to Gun Coil No. 1 Current

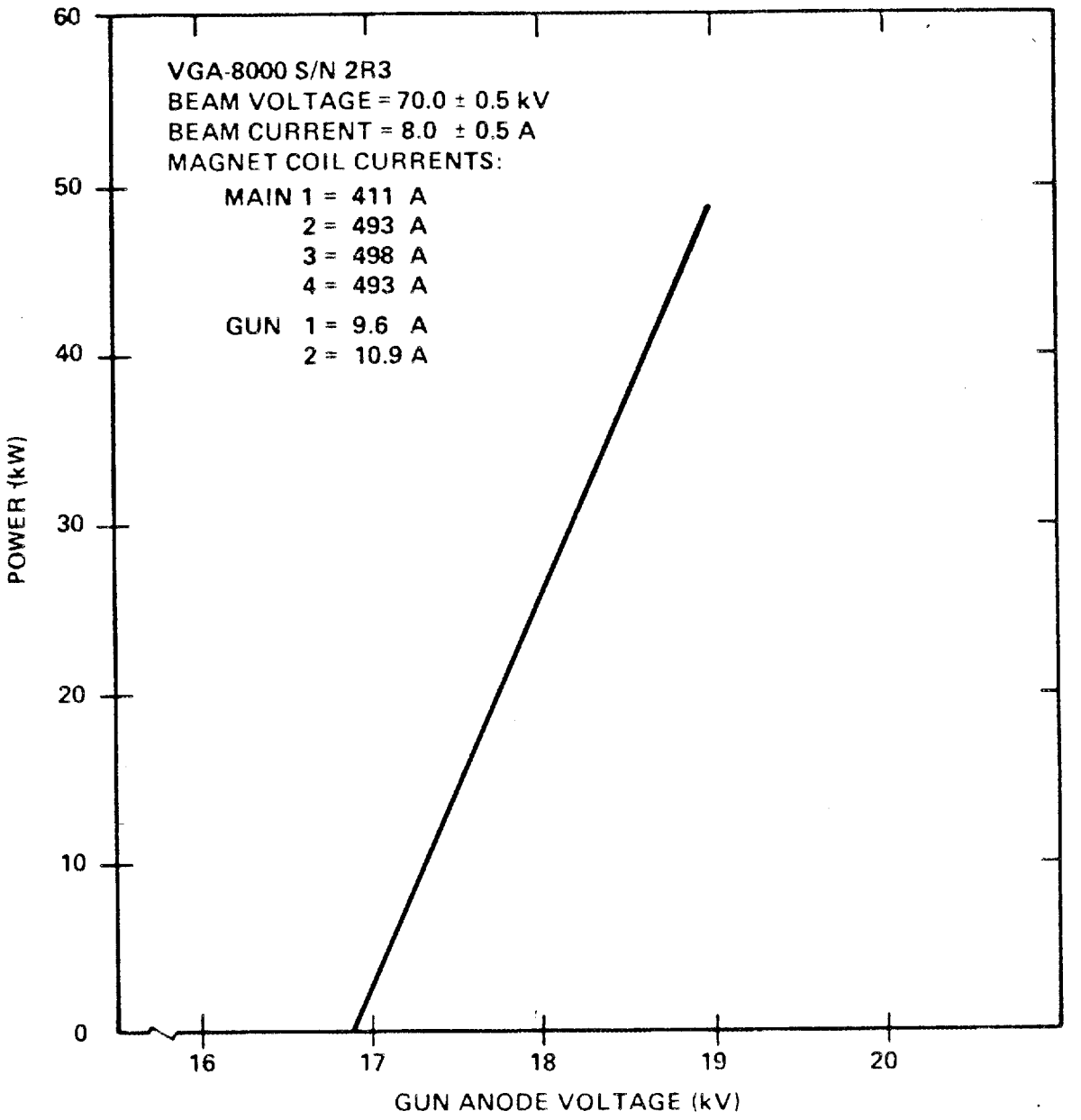

Figure 101. CW Power Output Sensitivity to Gun Anode Voltage

e. S/N 2R4

The vacuum leak in the previous rebuild model proved to have occurred in the cathode stem cooling oil channel. After repair, the tube was put into bakeout. However, a collector vacuum braze joint opened during this processing.

f. S/N 2R5

The collector vacuum braze joint was repaired. Bakeout and processing was carried out without incident. The tube was pulse tested first to 87.2 kw power output, then CW aged to 37.1 kW power output. Operating parameters for these tests are shown in Table 32. Spurious oscillations were detected under some conditions of magnetic field from 26.665 to 26.801 GHz, from 26.930 to 26.932 GHz, and from 27.010 to 27.134 GHz. The tube was shipped to the customer, where continued aging brought CW power output up to 50 kW.

After some use in the system, the tube was returned by the customer for a window change aiming at an operational level of 100 kW CW power output.

g. S/N 2R6

A double-disc face cooled window was used in this rebuild modification to increase window power handling capability. During bakeout, however, the tube collector developed a vacuum leak.

h. S/N 2R7

The collector vacuum leak was repaired. Bakeout and processing were carried out without incident. After pulse testing to peak power output of 138 kw, CW aging proceeded to a power level of 32.5 kW. At this point, the window failed. Subsequent examination showed that the

window unit had been improperly assembled and that the window, in fact, had had no cooling during test.

TABLE 32

Operating Parameters at Varian for the Fifth Rebuild of the Second CW Oscillator

		Pulsed	CW
Peak Output Power		82.7 kw	37.1 kW
Frequency (GHz)		27.895	27.874
Beam Voltage (kV)		68.1	70.3
Beam Current		8.6 a	7.0 A
Efficiency (%)		14.1	7.54
Gun Anode Voltage		17.1 kv	18.6 kV
RF Pulse Duration (μs)		278	CW
Pulse Repetition Rate (pps)		421	CW
RF Duty (%)		11.7	CW
Average Power (kW)		9.68	37.1
Magnet Coil Currents (A)			
Main	1	427	444
	2	497	489
	3	500	490
	4	562*	568*
Gun	1	8.6	10.2
	2	11.0	10.7

*Main coil 4 was partially shorted. Effective current was less.

i. S/N 2R8

A proper double-disc face cooled window structure was used in this rebuild. A number of other changes were also introduced. These are covered in detail in the Quarterly Report No. 12, January-March 1979.[15] Bakeout and processing were carried out without incident. The tube produced 92.1 kW CW power output prior to the occurrence of a vacuum leak in the

output window metallizing. Failure analysis of the tube indicated possible improvements in a number of areas.

j. S/N 2R9

The tube was rebuilt as an intermediate level power oscillator, capable of 50 to 100 kW CW power output, which it had been delivering when the output window metallizing failed. The key changes made were as follows:

1. The double-disc BeO type output window was assembled using less brazing material and with window cups that were stiffened at the end opposite the window;

2. A plug, with smaller pump-through holes, was brazed into the tee leading to the VacIon pump;

3. An external cooling channel was added to the stainless steel collector support plate.

Changes to the window assembly were designed to reduce mechanical stress and fatigue of the BeO ceramic caused by temperature rise and temperature cycling. Simultaneously, they were expected to alleviate buckling of the attached copper ring. The purpose of the smaller holes in the tee-plug leading to the VacIon pump was to cut off the third harmonic rf energy and thus eliminate pump rf heating.

A high quality filter was installed in the test station FC-75 cooling system. Higher velocity flow was used to cool the double-disc window.

During test, CW power output was increased gradually to a level of 63 kW. Difficulty was experienced in keeping the tube "on" for more than a few minutes because of power supply overcurrent and crowbar. Overcurrents were caused either by transient gas bursts or by microwave power reaching the electron gun.

During test of S/N 2R9, thermocouples were used to monitor the weld in the vicinity of the collector metal-ceramic. The temperature went up as CW power output increased. After several high power CW runs of approximately one hour duration, the collector ceramic cracked, letting the tube down to air. Figures 102 and 103 show the region of failure. The ceramic cracks are highlighted by means of dye. It appears that circumferential stress caused by nonuniform power flow through the ceramic and heating caused by rf losses in the ceramic and adjoining metal parts may have been responsible.

3. VGA-8000 S/N 3

This tube included the following changes:

a) Addition of an internal water load in the beam tunnel
b) Waveguide length change between cavity and first miter bend
c) Use of double-disc BeO output window
d) Relocation of VacIon pump
e) Addition of collector top spurious microwave output system

Details of these changes are given in Quarterly Report No. 10, July - September 1978.[13]

a. S/N 3

Bakeout and processing were uneventful. The tube was tested on a pulsed basis to a power output level of 71.2 kw peak. Operating parameters are shown in Table 33, at this power level 26.9 kw peak was also absorbed in the internal water load. Total microwave power removed from the beam was at least equal to the sum of these two. Such a large amount of power delivered to the internal load was considered unacceptable. The introduction of the internal load and the change in guide length between the cavity and miter bend apparently changed the cavity Q, leading to low efficiency. Because of the efficiency, it was impossible to evaluate improvement in the FC-75 face-cooled window.

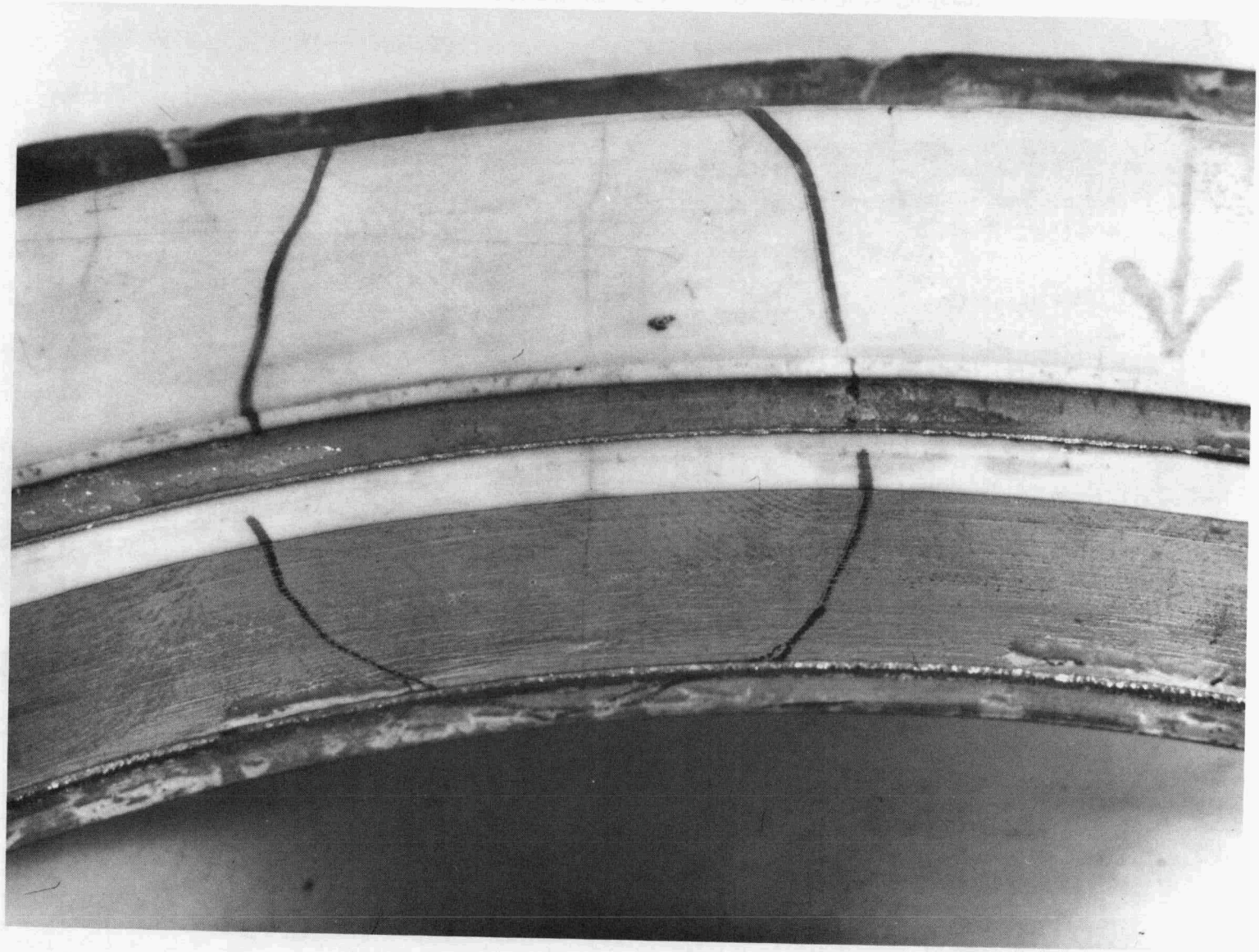

Figure 102. VGA-8000 S/N 2R9 Collector Ceramic (Inner and End Surfaces)

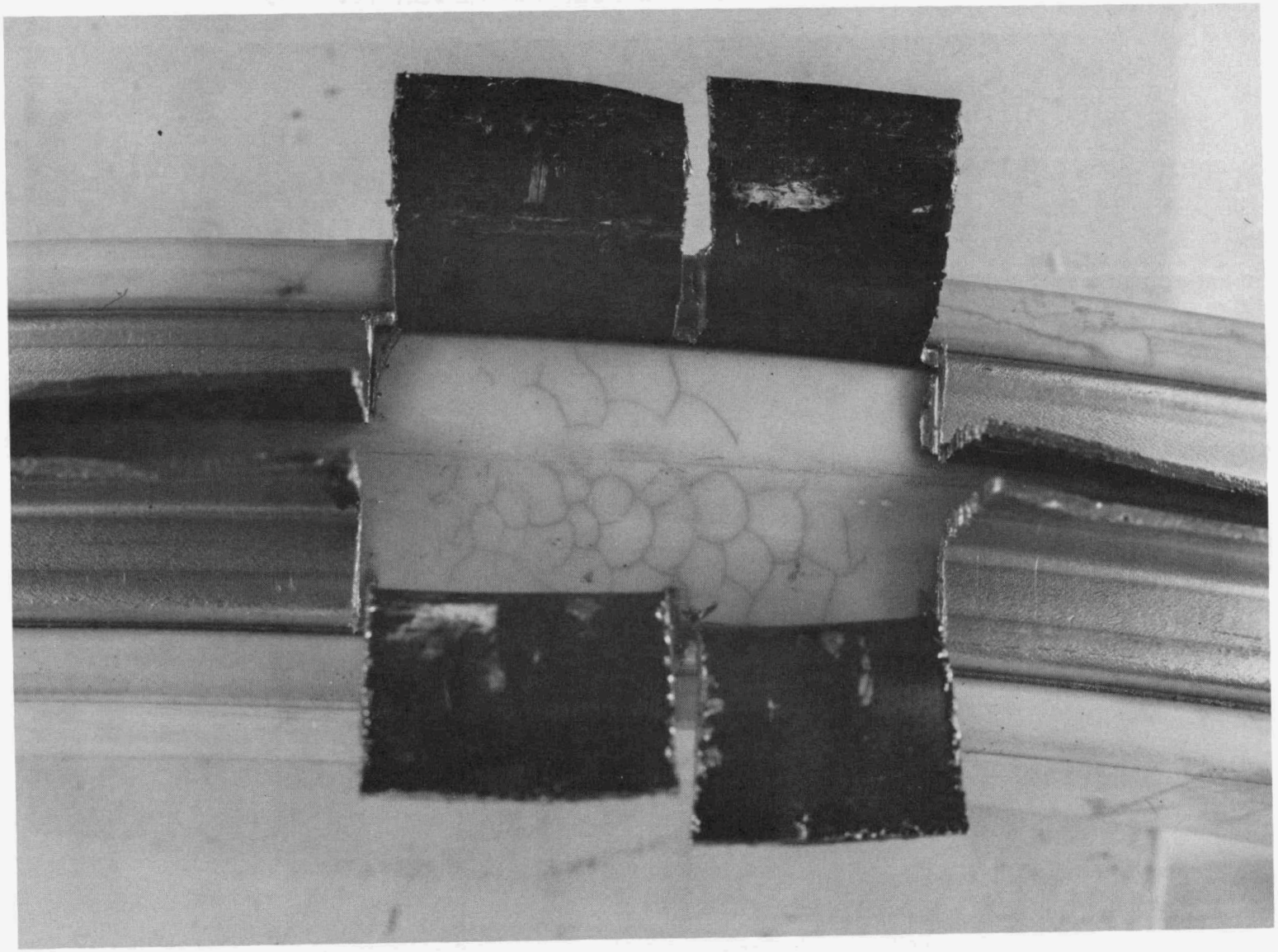

Figure 103. VGA-8000 S/N 2R9 Collector Ceramic (Outer Surface)

The new position of the VacIon pump eliminated the need to isolate the electrical connections to the pump. Heating of the miter bend at the top of the collector was found to be caused by electron bombardment. An external water-cooled plate was added to the miter plate to remove heat. Spurious oscillations were observed at 26.828, 26.860, and 26.870 GHz.

TABLE 33

Pulsed Operating Parameters for the Third CW Oscillator

Peak Output Power (kw)		71.2
Frequency (GHz)		28.006
Beam Voltage (kV)		78.7
Beam Current (a)		9.5
Efficiency (%)		9.52
Gun Anode Voltage (kv)		22.7
RF Pulse Duration (μs)		275
Pulse Repetition Rate (pps)		120
RF Duty (%)		3.3
Average Power (kW)		2.35
Magnet Coil Currents (A)		
Main	1	492
	2	463
	3	500
	4	478
Gun	1	11.8
	2	10.2

b. S/N 3R

The tube was rebuilt without the internal cavity load. Bakeout and processing were uneventful. Pulse testing yielded a peak power output of 171 kw and an average power of 18.5 kW. Peak power observed in the collector top load was 17.5 kw. CW testing at Varian was cut short by failure of a main magnet power supply. The tube was shipped to ORNL where

it was operated up to a CW output level of 38 kW. Operating parameters for the first rebuild of S/N 3 are shown in Table 34.

TABLE 34

Pulsed Operating Parameters for the Rebuild of the Third CW Oscillator

Peak Output Power (kw)		147
Frequency (GHz)		27.975
Beam Voltage (kV)		79.9
Beam Current (a)		8.8
Efficiency (%)		20.9
Gun Anode Voltage (kv)		24.4
RF Pulse Duration (μs)		300
Pulse Repetition Rate (pps)		420
RF Duty (%)		12.6
Average Power (kW)		18.5
Magnet Coil Currents (A)		
Main	1	502
	2	481
	3	482
	4	496
Gun	1	11.5
	2	4.5

4. VGA-8000 S/N 4

This tube used a new electron gun assembly, a new anode design, and a miter bend output assembly similar to that used in S/N 2. The collector was a repaired unit taken from S/N 2R6.

a. S/N 4

Bakeout and processing proceeded without incident. Pulse testing operational data are shown in Table 35. The collector developed a vacuum leak during CW beam only tests. No CW rf data were obtained.

TABLE 35

Operating Points for Maximum Peak and Average Power in Pulsed Operation for the Fourth CW Oscillator

		Max Peak	Max Average
Peak Output Power (kw)		138	119
Frequency (GHz)		27.973	27.970
Beam Voltage (kV)		80.2	80.6
Beam Current (a)		8.6	8.4
Efficiency (%)		20	17.6
Gun Anode Voltage (kv)		21.9	21.7
RF Pulse Duration (μs)		290	290
Pulse Repetition Rate (pps)		240	500
RF Duty (%)		6.96	14.5
Average Power (kW)		9.58	17.2
Magnet Coil Currents (A)	Main 1 =	500	499
	2 =	484	494
	3 =	501	500
	4 =	500	500
	Gun 1 =	10.6	10.7
	2 =	11.3	11.2

b. S/N 4R

The collector vacuum leak was attributed to metal porosity. The tube was rebuilt using the collector from S/N 2R7. Bakeout and processing were uneventful. Pulsed test data are shown in Table 36. CW test data are shown in Table 37.

S/N 4R was shipped to ORNL. Even though the tube had produced 97 kW CW in testing at Varian, it was found to be difficult to operate at ORNL. The model ultimately failed at ORNL because of a vacuum leak in the collector ceramic. The tube was returned to Varian for analysis and possible repair.

Analysis revealed collector ceramic damage, shown in the photographs of Figures 104, 105, and 106. Details of the analysis are given in Quarterly Report No. 12 January - March 1979[15]. Further rebuild of S/N 4 was not planned.

TABLE 36

Pulsed Operating Point for the Rebuilt Fourth CW Oscillator

Peak Output Power			137 kw
Frequency			27.972 GHz
Beam Voltage			80.3 kV
Beam Current			8.2 a
Efficiency			20.8%
Gun Anode Voltage			21.3 kv
RF Pulse Duration			300 μs
Pulse Repetition Rate			120 s^{-1}
RF Duty			3.6%
Average Power			4.93 kW
Magnet Coil Currents:	Main	1 =	496
		2 =	471
		3 =	498
		4 =	499
	Gun	1 =	10.0
		2 =	11.2

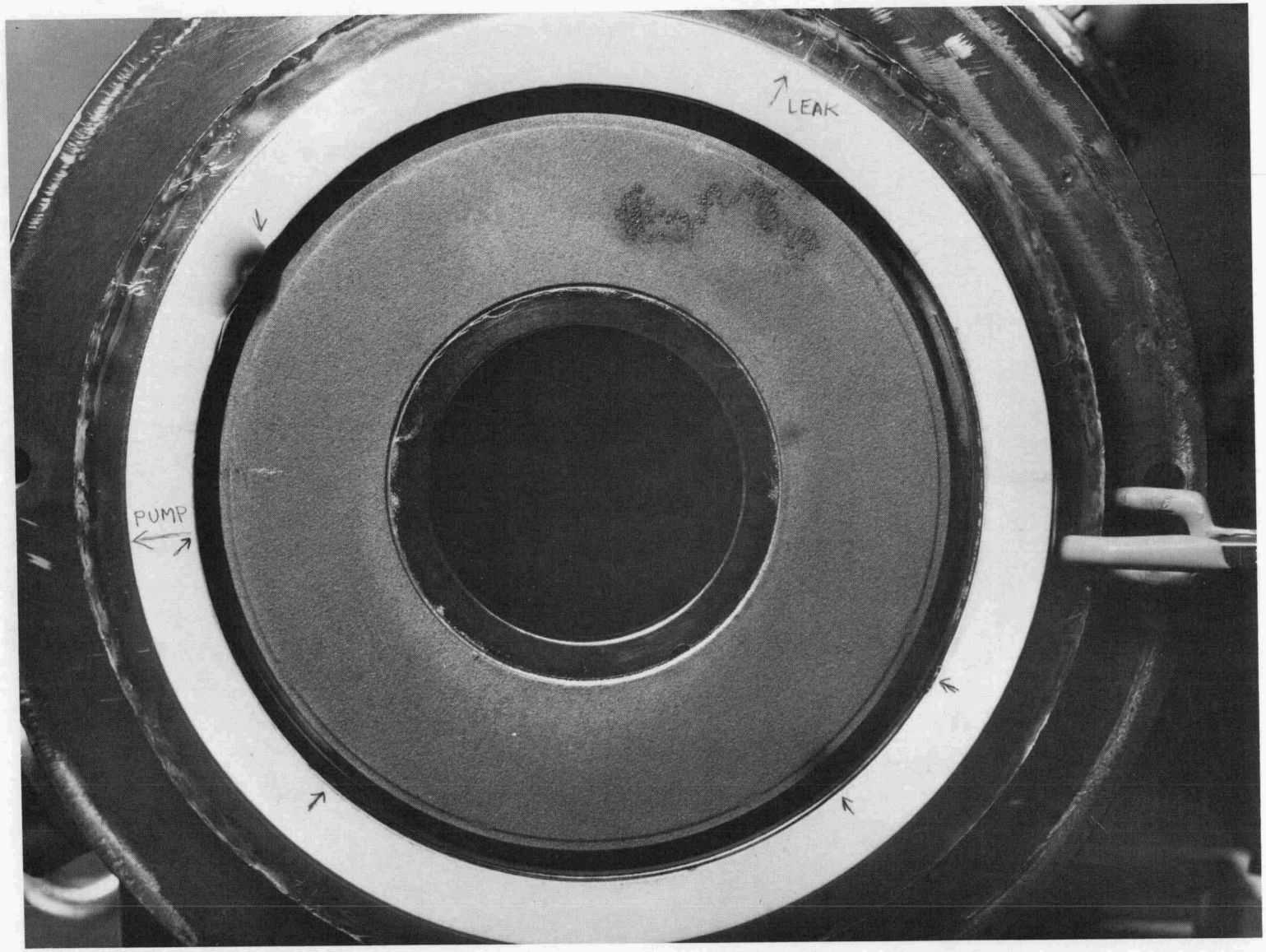

Figure 104. Collector Assembly and Ceramic Assembly from S/N 4R after Failure

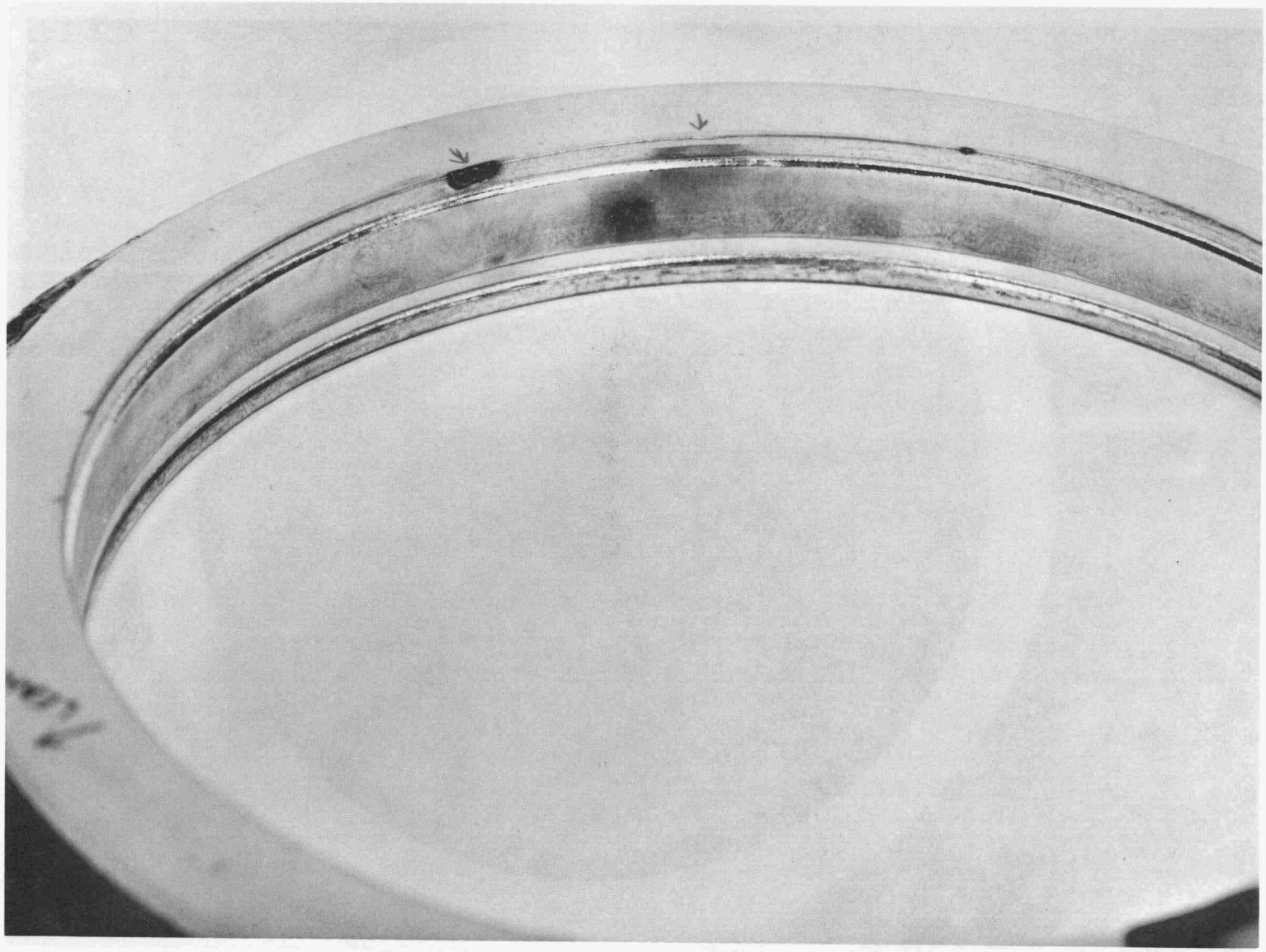

Figure 105. Collector Ceramic Assembly from S/N 4R after Failure, View 1

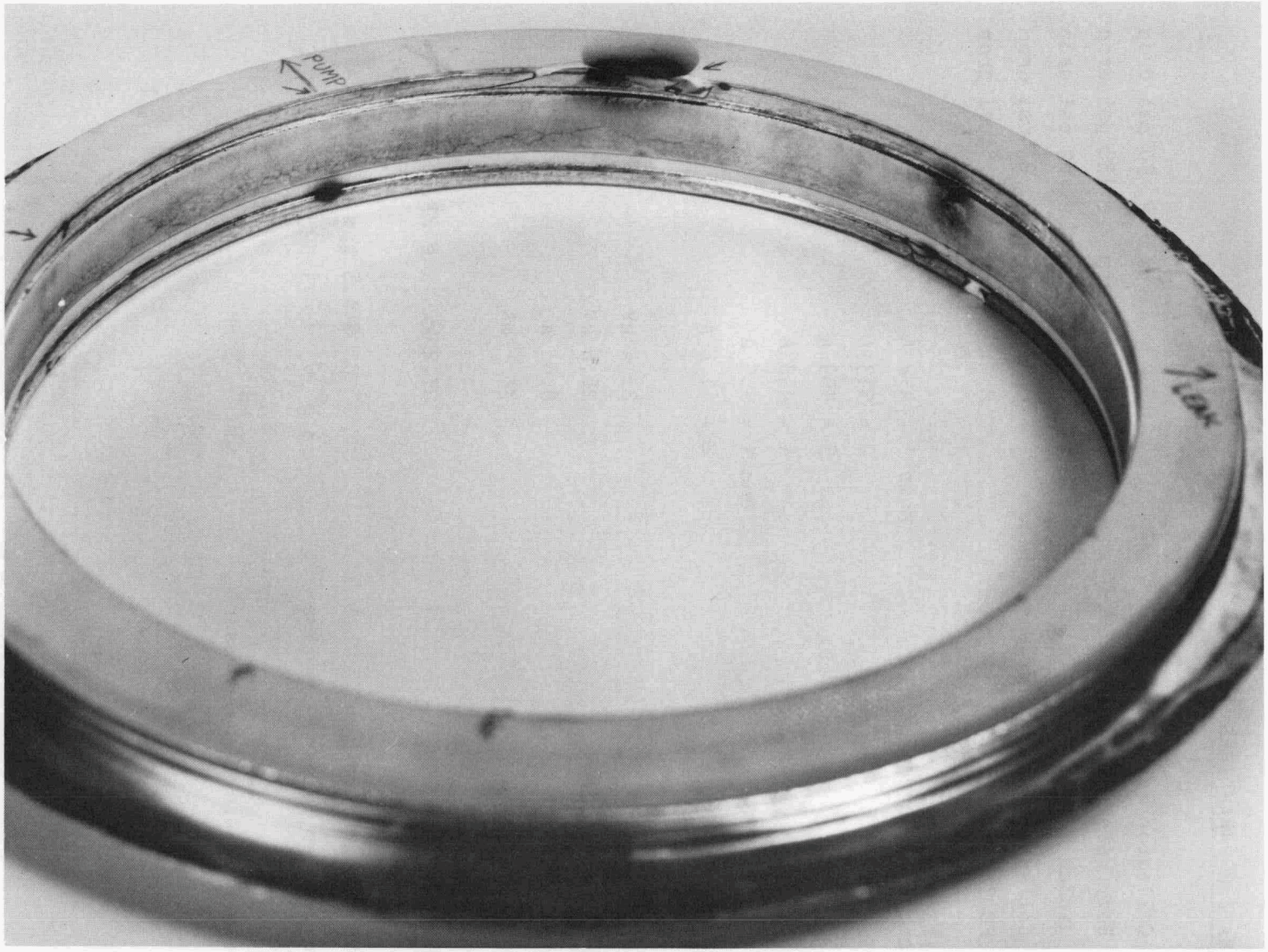

Figure 106. Collector Ceramic Assembly from S/N 4R after Failure, View 2

TABLE 37

VGA-8000 S/N 4R CW Test Data

OPERATING PARAMETERS

Collector Water Flow	350	gpm	@ 70 psi drop
Body Water Flow	4	gpm	@ 138 psi drop
Window Water Flow	2.1	gpm	@ 69 psi drop
Collector Seal Tubing Water Flow	0.25	gpm	@ 23 psi drop
FC-75 Flow	2	gpm	@ 8 psi drop

Magnet Coil Currents:	Main 1 =	492 A
	2 =	513 A
	3 =	499 A
	4 =	498 A
	Gun 1 =	9.5 A
	2 =	11.2 A

Beam Voltage	82.4 kV
Gun Andoe Voltage	26.6 kV
Cathode Current	8.6 A
Body Current	38 mA

Power Output	97.2 kW	@ 27.968 GHz

FC-75 Temperature Rise	9° C	@ 1.5 gpm
Window Water Temperature Rise	3.5^{o} C	@ 2.1 gpm

Normal Operating Tube Pressure	$<10^{-8}$ Torr

5. VGA-8000 S/N 7

This tube had a collector similar to S/N 3 with a 2.5-inch diameter waveguide loading the top of the collector. Significant features were as follows:

1. Double-disc BeO window, FC-75 cooling
2. Optimized spacing between the interaction cavity and the first miter bend.
3. Oscillator cavity with a groove to detune TM modes.
4. Secondary electron magnetic trap on the waveguide coming out the top of the collector.

Details of these features may be found in Quarterly Report No. 13, April - June 1979.

a. S/N 7

Bakeout and processing proceeded without incident. Pulsed testing yielded 120 kw peak power output. CW testing gave levels of 50 to 70 kW power output under various sets of operating conditions. Details of testing are given in Quarterly Report No. 14, July - September 1979.[17] The tube was shipped to ORNL. It went down to air shortly after turn-on and was returned to Varian for analysis and possible repair.

b. S/N 7RM

The letter M was added to the serial number to indicate a miter bend model. The S/N 7 vacuum leak was found in a cracked ceramic in the loaded drift tube assembly. After repair, tube bakeout and processing proceeded without incident. Pulsed mode testing yielded 127 kw peak power output. CW testing yielded up 69 kW power output. Various operational difficulties were encountered during CW tests and these are discussed in detail in Quarterly Report No. 15, October - December 1979.[18] CW operational test data are shown in Table 38. The tube was shipped to the customer for system use. It operated satisfactorily at the 50 kW CW power

output level over a period of several months, when it developed an open heater. It was returned to Varian for analysis.

The analysis of VGA-8000 S/N 7RM is the subject of a separate report submitted to the customer. Highlights are given in Quarterly Report No. 17, April - June 1980.[20] The tube was placed in storage. There was no plan for a further rebuild.

TABLE 38

VGA-8000

Serial Number 7RM Operating Parameters

Collector Water Flow	350	gpm
Body Water Flow	4	gpm
Window Water Flow (both)	1	gpm
FC-75 Flow	2.5	gpm
Magnet Water Flow	16	gpm
Upper Water Load	2	gpm
Magnet Coil Currents:	Main 1 = 552 A	
	2 = 512 A	
	3 = 480 A	
	4 = 480 A	
	Gun 1 = 10 A	
	2 = 10 A	
Beam Voltage	77.5 kV	
Gun Anode Voltage	30.6 kV	
Cathode Current	8.2 A	
Body Current	18 mA	
Power Output	67 kW	
Frequency	27.86 GHz	

c. VGA-8000 S/N 12M

This model was identical with S/N 7 except for a loaded Q reduced from 750 to about 500. At the time, it was imperative that the tube be completed and shipped to the customer as a backup for S/N 7RM.

Bakeout and processing proceeded without incident. Pulse testing yielded 130 kw peak power output. Efficiency vs beam current ranged from 22 to 34%, Figure 107. The tube produced up to 60 kW power output during a CW test period of ten hours. Then 103 to 113 kW power output was obtained for over one hour. The limiting factor was collector seal temperature rise. A number of special tests relating to modal content of the output waveguide were conducted. Details of these are given in the Quarterly Report No. 16, January - March 1980.[19] Table 39 summarizes routine test performance. The tube was shipped to the customer in March 1980.

During system operation, difficulty was reported in attempting to increase beam current and power output. Crowbars occurred frequently. After power supply repair and adjustment, a power output of 65 kW was achieved. After a number of experiments, S/N 12M was removed from the socket and replaced with VGA-8000 S/N 5R2, an axisymmetric model.

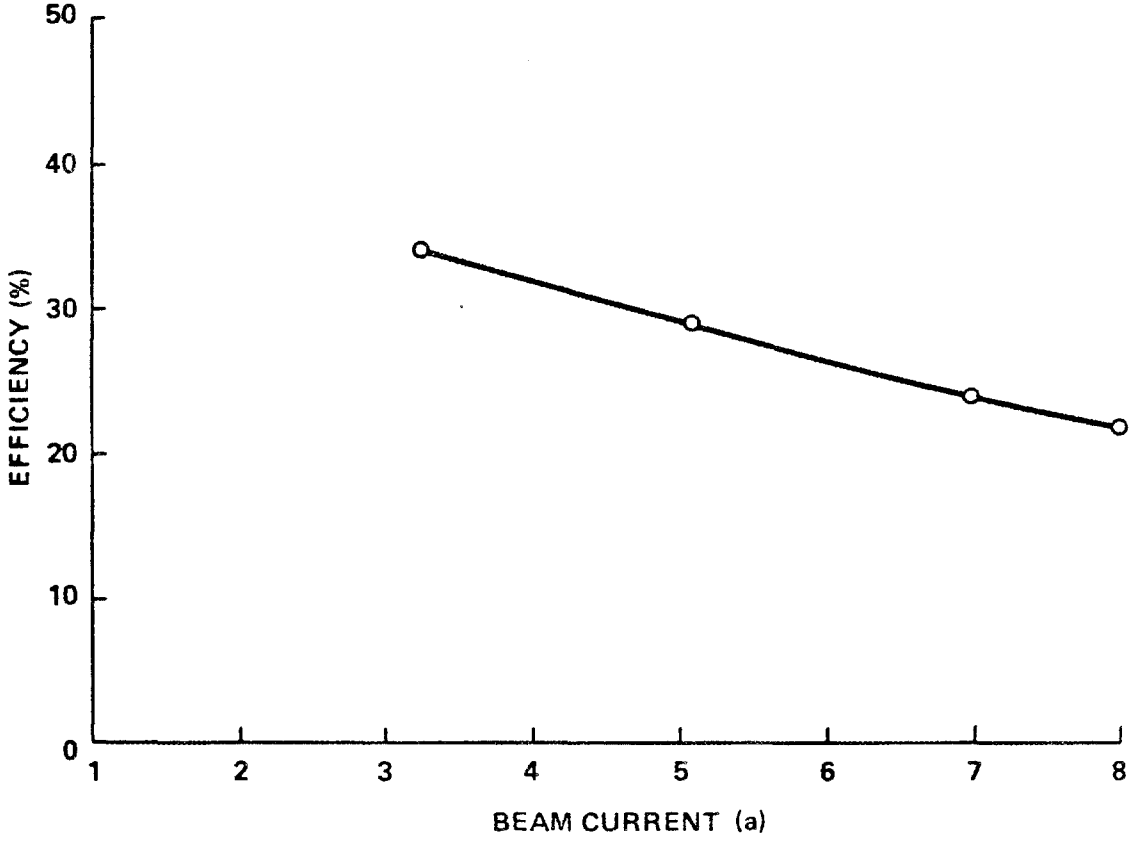

Figure 107. VGA-8000 Gyrotron, S/N 12M Efficiency vs Beam Current in Pulse Mode; 8% Duty

TABLE 39

VGA-8000 S/N 12M Test Performance

OPERATING PARAMETERS

Collector Water Flow	274 gpm	
Body Water Flow	3.8 gpm	
Window Water Flow (both)	1 gpm	
FC-75 Flow	3.0 gpm	
Upper Water Flow	1.8 gpm	
Magnet Coil Currents:	Main 1 =	500 A
	2 =	480 A
	3 =	479 A
	4 =	469 A
	Gun 1 =	10.5 A
	2 =	10 A
Beam Voltage		80.5 kV
Gun Anode Voltage		20.1 kV
Cathode Current		5.9 A
Body Current		20.0 mA
Power Output		107 kW
Frequency		27.991 GHz

J. AXISYMMETRIC MODELS

Axisymmetric models incorporated straight through collector output coupling systems, in which the collector took on the dual role of absorbing electron beam dissipation and acting as a waveguide microwave component.

Six models of this type gyrotron CW oscillator may be identified, VGA-8000 S/N's 5, 6, 8, 9, 10, and 11. Figure 108 is a layout showing the essential features of an axisymmetric CW gyrotron oscillator.

1. VGA-8000 S/N 5

This model used an output waveguide tapering to a 5-inch-diameter collector and then tapering back to a 2.5-inch diameter at the output window. Details of microwave circuit cold testing, electron beam dissipation considerations, and tube construction are given in Quarterly Report No. 12, January - March 1979.[15]

a. S/N 5

After bakeout and processing the tube was pulse tested. A peak power output of 75 kw was obtained. This level was the maximum possible with this model, evidently because the loaded Q was too high by a factor of three or four. Various experiments were conducted in analysis of the problem and it was eventually traced to a distortion which had caused a mismatch at the window. Details of these tests and discussion of the difficulty are given in Quarterly Report No. 13, April - June 1979.[16] It was decided to rebuild the tube with an improved window design.

b. S/N 5R1

Pulse testing after routine bakeout and processing yielded a peak power output of 195 kw, the highest so far attained with a CW tube. Data for the pulse tests are shown in Figure 109. CW testing gave 66 kW power output intermittently over a period of several hours, when a vacuum leak developed in the collector-ceramic seal. The leak was temporarily repaired with sealant, but it was decided to rebuild the model.

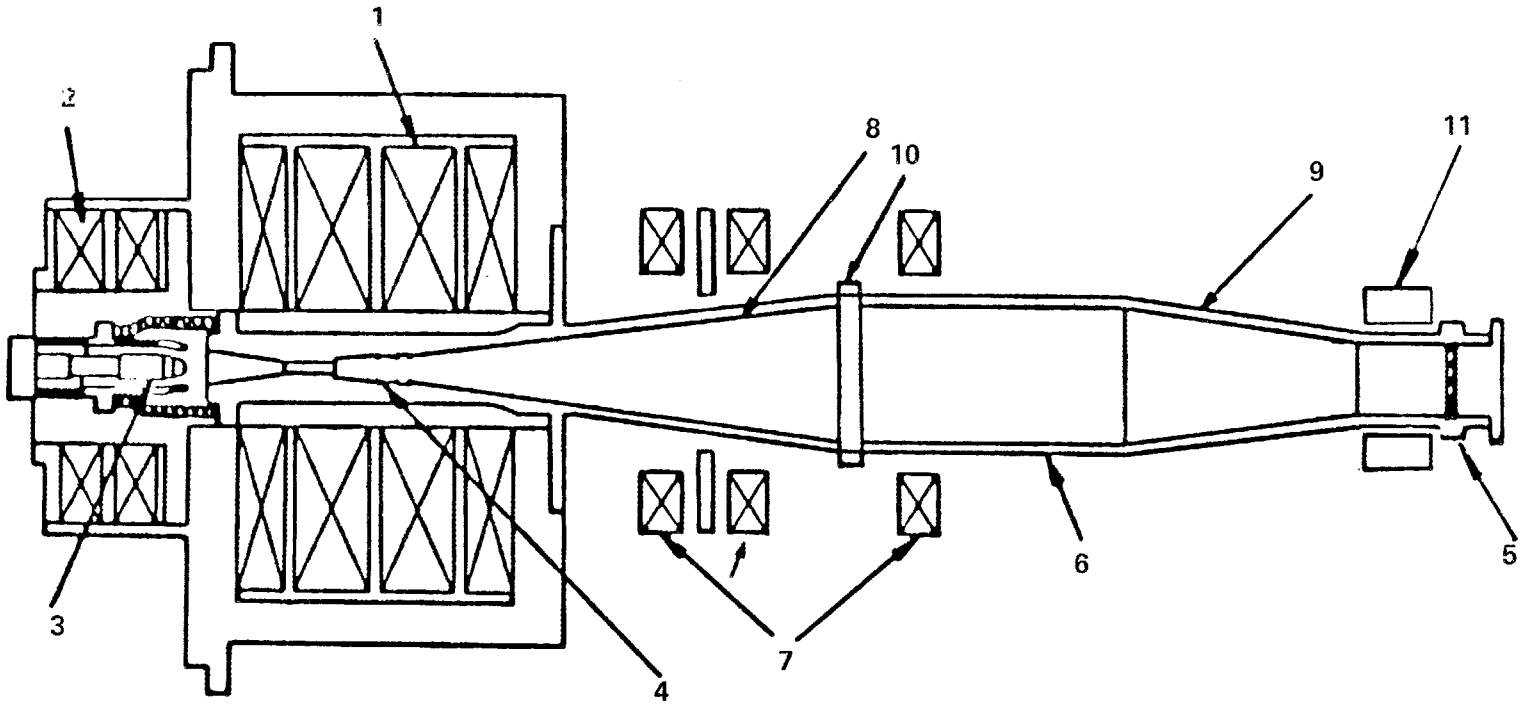

1. MAIN MAGNET COILS
2. GUN MAGNET COIL
3. ELECTRON GUN
4. CAVITY
5. OUTPUT WAVEGUIDE AND WINDOW
6. BEAM COLLECTOR
7. COLLECTOR MAGNET COILS
8. OUTPUT GUIDE UP-TAPER
9. OUTPUT GUIDE DOWN-TAPER
10. LOWER COLLECTOR GAP
11. TRANSVERSE FIELD MAGNET

Figure 108. Layout Drawing of an Axisymmetric CW Gyrotron with Tapered Output Waveguide

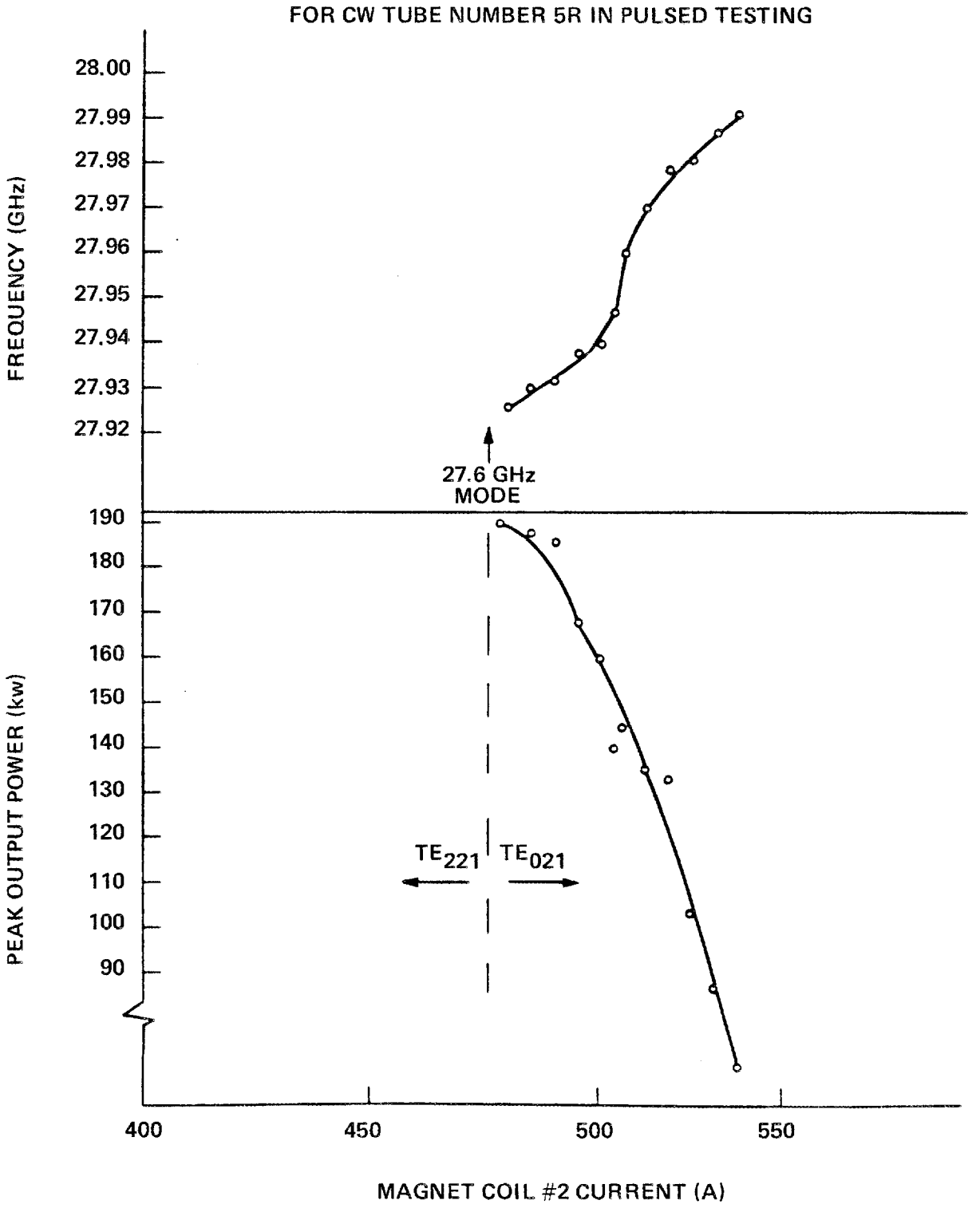

Figure 109. Frequency and Power Characteristics for CW Tube Number 5R in Pulsed Testing

c. S/N 5R2

After repair and routine bakeout and processing, the tube was tested in the pulse mode. A peak power output of 213 kw was obtained, despite some turn-on difficulty with modes at 32.5 and 33.2 GHz. Several CW experiments were conducted with the tube to characterize the VGA-8000 gyrotron oscillator and to provide information leading to better understanding of gyrotron operation. Figures 110, 111, and 112 show CW power output and frequency vs main magnet coil No. 2 current for beam currents of 3.6, 4.9, and 6.0 amperes, respectively. Examination of the curves shows two important factors.

1. An optimum magnetic field exists at each level of beam current.

2. The frequency decreases with decreasing magnetic field.

Efficiency vs beam current with optimized electron gun anode voltage is shown in Figure 113. A maximum value of 48.7% was noted. For beam currents larger than 5.2 amperes, efficiencies higher than the indicated values may have been possible, but testing was administratively restricted to power output of no more than about 200 kW CW. Further, efficiencies higher than those of Figure 113 might be possible with further main magnetic field optimization. On February 12, 1980, the tube produced 212 kW CW. This represented a major milestone in gyrotron development. Key CW test results are summarized in Table 40. Two curves of efficiency vs electron gun anode voltage are given in Figures 114 and 115.

One of the output window structure ceramic discs failed during a test in which the output waveguide system included a miter bend between two mode filters. Fortunately, it was the outer window that had failed, the tube still had vacuum. A detailed analysis of the window failure and discussion of improvements are given in Quarterly Report No. 17, April - June 1980.[20] Further details relating to test results with S/N 5R2 are given in Quarterly Reports Nos. 16 and 17, January through June 1980.[19-20] The outer window disc was replaced and the tube was

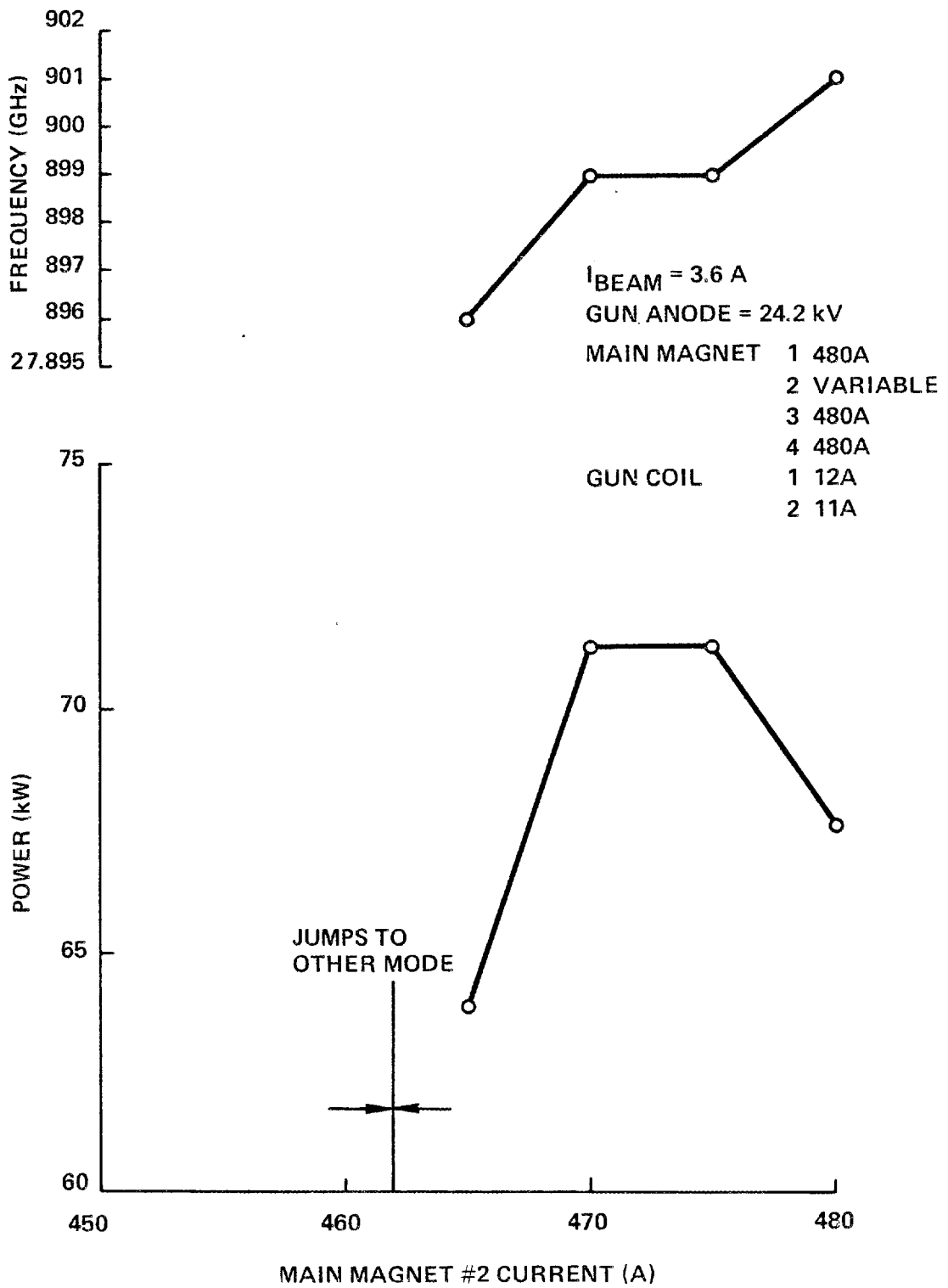

Figure 110. Frequency and Power vs Main Magnet No. 2 Current for VGA-8000 S/N 5R2 (I_{Beam} = 3.6A)

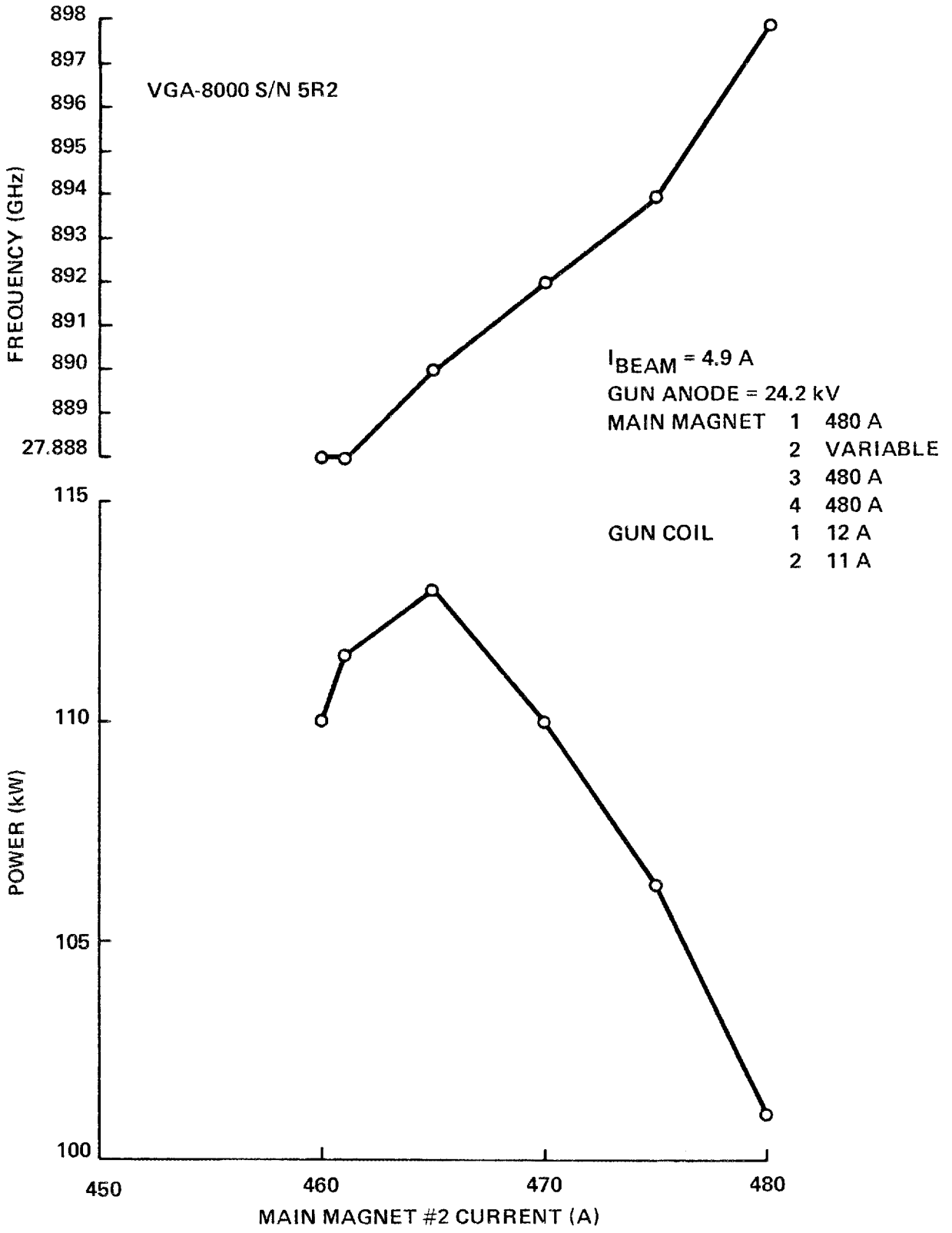

Figure 111. Frequency and Power vs Main Magnet No. 2 Current for VGA-8000 S/N 5R2 (I_{Beam} = 4.9A)

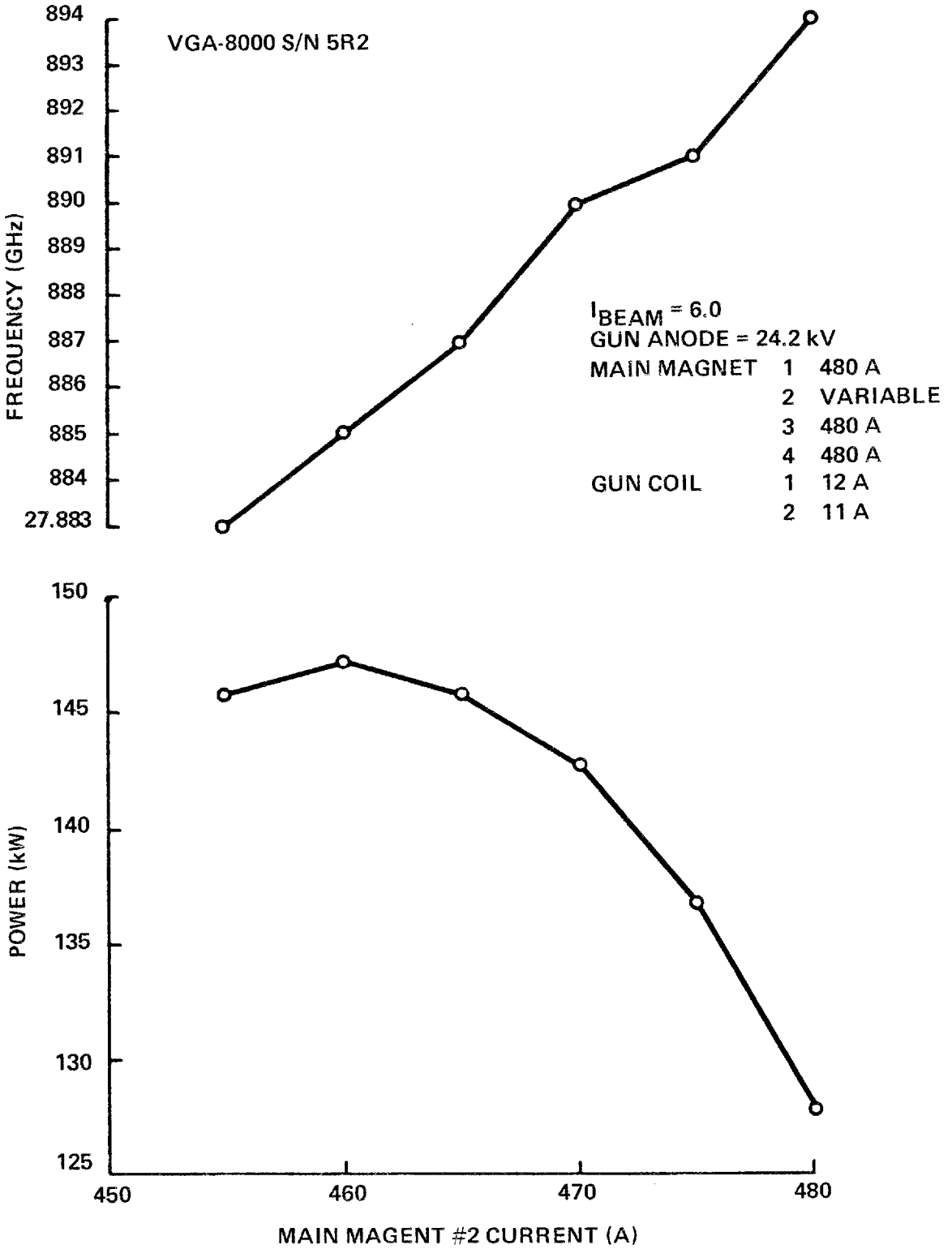

Figure 112. Frequency and Power vs Main Magnet No. 2 Current for VGA-8000 S/N 5R2 (I_{Beam} = 6.0A)

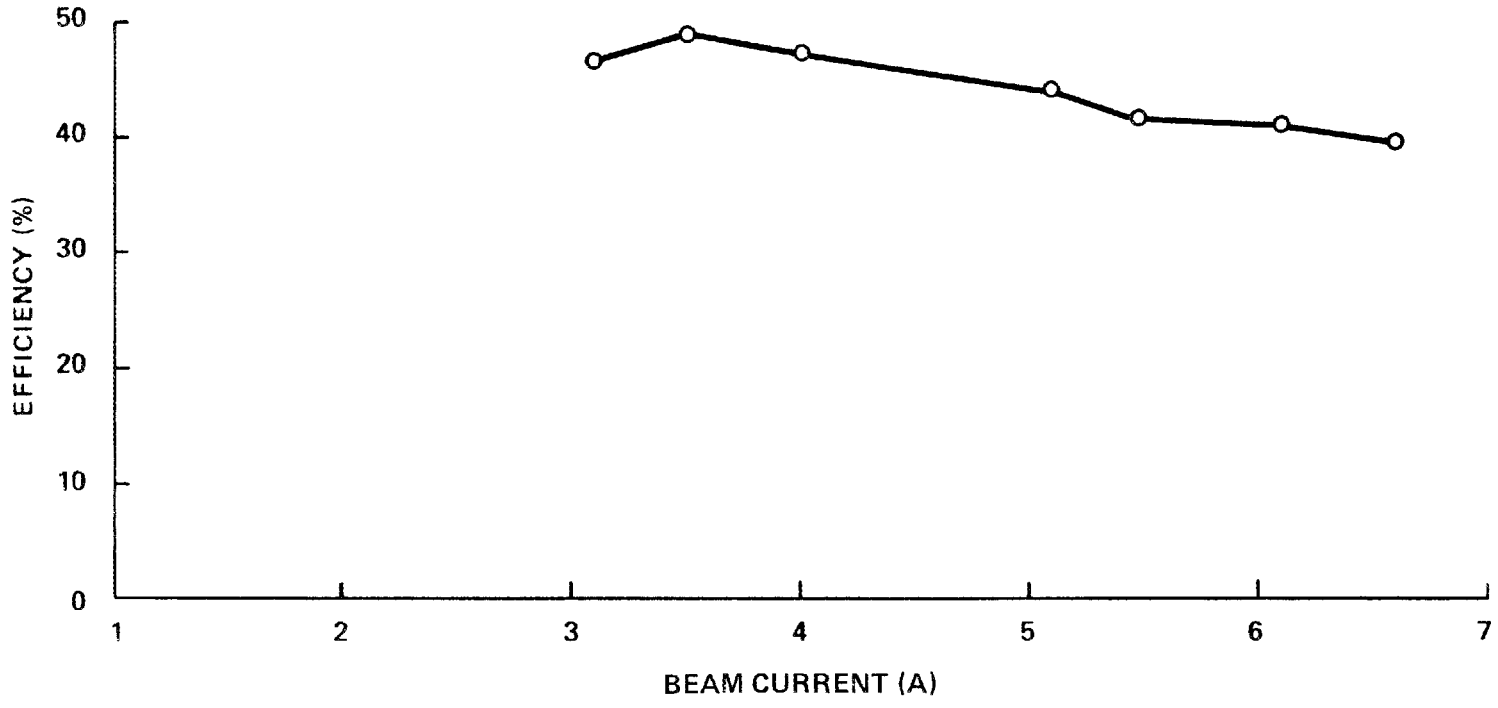

Figure 113. Efficiency vs Beam Current for VGA-8000 S/N 5R2 with Gun Anode Voltage Values Optimized for Peak Efficiency

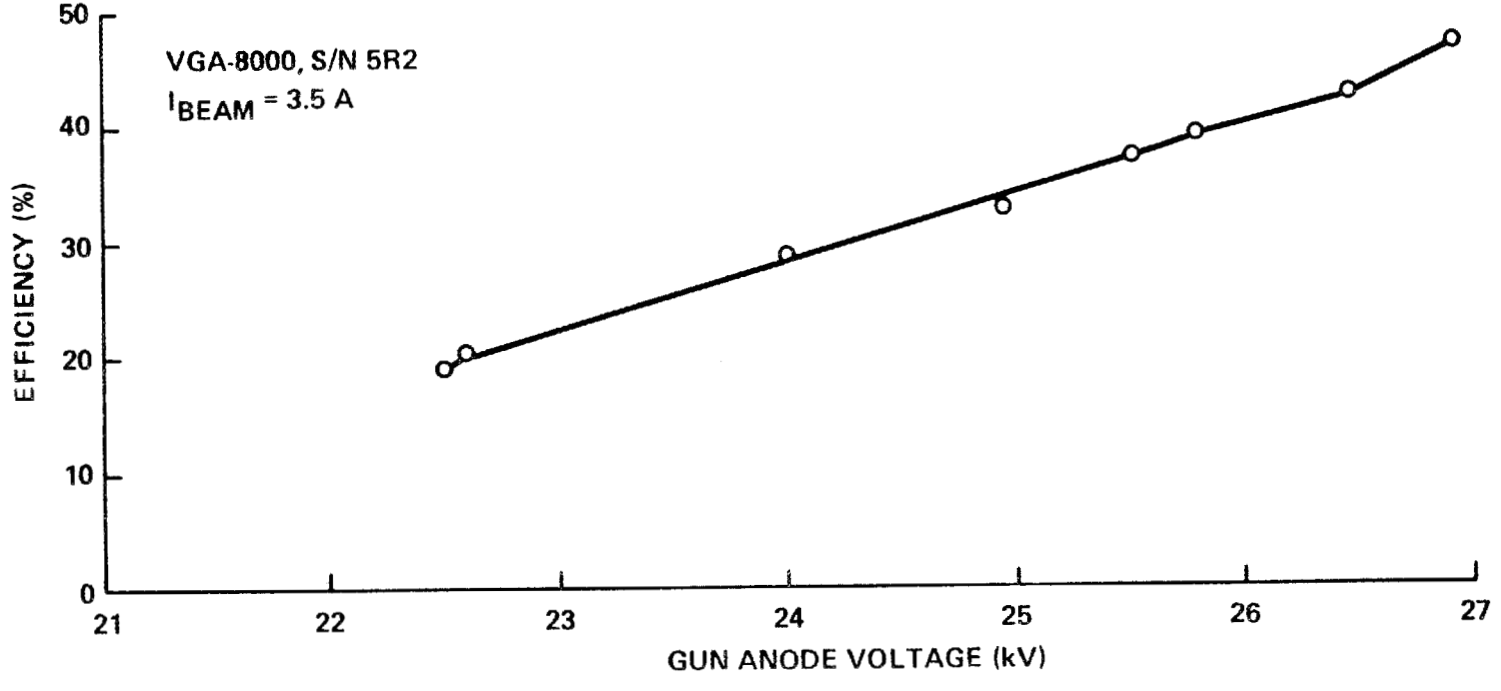

Figure 114. Efficiency vs Gun Anode Voltage (I_{Beam} = 3.5A)

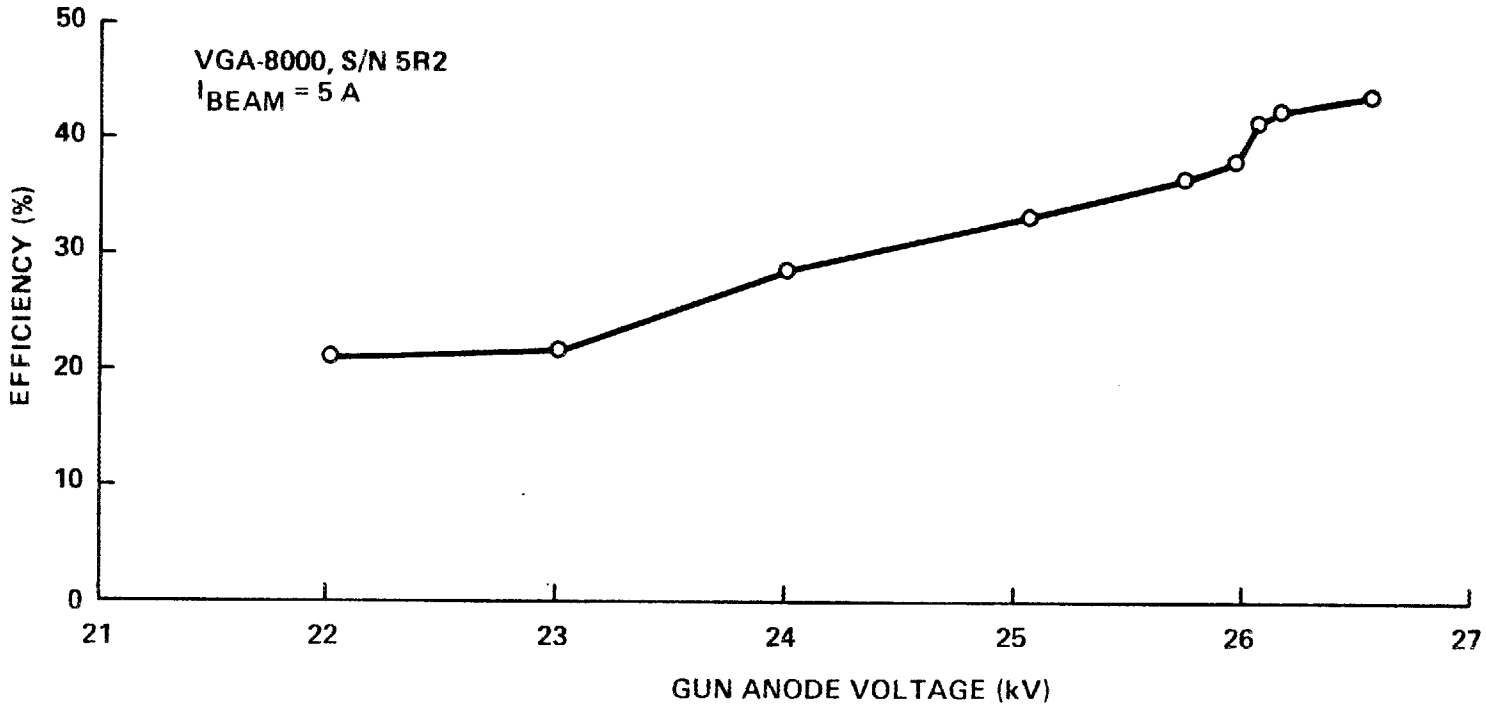

Figure 115. Frequency and Power vs Gun Anode Voltage (I_{Beam} = 5A)

operated again in pulsed and CW modes and found to be performing the same as before. The decision was made to ship the tube to ORNL for further testing.

TABLE 40

VGA-8000 S/N 5R2 Test Performance

OPERATING PARAMETERS

Collector Water Flow	261 gpm
Body Water Flow	3.6 gpm
Window Water Flow (both)	1 gpm
FC-75 Flow	3.0 gpm
Collector Seal Flow	2.5 gpm
Magnet Coil Currents:	Main 1 = 475 A
	2 = 469 A
	3 = 460 A
	4 = 478 A
	Gun 1 = 12.5 A
	2 = 11.0 A
Beam Voltage	80.2 kV
Gun Anode Voltage	25.3 kV
Cathode Current	6.7 A
Body Current	25 mA
Heater Voltage	10.8 V
Heater Current	6.03 A
Power Output	212 kW
Frequency	27.870 GHz

Following the initial installation at ORNL in June 1980, the tube was tested by ORNL and Varian personnel with rf output waveguide configurations appropriate for connection to EBT-S. The tube was operated into the load configurations shown on the following page.

Configuration No. 1 (Figure 116)

Tube - Mode Filter No. 1 - Stainless Steel Section No. 1 - Miter Bend - Mode Filter No. 2 - Stainless Steel Section No. 2 - Miter Bend - Copper Guide - Load.

The transmission efficiency $\frac{\text{Load power}}{\text{Tube output power}}$ was 70.3%

Configuration No. 2 (Figure 117)

Tube - Mode Filter No. 1 - Stainless Steel Section No. 1 - Miter Bend - Copper Guide - Stainless Steel Section No. 2 - Miter Bend Copper Guide-Load. The transmission efficiency was 82.1%

Configuration No. 3 (Figure 118)

Tube - Mode Filter No. 1 - Stainless Steel Section No. 1 - Mode Filter No. 2 - Miter Bend - Copper Guide - Stainless Steel Section No. 2 - Miter Bend - Copper Guide-Load. The transmission efficiency was 83.6%.

Varian VFA-8000A2 Mode Filters were used in these tests.

It was observed that the window FC-75 power dissipation followed that of the Mode Filter No. 1 closely as the tube parameters were adjusted, suggesting that the window itself is operating as a filter for non-circular electric modes.

During the month of September 1980, this tube was operated at 100 kW CW into the EBT-S plasma at ORNL.

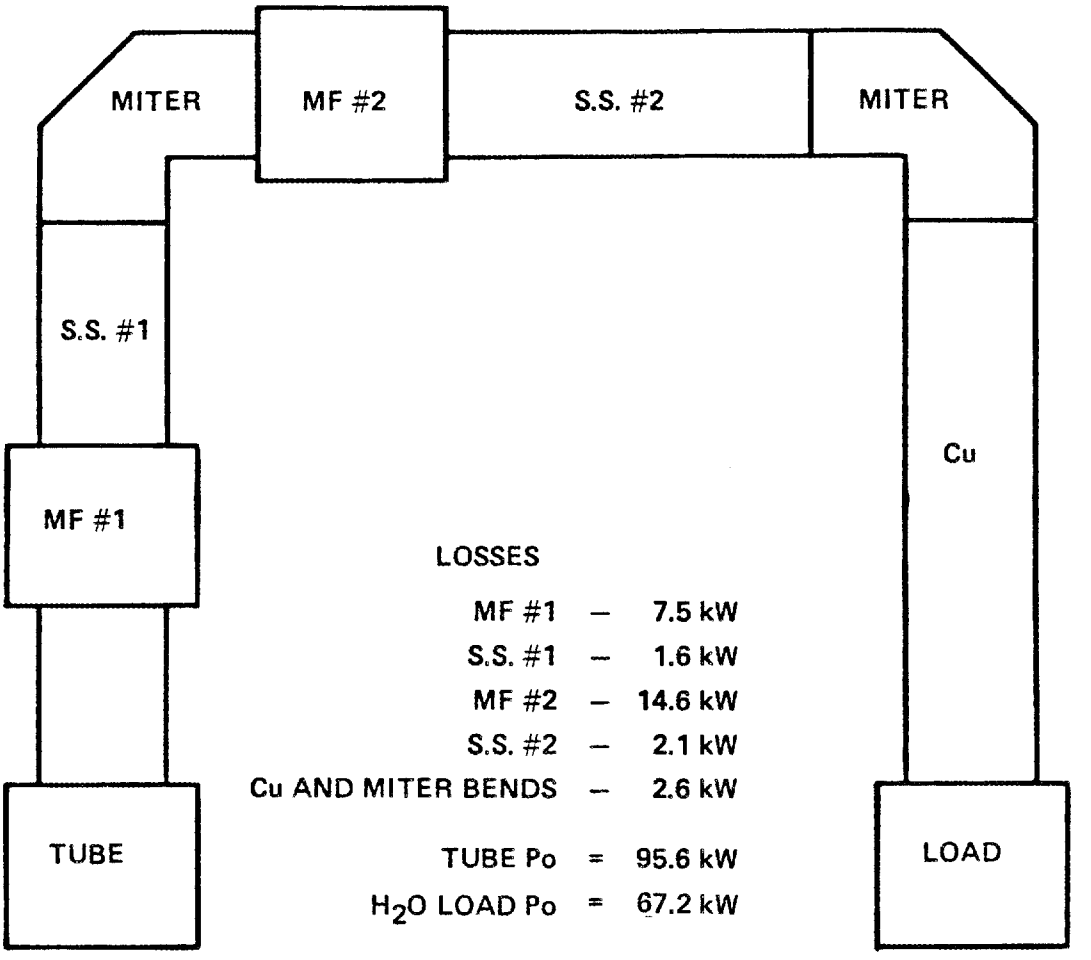

Figure 116. Waveguide Configuration No. 1

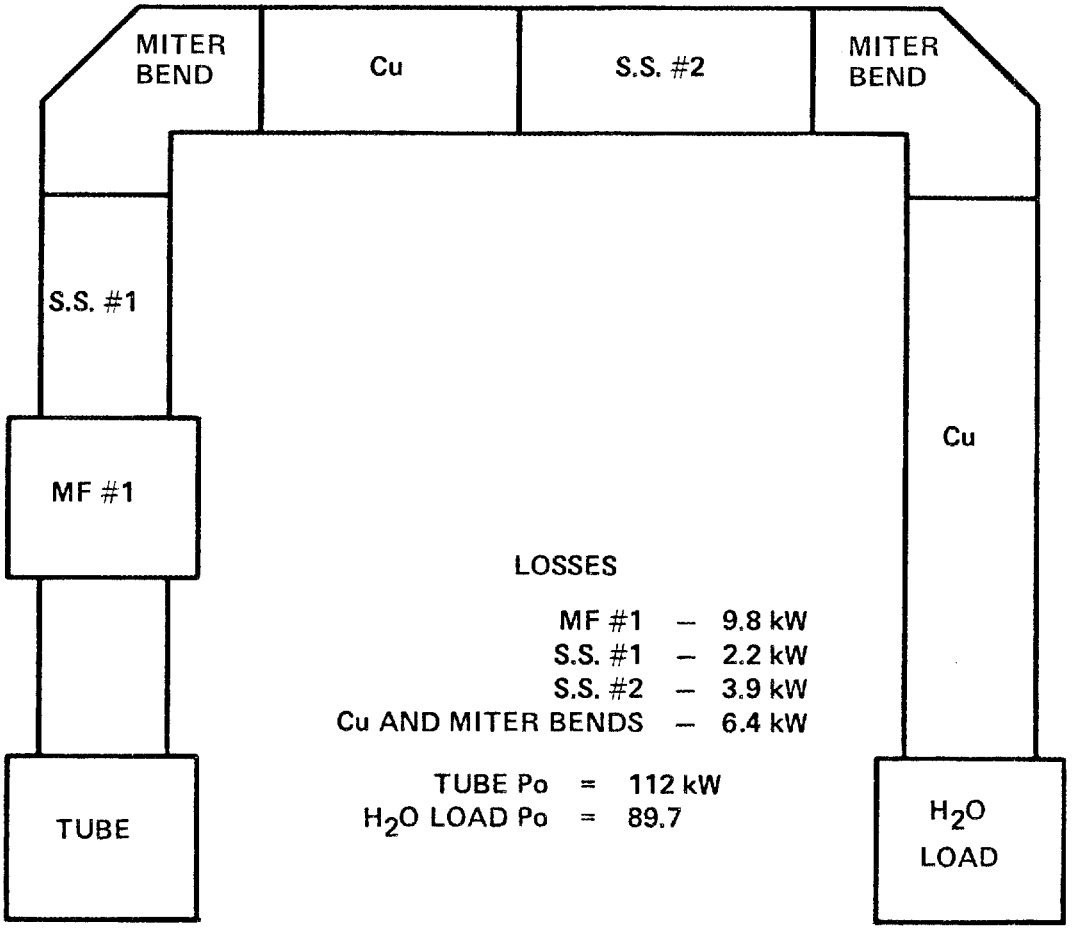

Figure 117. Waveguide Configuration No. 2

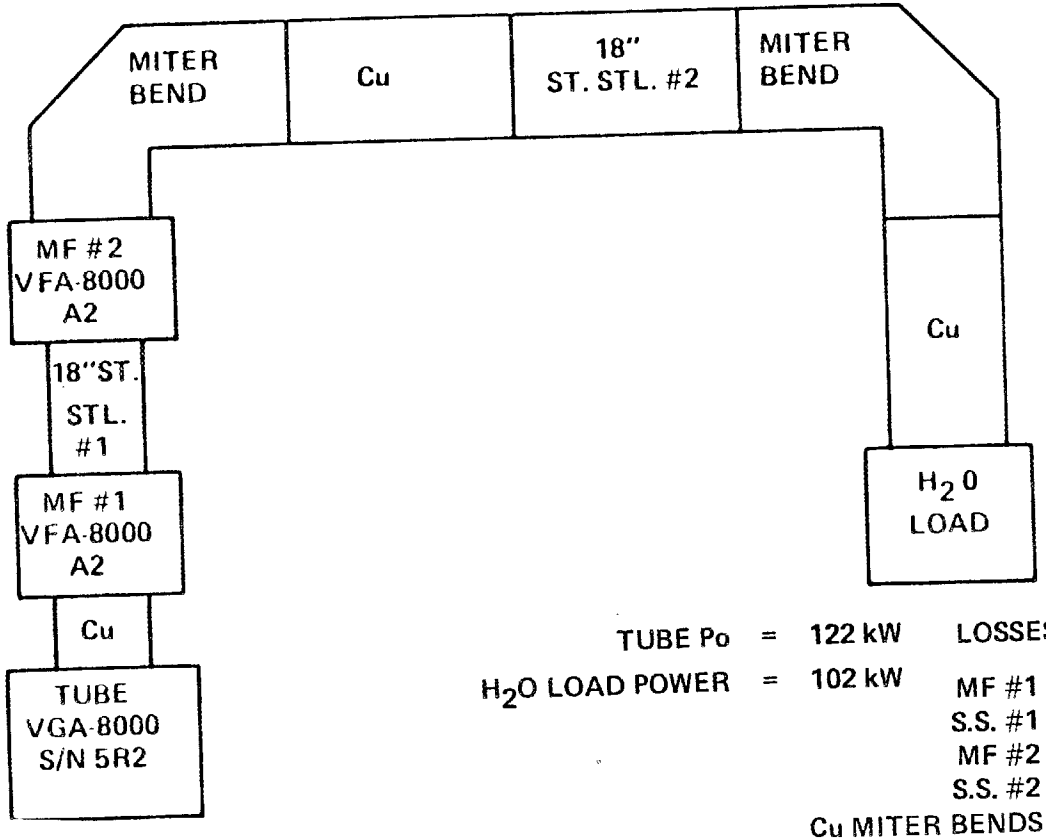

TUBE Po = 122 kW

H_2O LOAD POWER = 102 kW

LOSSES

MF #1	–	4.34 kW
S.S. #1	–	1.20 kW
MF #2	–	8.87 kW
S.S. #2	–	2.76 kW
Cu MITER BENDS	–	2.75 kW

Figure 118. Waveguide Configuration No. 3 (Tube, Mode Filter and Miter Bend Configuration at ORNL)

2. VGA-8000 S/N 6

This model was similar to S/N 5 except for modification in the following tube areas:

1. Lower collector insulator modified to eliminate the rubber water seal used on S/N 5.
2. Upper collector insulator eliminated
3. Improved design double-disc BeO window

The possible use of a water load mounted directly on the tube instead of the normal output window was contemplated, but the model was finally constructed using the double-disc BeO window. The ceramic of the lower collector insulator was 5/4 wavelengths thick with water in direct contact. This feature was expected to reduce microwave reflections and to provide excellent cooling.

AFTER NORMAL BAKEOUT, PROCESSING, AND PULSED OPERATION, S/N 6 WAS tested in the CW mode.

Tube No. 6 was operated with 50.3% efficiency at the 200 kW level. Efficiency of 52% was achieved at the 170 kW level. This is the highest gyrotron efficiency demonstrated to date. During August 1980, the tube was operated at the 200 kW CW level for more than 12 hours. Included in this was a 4-hour interval of continuous operation.

Figure 119 shows output power and efficiency vs the beam current. The calculated power curve of Figure 119 is calculated using a number of fixed parameters which may or may not remain fixed in actual operation. Some of these parameters are perpendicular energy, magnetic field, and the beam and gun anode voltages. As shown in Figure 119, the peak efficiency occurs around 4 amps. This is probably due to the Q of the cavity. For the peak efficiency to occur at 6 to 8 amps, the Q would have to be lowered, but the tube would be harder to start at the correct frequency.

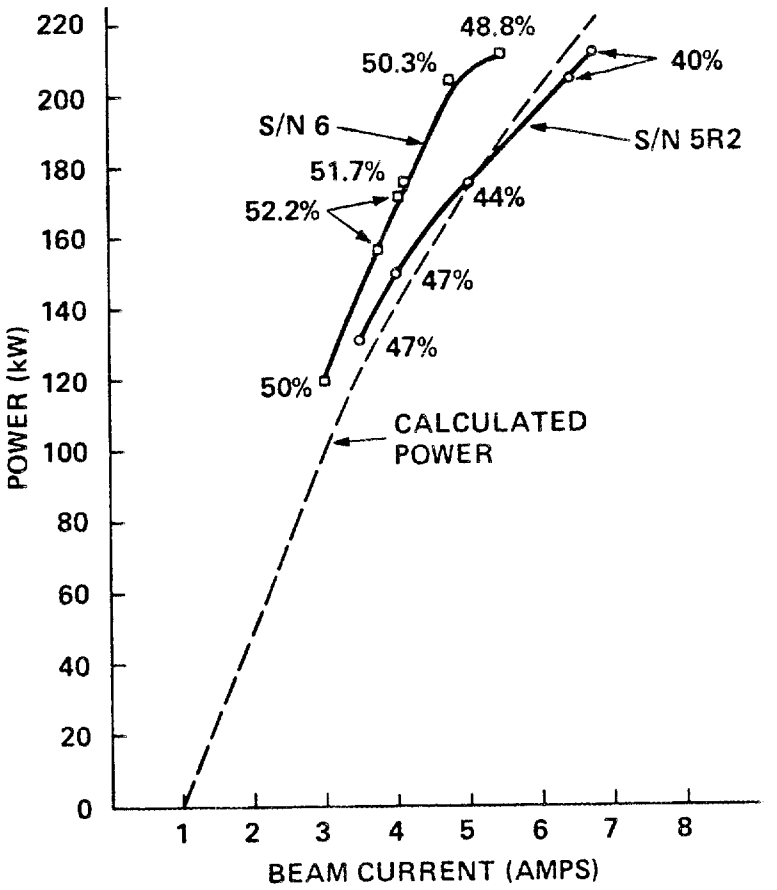

Figure 119. VGA-8000 S/N 5R2 and S/N 6 CW Power Output and Efficiency vs Beam Current

DC BLOCK

Because the window is at the same voltage as the collector S/N 6, it is necessary to have a dc insulator in the waveguide run between the window and ground. The dc block model VEA-8000C1 consists of a thin water-cooled teflon sheet separating the waveguide sections. This dc block had successfully operated for many hours on the tube and was used at the 200 kW rf power level.

Mode Filter and Miter Bend Tests

Three high power mode filters (Varian Model VFA-8000A3) were assembled, cold tested and flow tested. The maximum flow rate at 141 psi was increased to 26 GPM. Presuming a $10^{\circ}C$ temperature differential in the water, this will permit a dissipation of 68 kW.

These mode filters were then tested and evaluated in the configuration shown in Figure 120 using the VGA-8000 S/N 6 gyrotron as the power source.

The tube was operated in this configuration for 40 minutes after which testing was halted because of arcing. This was found to be due to overheating and oxidizing of miter bend No. 2 which created particles of copper oxide which fell on the output window. During this test the total rf power distribution was:

Mode Filter No. 1	6.8 kW CW
Mode Filter No. 2	9.3 kW CW
Water Load	159.0 kW CW
Total Power Output	175.1 kW CW

The miter bends are being modified for water cooling for future use. The window was cleaned and the tube re-tested to 200 kW CW output for two hours. A comparison of features, significant events and operating parameters for the VGA-8000A2 and VGA-8000A3 mode filters is shown in Figure 121. After consultation with ORNL, tests were halted due to the need to ship tube No. 6 to Oak Ridge.

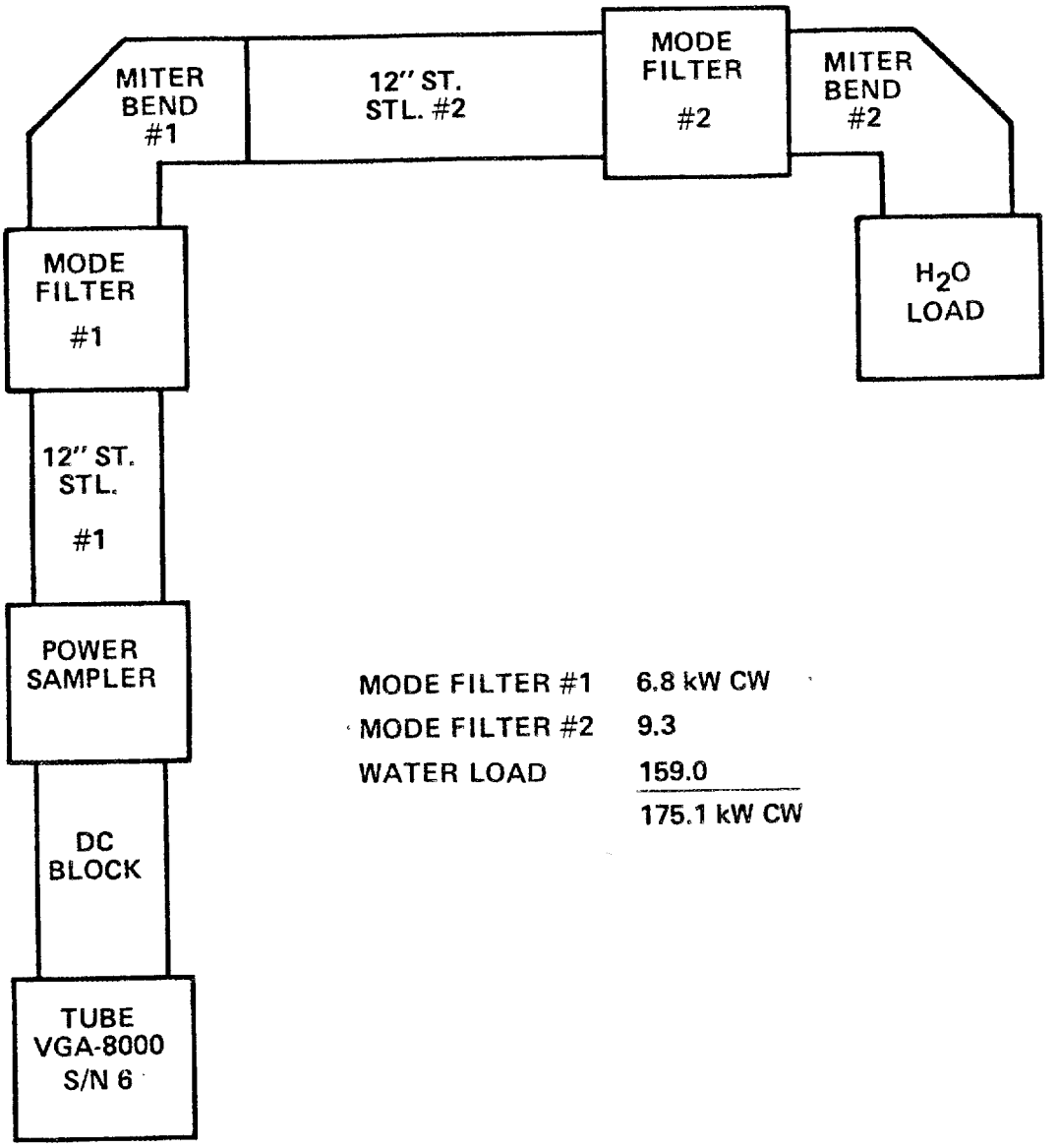

Figure 120. Mode Filter, Miter Bends and Tube Configuration for Testing High Power Mode Filter VFA-8000A3

VFA-8000 A2 MODE FILTER	VFA-8000 A3 MODE FILTER
FEATURES	
• 12 kW Power Handling Specification	50 kW Power Handling Specification
• Pulse and CW Operation	
• 4-6 dB Attenuation - Non Circular Modes	
• .3 to .5% Attenuation - Circular Modes	
SIGNIFICANT EVENTS	
• Tested to 183 kW Peak Power Flow - Mar 25	Tested to 9.3 kW CW August 26
• Tested to 148 kW CW Power Flow	Testing to be continued
• Two Units Delivered to ORNL - May 29	
• Tested to 14.6 kW CW Power Absorption	
• at ORNL - July 9	
OPERATING PARAMETERS	
• Water Flow/Pressure = 5 GPM - 120 PSI	25 GPM - 130 PSI
• Water Temperature $\Delta T = 9°C$	$\Delta T = 9°C$

Figure 121.. Comparison of VFA-8000A2 and VFA-8000A3 Mode Filters

Shipping

Tube No. 6 was shipped to ORNL in September. Accelerometers were placed at both ends of the tube as well as along the axis of the tube. The accelerometer on axis registered 15 Gs. At the collector end, the vertical read 22.5 Gs and the horizontal was 2.5 Gs. At the gun end, they were 25 Gs vertical and 7.5 Gs horizontal.

3. VGA-8000 S/N 8

This model was similar to S/N 6 except for three modifications:

1. Cooling water system redesigned
2. Addition of an outer shroud
3. Collector seal modified for improved strength

The new cooling water system aimed at improved tube cooling. The new outer shroud simplified plumbing connections and had the secondary effect of improving tube appearance. The outer rings of the collector seal were fashioned of monel instead of stainless steel to more closely match temperature coefficients of metal and ceramic, minimizing the differential expansion problem.

After routine bakeout testing of this tube began on September 11. It was successfully hipotted with no abnormal behavior observed. The test set was then connected for pulse operation and testing continued. Cathode emission was low initially and increased slowly to its rated 8 amperes after approximately 30 hours.

The slow increase of emission is judged to be due to the long storage time of the gun assembly. It was stored in a warm nitrogen atmosphere for approximately four months. Since early September, all completed gyrotron gun assemblies have been stored in a vacuum chamber to further minimize the possibility of contamination.

At the start of testing, the collector exhibited a water flow problem. At high flow rates a "water-hammer" effect took place. Using x-ray techniques, a single channel in the collector water flow was found to be blocked with braze material. The tube was run using a lower collector flow, 108 gpm vs 240 gpm. This is not seen to be a critical problem.

The tube has been processed up to 144 kw of peak output power at 7.2% duty. Further testing is planned on a follow-on program.

4. VGA-8000 S/N 11

This model was designed to be similar to S/N 8 except for oscillator cavity modifications aiming at improved mode separation. It incorporated an alumina window similar to that used in S/N 5 and the new, K-8002 electron gun. Unfortunately, a number of problems involving vacuum leaks were encountered during assembly. These problems were resolved by the end of the development program.

Difficulty was encountered with a vacuum leak in the drift tube load assembly. The leak was traced to a "pipe" through the stainless steel outer member. This was repaired by brazing but a second leak developed in a brazed joint near the weld flange which joins with the anode. This was also repaired and the assemby was found to be vacuum tight.

All subassemblies were completed, and final assembly began on September 26. Unfortunately, an irreparable leak developed in the weld joint between the anode and drift tube load. It is believed that alloying of the braze material used earlier embrittled the weld flange to a degree where a vacuum tight weld could not be made.

Because of this failure and similar experience with some of the previous assemblies, the stainless steel bar from which the parts were made was identified, located, sampled, and examined by Varian metallurgists. It was found to be within specifications but not recommended for thin cross

sections in the plane orthogonal to the "pipes". A design modification has been initiated which greatly reduces the "pipe" problem. It is planned for incorporation in tube No. 11.

This tube has an alumina window identical to that in VGA-8000 No. 5. It also will have the first K-8002 gun.

K-8002 Gun

This gun was developed during fiscal year 1980. The first assembly was completed in early September.

The K-8002 with respect to electron optics is identical to the K-8000 but incorporates several changes. The most notable change is a radiation heated cathode button compared to the "potted" heater in the K-8000. The internal stem structure has been redesigned to improve heater efficiency by better heat shielding and optimized routing of the cooling oil. The top of the stem has been redesigned to eliminate the top screw which will lessen the problem of sputtering on the upper ceramic seal.

d. VGA-8000 S/N 9

This model was designed to use a 5-inch-diameter double-disc BeO window, thus eliminating the taper between the 5-inch-diameter collector and the window assembly. Effort on the model was halted with the success of axisymmetric tubes incorporating the 2.5-inch-diameter double-disc windows. These latter models had produced 200 kW CW power output.

e. VGA-8000 S/N 10

This model, like S/N 9, was designed to use aa 5-inch-diameter double-disc BeO window. Effort on the tube was discontinued for the same reason.

V. SUMMARY

In 1975, Varian Associates, Inc., completed a study of a 120 GHz, 100 kW, CW gyroklystron amplifier. In 1976, Varian was funded to start a hardware development program with the goal of a 28 GHz, 200 kW, CW gyroklystron amplifier to provide electron cyclotron resonance heating for the Elmo Bumpy Torus - Scale experiment (EBT-S). In the design of this device, it was to be kept in mind the ultimate higher frequency goal.

The early gyroklystron development resulted in the development of a room temperature hollow core conductor solenoid magnet and an electron gun design that would be used throughout the development program. Computer programs were used quite successfully for designing the solenoid magnet with iron pole pieces and calculating electron trajectories for optimizing the gun design.

The early developments also produced the alternating copper and silicon carbide loaded beryllia rings successfully used for preventing rf from propagating back to the gun region.

Another successful development of this program has been the ceramic cone multimode broadband water load. There has never been a water load failure. The first water load is still in use at Varian.

Feedback coupling through the beam tunnel slowed successful gyroklystron development. Each succeeding experiment increased the stable gain and output power but efficiency was limited to 9 - 10%.

The back-up oscillator was in instant success relegating further gyroklystron development to the back burner. The first pulsed gyrotron oscillator produced 248 kw of rf output power.

Efforts to separate the rf output coupling from the spent electron beam collection by means of a triple miter bend were scuttled by mode conversion into non-circular electric modes and their deleteroius effects on guns, mode suppressors, collector insulators, VacIon pumps, and windows.

The use of an axisymmetric design and the introduction of the FC-75 face cooled double-disc window to gyrotrons resulted, on February 12, 1980, in the production of 212 kW, CW, at 28 GHz. This represents a major milestone in the development of gyrotrons.

VI. REFERENCES

1. H. R. Jory, E. L. Lien, and R. S. Symons, "Final Report, Millimeter Wave Study Program," Oak Ridge National Laboratory Order No. Y-12 11Y-49438V, November 1975.

2. D. V. Kisel', G. S. Korablev, V. G. Navel'yev, M. I. Petelin, and Sh. E. Tsimring, "An Experimental Study of a Gyrotron, Operating at the Second Harmonic of the Cyclotron Frequency, with Optimized Distribution of the High Frequency Field," Radio Engineering and Electronic Physics, vol. 19, No. 4, (1974), pp. 95-100.

3. V. L. Granatstein, P. Sprangle, M. Herndon, R. K. Parker and S. P. Schlesinger, "Microwave Amplification with an Intense Relativistic Electron Beam," JAP, vol. 46, No. 9, (1975) pp. 3800-3805.

4. F. Friedlander, E. Galli, H. Jory, F. Kinney, K. Miller, J. Shively and R. Symons, "Development Program for a 200 kW, CW, 28 GHz Gyroklystron", Quarterly Report No. 1, April through June 1976, report prepared by Varian Associates, Inc., under Subcontract Purchase Order No. 53X01617C for Oak Ridge National Laboratory operated by Union Carbide Corporation for the U.S. Department of Energy under Contract No. W-7405-eng-26.

5. F. Friedlander, E. Galli, H. Jory, K. Miller, J. Shively and R. Symons, Development Program for a 200 kW, CW, 28 GHz Gyroklystron", Quarterly Report No. 2, July through September 1976, report prepared by Varian Associates, Inc., under Subcontract Purchase Order No. 53X01617C for Oak Ridge National Laboratory operated by Union Carbide Corporation for the U.S. Department of Energy under Contract No. W-7405-eng-26.

6. F. Friedlander, E. Galli, S. Hegji, H. Jory, K. Miller, J. Shively and R. Symons", Development Program for a 200 kW, CW, 28 GHz Gyroklystron", Quarterly Report No. 3, October through December 1976, report prepared by Varian Associates, Inc., under Subcontract Purchase Order No. 53X01617C for Oak Ridge National Laboratory operated by Union Carbide Corporation for the U.S. Department of Energy under Contract No. W-7405-eng-26.

7. S. Hegji, H. Jory, J. Shively and R. Symons, "Development Program for a 200 kW, CW, 28 GHz Gyroklystron", Quarterly Report No. 4, January through March 1977, report prepared by Varian Associates, Inc., under Subcontract Purchase Order No. 53X01617C for Oak Ridge National Laboratory operated by Union Carbide Corporation for the U.S.Department of Energy under Contract No. W-7405-eng-26.

8. S. Hegji, H. Jory and J. Shively, "Development Program for a 200 kW, CW, 28 GHz Gyroklystron", Quarterly Report No. 5, April through June 1977, report prepared by Varian Associates, Inc., under Subcontract Purchase Order No. 53X01617C for Oak Ridge National Laboratory operated by Union Carbide Corporation for the U.S. Department of Energy under Contract No. W-7405-eng-26.

9. S. Hegji, H. Jory and J. Shively, "Development Program for a 200 kW, CW, 28 GHz Gyroklystron", Quarterly Report No. 6, July through

September 1977, report prepared by Varian Associates, Inc., under Subcontract Purchase Order No. 53X01617C for Oak Ridge National Laboratory operated by Union Carbide Corporation for the U.S. Department of Energy under Contract No. W-7405-eng-26.

10. H. Jory, S. Evans, S. Hegji and J. Shively, "Development Program for a 200 kW, CW, 28 GHz Gyroklystron", Quarterly Report No. 7, October through December 1977, report prepared by Varian Associates, Inc., under Subcontract Purchase Order No. 53X01617C for Oak Ridge National Laboratory operated by Union Carbide Corporation for the U.S. Department of Energy under Contract No. W-7405-eng-26.

11. H. Jory, S. Evans, S. Hegji and J. Shively, "Development Program for a 200 kW, CW, 28 GHz Gyroklystron", Quarterly Report No. 8, January through March 1978, report prepared by Varian Associates, Inc., under Subcontract Purchase Order No. 53X01617C for Oak Ridge National Laboratory operated by Union Carbide Corporation for the U.S. Department of Energy under Contract No. W-7405-eng-26.

12. H. Jory, S. Evans, S. Hegji, J. Shively, R. Symons and N. Taylor, "Development Program for a 200 kW, CW 28 GHz Gyroklystron", Quarterly Report No. 9, April through June 1978, report prepared by Varian Associates, Inc., under Subcontract Purchase Order No. 53X01617C for Oak Ridge National Laboratory operated by Union Carbide Corporation for the U.S. Department of Energy under Contract No. W-7405-eng-26.

13. H. Jory, S. Evans, S. Hegji, J. Shively, R. Symons and N. Taylor, "Development Program for a 200 kW, CW 28 GHz Gyroklystron", Quarterly Report No. 10, July through September 1978, report prepared by Varian Associates, Inc., under Subcontract Purchase Order No. 53X01617C for Oak Ridge National Laboratory operated by Union Carbide Corporation for the U.S. Department of Energy under Contract No. W-7405-eng-26.

14. H. Jory, S. Evans, S. Hegji, J. Shively, R. Symons and N. Taylor, "Development Program for a 200 kW, CW 28 GHz Gyroklystron", Quarterly Report No. 11, October through December 1978, report prepared by Varian Associates, Inc., under Subcontract Purchase Order No. 53X01617C for Oak Ridge National Laboratory operated by Union Carbide Corporation for the U.S. Department of Energy under Contract No. W-7405-eng.26.

15. H. Jory, S. Evans, S. Hegji, J. Shively, R. Symons and N. Taylor, "Development Program for a 200 kW, CW, 28 GHz Gyroklystron", Quarterly Report No. 12, January through March 1979, report prepared by Varian Associates, Inc., under Subcontract Purchase Order No. 53X01617C for Oak Ridge National Laboratory operated by Union Carbide Corporation for the U.S. Department of Energy under Contract No. W-7405-eng-26.

16. H. Jory, S. Evans, J. Shively, R. Symons and N. Taylor, "Development Program for a 200 kW, CW, 28 GHz Gyroklystron", Quarterly Report No. 13, April through June 1979, report prepared by Varian Associates, Inc., under Subcontract Purchase Order No. 53X01617C for Oak Ridge National Laboratory operated by Union Carbide Corporaton for the U.S. Department of Energy under Contract No. W-7405-eng-26.

17. H. Jory, et al., "Development Program for a 200 kW, CW 28 GHz Gyroklystron", Quarterly Report No. 14, July through September 1979, report prepared by Varian Associates, Inc., under Subcontract Purchase Order No. 53X01617C for Oak Ridge Natoinal Laboratory operated by Union Carbide Corporation for the U.S. Department of Energy under Contract No. W-7405-eng-26.

18. H. Jory et al., "Development Program for a 200 kW, CW 28 GHz Gyroklystron", Quarterly Report No. 15, October through December 1979, report prepared by Varian Associates, Inc., under Subcontract Purchase Order No. 53X01617C for Oak Ridge National Laboratory operated by Union Carbide Corporation for the U.S. Department of Energy under Contract No. W-7405-eng-26.

19. H. Jory et al., "Development Program for a 200 kW, CW 28 GHz Gyroklystron", Quarterly Report No. 16, January through March 1980, report prepared by Varian Associates, Inc., under Subcontract Purchase Order No. 53X01617C for Oak Ridge National Laboratory operated by Union Carbide Corporation for the U.S. Department of Energy under Contract No. W-7405-eng-26.

20. H. Jory et al., "Development Program for a 200 kW, CW 28 GHz Gyroklystron", Quarterly Report No. 17, April through June 1980, report prepared by Varian Associates, Inc., under Subcontract Purchase Order No. 53X01617C for Oak Ridge National Laboratory operated by Union Carbide Corporation for the U.S. Department of Energy under Contract No. W-7405-eng-26.

21. C. H. Collie, J. B. Hasted and D. M. Ritson, "The Dielectric Properties of Water and Heavy Water", Proc. Phys. Soc. 60, p. 145, 1948.

22. Yu. V. Bykov and A. L. Gol'denberg, "Influence of Resonator Profile on the Power of a Cyclotron Resonance Maser", Izvestia vuz. Radiofizika, Vol. 18, No. 7, pp. 791-792, July 1975.

23. H. R. Jory, and R. S. Symons, "Supplementary Report No. 2, Millimeter Wave Study Program", prepared by Varian Associates, Inc., under Subcontract Purchase Order No. 11Y-49438V for Oak Ridge National Laboratory operated by Union Carbide Corporation for the U.S. Department of Energy under Contract No. W-7405-eng-26, April 1976.

24. H. R. Jory and R. S. Symons, "Supplementary Report, Millimeter Wave Study Program", prepared by Varian Associates, Inc., under Subcontract Purchase Order No. 11Y-49438V for Oak Ridge National Laboratory operated by Union Carbide Corporation for the U.S. Department of Energy under Contract No. W-7405-eng-26, February 1976.

APPENDIX A
THEORY OF GYROKLYSTRONS

A. COMPARISON OF SMALL-SIGNAL THEORY WITH BALLISTIC CODE

The gain of a gyroklystron was determined using the ballistic trajectory code and then was calculated using the small-signal theory outlined in a prior report.[23] The parameters listed in Table A-I were used in the calculations and are those we plan to use for the first experimental tube.

Table A-I
Gyroklystron Parameters

Input cavity length, L_1	1.5 λ
Output cavity length, L_2	2.0 λ
Drift tube length	3.0 λ
Beam voltage, V_b	80 kV
Beam current, I_b	8 A
$\beta_\perp = v_\perp/c$	0.45
$\beta_\parallel = v_\parallel/c$	0.225
$\gamma = (1 - \beta_\perp^2 - \beta_\parallel^2)^{-1/2}$	1.157
$k_\parallel = \omega/v_\parallel = 2\pi\ c/\beta_\parallel\ \lambda$	
Beam radius, r_b	0.293 λ
Operating frequency/cyclotron frequency, ω/Ω	1.06
$V_n = m_o c^2/e =$	511,000 V

In the computer calculation, relatively low values of input and output cavity fields were chosen in order to assure small-signal conditions in the cavities. Unfortunately, as will be discussed later, because of the long drift length, the input cavity field was not quite small enough to provide much margin below current saturation. The fields were $E_1\lambda$ = 7472 V in the input cavity and $E_2\lambda$ = 14,943 V in the output cavity. The computer gave an average energy loss of 7640 V for eight electrons started at equal phase

increments during a cycle. The power output for this extremely overloaded case was 7640 V multiplied by 8 A, or 61,120 W. The load conductance was therefore

$$G_L = \frac{2P}{(E\lambda)^2} = \frac{2(61,120)}{(14,943)^2} = 5.474 \times 10^{-4} \text{ mhos} \tag{1}$$

The electronic conductance, G_{e2}, resulting from the interaction of the beam with the output cavity can be calculated using Equation 5 in the reference[23]. It is -0.582×10^{-4}. The transconductance may also be calculated using formulas in the reference.

$$\frac{G_{21}}{G_b} = M_1 M_2 R \Theta_{21} \tag{2}$$

in which

$$M = \frac{1}{2\pi^2} (k_{\parallel} L) \beta_{\perp} \sqrt{g(\delta k_{\parallel} L)} \tag{3}$$

$$R = \frac{V_b/V_n}{1 + V_b/V_n} \quad . \tag{4}$$

For the parameters listed in Table A-I, Θ_{21}, the cavity midplane-to-midplane drift angle is 132.64 radians. M_1 for the 41.88 radian input cavity at 6% slip between the signal frequency and cyclotron frequency is 0.758. M_2 for the 55.85 radian output cavity is 0.900 and R is 0.135. G_{21} is therefore 10.01×10^{-4} mhos. Both the coupling coefficients and the electronic conductances given above have been corrected to compensate for the fact that the maximum electric field at the electron orbit is 93% of the maximum cavity field.

By the use of Equation 3 in the reference, it is possible to verify the small-signal theory by calculating

$$E_1 \lambda = E_2 \lambda \left(\frac{G_{e2} + G_{02} + G_{E2}}{G_{21}} \right) \quad . \qquad (5)$$

Noting that G_{02} is negligible compared to the other conductances, one obtains $E_1 \lambda = 7{,}297$ V which compares with 7.472 V used in the computer calculation.

There is one problem with this comparison, and that is that G_{21} is based on the small argument approximation of J_1 (z); that is, as stated in Reference 23

$$\left| \frac{I_2}{M_2} \right| = 2 I_b J_1 \left(M_1 R \Theta_{21} \frac{E_1 \lambda}{V_b} \right) \qquad (6)$$

$$= 2 I_b J_1 (1.267)$$

$$= 1.029 I_b$$

for $E_1 \lambda = 7.472$ V. Using this value of current gives $E_2 \lambda = 15{,}144$ when nonlinear bunching is considered.

A comparison of these calculations is given in Table A-II.

Table A-II
Calculation Comparison

Method of Calculation	$E_2 \lambda / E_1 \lambda$
Computer	1.999
Small-signal, linear bunching	2.0477
Small-signal, non-linear bunching	2.026

B. SPACE-CHARGE GAIN ENHANCEMENT

An equation derived in the first quarterly report[4] permits us to estimate the effect of space charge on the gain of the Gyroklystron. The equation was

$$A = \frac{I_{rf}}{I_b} = C_1 \quad e^{k_\parallel z/\Theta} + C_2 e^{-k_\parallel z/\Theta} \tag{7}$$

in which

$$\frac{1}{\Theta} = \left\{ \frac{1}{6\pi^4} \quad \frac{I_b}{V_n} \quad \frac{\eta_1}{\gamma\ \beta_\perp\ \beta_\parallel} \quad \frac{\lambda}{r_b} \left[1 + 2\beta_\perp^2 \gamma^2 \left(1 - \beta_\perp^2 \right) \right] \right\}^{1/2}$$

η_1 = 377 ohms, the characteristics impedance of free space; the other parameters are as defined in Table A-I, and C_1 and C_2 arbitrary constants used to match the growth rate of radio-frequency current on the beam to the degree of angular velocity modulation at the first cavity. (Note that Θ in the above expression is a drift angle for exponentiation of the current modulation and $\Theta_{21} = k_\parallel z_{21}$ is the drift length between cavities. Beyond the fact that they are both drift angles, there is no relationship between them.) The ratio frequency current in the beam is given by

$$\frac{I_{rf}}{I_b} = M_1 \ R\ (k_\parallel z) \frac{E_1 \lambda}{V_b} \ ;$$

consequently, at the center of the input cavity where we assume the rf current is zero and increasing with a slope determined by the first cavity voltage, this slope will be

$$\frac{d}{d\ (k_\parallel\ z)} \left(\frac{I_{rf}}{I_b} \right) = M_1\ R \left(\frac{E_1\ \lambda}{V_b} \right) \quad . \tag{8}$$

From Equation 7 and the initial conditions above, we can therefore write

$$C_1 + C_2 = 0 \tag{9}$$

and

$$M_1\ R \left(\frac{E_1\ \lambda}{V_b} \right) = \frac{C_1}{\Theta} - \frac{C_2}{\Theta} \quad . \tag{10}$$

Using again $E_1 \lambda = 7{,}472$ V, $V_b = 80 \times 10^3$ V, $M_1 = 0.758$, $R = 0.135$, and $\Theta = 50$ radians which was calculated in a prior report[4], we obtain $C_1 = 0.239$ and $C_2 = -0.239$. If these values are used in Equation 7, at the midplane of the output cavity we have $(I_{rf}/I_b) = 3.34$. This compares with 1.26 based on linear bunching. The prediction, therefore, is that space charge effects could increase the gain by 20 log (3.34/1.26) = 8.46 dB.

Two comments should be made about this calculation. The first is trivial and is that the value of I_{rf}/I_b of 3.34 is larger than the maximum value of 2 which can be achieved for infinitely short current bunches. A more realistic value would have resulted had we used a lower value of $E_1 \lambda$. The important answer, the 8.46 dB gain increase due to space charge, would not have been any different, however.

The second comment is more important. The assumption used in the derivation of Equation 7, that all electron helix axes are contained by an infinitely thin circular cylinder, makes the effect of the space charge much greater than would be the case if the axes were contained in a cylinder of some wall thickness. We therefore believe the estimate of a 8.46 dB increase in gain due to space charge is really an upper bound on the magnitude of the effect.

C. BEAM COUPLING AND LOADING FOR HIGHER ORDER AXIAL MODE NUMBERS

Because we have had so much difficulty loading long output cavities, having a single half-sinusoidal field variation, to a Q low enough to provide either an optimum load or stability, we decided to investigate the interaction of the beam with cavities having more half-sinusoids of field variation along their length. Such cavities are more easily loaded to low Q because of the higher group velocity of the waves in them.

In prior reports,[1,23] a coupling coefficient was derived which related the energy change of an electron to the cavity voltage $V \equiv E \lambda$, in which E is the peak value of electric field in both space and time and λ is the free

space wavelength. For cavities in which the transverse electric field varies as a half-sinusoid, it was shown that this coupling coefficient is

$$M = \frac{\Delta V_b}{V_b} = \frac{(k_{\parallel} L)\, \beta_{\perp}}{2\pi^2} \sqrt{g\,(\delta k_{\parallel} L)} \tag{11}$$

in which

$$\sqrt{g(\delta k_{\parallel} L)} = \sqrt{\frac{\cos^2 (\delta k_{\parallel} L/2)}{\left[1 - \left(\frac{\delta k_{\parallel} L}{\pi}\right)^2\right]^2}}$$

L is the length of the cavity and $\delta = (\omega - \Omega)/\omega$ is the normalized amount by which the signal frequency ω exceeds the electron cyclotron frequency Ω. The expression for $g\,(\delta k_{\parallel} L)$ has been generalized to apply to cavities having any number, ℓ, of half-sinusoid field variations. The generalized expression for g is

$$g(\delta k_{\parallel} L) = \left[\frac{\ell}{\ell^2 - (\delta k_{\parallel} L/\pi)^2}\right]^2 \left[\frac{1 - \cos \ell \pi \cos \delta k_{\parallel} L}{2}\right] \tag{12}$$

Figure A-1 shows $\sqrt{g(\delta k_{\parallel} L)}$ for $\ell = 1$, 2 and 3. It is interesting that the maximum value of this function rapidly approaches 0.79 as ℓ is increased. 0.79 is the value of $\sqrt{g}$ for $\ell = 1$ and $\delta k_{\parallel} L = \pi$, so it is clear that for higher values of ℓ, maximum coupling is achieved when the angular coordinate of the electrons advances by π with respect to the radio frequency field in order to compensate for each spatial phase reversal of the standing wave in the cavity.

The expression for beam loading has also been generalized. The form of the equation remains as before,[24]

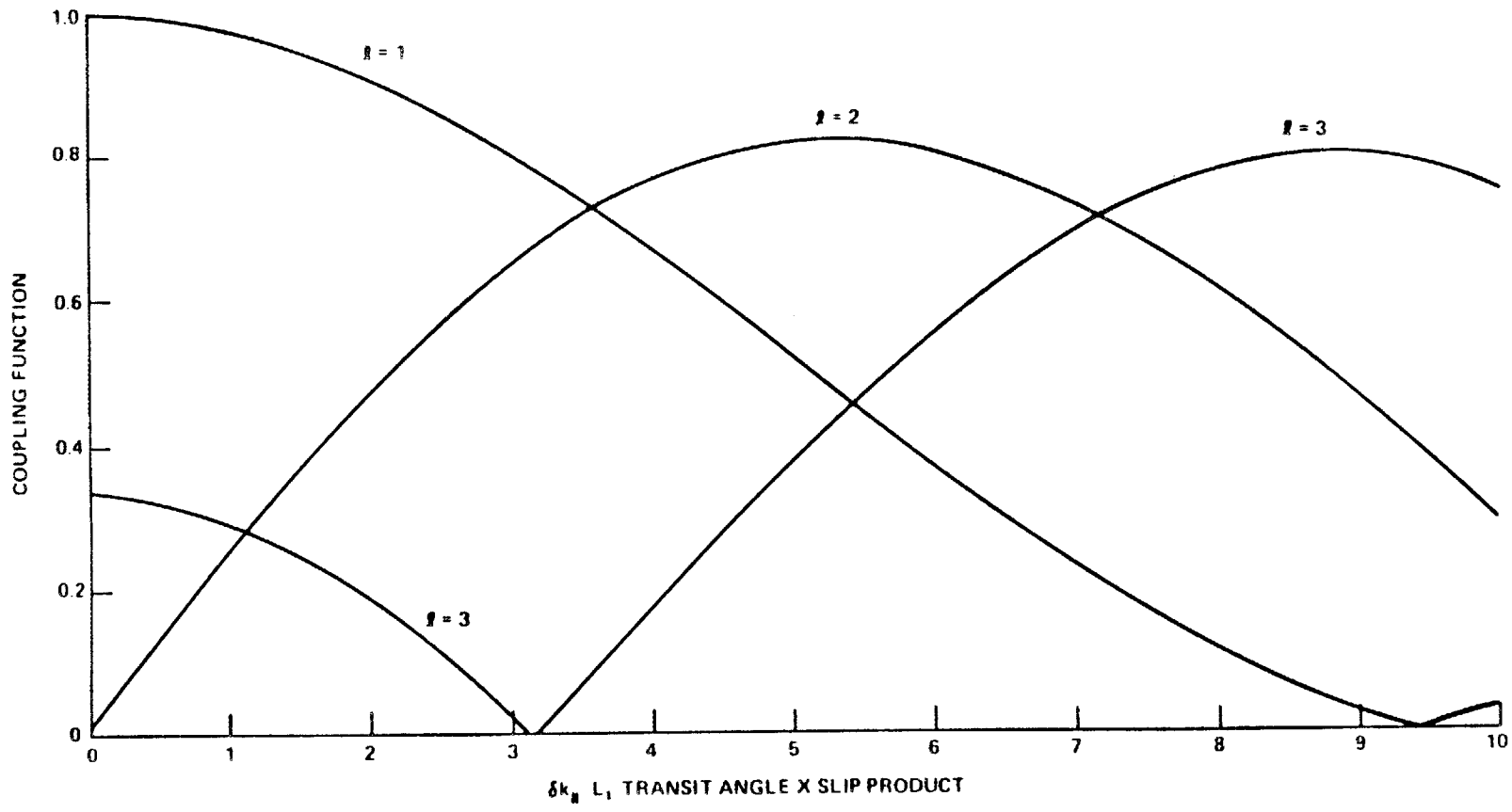

Figure A-1. The Coupling Function $\sqrt{g(\delta k_{\parallel} L)}$ vs $\delta k_{\parallel} L$, the Transit Angle X Slip Product

$$G_e = \frac{I_b}{V_b} \frac{(k_\parallel L)^2}{8\pi^4} \frac{V_b}{V_n}\left(1 + \frac{V_b}{V_n}\right)\left[\frac{2 - \beta_\perp^2}{\left(1 + \frac{V_b}{V_n}\right)^2} g(\delta k_\parallel L) + k_\parallel L \beta_\perp^2 (1-\beta_\perp^2) \frac{\Omega}{\omega} f(\delta k_\parallel L)\right] \tag{13}$$

but now g is as given by Equation 12 and

$$f(\delta k_\parallel L) = \left[\frac{\ell}{\ell^2 - (\delta k_\parallel L/\pi)^2}\right]^2 \left[\frac{1}{2}\cos \ell\pi \sin \delta k_\parallel L + \frac{2}{\pi} \frac{\delta k_\parallel L/\pi}{\ell^2 - (\delta k_\parallel L/\pi)^2} (1 - \cos \ell\pi \cos \delta k_\parallel L)\right]$$

The functions f and g are shown in Figures A-2, A-3 and A-4 for ℓ = 1, 2 and 3, respectively. It can be seen that the maximum values of the functions are relatively independent of mode number, ℓ, so it should be possible to make use of higher modes when desired.

D. LARGE-SIGNAL GAIN AND EFFICIENCY

Additional calculations were made to study the characteristics of the two-cavity amplifier. The calculations used an input cavity 1.5 λ long, a drift length of 3 λ, and an output cavity 2 λ long. The magnetic field was set for a slip of 6%.

Figure A-5 shows a calculation of output power as a function of input cavity field with the output cavity field held constant at a fairly low value. In effect, then, the curve shows the microwave component of beam current as a function of input cavity field. The curve indicates that beam current is very near to its maximum value for normalized input cavity fields ranging from 0.001 to 0.002. This range of input cavity fields corresponds to input power of 100 to 400 W with a Q of 519; which is the design value including beeam loading effects.

Figure A-6 shows output power as a function of output cavity field with a fixed input cavity field. This curve corresponds to the behavior that would be obtained if one varied the coupling between the ouput cavity and the external

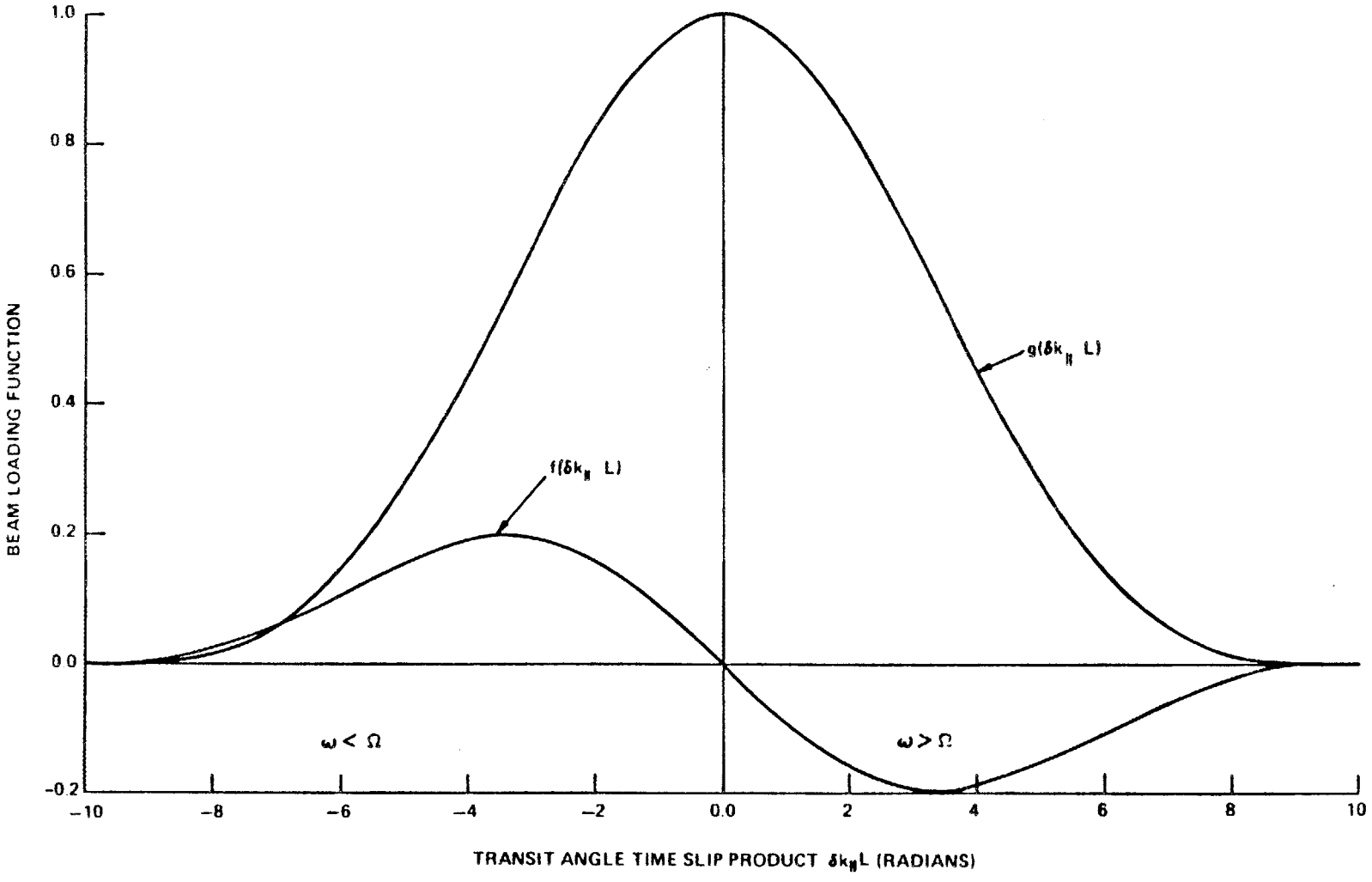

Figure A-2. Beam Loading Functions for Cavities One Half-Wavelength Long ($\ell = 1$)

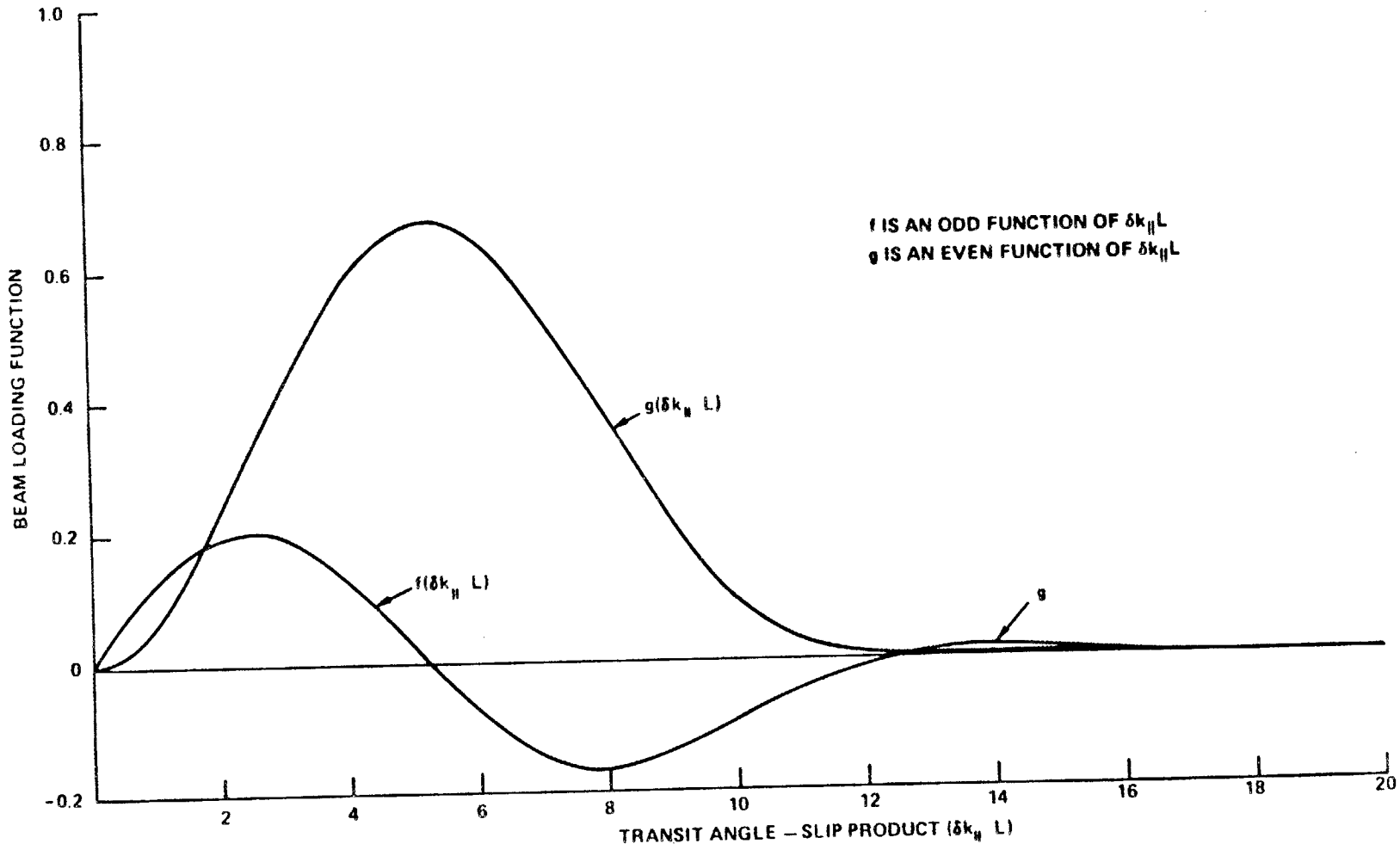

Figure A-3. Beam Loading Functions for Cavities Two Half-Wavelengths Long ($\ell = 2$)

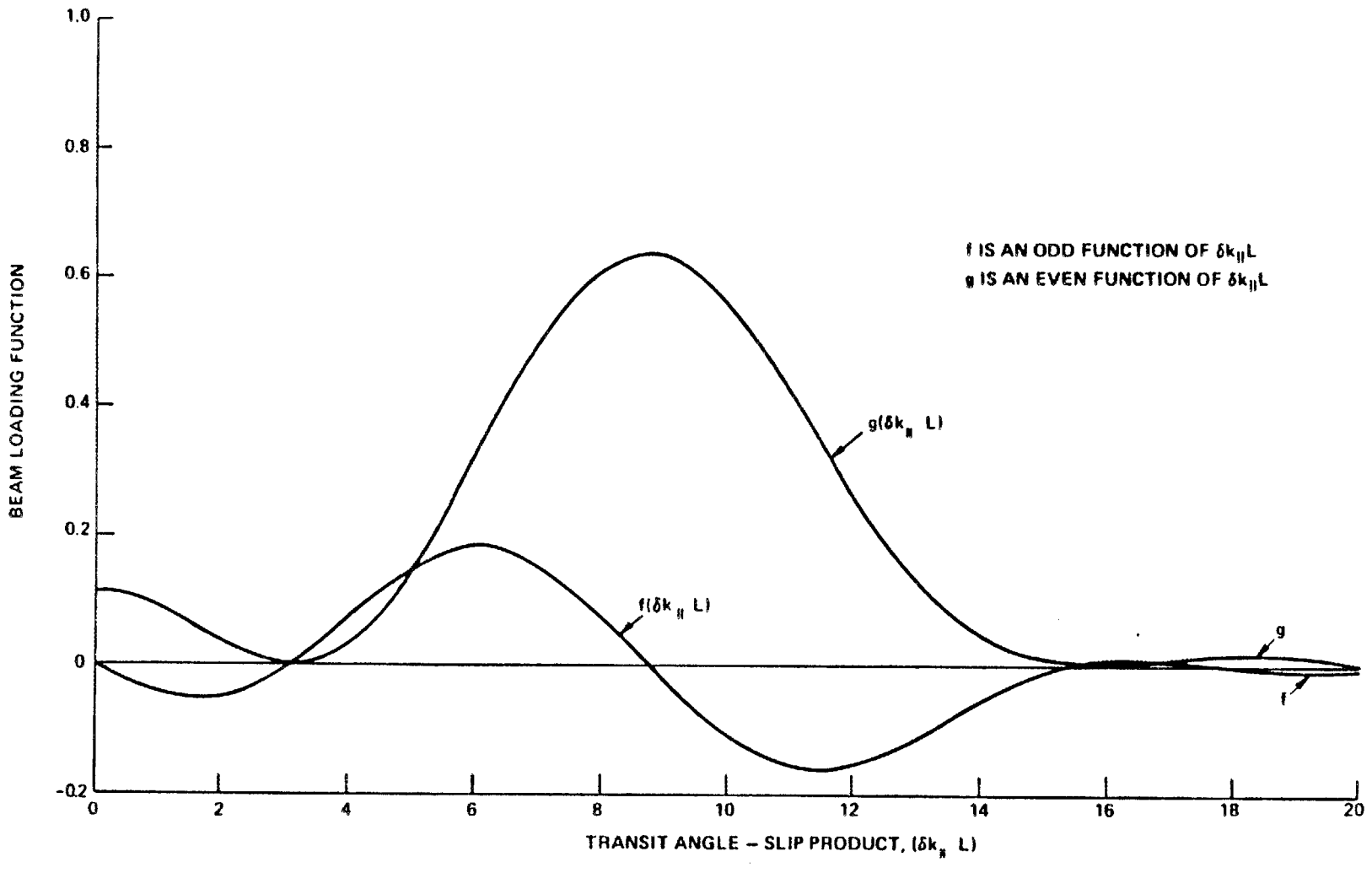

Figure A-4. Beam Loading Functions for Cavities Three Half-Wavelengths Long ($\ell = 3$)

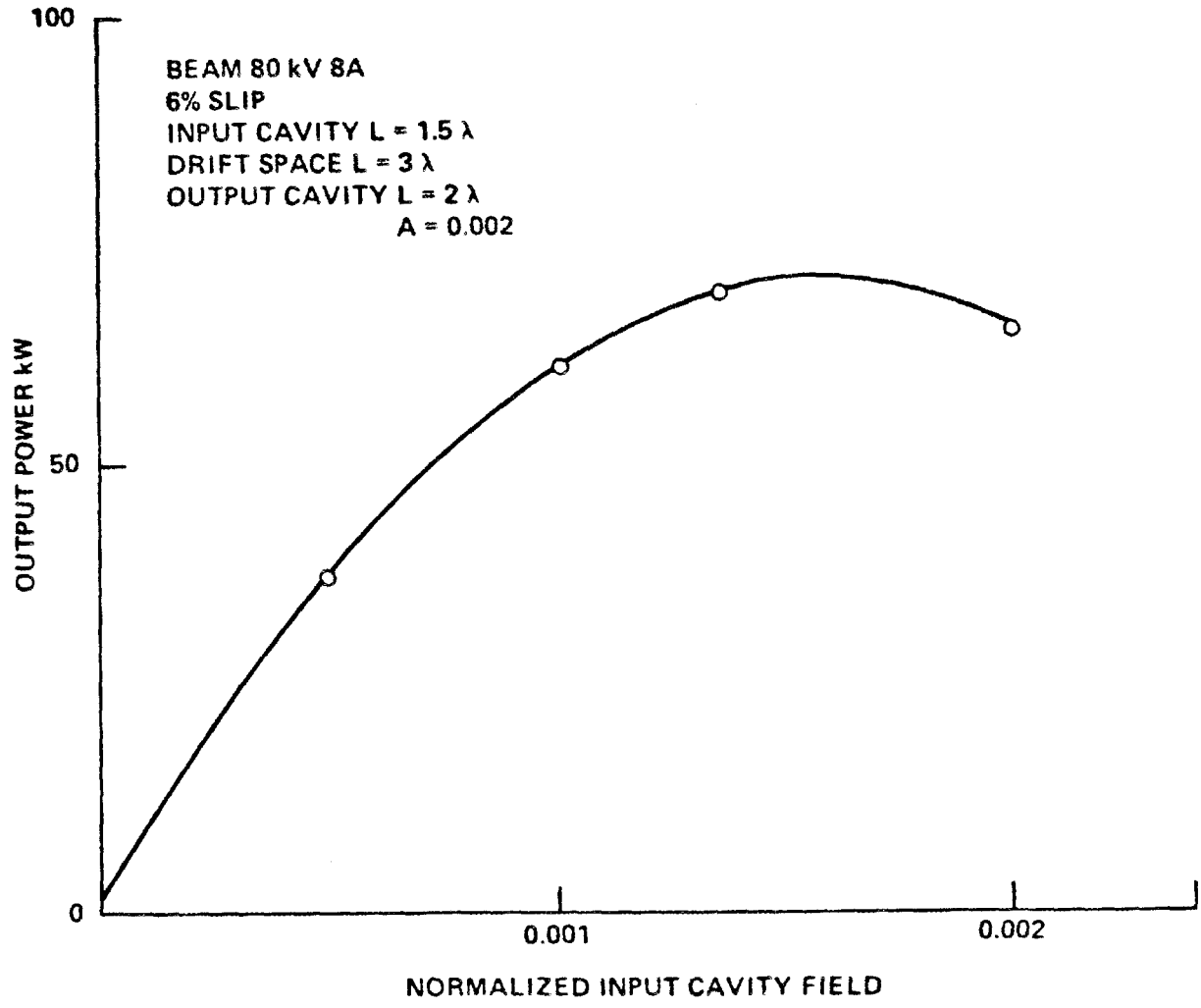

Figure A-5. Two-Cavity Amplifier Output Power Variation with Input Cavity Field

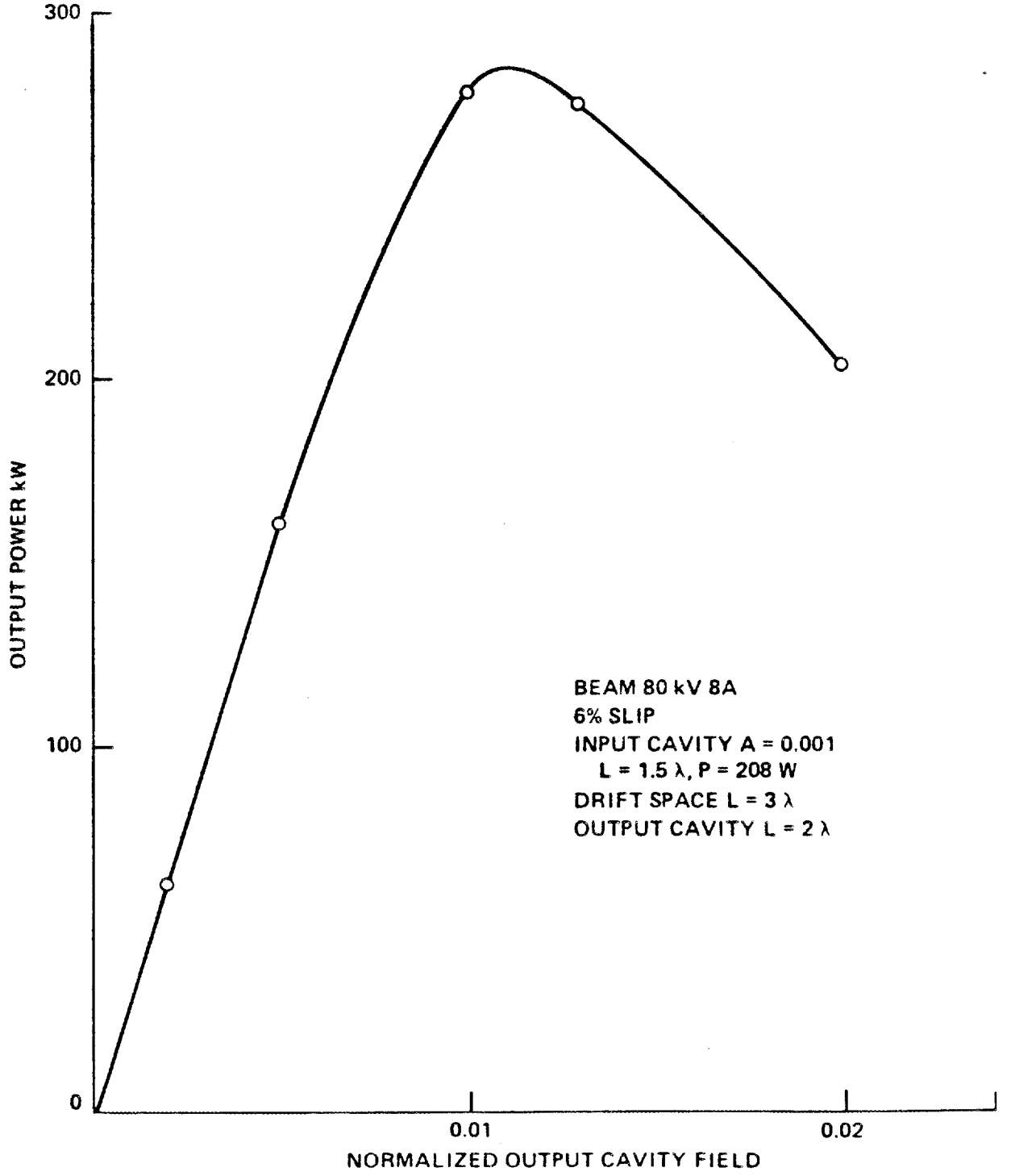

Figure A-6. Two-Cavity Amplifier Output Power Variation with Output Cavity Field

microwave load. The relatively sharp peak of this curve indicates that output cavity loading is a fairly important parameter.

In a previous quarterly report[4], calculations had been reported for input cavity amplitude = 0.001 and output cavity amplitude = 0.01. Reference to Figures A-5 and A-6 indicates that these values were sufficiently close to the optimum values to be kept as design values. Accordingly, the total loaded Q of the output cavity should be about 200.

INTERNAL DISTRIBUTION

1. P.F. Becher
2. L.A. Berry
3. T.S. Bigelow
4. J.M. Galyon
5. H.H. Haselton
6-8. G.R. Haste
9. H.D. Kimrey, Jr.
10. R.P. Jernigan
11. H.C. McCurdy
12. D.H. Metzler
13. O.B. Morgan
14. J. Sheffield
15. T.L. White
16-17. Laboratory Records Department
18. Laboratory Records, ORNL-RC
19. Y-12 Document Reference Section
20-21. Central Research Library
22. Fusion Energy Division Library
23. Fusion Energy Division Publications Office
24. ORNL Patent Office, ATTN: J.M. Spicer
25-26. TIC, Oak Ridge, Tennessee 37830

EXTERNAL DISTRIBUTION

27. M.N. Afsar, Francis Bitter National Magnet Laboratory, Massachusetts Institute of Technology, Cambridge, MA 02139.

28. D.S. Beard, Office of Fusion Energy, Office of Energy Research, ER-531 GTN, U.S. Department of Energy, Washington, DC 20545.

29. N. Bowen, Princeton University, Plasma Physics Laboratory, P.O. Box 451, Princeton, NJ 08540.

30. R.A. Dandl, AMPC, Inc., 2210 Encinitas Blvd, Suite P, Encinitas, CA 92024.

31. J.F. Decker, Office Fusion Energy, Office of Energy Research, ER-1, GTN, U.S. Department of Energy, Washington, DC 20545.

32. N.J. Dionne, Raytheon Co., Microwave and Power Tube Division, Waltham, MA 02254.

33. W. Friz, AFAL/DHM, Wright Patterson AFB, OH 45433.

34. T.V. George, Office of Fusion Energy, Office of Energy Research, ER-531, GTN, U.S. Department of Energy, Washington, DC 20545.

35. T. Godlove, Office of Energy Research, ER-20, GTN, U.S. Department of Energy, Washington, DC 20545.

36. M.J. Gouge, U.S. Department of Energy, Oak Ridge Operation, P.O. Box E, Oak Ridge, TN 37831.

37. V.J. Granatstein, Naval Research Laboratory, Code 6740, Washington, DC 20545.

38. G.M. Haas, Office of Fusion Energy, Office of Energy Research, ER-533, GTN, U.S. Department of Energy, Washington, DC 20545.

39. J.L. Hirshfield, Yale University, Department of Engineering and Applied Science, P.O. Box 2159, Yale Station, New Haven, CT 06520.

40. W.W. Ho, Rockwell International Science Center, 1049 Camino dos Rios, Thousand Oaks, CA 91360.

41. H. Hsuan, Plasma Physics Laboratory, Princeton University, P.O. Box 451, Princeton, NJ 08544.

42. K. Krause, MFE Electronics Engineering Department, Lawrence Livermore National Laboratory, P.O. Box 5511 (L-634) Livermore, CA 94550.

43. J.V. Lebacqz, Stanford Linear Accelerator Center, Stanford University, P.O. Box 4349, Stanford, CA 94305.

44. C.M. Loring, Varian Associates, Inc., EIMAC Division, 301 Industrial Way, San Carlos, CA 94070.

45. C.P. Moeller, GA Technologies, Inc., Fusion and Advanced Technology, P.O. Box 85608, San Diego, CA 92138.

46. R. Prater, GA Technologies, Inc., Fusion and Advanced Technology, P.O. Box 85608, San Diego, CA 92138.

47. R. Profant, Office of Nuclear Materials Production, DP 13.2, GTN, U.S. Department of Energy, Washington, DC 20545.

48. M.E. Read, Naval Research Laboratory, Code 6740, Washington, DC 20375.

49. D.B. Remsen, GA Technologies, Inc., Fusion and Advanced Technology, P.O. Box 85608, San Diego, CA 92138.

50. T.E. Romesser, TRW, 1 Space Park, Bldg R-1, Room 2044, Redondo Beach, CA 90278.

51. G. Simonis, Harry Diamond Laboratory, 2800 Powder Mill Road, Adelphi, MD 20783.

52. M.S. Sparks, Science Research Center, 9507 High Ridge Place, Beverly Hills, CA 90210.

53. B.L. Stallard, Lawrence Livermore National Laboratory, P.O. Box 5511 (L-637), Livermore, CA 94550.

54. H.S. Staten, Office of Fusion Energy, Office of Energy Research, ER-531, GTN, U.S. Department of Energy, Washington, DC 20545.

55. M.A. Stroscio, AFOSR, Bolling Air Force Base, Washington, DC 20332.

56. R.S. Symons, Litton Industries Inc., Electron Tube Division, 960 Industrial Road, San Carlos, CA 94070.

57. P.J. Tallerico, AT-5, Accelerator Technology Division, Los Alamos Scientific Laboratory, MS 821, P.O. Box 1663, Los Alamos, NM 87545.

58. J.J. Tancredi, Hughes Aircraft Company, Electron Dynamics Division, 3100 W. Lomita Blvd, Torrance, CA 90509.

59. R.J. Temkin, Plasma Fusion Center, Massachusetts Institute of Technology, 167 Albany Street AW16-254, Cambridge, MA 02139.

60. Director, U.S. Army Ballistic Missile Defense Advance Technology Center, ATTN: D. Schenk, ATC-R, P.O. Box 1500, Huntsville, AL 35807.

61. Office of Assistant Manager for Energy Research and Development, Oak Ridge Operations Office, Department of Energy, Oak Ridge, TN 37831.

VARIAN DISTRIBUTION

62. R. Berry
63. R. Bier
64-66. J.E. Camp
67. M. Caplan
68. C. Conner
69. L.J. Craig
70. S. Evans
71. K.L. Felch
72. F. Friedlander
73. L.J. Fox
74. H. Huey
75. G. Huffman
76. R.L. Ives
77. H.R. Jory
78. F. Kinney
79. A. LaRue
80. E. Lien
81. J.J. Manca
82. K. Miller
83. J.F. Moran
84. N. Lopez
85. J.F. Shively
86. E. Shih
87. S.T. Spang
88-89. A. Staprans
90. N. Taylor
91. Technical Library
92. G. Thomas
93-95. C. Frazer